Luc Illien

Time-dependent properties of the shallow subsurface

Groundwater and earthquake damage dynamics from seismic interferometry

Cumulative Dissertation
for obtaining the academic degree "Doctor of Natural Sciences" (Dr. rer. nat.)
in the discipline of *Geophysics*

Institute of Geosciences - University of Potsdam
Prepared at the Helmholtz Center - German Centre for Geosciences GFZ

Date of disputation: 5th May 2023
Grade: *Summa Cum Laude*

2023

Published online on the
Publication Server of the University of Potsdam:
https://doi.org/10.25932/publishup-59936
https://nbn-resolving.org/urn:nbn:de:kobv:517-opus4-599367

To my parents

Declaration

I hereby declare that this dissertation was prepared independently by myself, under the supervision of Prof. Niels Hovius and Dr. Christoph Sens-Schönfelder. This thesis is submitted in partial fulfillment of the requirements for the degree of *Philosophiae Doctor* at the University of Potsdam and has not been submitted to any other institution of higher education. The research was conducted at the Helmholtz Center - German Center for Geosciences (GFZ Potsdam). The manuscripts composing the main body of this work were collaborative efforts, and co-authors and their respective roles are defined in the author's contributions. Finally, the pronoun 'I' stands for Luc Illien in the 'Introduction' and 'Conclusion' Chapters.

Luc Illien
Potsdam, August 2023

Supervisor: Prof. Dr. Niels Hovius
Co-Supervisor: Dr. Christoph Sens-Schönfelder
Mentor: Dr. Florent Gimbert

Member of the committee:

Prof. Dr. Niels Hovius (Uni. Potsdam, Supervisor)
Prof. Dr. Parisa Shokouhi (Penn State University, External reviewer)
Dr. Marine Denolle (University of Washington, External reviewer)

Prof. Dr. Bodo Bookhagen (Uni. Potsdam, Chairman)
Prof. Dr. Fabrice Cotton (Uni. Potsdam, Internal examinator)
Prof. Dr. Thorsten Wagener (Uni. Potsdam, Internal examinator)

Acknowledgement

Well, finally. I don't know where to start. For the last ten years, I actually pictured this moment: the day I will write the acknowledgement section of my PhD dissertation. Time flies. If I ever would be at the start of this journey again, I would repeat the same things (and mistakes) all along. It is mostly because of the incredible people I crossed paths with. You are way too many, but I will try to give it my best shot.

First, I would like to thanks Niels Hovius for answering my e-mail on an early morning of 2016: You accepted my internship request immediately and here we are 6 years later. Thank you for your guidance, your thinking *outside the box* and your curious mind. I will remember your informal lessons for most of my life surely. I hope to see you soon for further discussions and field work campaigns. Obviously, the second name in this list is Christoph Sens-Schönfelder. It's not without saying that my ambient noise knowledge and passion would be nonexistent without you ! Thank you so much for your help, kindness

and the role of mentor you took on during covid times. To future collaborations and maybe rope climbing sessions !

Being at the GFZ meant having great professional and personal relationships. I would like to thanks the geomorphology section for having bared with me for four years. Christoff Andermann has paved the way for my Nepal work and initiated me to the topic of mountain hydrology. He is also a great friend. My other guide to Nepal was Kristen Cook, who provided me a good ear during difficult times from science writing to local gossip: I hope I returned the favor :) I would also like to thanks Jens Turowski for his dedication to the students of the section and to have introduced me to non-linear analysis. I will remember to have an objective look at my data ! The section was full of many other wonderful people from past members to more recent ones: special mentions to my former office mates Camilla and Marisa (of course Andi you are the best !). Finally, I would like to thank my second family at GFZ: the seismology section. You made me feel welcomed.

I had the chance of having incredible mentors. Florent Gimbert has been determining in my pursuit of science. Despite my moodiness at the time, our first trip to Nepal together is one of my most vivid memory (the journey in the jeep back to Pokhara ahah). Nicolas Brantut, if I can reach 50% of your drive and ethics one day, I would be at peace. My imagery of London will always be associated with you, Regent's street canal and the pints we had together at gig's venues. Thank you so much ! I also want to thanks Harsha Bhat for his kindness and help when I was still a master student. Working with you had only one flaw: it was way too short for all the fun and wisdom you encapsulate.

Since I started this journey, I made incredible friendships along the way. I want to start with my friends from ENS. Gaspard Farge, without him, my quest for 'The Truth' would be vain: thanks for introducing me to the physicist mindset I use everyday. Clement Berenfeld, my logistician friend (don't worry, one day you will be a campaigner), who kept me busy and answered my pesky phone calls during Covid. Of course, all the others from ancient times, Sevan, Cecile, Maude... Thank you so much ! At GFZ, Donovan Dennis, my creative partner in crime, I hope we keep on spreading boarding school stories forever. Niels Meijer, my man, thanks for being here through all the **, the lows, the highs and the madness. Zak, one day, we will open 'The office' in Nepal, count on me my friend. Peter, thanks a lot for our outdoors adventures ! Manon, thanks for teaming up with me during our time at IPGP ! Of course, I also want to thanks my crazy friends from the seismolab of University College London (Team B. represents). This list is long and I apologise. There are more people but you are way too many, I am so sorry !

In no particular order, I would like to thanks: the geomorphology team of Rennes for lighting the research spark in me, my teachers at ENS Paris for their encouragements and giving me opportunities, my guitar, the lovely people who helped me with my movie projects, my friends from 'countryside' as I like to call them (LCxHc never dies guys), Odin Marc for giving birth to my PhD topic and inspiring discussions, my improvisation group at the Scratch theater company, the 7Aplus climbing gym and my favorite psychonauts, Almuth Janisch for her help, kindness and support, Bhairab Sitaula for my Nepalese field work, Phoebe Bridgers, Antonius Golly for our late-night discussions at the bar and of course, Pelle and all my favorite Dutsch crew !

I would like to thanks my parents who have always told me to pursue my dreams, despite any background. I am grateful you pushed me and I know it was not always easy. You are my biggest source of inspiration. Vanessa, thanks a lot for being my annoying sister. At least you chose a wise partner :) And talking about partner, I am grateful to have mine in life: Elodie, your support and love across long distance or within tiny flats in Potsdam, Paris, Berlin or London were the main fuel for this work.

Finally, I hope that wherever she is, my grandma brags about having a grandson pursuing a PhD.

Today is the very best day (like most of days) :)

Contents

General Summary

The shallow Earth's layers are at the interplay of many physical processes: some being driven by atmospheric forcing (precipitation, temperature...) whereas others take their origins at depth, for instance ground shaking due to seismic activity. These forcings cause the subsurface to continuously change its mechanical properties, therefore modulating the strength of the surface geomaterials and hydrological fluxes. Because our societies settle and rely on the layers hosting these time-dependent properties, constraining the hydro-mechanical dynamics of the shallow subsurface is crucial for our future geographical development. One way to investigate the ever-changing physical changes occurring under our feet is through the inference of seismic velocity changes from ambient noise, a technique called seismic interferometry. In this dissertation, I use this method to monitor the evolution of groundwater storage and damage induced by earthquakes. Two research lines are investigated that comprise the key controls of groundwater recharge in steep landscapes and the predictability and duration of the transient physical properties due to earthquake ground shaking. These two types of dynamics modulate each other and influence the velocity changes in ways that are challenging to disentangle. A part of my doctoral research also addresses this interaction. Seismic data from a range of field settings spanning several climatic conditions (wet to arid climate) in various seismic-prone areas are considered. I constrain the obtained seismic velocity time-series using simple physical models, independent dataset, geophysical tools and nonlinear analysis. Additionally, a methodological development is proposed to improve the time-resolution of passive seismic monitoring.

Allgemeine Zusammenfassung

Die oberflächennahen Erdschichten sind ein Zusammenspiel vieler physikalischer Prozesse: Einige werden durch atmosphärische Einflüsse (Niederschlag, Temperatur...) angetrieben, während andere ihren Ursprung im Untergrund haben, beispielsweise Bodenerschütterungen aufgrund seismischer Aktivität. Diese Kräfte führen zu sich ständig ändernden mechanische Eigenschaften des Untergrunds, und damit auch Änderungen der Festigkeit der Geomaterialien der Oberfläche, sowie der Wasserflüsse. Als Gesellschaft leben wir auf der Erdoberfläche, und sind auf diese zeitabhängigen Eigenschaften angewiesen. Für unsere zukünftige, geographische Entwicklung ist es daher essentiell, die hydromechanischen Dynamiken des flachen Untergrunds zu verstehen. Eine Möglichkeit, die sich stetig ändernden physikalischen Eigenschaften unter unseren Füßen zu untersuchen, ist die Ableitung seismischer Geschwindigkeitsänderungen aus dem Umgebungslärm, mit Hilfe einer Technik namens seismische Interferometrie. In dieser Dissertation verwende ich diese Methode, um die Entwicklung der Grundwasserspeicherung, sowie durch Erdbeben verursachte Schäden zu untersuchen. Es werden zwei Forschungslinien untersucht, diese umfassen die Hauptkontrollen der Grundwasserneubildung in steilen Landschaften und die Vorhersagbarkeit und Dauer der transienten physikalischen Eigenschaften aufgrund von Erdbebenerschütterungen. Beide Dynamiken beeinflussen sich gegenseitig, sowie die Geschwindigkeitsänderungen im Untergrund in einer Weise, die schwer zu entschlüsseln ist. Ein Teil dieser Doktorarbeit behandelt daher auch diese Wechselwirkung. Wir verwenden seismische Daten, die unter verschiedenen klimatischen Bedingungen (feuchtes bis trockenes Klima) in mehreren, seismisch gefährdeten Gebieten erhoben wurden. Die gewonnenen seismischen Geschwindigkeitszeitreihen werden mit Hilfe einfacher, physikalischer Modelle, unabhängiger Datensätze, geophysikalischer Instrumente und nichtlinearer Analysen untersucht. Darüber hinaus wird eine methodische Entwicklung vorgeschlagen, um die zeitliche Auflösung des passiven, seismischen Monitorings zu verbessern.

Extended Summary

The Earth's surface is restless: the landscape always changes its shape and provides resources for our societies at variable rates. Some of the drivers of this overall time-evolution come from above the surface in forms of changing atmospheric conditions e.g precipitation, temperature. The other drivers originate from the opposite direction, at depth, and are caused by tectonic forces. These forces generate intermittent earthquakes, which generate ground shaking at the surface during the passage of seismic waves. All these external forcings induce time-dependent physical changes of the invisible shallow Earth's subsurface properties and modulate visible critical environmental surface features such as landslides rates or the availability of freshwater. Therefore, probing and constraining the state of the time-dependent subsurface at regular time-intervals are keys to anticipate spatial planning and environmental management.

In this dissertation, I estimate relative seismic velocity changes at high temporal resolution (from one day to one minute time-step) with seismic ambient noise correlations to study the hydro-mechanical evolution of the shallow subsurface. This technique, called seismic interferometry, is sensitive to the integrated physical state of the subsurface and has the advantage of using passive sources of energy at the Earth's surface. I employ an interdisciplinary approach in which I combine my seismological analyses with independent climatic and surface observations, geochemistry, simple empirical and physical modelling and other geophysical methods. The resulting work spreads over four studies from the Nepalese Himalayas to the Atacama desert in Chile. This range of geological and environmental conditions allows me to investigate the dynamics of groundwater in mountains and the key controls of earthquake damage due to seismic ground shaking. I also explore the interactions between the two topics and advance our understanding of seismic interferometry methods.

First, I focus my attention on a steep catchment of the Nepal Himalayas to investigate the groundwater recharge and discharge generation due to the Indian Summer Monsoon. I demonstrate the importance of the superficial moisture reservoir, often overlooked in mountainous environments, in controlling the hydrological fluxes. In this study, I test whether this reservoir has an impact on groundwater recharge in mountainous environments. For three monsoon seasons, I measure several parameters including relative seismic velocity changes, hydrological measurements and geochemistry. The obtained data shows that pre-monsoon precipitation does not affect discharge and groundwater storage and instead recharges the subsurface moisture reservoir. The onset of groundwater recharge only occurs when the superficial reservoir reaches saturation. A simple model accounting for this dynamics is proposed to model the resulting seismic velocity changes.

In a second study, I use the same Nepalese data and my local hydrological model to constrain the impact of the 2015 Mw 7.8 Gorkha earthquake on the subsurface. I quantify the effect of the relaxation phenomenon, in which the recovery of material properties after earthquake damage is not instantaneous. By fitting the velocity data, I model the transient damage effects (expressed as a drop followed by a postseismic recovery in the velocity changes) with a universal relaxation function that contains a unique maximum relaxation timescale for the main shock and the aftershocks, independent of the ground shaking intensity. The hydrological model is then used to study the residuals obtained with this assumption and characterise another transient behaviour, interpreted as an enhanced

permeability. These results indicate that the coupling between hydrological properties and the non-linear mechanical recovery after earthquake damage can be disentangled with seismic interferometry and that the relaxation phenomena may not be dependent on ground shaking.

Moving away from the wet Himalayan conditions, I process seismic data from a dense array located in the Atacama desert of Chile in a third study. The dry conditions allow me to focus on constraining the effect of ground shaking on subsurface properties without hydrological effects. Seismic velocity changes were estimated at a 10-minutes resolution for a two weeks period. A moderate ground shaking event (PGV $\sim$ 1 cm/s) induced a velocity drop of $\sim$0.5% at this time resolution and was succeeded by a two-days recovery. With the 16 stations array, I test for the ergodic property of seismic interferometry, which permits to observe the recovery due to the relaxation down to a one-minute resolution. Moreover, I combine this analysis with imaging and inversion techniques to show that the relaxation phenomenon at this site is located in hard rocks in the first 200 m.

Finally, I address the predictability of the duration of the relaxation phenomena after earthquake damage. I analyse the successive effect of two large earthquakes (the 2007 Mw 7.7 Tocopilla and 2014 Mw 8.2 Iquique earthquakes) on seismic velocity changes. After quantifying the recovery timescales after these two events and their aftershocks, I propose that the relaxation duration is a function of the current state of the subsurface when perturbed by earthquakes. This interpretation suggests that earthquake damage dynamics in the Earth's near-surface is predictable. I reconcile my observations with existing physical frameworks by considering the superposition of different populations of damaged contacts and voids, each with their own timescales of recovery, in the subsurface.

All together, these studies push further our understanding of the time-dependent properties of the shallow subsurface through the study of two parameters ubiquitous to the near-surface: the water content and voids/cracks dynamics. I show that these parameters are coupled in the field and are better understood with an interdisciplinary approach. Despite this complexity, the simple models brought in this dissertation reproduce the first-order evolution of the relative seismic velocity changes and highlight the salient features to investigate in future research: the location, type and storage of water reservoirs in the near surface and the characterisation of the density and distribution of flaws within these shallow layers. These modulate the delivery of exploitable water and the long-term response to seismic ground shaking.

List of Figures

Chapter 1

Introduction

We all have made the experience of travelling back to a cherished place but only soon to realise that the landscape has changed: our favorite secret place is now a distant childhood memory. There are no natural systems that are fixed in time. This is a striking feature of Earth surface observations: if one waits long enough, everything will move from the pebble in the river to the large landslide that gave up to gravity. These time-dependent behaviours directly impact how our societies settle, rely and interact with the Earth's surface and its shallow layers. As a consequence, taking a fixed snapshot of these processes is undeniably not sufficient to make accurate predictions.

In this thesis, I have focused my attention to understanding the impact of major external forcings of the Earth's surface. Some of these driving perturbations come from above in forms of precipitation or temperature changes. On the other side, the landscape is constrained from below by tectonic forces inducing incoming seismic waves. These restless processes induce a continuous change of properties in the shallow subsurface, which in turn influence Earth surface observations. To monitor the geomaterials under our feet at high-temporal resolution, I used a specific probe: the seismic ambient noise, the wavefield constantly recorded by seismometers.

First, I briefly review the remarkable time-dependent behaviours exhibited by these systems and the corresponding observations of seismic velocity changes previously retrieved and reported from ambient noise. This part naturally leads to my research outline and the foundations for the four separate studies of the dissertation. Note that this introduction contains citations anterior to the first publication of this dissertation to depict the existing science prior to the doctoral research.

1.1 Time-dependent observations at the Earth's surface

In this section, I present some salient time-dependent behaviours that were discovered in the subsurface. First, I focus on the complex boundary conditions that govern groundwater storage in steep landscapes. In a second part, I review transient surface observations after large earthquakes. The literature review presented in this section is highly non-exhaustive for the sake of brevity. More comprehensive overviews can be found in the paper's chapters.

1.1.1 Groundwater storage in steep landscapes

The underground storage of water is at the core of many surface processes and societal challenges and is therefore one of the most important variables in the dynamic Earth subsurface. It modulates flooding (Bosserelle et al., 2022), contaminants transfers (Li et al., 2021) and landsliding (Iverson, 2000), and constitutes a major part of our freshwater resources (Carrard et al., 2019). In the Himalayas, the groundwater reservoir has been the main source of discharge (Andermann et al., 2012) but it has received relatively less attention in comparison to melt water in science-to-policy proceedings like the recent IPCC reports (Jiménez Cisneros et al., 2015; Regine Hock, 2019). Nevertheless, mountainous

environments provide a major part of the worldwide surface runoff when compared to lowlands runoff contribution (Fig. 1.1) (Viviroli et al., 2007), hence earning them the reputation of 'water towers' (Immerzeel et al., 2010).

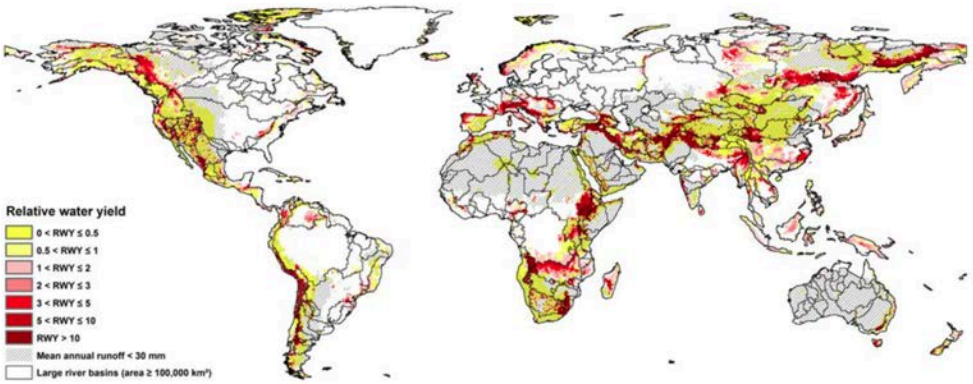

Figure 1.1: *Contribution of runoff generated in mountains relative to lowland contributions.* Values above 1 (from pink to red) indicate the mountainous areas in which more discharge is generated in comparison to the lower parts of basins with which they are connected. Map from Viviroli et al. (2007).

Through a simple hydrological mass balance equation, the physical representation of the underground water storage dynamics is inherently time-dependent due to its ever-changing boundary conditions :

$$\frac{dS}{dt} = P - E - Q. \tag{1.1}$$

In this relation, P, E and Q are the precipitation, evapotranspiration and discharge fluxes (depth per time), typically averaged over an entire catchment. S is the water stored underground (unit of depth) in different reservoirs such as soil moisture or water stored in the saturated groundwater bedrock aquifers.

Each of the fluxes presented in equation (1.1) can be measured in the field but the estimation of S remains a challenge as it is not directly observed. Classically, estimations of S are performed with boreholes that only give a point-based measurement of the local groundwater level. In steep landscapes, drilling wells often presents logistical challenges and fail to represent an averaged measure of S due to heterogeneous complexities(Dralle et al., 2018). Another complementary technique is to measure gravity anomalies with the GRACE satellite (Chen et al., 2016). This method has the advantage of integrating all the reservoirs included in S in a non-destructive fashion. However, it fails to capture the local dynamics at the finer scale of small mountainous catchments due to its large spatial resolution, downscaled to about 100 x 100 km.

A step change for monitoring storage in steep catchments came with the paper of Kirchner (2009). Considering equation (1.1) as a dynamical system, he showed that S can be estimated from measuring Q in hydrograph time-series. Considering the recession limb of these hydrographs (Fig. 1.2a), one can assume that $P \ll Q$ and $E \ll Q$. Under these conditions, the discharge Q is only a function of storage S through a sensitivity function g:

$$\frac{dQ}{dS} = g(Q). \tag{1.2}$$

This function can be integrated to find S, while g can be obtained by measuring the rate of discharge change dQ/dt during recession period (Fig. 1.2ab) with the approximation

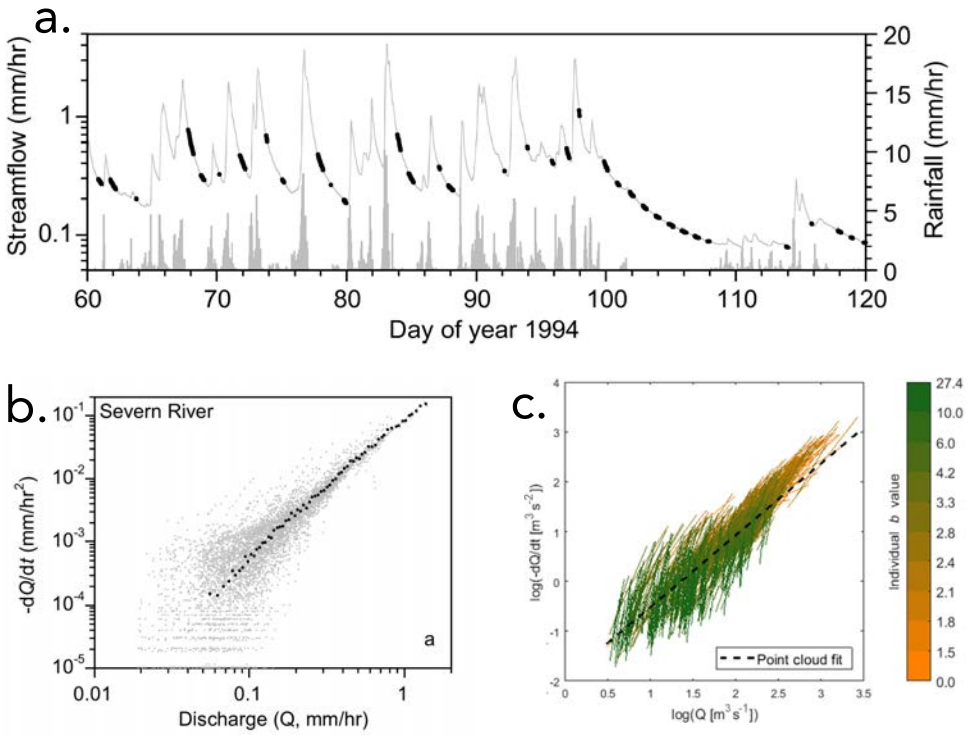

Figure 1.2: *Illustration of a recession analysis and impact of time-dependent boundary conditions.* **a.** A classic precipitation time-series with the local hydrograph. The black dots indicate the periods in which dQ/dt is calculated. **b.** The recession plot from the data shown in **a.**. Subplots **a** and **b** are from Kirchner (2009). **c.** Time-dependent recession analysis. Each curve corresponds to a different recession event. The colour indicates the value of b, the exponent of the power law 1.4. Plot is from Jachens et al. (2020).

$$g(Q) \approx \frac{-dQ/dt}{Q}. \tag{1.3}$$

For an ideal single aquifer (Brutsaert & Nieber, 1977; Rupp & Selker, 2005), a power law is predicted such as

$$-dQ/dt = aQ^b. \tag{1.4}$$

This law is extensively fitted in the literature in recession analysis (Kirchner, 2009; Roques et al., 2017), and the recession parameters a and b completely characterise the aquifer behaviour and determines the storage prediction in the catchment. Although this development is elegant, storage S has remained under discussion: the values a and b are highly biased by the parameter estimation method (Roques et al., 2017) and highly time-dependent (Jachens et al., 2020), even when measured in the same catchment. This time-dependency is evident when comparing estimates of a and b that were obtained after different recharge events (Fig. 1.2c). More specifically, inter-arrival time, antecedent precipitation conditions and magnitudes have been shown to influence the recession parameters, which suggests a seasonal influence on storage recharge.

The previous equation and the recession framework make the assumption of a single aquifer, directly recharged by precipitation and feeding the river discharge. Often, these simplifications are being made in hillslope hydrology. In a seminal string of studies (Montgomery et al., 1997; Anderson et al., 1997; Torres et al., 1998), natural and artificially-induced rainfall was found to take complex pathways through the subsurface of a steep hillslope in the Oregon Coast Range. Volumetric measurements showed that a large proportion of the discharge water and the saturation of the soils was controlled by fast pathways through the shallow bedrock underneath the surface slope (Montgomery et al., 1997; Anderson et al., 1997). However, this pattern was heterogeneous and ultimately, a direct causal link between precipitation and discharge was only established when a steady pore pressure gradient was developed in the vadose zone (Torres et al., 1998). More recently, Rempe and Dietrich (2018) have shown that the moisture reservoir can be of an important volumetric size due to a storage not only in soils but also in the weathered rocks in the subsurface (Fig. 1.3). Consecutive measurements during several years highlighted a finite seasonal maximum capacity of this reservoir. The associated storage was not hydraulically connected to streams (Dralle et al., 2018) which suggests that the link between S and Q shown in equation (1.2) may be seasonally dependent and a source of bias in recession curve analysis. These observations highlight a changing complex boundary condition to the surface due to processes in the unsaturated zone.

Lastly, the complex water flow patterns modulating the boundary conditions are not the only time-dependent variables in hydrological mountain systems. In fact, the fundamental properties of the rocks constituting the aquifers can also experience a transient behaviour as shown by permeability changes following large earthquakes. This phenomenon is reviewed in the next section.

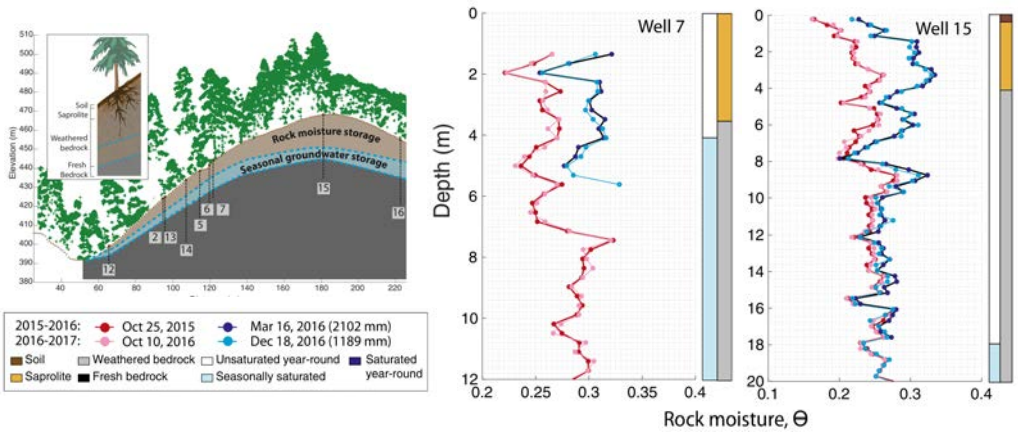

Figure 1.3: *Rock moisture profiles in the subsurface.* The schematic shows a cross section of a hillslope and the location of wells into the groundwater system. Corresponding profiles for two of them are shown. The profile colours correspond to different time-periods described in the legend inset. The similarity of the profiles in 2015-2016 and 2016-2017 suggests a finite storage capacity. Modified from Rempe and Dietrich (2018).

1.1.2 Transient perturbations introduced by earthquakes

Severe ground shaking during earthquakes can cause damage to infrastructure and widespread landsliding (Keefer, 1994; Meunier et al., 2007; Marc et al., 2016). These

coseismic effects are well known but the extent of their legacy in shallow subsurface properties is less familiar. Nevertheless, transient postseismic surface observations have shown that the landscape carries a real 'memory' of these seismic effects that can last for several years.

Co-seismic release of water in streams has been reported for several large earthquakes (Manga et al., 2003; Montgomery & Manga, 2003; C. Y. Wang et al., 2004; Mohr et al., 2017). The corresponding hydrographs often exhibit a step change in discharge not long after the onset of ground shaking (Fig. 1.4b), after which the streamflow restores to background values on timescales that can vary from a few days to a few months (Mohr et al., 2017). The origin of these changes is debated, with hypotheses that include transient groundwater flow due to coseismic changes in the hydraulic head (Mohr et al., 2017) or ground motion shaking water out of soils(Mohr et al., 2015). A few observations point at a temporary increase of permeability in the feeding aquifer(Manga et al., 2012; Hosono et al., 2020). The evolution of stable isotopes in wells, springs, streams and precipitation water after the 2016 Kumamoto earthquake indicates new pathways through a fractured aquifer (Hosono et al., 2020). This chemical signal corroborates many physical observations in groundwater wells. Hydraulic head measurements show either an increase or a decrease of the water table depth (Montgomery & Manga, 2003; Shi et al., 2015; Hosono et al., 2019) indicating a reorganisation of the groundwater system. Importantly, the permeability around these wells inferred from the phase of tidal variations shows an initial increase after the passage of seismic waves (Elkhoury et al., 2006) that can be followed by a recovery phase of several years Xue et al. (2013) (Fig. 1.4c). Potential candidates for this permeability increase and healing mechanism are the mobilisation of particles in the fracture system and poroelastic effects (Manga et al., 2012) or aquitard breaching (C. Y. Wang et al., 2016). A minimum threshold in ground motion is necessary to initiate most of these phenomena but interestingly, recent work has shown that the groundwater discharge to streams release does not increase further when past the initiation threshold (Mohr et al., 2018).

Moving away from the aquifer system, other transient perturbations are observed at and near the Earth's surface after major earthquakes. The study of Marc et al. (2015) showed sustained high landslides rates in the aftermath of four large earthquakes (Marc et al., 2015). From satellite imagery, mapped postseismic landslide areas were shown to be more elevated for equivalent meteorological forcing during the preseismic period (Fig 1.4d). Analogous to permeability, these landslide rates returned to background values with a recovery timescale that ranged from one to to four years. The landslides rooted at superficial depths (0-10 m, (Marc et al., 2015)) suggesting that the damage-recovery mechanisms for these perturbations occur in the layers immediately below the Earth's surface. The weakening induced by these processes may enhance the transfer of hillslope materials to rivers, which would explain the sustained high sediment load that is observed for many years after large earthquakes (Hovius et al., 2011). Earthquake-induced landslides can also cause a decrease in overall vegetation activity of several years as shown by NDVI values (a remote-sensing indicator of leaf colour) due to damage to a large portion of soils and trees (Zhang et al., 2018; Gan et al., 2019; Allen et al., 2020). The case of the Wenshuan earthquake is reported in Figure (Fig 1.4a). Vegetation recovery can take up to several years after the initial phase of degradation (Gan et al., 2019).

The striking observation of similar damage-recovery dynamics at different depths points at a universal underlying mechanism. This mechanism also affects the properties of aquifers in which groundwater is stored. To unravel its possible physics and key controls, we need an investigation tool that is sensitive to the hydro-mechanical properties of the subsurface with a well resolved temporal resolution. In the following, I argue that seismic interferometry

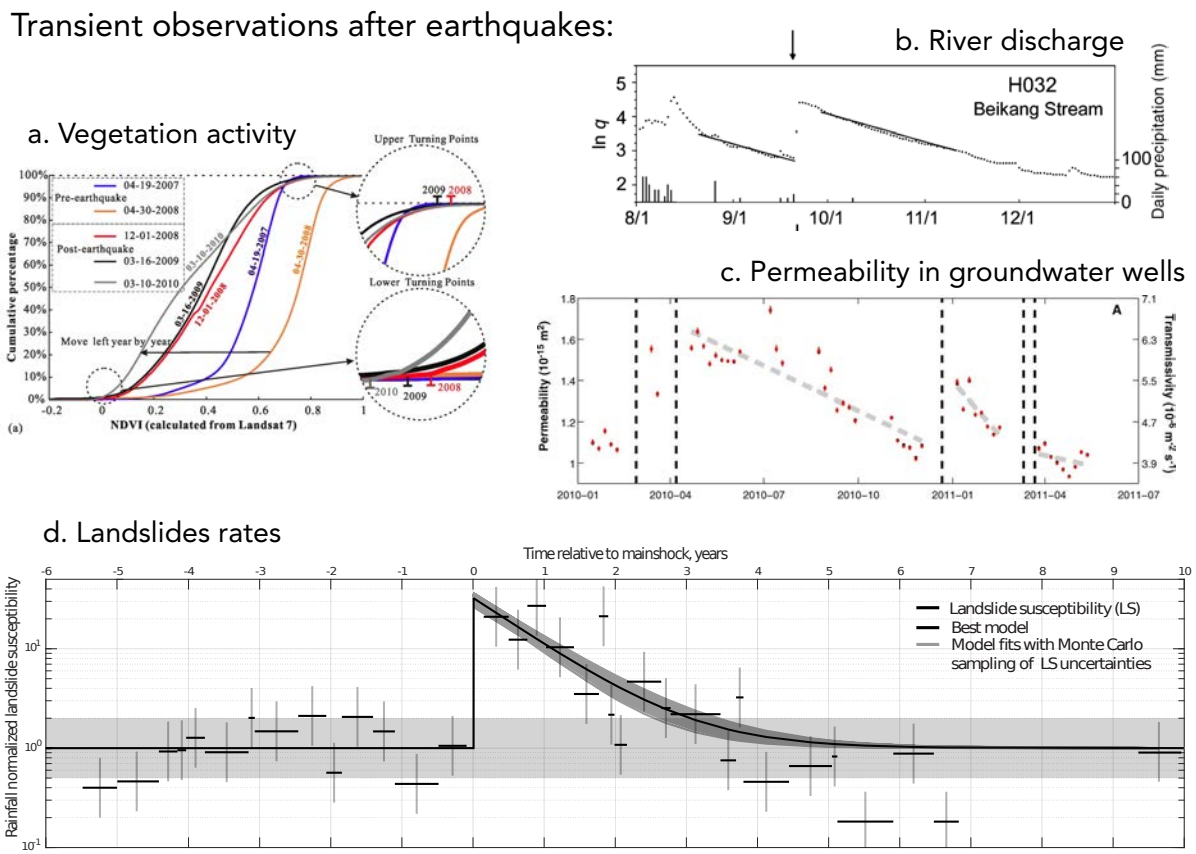

Figure 1.4: *Observations of transient surface response after large earthquakes:* **a.** Cumulative NDVI (Normalised Density Vegetation Index) pixel values for years prior and after Wenshuan earthquake, China. High NDVI values signal more greenness and vegetation density in the satellite image. From Gan et al. (2019). **b.** Increase in streamflow following the Chi-Chi earthquake, Taiwan. The arrow indicates the onset of groundshaking. From C. Y. Wang et al. (2004). Note that the earthquake occurred during a period without significant rainfall. **c.** Transient permeability evolution in groundwater wells in the Wenshuan fault zone area. Dashed lines indicate the onset of the teleseismic events. Modified from Xue et al. (2013) **d.** Transient landslide rates induced by Chi-Chi earthquake. From Marc et al. (2015).

with ambient noise is such a method.

1.2 Using seismic interferometry for monitoring subsurface changes

The seismic ambient noise wavefield allows for the monitoring of relative seismic velocity changes in the subsurface. Here, I present the main concepts behind this method and show applications related to groundwater and earthquake damage monitoring.

1.2.1 Estimation of seismic velocity changes from the ambient noise wavefield

The Earth's surface is the theater of many processes: rivers flowing, storms in the oceans, meteorological conditions, anthropic activities ... The resulting forces generate continuous sources of seismic energy that are recorded by seismometers, the so-called seismic ambient noise wavefield. The early recognition of these seismic sources dates back to the start of the 20th century (Cook & Dietze, 2022) but for a long time, the background ambient noise was mostly considered as a nuisance to be minimized in order to have a clear view of earthquake signals. At a first glance, it is true that the noise wavefield does not seem to carry any information (Fig. 1.5a). Its apparent randomness is due to the sources forever shifting in time and space. In the late 50's, pioneering work from Aki showed that deterministic useful information about the subsurface structure can be extracted from these signals by cross-correlating the ambient noise recorded at different stations (Aki, 1957). With the advancement of computing power and the improvement of seismic stations, the idea of Aki has seen a revival in the early 2000's under the umbrella term 'seismic interferometry'. The field has persistently expanded since.

The cross-correlation between two seismic waveforms at positions A and B can be expressed as

$$\langle C_{AB}(t) \rangle = \int u_A(\tau) u_B(t+\tau) d\tau. \tag{1.5}$$

where u indicates the seismic trace and τ is the lapse time of the correlation function. Because the ambient noise is a diffuse wavefield, the correlation C_{AB} must be averaged over a long time (typically $\sim$ days, hence the angle brackets) for any information to emerge from the correlation (Fig. 1.5a). In simple words, the correlation averaging between A to B (or B to A with C_{BA}) converges to a virtual seismogram that would be recorded if a wave would leave from A and would be recorded at B (and vice-versa). When the noise sources are randomly distributed and isotropic in space, this convergence leads to C_{AB} being equivalent to the Green's function between the receivers (Lobkis & Weaver, 2003). The ideal condition of isotropic source distribution is rarely met in nature but for monitoring purpose, a localised source of noise is acceptable as long as it is statistically stable in time (Hadziioannou et al., 2009). The resulting correlations contain a ballistic arrival (often surface waves (Shapiro, 2019)), that is followed by coda waves. Because the coda waves travel longer scattered paths through the medium, they are more sensitive to small *in situ* physical changes and are therefore often used for monitoring tasks. To emphasize these coda waves, one can also consider the correlation between the components of a single station (Hobiger et al., 2014), or autocorrelations, to mostly retrieve local scattered waves. The correlation C can always be computed to build a time-series as long as the source conditions at all monitoring intervals are similar: this is a remarkable advantage compared to active seismic methods.

When all correlations are computed, they can be arranged in a matrix (the correlogram) in which the coda waves can be compared. Despite not knowing the absolute paths of the waves, we can estimate the evolution of their relative velocities dv/v. Assuming that the velocity change in the medium is homogeneous, the coda waveform will be stretched or compressed proportionally to the velocity change:

$$\epsilon = \frac{dv}{v} = -\frac{dt}{t}. \tag{1.6}$$

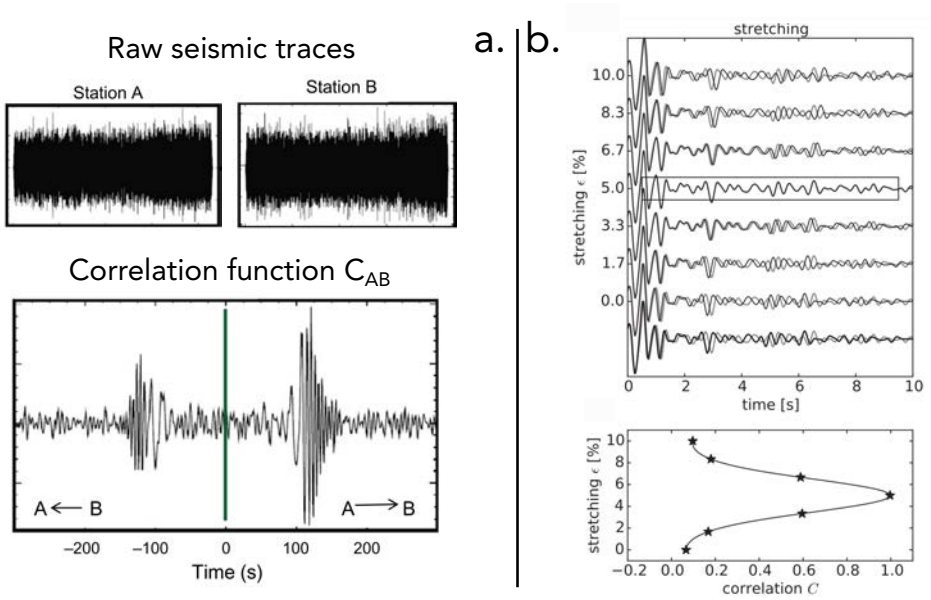

Figure 1.5: *Ambient noise cross-correlation concept and estimation of relative seismic velocity changes with the stretching technique.* **a.** Top panels show two seismic random noise traces. The correlation of these two signals can be seen on the lower panel. Negative and positive lapse time stand for the direction of the correlation. From Obermann and Hillers (2019). **b.** The top panel illustrates the stretching algorithm in which the correlation function in black is stretched to match the grey correlation function. This process leads to the exploration of the best fitting stretching factor ϵ shown on the lower plot. From Sens-Schönfelder and Brenguier (2019).

In this equation, ϵ is the stretching coefficient (Sens-Schönfelder & Wegler, 2006). To calculate the evolution of dv/v, we extract a reference, often taken as the averaged cross-correlation of the whole monitored period (dark waveforms in Figure 1.5b) and numerically stretch it along several tested values for ϵ. For each increment of ϵ, the observed correlation function is then compared to the modified reference at monitoring time t_i. The value of ϵ leading to the best correlation between the reference and the correlation function will be retained as the velocity change (Fig. 1.5b). This process can be repeated until reaching the last correlation function corresponding to time t_N. Note that a specific time-window ($[\tau_1, \tau_2]$) in the correlation functions can be used for the stretching technique. The choice of the time window allows for emphasizing a larger sampling depth and surface around the stations towards late times τ (Pacheco & Snieder, 2005; Obermann et al., 2013). Other methods can be used to measure velocity changes, but the stretching technique is the anchor point of this dissertation due to its past reliability in countless studies and stability with noisy correlation functions.

More relevant details of seismic interferometry are described in the later chapters, notably the choice of pre-processing techniques to remove the effects of sudden high-amplitudes signals (such as earthquakes) prior to correlation.

1.2.2 Groundwater dynamics

The first study utilising seismic noise to monitor velocity changes in the subsurface was performed on the Merapi volcano (Sens-Schönfelder & Wegler, 2006). The inferred seismic

velocity changes were highly anti-correlated with the daily precipitation rates, suggesting that groundwater variations influenced subsurface properties. The presence of water in rocks changes their elastic moduli due to pore pressure variations (Gueguen & Palciauskas, 1994). In poroelasticity theory, rocks have two elastic moduli, one for the unsaturated state and another for the saturated state with lower S-wave velocities for the latter (Gueguen & Palciauskas, 1994). The coda waves often exhibit a shear wave sensitivity due to a favored energy equilibration towards S-waves at late lapse time τ in the correlation function (Snieder & Page, 2007). In consequence, the relative velocity change dv/v will drop if the groundwater level rises and the proportion of saturated medium increases in the volume probed by the waves.

The influence of groundwater fluctuations on dv/v has since been reproduced in different settings: with a borehole array drilled into an earthquake rupture plane in Taiwan (Hillers et al., 2014), at the crustal scale in Japan (C. Y. Wang et al., 2016), and on a slow-moving landslide (Bontemps et al., 2020). However, the idea of using precipitation-induced dv/v variations to monitor groundwater for freshwater resources applications is fairly recent. The study of Lecocq et al. (2017) used four historical German seismic stations to infer the groundwater storage dynamics during $\sim$ 30 years. Another similar proof of concept was conducted in the San Gabriel Basin, an area prone to consecutive droughts (Clements and Denolle (2018), Fig. 1.6). These studies show the potential of seismic interferometry for monitoring groundwater storage at any location in the vicinity of a seismic station. In mountainous areas, the logistic advantage is substantial as drilling boreholes in remote settings is not always an option, and the mountain borehole network is sparse as a result. Furthermore, the average spatial sensitivity of the method (probing volumes of $\sim 10^1$ to 10^3 m^3) allows to bridge the gap between point-based well observations and large scale gravimetric measurements and target specific locations in a catchment.

The seismic velocity changes dv/v are often modeled with a simple hydrological framework that can be justified by a few direct co-located observation of relative velocity changes and groundwater depth changes in wells. These changes are directly proportional to the hydraulic head height $h(t)$ through a decay parameter a and can be modelled with the expression

$$\frac{dh}{dt}(t) = \frac{P(t)}{\Phi} - ah(t) \tag{1.7}$$

in which P is the precipitation (often measured at the time resolution of the dv/v measurement) and Φ is the porosity of the aquifer reservoir. It has been reported that variations of the water table on the order of 10^{-2} m are sufficient to induce a change in relative velocity changes (Voisin et al., 2017; Clements & Denolle, 2018). In the details, this framework can change slightly (pore pressure can also be modelled with an error function (C. Y. Wang et al., 2016)) but most of resulting models predict approximately the same dynamics: a very fast transfer of precipitation to the groundwater reservoir and an exponential decay of the water table as described by Darcy's law. At the first order, this modelling effort succeeds in reproducing precipitation-induced velocity changes (Sens-Schönfelder & Wegler, 2006; Hillers et al., 2014; C. Y. Wang et al., 2016) but the validity of equation (1.6) is limited to the situation of a highly permeable subsurface with a single reservoir or as an average representation of large areas. The potential complexity of the near-surface and the unsaturated zone processes mentioned earlier in the introduction may affect the velocity in ways that have not yet been probed.

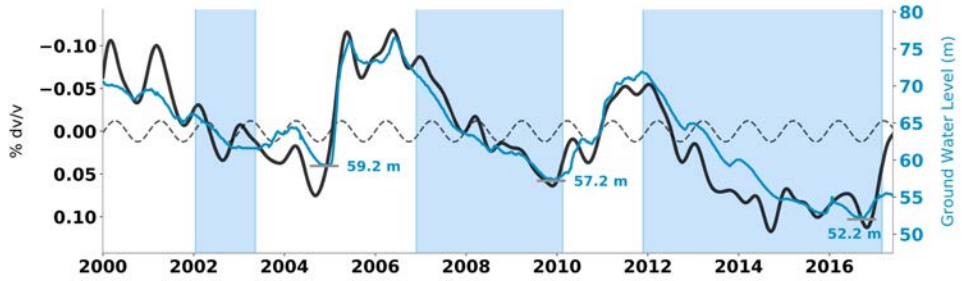

Figure 1.6: *Seismic velocity changes and groundwater depths in the San Gabriel Basin, California.* The black line indicates the relative seismic velocity changes averaged over the whole basin after correction for thermo-elastic strain (dashed line). The y-axis is reversed. The blue line shows the groundwater depth in a local borehole for the same time interval. From Clements and Denolle (2018).

1.2.3 Earthquake damage and induced relaxation

Early interferometry studies carried in Niigata (Wegler & Sens-Schönfelder, 2007) and Parkfield (Brenguier et al., 2008) aimed at monitoring changes of fault zone properties due to seismic activity. In this context, the evolution of seismic velocity in the subsurface followed a recurring pattern: the seismic velocity dropped sharply at the co-seismic time and recovered during a post seismic period found to last up to some years. These observations were initially attributed to 'healing' phenomena acting in the fault zone. The reproduction of these results for many earthquakes (Sawazaki et al., 2009; Nakata & Snieder, 2011; Sawazaki et al., 2018; Viens et al., 2018) has revealed that these velocity changes are emphasized when using high-frequency noise, more sensitive to shallower depths. This trend has led to a community consensus that the response of near-surface materials is responsible for most of the drop and recovery signature due to non-linear behaviour induced by dynamic strain during ground shaking. Hence, repeated perturbations by seismic waves cause the Earth surface to change its properties in multiple cycle of velocity reduction and recovery (Gassenmeier et al., 2016). These continuous changes can be coined as Non-Linear Mesoscopic Elasticity, with the term mesoscopic used to distinguish the field scale observation from pre-existing experimental results, which are described in the next paragraph.

The behaviour shown in field observations has been documented in the laboratory since the 90's under the name of 'slow dynamics' or "relaxation" (TenCate & Shankland, 1996; TenCate et al., 2000). During experimental rock deformation, seismic velocity and/or resonant frequencies (both being a function of elastic moduli and density) can be measured with piezo-electric transducers at a scale of $\sim 10^{-2}$ m. This approach has helped to establish the universality of the time-dependent phenomena. First, slow dynamics have been observed in a wide variety of rocks (Fig. 1.8, (TenCate et al., 2000; Brantut, 2015; Shokouhi et al., 2017)) and media such as granular assemblies (Knight et al., 1995) and concrete (TenCate et al., 2000). The onset of relaxation can be caused by either a dynamic strain perturbation (of a mere 10^{-6} in the seminal study of TenCate et al. (2000)) or by a static strain increase (Brantut, 2015). The recovery shape is always logarithmic and can last from a few seconds (Shokouhi et al., 2017) to several years (Brenguier et al., 2008). The fact that there is overlap between laboratory and field-scale observations further underlines the likely scale-invariance and universality of this behavior.

Despite the convergence of research findings at different scales and settings, a unified

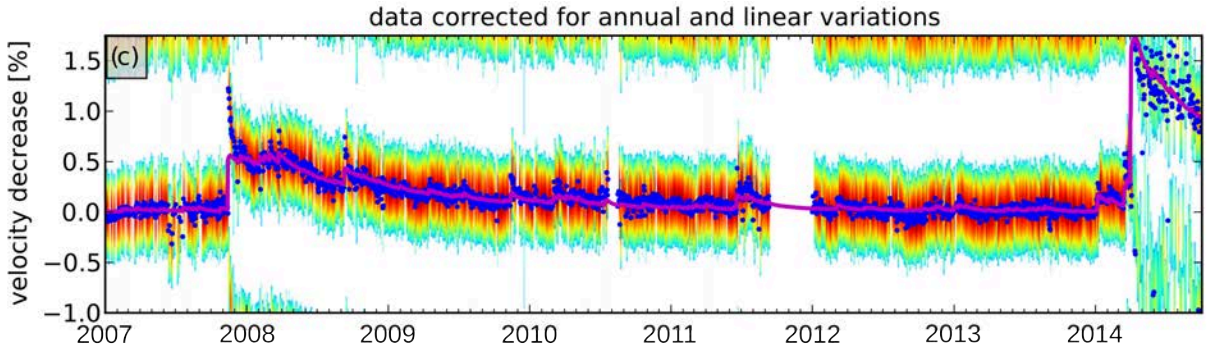

Figure 1.7: *Seismic velocity evolution induced by Tocopilla earthquake at Patache, Chile.* Sharp velocity drops are visible during the Tocopilla earthquake, its aftershocks and the Iquique earthquake at the end of the time-series. A non-linear post-seismic velocity recovery that spans several years is visible in the dataset. The magenta line indicates an exponential decay fit. Each blue dot is a daily best velocity estimation. From Gassenmeier et al. (2016).

physical description of slow dynamics in all materials has not been derived. Nevertheless, the logarithmic evolution of the velocity recovery hints at an aging behaviour similar to the one found in friction frameworks (Dieterich, 1979) and/or thermally activated creeping dynamics (Aharonov & Scholz, 2018). A general phenomenological description consists of an initial destruction of contacts or connections with voids creation (Ostrovsky et al., 2019) during a straining perturbation. This 'damage' phase creates metastable contacts that subsequently return to a new equilibrium through non-instantaneous thermally activated processes. Several models have been developed along these lines and inspired by contact physics (Baumberger & Caroli, 2006), or microcrack dynamics (Kachanov & Sevostianov, 2005) exist (Ostrovsky et al., 2019; Sens-Schönfelder & Eulenfeld, 2019) but their corresponding parameters are underconstrained in the field. The processes driving recovery are not necessarily purely mechanical, but can also have chemical origins (Brantut, 2015).

Due to this complexity, relaxations observed in the field are empirically fitted with an exponential function, characterised by one timescale τ. The exponential decay shows a limited agreement with data during the early phase of relaxation (Fig. 1.7). An alternative is to fit a logarithmic slope $\log(t)$ that is more representative of the data. However, the logarithm diverges at the limits $t \to 0$ and $t \to +\infty$, which poses a conceptual problem for the physical description of the recovery. We also know from highly resolved laboratory experiments that the logarithmic slope breaks down at a minimum timescale $\tau_{\min}$ after the initial perturbation and before the onset of the recovery (Fig. 1.8c). To address these limitations, Snieder et al. (2016) used a phenomenological approach and introduced a universal relaxation function $R(t)$ characterised by a superposition of exponential recoveries:

$$R(t) = \int_{\tau_{\min}}^{\tau_{\max}} \frac{1}{\tau} e^{-(t-t_0)/\tau} \, \mathrm{d}\tau. \tag{1.8}$$

This expression is finite at both t_0 (the onset of the relaxation) and $t_{+\infty}$ and has a logarithmic evolution between the minimum and maximum relaxation timescales ($\tau_{\min}$ and $\tau_{\max}$). The expression has not yet been scaled to field measurements. A potential complication arises when aftershocks induce successive relaxation cycles, which makes the quantification of the timescales challenging. Nevertheless, knowledge of the key controls of $\tau_{\max}$ is needed to predict the duration of transient mechanical properties and of other Earth

surface phenomena, such as enhanced landsliding and permeability after earthquakes.

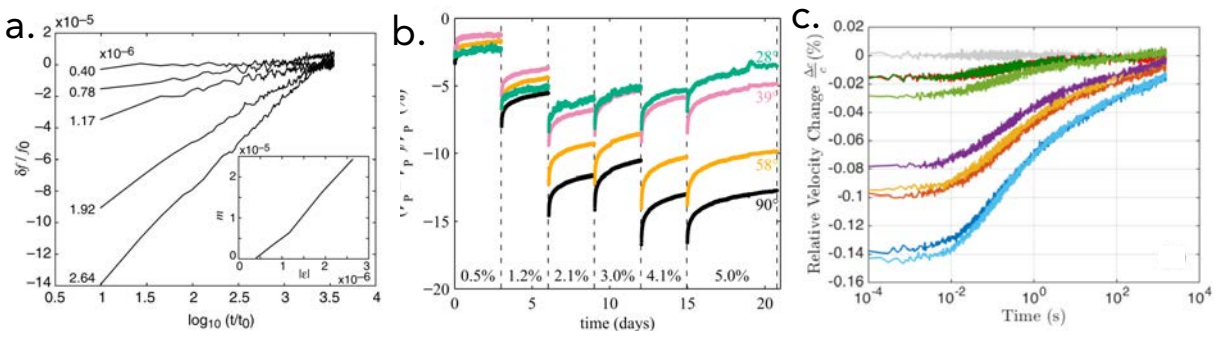

Figure 1.8: *Relaxation behaviours observed in different experimental settings and materials.* **a.** Evolution of the resonance frequency in a sandstone sample after a dynamic longitudinal strain pertrubation. Time is plotted on the X-axis with a logarithmic scale. The different curves indicate different perturbation amplitudes. The inset shows the speed of the recovery m as a function of this amplitude. From TenCate et al. (2000) **b.** P-wave velocity recovery after static strain load episodes (amplitudes indicated in %) in limestones. The different colours show the different probing angles in the experiment. From Brantut (2015) **c.** On this figure, the onset of the logarithmic regime occurs after a minimum time $\tau_{\min}$ in several consolidated granular media. From Shokouhi et al. (2017).

1.3 Research outline

1.3.1 Main questions

In the previous sections, I have shown time-dependent surface observations that are likely to take their roots in the hydro-mechanical properties variations in the subsurface. I introduced the tool of seismic interferometry and showed its capability for monitoring groundwater storage dynamics and damage induced by earthquakes. These two topics are often treated separately but they are linked in many ways: groundwater dynamics affect the reigning pore pressure in the subsurface, which preconditions the mechanical state prior to further seismic or atmospheric perturbations. In the other direction, seismic ground shaking durably affects the elastic moduli through the relaxation phenomenon and often causes permeability changes. Moreover, as seismic velocity changes integrate the whole state of the subsurface, the entanglement between water storage and damage is particularly relevant.

Here, I outline four areas of questions, some being focused on one aspect of the dynamic subsurface system while others look at deciphering the many probed interactions. These questions are:

Q1: *How do variations in subsurface moisture affect groundwater recharge in a large mountain belt ?* Mountains, and in particular the Himalayas, are often seen as 'water towers' due to their large contribution to the global runoff. Despite this importance, there are two simplistic views that dominate hydrological modelling: Mountain belts are either seen as composed of impermeable rock mass covered by a shallow conductive layer (in hillslope hydrology Tromp-Van Meerveld and McDonnell (2006)), or as

highly fractured basements that promote fast flow in deep aquifers (Andermann et al., 2012; Padilla et al., 2014). Growing evidence of a more complex time-dependent storage behaviour may be linked to moisture dynamics within the vadose zone. Little is known about the vadose zone in mountain settings, and about its possible role in regulating groundwater recharge and discharge. To study this potential effect, more ground surface observations are needed in remote mountainous areas.

In Chapter 2, I use seismic interferometry to monitor relative seismic velocity changes dv/v as a proxy for groundwater storage dynamics in a steep Himalayan catchment during three consecutive monsoon seasons. The velocity evolution is compared to hydrological and geochemical variables to constrain the groundwater and discharge cycle at our field site. The data shows that the fast recharge of groundwater by precipitation is only effective when the subsurface moisture is at saturation. Based on this observation, a simple model is derived, taking into account the precipitation history and providing a good agreement with the estimated velocity changes.

The Himalayan catchment studied in Chapter 2 is also prone to seismic hazard and was in the epicentral area of the 2015 Mw 7.8 Gorkha earthquake. The relevance of the hydrological model may be limited to reproduce the dv/v data in the aftermath of the earthquake. This leads to our next question.

Q2: *How can the hydrological and geomechanical effects on relative seismic velocity be disentangled ?* Seismic interferometry with ambient noise integrates many different processes that acts simultaneously in the complex subsurface (Fig. 1.9). In physics terms, the representative elementary volume sampled by the noise wavefield has heterogeneous properties and the derivation of a simple differential equation is challenging. To find physical drivers and to bridge the seismic velocity changes to other processes, one has to play a detective game. In the dissertation, I use a range of methods to decipher relationships and controls.

First, well calibrated model for one aspect of the subsurface can be used to strip the dv/v data from a particular process, and study the obtained residuals. For instance, I use one of the Nepalese seismic station of Chapter 2 to estimate the relaxation timescales after the 2015 Gorkha earthquake and its aftershocks in Chapter 3: The hydrological model derived in Chapter 2 allows me to highlight a separate relaxation timescale τ_{hydro} that stands for the permeability increase and recovery in the local fractured aquifer.

In most of the Chapters, I compare the estimated seismic velocity changes with independent observations such as hydrological and meteorological dataset, remote sensing products and geochemical analysis. In Chapter 4, I use complementary geophysical analysis such as the focal spot imaging technique and transdimensional Bayesian inversion. I also test a series of physical-based and empirical functions to fit the interferometry data. Finally, I show in Chapter 5, that the seismic velocity changes can be considered as a dynamical system such that dimensional analysis and phase portrait plotting are useful tools to discover underlying relationships. These techniques show that despite the subsurface complexity, there is often one process that dominates the velocity changes, which allows for a reduced complexity approach.

Certainly, one can also perform seismic interferometry on stations located in targeted environments. In the middle of the thesis, I move from the complex wet Himalayas to the arid Atacama desert in Chile, an area with very low hydrological variability. Therefore, the next question regarding seismic damage can be addressed.

Q3: *What controls the timescales of subsurface relaxation after small and large earthquakes ?* Many post-seismic processes such as transient landslides rates and enhanced permeability exhibit a similar time evolution that is comparable to the universal relaxation phenomenon observed with seismic velocities (Section 1.1.2 and 1.2.3). However, we lack a firm understanding of what controls the timescales of recovery after a straining perturbation, especially at the field scale. The knowledge of these key controls and the prediction of the recovery timescale would be a step toward quantitative anticipation of post-seismic geological hazards and their mitigation.

In Chapter 4, a dense network of 16 stations located in the Atacama desert is used to monitor the response to moderate ground shaking (PGV $\sim$ 1 cm/s) at a 10-minutes resolution. I show that most of the velocity recovery occurs at a sub-daily timescale. Using the array capability and a Bayesian inversion scheme, I also constrain the 1D subsurface structure under the array and show that the relaxation phenomena is located within hard rocks (the shallow layer has a shear wave velocity of $V_S \sim 1500$ m/s).

In Chapter 5, I stay in the same arid environment of Chapter 4 and estimate 13 years of seismic velocity evolution with the permanent PATCX station. After correcting for temperature-induced variations, the time-series gives the unique opportunity to study the effect of two consecutive large earthquakes (2007 Mw 7.7 Tocopilla and 2014 Mw 8.2 Iquique earthquakes) on subsurface material properties. I show that both earthquakes have the same relaxation timescale when normalised by their respective velocity drop. Using additional information gleaned from the aftershocks of these earthquakes, I demonstrate that the timescale of recovery is controlled by the initial velocity baseline before the drop onset. I reconcile this observation with a state-variable framework in which different contact dynamics superpose, each with their own characteristic relaxation timescale.

Note that the results from Chapter 5 were anticipated by some of the preliminary results of my second Nepalese study (Chapter 3): I use an original approach in which a constant maximum timescale of relaxation $\tau_{\max}$ after small and large ground shaking perturbations is fitted to the velocity data. The goodness of fit obtained from this assumption suggests that the relaxation timescales are mostly controlled by the medium and ambient conditions rather than the strain intensity. This conclusion is further validated in Chapter 5.

All the questions and their answers presented so far rely on noiseless dv/v data obtained at a well-resolved time resolution, essential to access the full dynamics of a system. In consequence, I spent some time on the next final question.

Q4: *How can we obtain a better time-resolution in seismic velocity estimates ?* To compute a representative correlation function that can be used for seismic interferometry, one has to correlate long segments of ambient noise data (eq. 1.5), that can be on the order of several days to months. The requirement for long-time averaging limits the resolution of any time series of relative seismic velocity changes. Therefore, processes acting at relatively shorter timescales cannot be studied.

In Chapter 4, we use 16 co-located stations to decrease the time-averaging of the correlation functions. Instead of using long-time segments of ambient noise, we use smaller time-segments from different stations and average their results. This method is a direct test of the ergodic hypothesis potential for seismic interferometry

studies. I demonstrate how highly resolved seismic velocity measurements over ten-minute intervals can be obtained, which paves the way for future detailed studies of time-dependent behavior using seismic data.

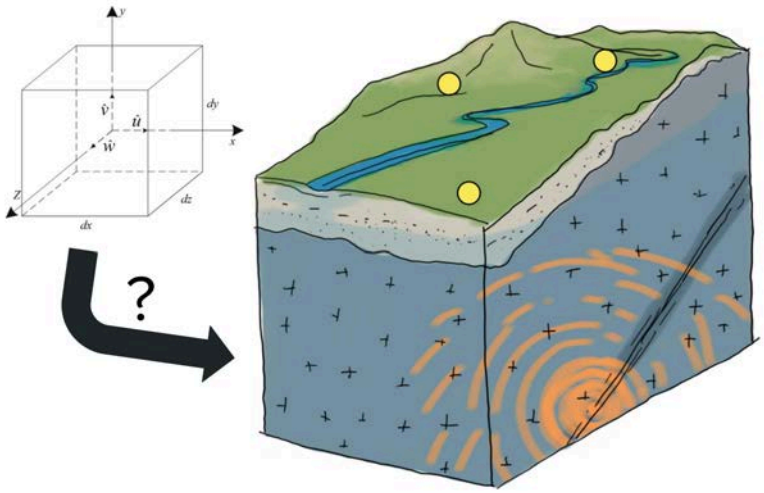

Figure 1.9: *The concept of the field-probed volume.* The conceptual probed volume (right side, drawing by Anne Voigtländer for this dissertation.) in this dissertation in comparison with a classic elementary volume in physics (left side, from Ting (2016)). The yellow marks at the surface stands for hypothetical seismometers location. Different colours in the subsurface indicate the presence of water.

1.3.2 Structure of the dissertation

This dissertation has seven Chapters, including the Introduction in which I have provided a background and rationale for the work presented in Chapters 2-5. This central part of the dissertation consists in four paper chapters, that are either already published, in review or about to be submitted to international peer-reviewed journals. In the second to last Chapter, I bring together the main conclusions of the dissertation. Finally, I present the main overall insights and outcomes from my doctoral research in a synthesis Chapter. The reference list closes the dissertation.

1.4 Contributions of the author and publications

This dissertation comprises to the following studies that are either published or awaiting publication:

1. L. Illien, C. Andermann, C. Sens-Schönfelder, K. L. Cook, K. P. Baidya, L. B. Adhikari, N. Hovius: Subsurface Moisture Regulates Himalayan Groundwater Storage and Discharge, *AGU Advances*, doi.org/10.1029/2021AV000398
   Contributions: LI and CA conceived the study with research inputs from CSS, KC and NH. LI conducted all data analysis and wrote the manuscript with inputs from CA, NH, CSS and KC. LBA and KPB participated in important data collection missions.

2. L. Illien, C. Sens-Schönfelder, C. Andermann, O. Marc, K. L. Cook, L. B. Adhikari, N. Hovius: Seismic Velocity Recovery in the Subsurface: Transient Damage and Groundwater Drainage Following the 2015 Gorkha Earthquake, Nepal, *Journal of Geophysical Research: Solid Earth*, doi.org/10.1029/2021JB023402
   Contributions: LI, CSS, CA, OM, KC and NH conceived the study. LI conducted all data analysis and wrote the manuscript with inputs from CA, NH, OM, CSS and KC. LBA participated in important data collection.

3. L. Illien, C. Sens-Schönfelder, KY Ke: Resolving minute temporal seismic velocity changes induced by earthquake damage: The more stations, the merrier ?, in review at *Geophysical Journal International*.
   Contributions: LI and CSS conceived the study. LI conducted all data analysis and wrote the manuscript with inputs from CSS. KYK provided guidance during the inversion analysis. CSS conducted the data collection.

4. L. Illien, J. M. Turowski, C. Sens-Schönfelder, C. Berenfeld, N. Hovius: Predictable healing rates after earthquakes near-surface damage, *In preparation*.
   Contributions: LI conceived the study with research inputs from JMT, CSS, CB and NH. LI conducted all data analysis and wrote the manuscript with inputs from JMT, CSS, NH and CB. LI and CB contributed equally to the mathematical theory of the paper.

Additionally, I have been involved in the following published studies:

- O. Marc, R. Behling, C. Andermann, J. M. Turowski, L. Illien, S. Roessner, N. Hovius: Long-term erosion of the Nepal Himalayas by bedrock landsliding: the role of monsoons, earthquakes and giant landslides, *Earth Surface Dynamics*, doi.org/10.5194/esurf-7-107-2019

- E. R. C. Baynes, D. Lague, P. Steer, S. Bonnet, L. Illien: Sediment flux-driven channel geometry adjustment of bedrock and mixed gravel–bedrock rivers, *Earth Surface Processes and Landforms*, doi.org/10.1002/esp.4996

- M. Dietze, K. L. Cook, L. Illien, O. Rach, S. Puffpaff, I. Stodian, N. Hovius: Impact of nested moisture cycles on coastal chalk cliff failure revealed by multi seasonal seismic and topographic surveys, *Journal of Geophysical Research: Earth Surface*, doi.org/10.1029/2019JF005487

- M. Dietze, M. Krautblatter, L. Illien, N. Hovius: Seismic constraints on rock damaging related to a failing mountain peak: the Hochvogel, Allgäu, *Earth Surface Processes and Landforms*, doi.org/10.1002/esp.5034

- O. Marc, C. Sens-Schönfelder, L. Illien, P. Meunier, M. Hobiger, K. Sawazaki, C. Rault, N. Hovius: Toward using seismic interferometry to quantify landscape mechanical variations after earthquakes, *Bulletin of the Seismological Society of America*, doi.org/10.1785/0120200264

Papers

Chapter 2

Subsurface Moisture regulates Himalayan groundwater storage and discharge

Luc Illien, Christoff Andermann, Christoph Sens-Schönfelder, Kristen L. Cook, Lok B. Adhikari, Niels Hovius

Published in *AGU Advances*, May 2021, volume 2, issue 2, DOI: 10.1029/2021AV000398.

Abstract

Through the release of groundwater, most mountain rivers run year-round despite their small catchments and sporadic precipitation. This makes mountain ranges important sources of reliable fresh water for downstream populations in many parts of the world. However, due to a lack of observations, very little is known about groundwater dynamics in steep landscapes. Recent research has shown the existence of a superficial moisture reservoir that does not lead to discharge. In this study, we test whether this reservoir has an impact on groundwater recharge in mountainous environments. We present results from an observatory located in the Nepal Himalayas. During three monsoon seasons, we measured an array of parameters including relative seismic velocity changes from ambient noise correlations. This non-invasive technique allows us to monitor groundwater dynamics in conjunction with classical hydrological measurements. We found that pre-monsoon precipitation does not affect discharge and groundwater storage and instead recharges the subsurface moisture reservoir. Only when this superficial reservoir reaches saturation does groundwater become connected to precipitation inputs and transpiration losses. We model these dynamics using a surface layer that has a finite storage capacity that controls the connectivity of groundwater to surface flux. The extension of this concept, which is thought to apply widely in flat and undulating landscapes, to steep mountain topography with thin and discontinuous soils underlain by regolith and bedrock is a paradigm shift in mountain hydrology.

2.1 Introduction

The fate of water in mountains involves flow pathways through reservoirs with different physical properties and capacities (Alley et al., 2002; Oki & Kanae, 2006). Accurate water budget estimation requires knowledge of these reservoirs and their connections, specifically of groundwater storage dynamics in response to precipitation inputs and its export to discharge. Most water in rivers has an age of years to decades (McGuire & McDonnell, 2006; Gleeson et al., 2016), which suggests that it has spent a significant amount of time

in storage. This 'old' water concept is especially relevant in steep mountain catchments, where deeper vertical infiltration seems more prevalent than direct runoff (Jasechko et al., 2016). It is widely accepted that these mountain areas act as water towers that supply essential fresh water resources downstream. The prime example is the Himalayan Range, which provides water for $\sim$ 800 million people in the Indus, Ganges and Brahmaputra basins. The evolution of this resource is often viewed through the prism of glacier melt (Viviroli et al., 2007; Immerzeel et al., 2010), whereas the larger and more ubiquitous mountain groundwater reservoir has received less attention. With $\sim$ 2/3 of the annual river discharge in the Nepal Himalayas coming from groundwater (Andermann et al., 2012), understanding the key controls on this reservoir is essential for projecting the future of mountain water resources in the light of global climate change and increasing hydropower and land use. However, constraints on groundwater recharge and dynamics in this area and more generally in mountainous landscapes are rare due to the scarcity of ground observations in steep remote locations.

Before reaching groundwater and ultimately streams, precipitation must generally first pass through the unsaturated superficial zone of the subsurface (vadose zone), which suggests that any change in physical conditions within this shallow layer may modulate groundwater recharge and runoff. In steep catchments, the importance of this conditioning for controlling hydrological fluxes is often debated due to the lack of instrumentation and contradicting observations. A first string of studies have shown that hydrological fluxes in steep catchments are mainly controlled by the presence of a fractured bedrock basement in these locations that promotes fast flow and efficient infiltration to the groundwater table, therefore quickly bypassing the vadose zone (Zillgens et al., 2007; Katsura et al., 2008; Salve et al., 2012; Andermann et al., 2012; Padilla et al., 2014, 2015). This preferential flow path along fractures has been reported to cause an important volumetric contribution of bedrock groundwater to both the baseflow and stormflow component of discharge in these studies. This observation could also explain the weak dependence of groundwater recharge and runoff dynamics with subsurface conditions and the soil/sediment cover (Salve et al., 2012; Padilla et al., 2014, 2015). Nevertheless, a few studies have also shown that hydrograph response to precipitation is dependent on initial baseflow and various pre-conditions in the vadose zone. Such pre-conditions include current soil wetness that determines soil hydrological conductivity (Tani, 1997) or a finite water storage capacity in the regolith which modulates the transfer of precipitation to rivers and to deeper reservoirs (Onda, 1989; Montgomery et al., 1997). Recent research has shown that a significant volume of water stored in the regolith is in fact 'rock moisture' that is trapped below the soil layer in the unsaturated weathered layer of bedrock (Salve et al., 2012; Rempe & Dietrich, 2018). In this study, we will use the term subsurface moisture reservoir for all exchangeable water in the vadose zone, encompassing soil and rock moisture. Because this reservoir can represent a significant part of seasonal dynamic storage (Dralle et al., 2018) and is located above the groundwater table, it has been shown to buffer groundwater recharge by precipitation and hinder runoff in a steep (32°) 4km^2 hillslope in the Northern California Coast Ranges (Rempe & Dietrich, 2018). However, a very limited effect of subsurface moisture on groundwater storage and discharge has also been reported close to the same study site due to the previously mentioned fracture pathways (Salve et al., 2012). This discrepancy in the literature raises the question of the relevance of the subsurface moisture for regulating water transfers at larger scales, as this control is generally observed locally on rather small hillslopes. In this study, we hypothesize that the highly variable conditions in subsurface moisture due to the monsoon seasonality in the Nepal Himalayas regulate groundwater recharge and runoff generation at the catchment scale and thus control the

annual availability of hydrological resources downstream.

To track subsurface water in a spatially integrated way in remote locations where standard techniques and data may be limited, new approaches are needed for monitoring groundwater dynamics. Here, we use non-invasive seismic interferometry, based on data from broadband seismometers. From ambient seismic noise correlations, SI retrieves relative seismic velocity changes (dv/v) in the subsurface, allowing for the monitoring of rock properties through time (Lobkis & Weaver, 2001; Sens-Schönfelder & Wegler, 2006; Gassenmeier et al., 2016). Because fluid content in rocks affects elastic moduli and therefore seismic velocity, seismic interferometry can be used to estimate relative groundwater storage evolution (Sens-Schönfelder & Wegler, 2006; Lecocq et al., 2017; Clements & Denolle, 2018; Kim & Lekic, 2019b). This method is sensitive at the mesoscale (10^1–10^2 m, length scale of the 3D volume of influence), allowing for spatially integrated monitoring of the groundwater system and its dynamics. Thus, it bridges the gap between point-based well measurements and larger scale methods such as catchment scale hydrograph analysis or satellite-based gravimetry. It also avoids possible observational artifacts compared to piezometric measurements, where borehole installation often alters the subsurface condition.

We have used seismic interferometry to study groundwater dynamics in the Himalayas, focusing on the Bhote Koshi catchment in Nepal (Fig. 2.1a). Like most catchments in the central Himalaya, the Bhote Koshi receives up to $\sim$ 80 % of its annual precipitation during the Indian Summer Monsoon (Bookhagen & Burbank, 2010). We analysed $\sim$ 2.5 years of seismic data, covering three monsoon seasons, recorded at two seismic stations (Fig. 2.1a). Listi station was located at 2310 masl., near a ridge crest with steep flanks (slope of $\sim$ 80 %), and $\sim$ 1100 m above the Chaku station, which was located on a bedrock terrace 75 m above the Bhote Koshi River. Both stations are underlain by sheared metasedimentary rocks of the Lesser Himalayan series, below a layer of regolith and colluvium. To resolve interactions between precipitation, subsurface moisture, groundwater, and river discharge in this typical mountain setting, we combined the observations from these stations with complementary measurements (Fig. 2.1a). Soil moisture sensors installed in the surface layer (0-20 cm depth) were located at both seismic stations and precipitation was measured at six weather stations. In addition, we measured the flow stage height of the Kahule Khola upstream of its confluence with the Bhote Koshi River using a pressure sensor. This stream drains a $\sim$ 35 km^2, glacier-free catchment, the flow of which reflects the drainage of the instrumented ridge by which it is bounded. At the stage gauge, stream water samples were taken twice a week from January 2016 to October 2018. The stable oxygen isotope ratio ($\delta^{18}O$) of these samples was measured as a tracer for seasonal water input variations and to probe for evaporative loss. Finally, we extracted the normalized difference vegetation index (NDVI) from MODIS multi spectral imagery. NDVI is generally correlated with soil moisture (Taktikou et al., 2016) and is a good proxy for vegetation activity and transpiration (Running & Nemani, 1988; Ichii et al., 2010). This multi-proxy approach allowed us to assess the temporal evolution of groundwater storage, and revealed the first-order importance of subsurface moisture in regulating groundwater recharge and baseflow release during the monsoon in the Nepal Himalayas.

2.2 Materials and Methods

Precipitation was measured at six locations using fully automated VAISALA WXT510 Weather Transmitters (Fig. 2.1a). All weather parameters were logged at 1-min intervals. To obtain a representative time series and account for potential orographic effects, all

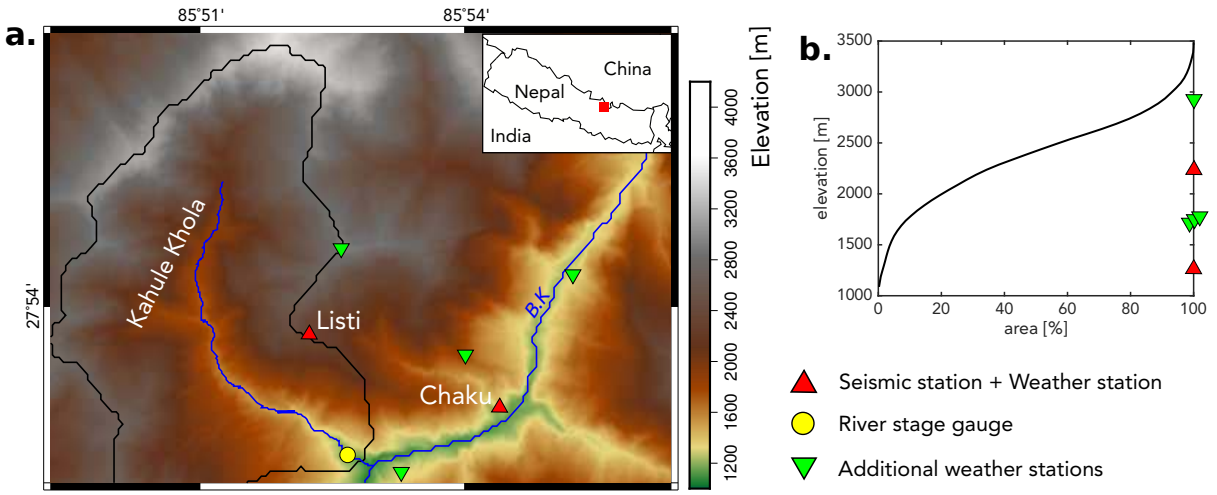

Figure 2.1: **a.** *Map showing the Bhote Koshi observatory.* Red triangles indicates the sites that contain seismic stations, soil moisture sensors and precipitation gauges. Yellow circle in the Kahule Khola tributary indicates the hydrometric station where stage height and $\delta^{18}O$ are measured. Green triangles are additional weather stations used for estimating average precipitation. Red square in inset shows location of the observatory in Nepal. BK: Bhote Koshi river. **b.** *Hypsometric curve of the Kahule Khola catchment.* Symbols on the right axis of the plot represent the elevation of the stations relatively to the Kahule Khola hypsometry.

six precipitation measurements were interpolated in a square box extending $\sim$ 10*10 km by applying a Voronoi-Thiessen tessellation on the daily precipitation sums (Fig. 2.5). The aggregated precipitation time series represents the spatial mean precipitation of the integration area. Stations with missing data at certain dates were not used for spatial interpolation. We used the dirichlet(X) function in the R spatstat package. Because most of the Kahule Khola catchment lies under 3000 m altitude (Fig. 2.1b), snowfall is neligible at our field site (Putkonen, 2004).

Relative river stage height of the Kahule Khola river was measured $\sim$ 100 m upstream of the confluence with Bhote Koshi River (Fig. 2.5). Stage height was logged using Hobo Onset pressure transducers. The logging interval was set to either 15 or 30 min intervals depending on the deployment period. The relative stage height record was corrected for atmospheric variations using the barometric time series recorded at our closest weather station, Tyantali station (Fig. 2.5).

For the measurement of $\delta^{18}O$, daily water samples were taken by a trained onsite operator every day at around 9AM. Sampler were filtered onsite (0.22 μm filter) and stored in 30 ml Nalgene vials at ambient temperature before being shipped to Germany. All samples were analysed in the GFZ Potsdam OSG-Lab, using a Picarro L-2140i Ringdown spectrometer.

Soil moisture was acquired at the six weather stations using a Campbell Scientific CS650 soil moisture sensor. The sensor was installed close to the surface and integrates approximately 8 liters of soil volume and records volumetric water content as a function of bulk electric conductivity.

NDVI was extracted from the online MODIS / VIIRS Land Products global Subsetting Tool. The subsetting area was picked to cover the entire Kahole Kohla landscape to integrate valley-to-ridge variability of vegetation types and agricultural land use. The Tool

is available at https://modis.ornl.gov/globalsubset/.

Broadband seismic stations (Nanometrics - Trillum Compact 120s) were used in this study. Data were acquired at a sampling rate of 200 Hz. We estimated daily relative seismic velocity changes from ambient seismic noise correlations in the frequency range of 4 - 8 Hz. We used single-station cross correlation technique (Hobiger et al., 2014) and computed the velocity time serie from the stretching method using multiple references (Sens-Schönfelder & Wegler, 2006; Sens-Schönfelder et al., 2014). Detailed method is available in *Appendix A*.

2.3 Results and Discussion

2.3.1 Co-evolution of hydrological variables

The Indian Summer Monsoon imposes a strong annual cycle on the hydrology of the Bhote Koshi catchment, with a distinct dry and wet season (Fig. 2.2a). The seasonality of precipitation input is matched by a sustained increase in discharge of the Kahule Khola stream during the monsoon, followed by a well-defined long-lasting recession throughout the dry part of the year. Importantly, we observed little to no discharge generation in the pre-monsoon season ($\sim$ March to $\sim$ June). Despite significant precipitation in the pre-monsoon season, the hydrograph shows a continuous decrease in baseflow-generated river discharge with only a few short-lived rise-and-fall type events from direct runoff. This decoupling suggests that there are different hydrological regimes throughout the year. Because the stream is predominantly fed by groundwater (Andermann et al., 2012), the transition between these regimes is likely to be controlled by the onset of groundwater recharge, initiating a period when groundwater and precipitation are coupled. If this is correct, then understanding the timing of this coupling in relation to precipitation input is essential, requiring observation of groundwater storage through time. We defined two seasonal boundaries based on this coupling in Figure 2.2: from a dry to an uncoupled-wet season and from an uncoupled-wet to a coupled-wet season.

Previous work has linked seismic velocity decreases to increased groundwater levels (Sens-Schönfelder & Wegler, 2006; Lecocq et al., 2017; Clements & Denolle, 2018; Kim & Lekic, 2019b) and increases in pore pressure (Q.-Y. Wang et al., 2017). Thus, the time series of estimated daily relative seismic velocity changes dv/v at Listi and Chaku stations (Fig. 2.2b) may serve as a relevant proxy for groundwater storage. The annual cyclicity of dv/v, with a decrease during each recorded monsoon seasons followed by a recovery during the subsequent dry season is in agreement with these studies. At $\sim$ 8%, the amplitude of change at our stations was significantly larger than in previously reported cases (Lecocq et al., 2017; Clements & Denolle, 2018; Kim & Lekic, 2019b), suggesting a dominant hydrological forcing on the velocity changes through substantial variations in groundwater content and level. Both stations exhibited similar dv/v dynamics, with a lower amplitude at Listi. This amplitude difference could reflect smaller groundwater variations at Listi because it is at a higher topographic position with less upstream area. However, because the seismic interferometry technique loses sensitivity to changes with increasing depth (Pacheco & Snieder, 2005; Obermann et al., 2013), our observations could also point to a deeper average groundwater level higher in the landscape (Jasechko et al., 2016). A striking co-evolution between the streamflow (Fig. 2.2a) and the dv/v time series occurred during major parts of the monitored period: the variables were negatively correlated during monsoons, and the recovery of velocities during the post-monsoon period

coincided with a discharge recession. Remarkably, the sharp decrease of seismic velocity during the monsoon systematically coincided with a sustained increase in streamflow.

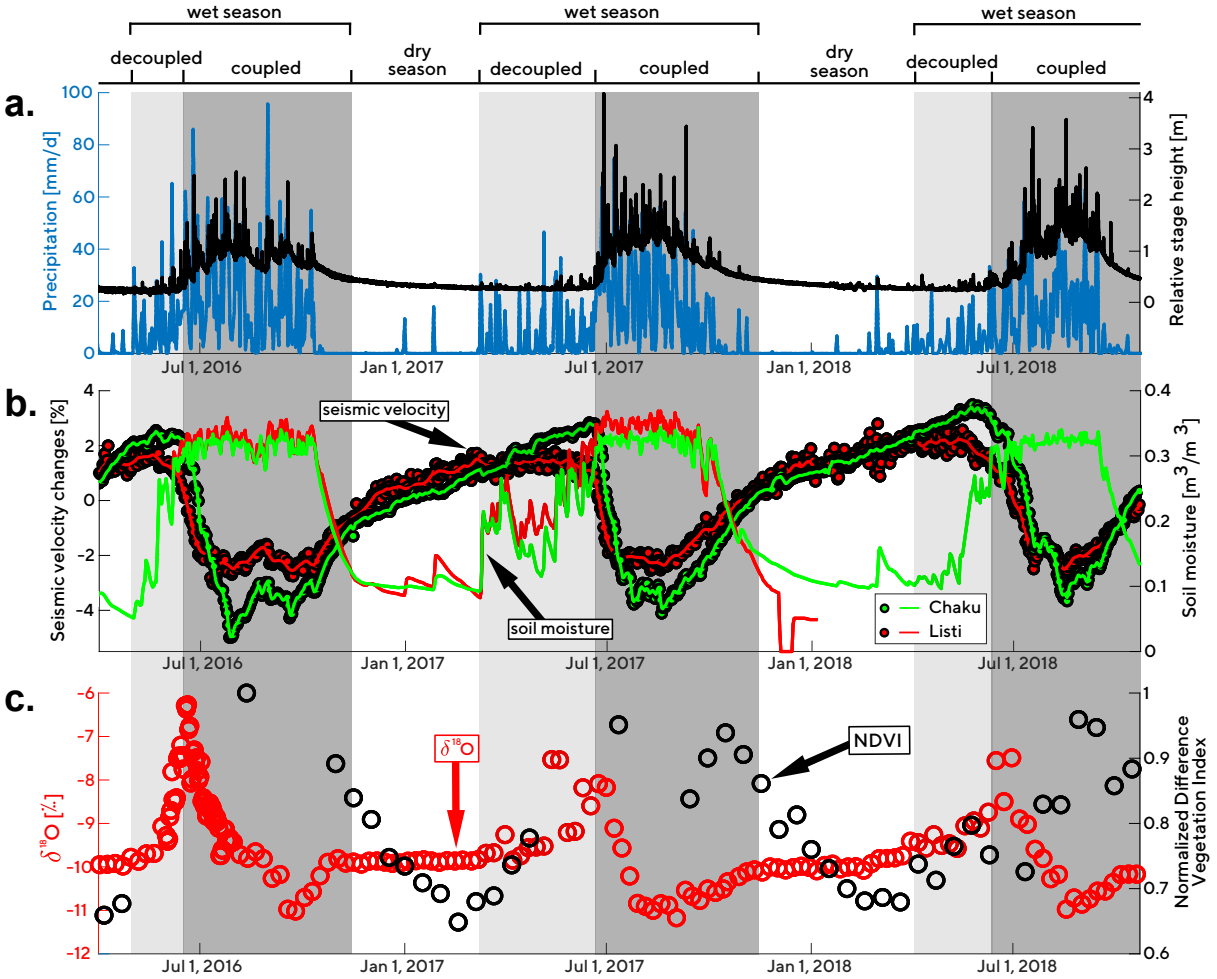

Figure 2.2: *Observations from the Bhote Koshi observatory.* **a.** Black solid line indicates the river stage height measured at the Kahule Khola. Daily precipitation is plotted in blue. **b.** Daily relative seismic velocity changes variations in the 4 - 8 Hz frequency band is plotted as circles with a 3 days moving average for visualisation. Measurements of soil moisture volumetric content are reported by the solid lines. Green and red colours indicate Chaku and Listi sites respectively. **c.** Red dots represent $\delta^{18}O$ values measured at the Kahule Khola. Black Dots represents Normalised Difference Vegetation Indexes (NDVI) computed in our study area, that is a proxy for vegetation activity. The different seasons and regimes of the hydrological system are indicated in the background and labeled at the top.

Further insight into the timing of this onset and the fate of pre-monsoon precipitation comes from soil moisture measurements (Fig. 2.2b). Over the annual cycle, the measured soil moisture concentration had a pronounced relation with precipitation (Fig. 2.2a-b). From the onset of pre-monsoon precipitation, soil moisture increased, while dv/v remained unaffected, suggesting that any infiltrating rainwater was stored in the shallow subsurface unconnected to the groundwater. The onset of coupling of precipitation and groundwater occurred around the start of the summer monsoon, after reaching $\sim$ 610, 660 and 400 mm of cumulative precipitation in 2016, 2017 and 2018, respectively. Coupling coincided with

the stabilization of soil moisture concentrations, despite mounting precipitation totals. We attribute this stabilization to reaching a mean field capacity of the vadose zone. Under these conditions, the equivalent volume of any additional water input to the subsurface is gravitationally transferred into the groundwater reservoir, leading to rising groundwater levels reflected by the seismic velocity decrease. We note that the buildup of moisture in the subsurface during the pre-monsoon period was barely recorded by the seismic velocity observations (Fig. 2.2b). This may be due to the frequency-dependent response of velocity changes to partial fluid content (J. E. White, 1975; Helle et al., 2003), or to the limited depth extent of the layer prone to soil moisture changes. The duration of the soil moisture buildup phase was different for the three seasons on record with different cumulative precipitation totals, likely because of differences in precipitation intensity. In addition, transpiration losses could have slowed the increase in moisture. The onset of vegetation activity signaled by increasing NDVI values during the pre-monsoon period underpins this interpretation (Fig. 2.2c).

The co-evolution of our hydrological observables gives insight into the transition from the coupled to the uncoupled hydrological regimes after the monsoon season. Early in the dry season, a distinct and sustained decrease in the rate of recovery of dv/v occurred in both recorded years (Fig. 2.2b), especially visible at Chaku station. This change of slope suggests a step change in groundwater depletion, from fast in the early post-monsoon to steady, but slower depletion during the dry season from $\sim$ November until around the start of the next monsoon. Because this feature follows the last monsoon precipitation and the decrease in soil moisure, we used it to conservatively define the end of the wet season (boundary between the wet-coupled to dry season in Figure 2.2). We note that the stage height of the Kahule Khola does not share the slope break observed in dv/v. This hints at the operation of a second groundwater depletion pathway, connected not to streamflow, but rather upwards via transpiration, which operates during the coupled hydrological regime, but not during the subsequent dry season. This hypothesis can be tested with the oxygen isotope record of the Kahule Khola.

Over the monitoring period, which comprised two annual cycles, $\delta^{18}O$ values of Kahule Kohla discharge were constant around -10‰ during the dry season, increased progressively to -6‰ from the onset of pre-monsoon precipitation, dropped rapidly to around -11‰ early in the monsoon season, and restored to values around -10‰ later in that season (Fig. 2.2c). The stable isotopic composition of stream water is determined by the precipitation input and any subsequent fractionation. We constrain precipitation chemistry using a contemporaneous precipitation $\delta^{18}O$ measurement time series of samples from Kathmandu (Fig. 2.11). Kathmandu is located at 1400 masl., about 50 km to the SW of our study area, and exposed to the same general weather systems. During 2016 and 2017, Kathmandu precipitation $\delta^{18}O$ showed a similar pattern, with sparse dry season values around -9‰, pre-monsoon values increasing up to 5‰, early monsoon rain around -15‰ increasing to -10‰ later in the monsoon season. Fractionation after precipitation appears to be limited, as the Kahule Khola $\delta^{18}O$ data consistently plot on a local meteoric waterline (Fig. 2.10).

In this context, and in view of the paucity of winter precipitation, we interpret the constant, intermediate $\delta^{18}O$ values for Kahule Khola dry season water samples to indicate that the stream was mainly fed by a groundwater reservoir in which isotopically light monsoon input is mixed with some isotopically heavier pre-monsoon input on time scales exceeding an annual cycle. It is likely that this mixing occurs after the vadose zone has reached field capacity and water starts to move downward into the groundwater reservoir. Heavier isotopic values of Kahule Khola stream water indicate that a part of pre-monsoon rainfall translates into fast direct runoff. At the onset of the coupled hydrological regime,

with incoming isotopically light monsoon precipitation, the oxygen isotopic values of the stream water decreased to slightly below the characteristic value of the groundwater reservoir. We attribute this to a combination of groundwater evacuation and direct runoff during intense monsoon rainfall. The Kahule Khola water reverted to its steady, well mixed $\delta^{18}O$ signature independently of the slope break in the dv/v time series at Chaku, early in the post-monsoon dry season. We infer that the secondary, upward loss of water in the period before the break is largely due to vegetation transpiration which can modulate the drainage of water tables close to rooting depth (Maxwell & Condon, 2016; Koirala et al., 2017) without oxygen isotope fractionation.

2.3.2 Soil moisture and groundwater recharge

Our results suggest that two distinct hydromechanical regimes are active in the steep Kahule Khola catchment. A key parameter controlling the passage between these regimes could be the pore connectivity in the vadose zone. When this zone is undersaturated, the pores are not efficiently connected and the presence of air may impede flow, causing infiltrated rainwater to be stored as tightly bound water (Renée Brooks et al., 2010) that is removed by root uptake building up early season biomass . This state is characterised by short-lived episodes of direct runoff generation and a continuous decrease of baseflow. When the subsurface moisture reservoir reaches a characteristic storage capacity, the subsurface can no longer store additional water and begins to transmit to the deeper groundwater reservoir. This behavior is analogous to a 'sponge' where prior hydrophiling of the surfaces modulates the infiltration (DiCarlo, 2004, 2006). After the monsoon, the bound water depleted by transpiration can be replaced by groundwater through upward percolation processes (Renée Brooks et al., 2010), allowing vegetation to use groundwater indirectly at depths exceeding the root zone (Koirala et al., 2017; Condon et al., 2020). Therefore, evapotranspiration of subsurface moisture competes directly with precipitation input to regulate groundwater recharge. Because we can not differentiate between a shallow and deep groundwater reservoir at our field site, the hypothesis of a perched seasonal groundwater reservoir (Padilla et al., 2015; Salve et al., 2012) depleted by transpiration is also plausible. Therefore, the dynamics would be an integrated measure of both shallow and deep groundwater storage. We conclude that despite evidence for a fractured bedrock basement in the Nepal Himalayas (Tipper et al., 2006; Andermann et al., 2012), the subsurface moisture reservoir governs hydrological fluxes in the Kahule Khola.

While this concept explains our observations at Chaku station, low in the Bhote Koshi valley, it may not apply to higher positions in the mountain landscape. At Listi station, close to a mountain ridge crest, seismic velocities decreased somewhat during pre-monsoon despite the soil moisture not being at saturation, suggesting that precipitation became connected to the groundwater reservoir (Fig. 2.2a-b). This early connection may be due to a greater permeability of the surface, associated with thin soil cover and the presence of deep-reaching tension fractures that allows localized areas of rapid recharge (Gleeson et al., 2009). Moreover,the clear slope break that we attribute to the termination of transpiration losses from the groundwater reservoir at Chaku is not as striking at Listi, where the recovery in dv/v appeared more gradual from the wet to the dry season. This can be explained by a groundwater reservoir that is below rooting depth (Maxwell & Condon, 2016). The similar but yet different seismic velocity evolution at Listi and Chaku shows that the seismic interferometry approach is a promising tool to monitor groundwater dynamics in different parts of a landscape, including those that may be representative of the catchment and its

subsurface. Thus, local gradients in the groundwater system can be targeted, something that is beyond the reach of classic hydrograph analysis.

2.3.3 Modelling of seismic velocity changes

Our data suggest that subsurface moisture is a first-order control on groundwater storage and discharge in the Himalayan Bhote Koshi catchment. We further demonstrate our findings by reproducing the dv/v data with a hydrological model.

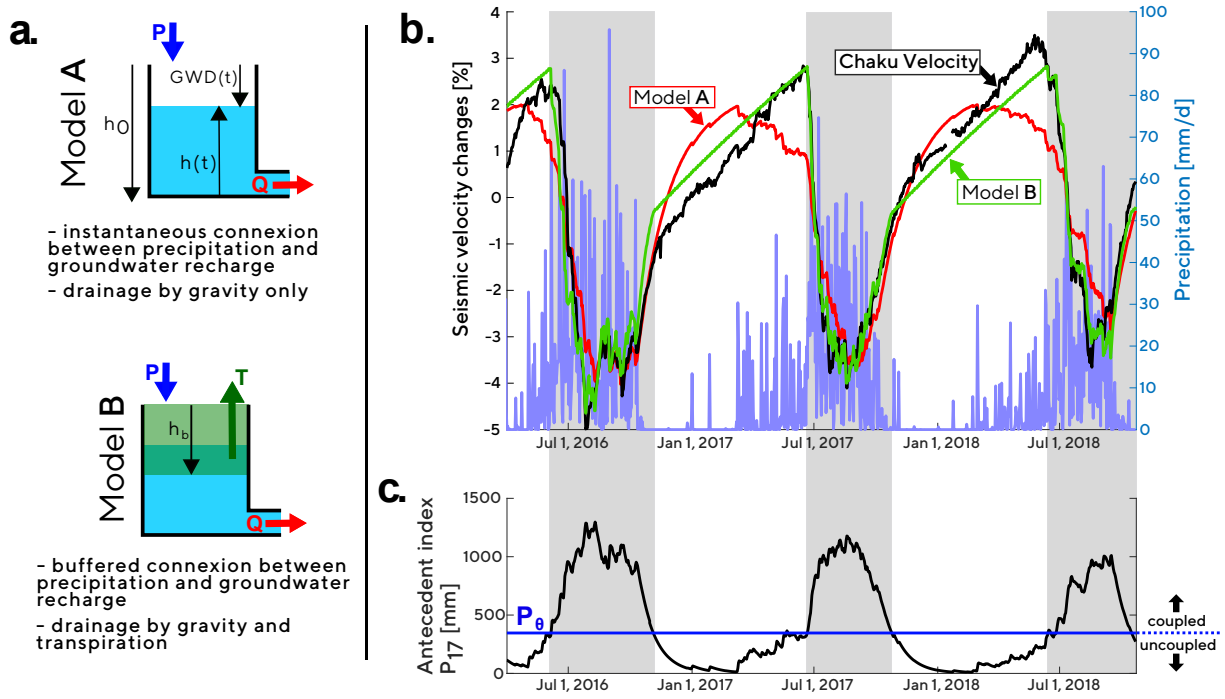

Figure 2.3: *Results of dv/v modelling.* **a.** The sketches indicate models tested in the paper with sign conventions shown by black arrows. Coloured arrows accounts for the fluxes regulating groundwater dynamics (P: Precipitation, Q: Discharge, T: transpiration). GWD (Groundwater Depth), h (hydraulic head), h_0 (asymptotic level) and h_b (critical depth for transpiration) are the variables described in equation (2.1) and (2.3). **b.** Observations from Chaku station and the best fitting dv/v predictions of models **A** and **B**. **c.** Antecedent precipitation index P_{17} used in model **B** and the P_θ threshold. Grey areas depict the periods when the groundwater is connected to precipitation and transpiration e.g. at the field capacity of the vadose zone when $P_{17} > P_\theta$.

Simple hydrological models have succeeded in reproducing key features of dv/v variation in various settings (Sens-Schönfelder & Wegler, 2006; Gassenmeier et al., 2015; Hillers et al., 2014). Although the details of these models have varied, they shared the assumption of instantaneous transfer of precipitation to the groundwater system on the daily timescale. Such models predict an exponential decay of the modeled hydrological variable (evolution of groundwater table level, pore pressure, groundwater storage) after precipitation input. To test whether these models can capture the essence of groundwater hydrology at our field site, we have tried to fit the velocity changes observed at Chaku station with a groundwater-level evolution model (Sens-Schönfelder & Wegler, 2006; Hillers et al., 2014). We computed the hydraulic head $h(t)$ as follows:

$$\frac{dh}{dt} = \frac{P(t)}{\phi} - ah(t) \tag{2.1}$$

where P is the daily precipitation measured at the site, ϕ is the porosity of our reservoir, and a is a decay parameter that describes the recession of the hydraulic head after precipitation. We then converted changes in hydraulic head $h(t)$ into synthetic relative seismic wave velocity changes, by linking the relative variation in saturated rock mass with a relative slowness perturbation of the medium (details in *Appendix B01*). Results from this model do not adequately reproduce the Chaku data (Fig. 2.3b). For example, the synthetic velocities decrease during the pre-monsoon, as model precipitation is directly passed to the groundwater reservoir (model **A**, Fig. 2.3a). This model may be valid in places such as volcanoes (Sens-Schönfelder & Wegler, 2006) where highly permeable bedrock is exposed at the surface. However, in our setting, the subsurface moisture reservoir buffers groundwater recharge and may be represented by including a second layer in the model. To do this without introducing unconstrained physical quantities, we computed the antecedent precipitation index $P_M(t)$ (Katsura et al., 2008; Kosugi et al., 2008):

$$P_M(t) = P_M(t-1)\exp(\ln 0.5/M) + R_h(t)\exp(\ln 0.5/2M). \tag{2.2}$$

Here, $R_h(t)$ is the cumulative precipitation from $t-1$ to t, and M the time in days required for precipitation input to the layer to decay to half its initial value. We assumed that the filling of the subsurface moisture reservoir can be represented by the cumulative nature of equation (2.2) and that the half-time M captures the reduction of the moisture content by transpiration. Then, we introduced a threshold P_θ to represent the field capacity of the vadose zone. The P_θ threshold was taken as the mean value of $P_M(t)$ at the dates corresponding to the onset of the seismic velocity decrease between the uncoupled to coupled regimes in 2016, 2017 and 2018 (details in *Appendix B02*). Precipitation is only passed to the groundwater reservoir when $P_M(t) > P_\theta$ with

$$\frac{dh}{dt} = \frac{P(t)}{\phi} - ah(t) - b\ (\min(0, GWD(t) - h_b)) \tag{2.3}$$

where $GWD(t)$ is the groundwater depth, and h_b is the depth range in which transpiration is active (model **B**, Fig. 2.3a-b). b is a coupling constant linking the transpirative flux with the groundwater level through an increase of root density toward the surface (Canadell et al., 1996). This scaling is a simplification as water may be used directly and indirectly by roots. For periods with $P_M(t) < P_\theta$, we used equation (2.1) without a precipitation input term. Our model best fits the seismic velocity data of Chaku station with (least-squares misfit criterion $L^2 = 0.022$, model **B** shown in Figure 2.3b-c), and M values from $\sim$ 10 d to $\sim$ 40 d produce reasonable fits (L^2 shown in Figure 2.9). We attribute this broad range of suitable half time values to a lack of constraints in our model and to the simplicity of our approach.

A few offsets between our model and the data occurred during dry seasons, possibly due to changing local hydro-geological complexities, the single groundwater reservoir assumption, thermal strain (Richter et al., 2014), or a long term mechanical effect of the 2015 Gorkha earthquake and aftershocks on seismic velocity (Brenguier et al., 2008). In general, though, our modelling captures the dv/v dynamics and shows that key hydrological observations in the Bhote Koshi catchment require a subsurface moisture layer which is governed by the balance of precipitation input and transpirative loss, and acts as a gatekeeper that either separates the groundwater reservoir from surface precipitation or to permits recharge.

2.4 Conclusions and perspectives

Based on our combined seismological, hydrological, meteorological and geochemical observations and modelling, the precipitation-subsurface moisture-groundwater-stream water complex in the central Nepal Himalayas undergoes an annual cycle with four stages (Figure 2.4). (1. *Dry Stage*) The background is defined by a dry season, during which stream flow is fed only by gravity-driven groundwater discharge, causing progressive depletion of the groundwater reservoir. (2. *Decoupled Stage*) Pre-monsoon precipitation is converted to subsurface moisture and direct runoff, but does not result in groundwater recharge, such that the groundwater reservoir continues to be depleted. During this period, precipitation and groundwater are decoupled, and this state is prolonged by transpiration loss of subsurface moisture. (3. *Coupled Stage*) When the shallow subsurface, i.e. the vadose zone, has reached field capacity, precipitation causes direct runoff as well as groundwater recharge and evacuation. During this coupled phase, when precipitation and groundwater are connected, moisture that accumulated in the vadose zone over the pre-monsoon season remains constant and additional precipitation is removed by transpiration or mixed with the pre-monsoon input and is moved into the groundwater reservoir at a rate determined by the local hydraulic conductivity and the infiltration capacity. Mixed water resides in this reservoir for at least one full annual cycle, meaning that evacuated mountain groundwater is older water. (4. *Coupled Stage*) As monsoon precipitation wanes, groundwater recharge slows down and a combination of evacuation to streams and upward loss through transpiration causes the groundwater table to drop. This drop is initially fast, but slows down once plants are no longer connected to the groundwater reservoir. At this point, the dry state sets in anew.

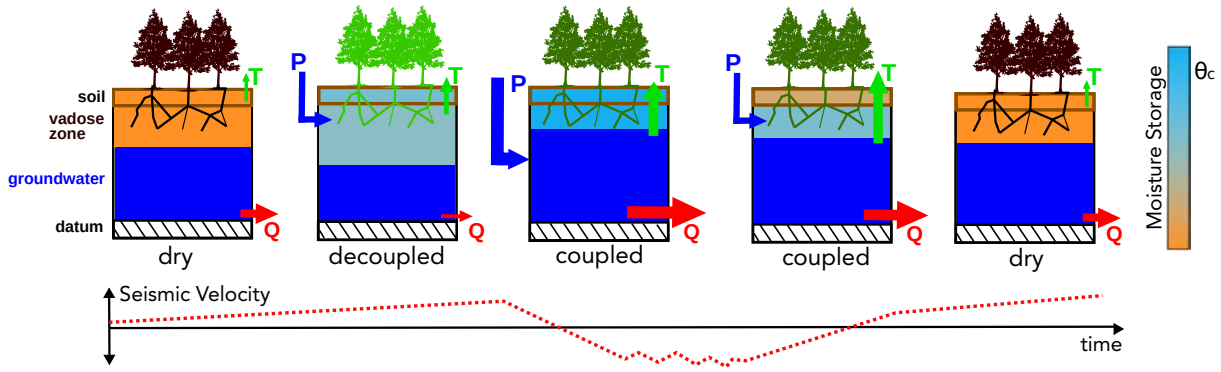

Figure 2.4: *Conceptual sketch of the evolution of hydrological systems throughout the monsoon cycle.* The arrows indicates the fluxes that control groundwater and subsurface moisture storage with T being transpiration, P the precipitation and Q the discharge. The colourbar indicates the scale for subsurface moisture storage where θ_c is the characteristic field capacity required to connect the precipitation input and the transpiration outtake to the groundwater. colours in trees indicate the evolving vegetation activity during one complete seasonal cycle. Sketches are in a 1D representation. Schematically, we also report the corresponding dv/v variations observed at Chaku at the different part of the Monsoon cycle. Time axis is not scaled.

The annual cycle we have described has hydrological seasons, which may differ from the meteorological seasons (Müller et al., 2014; Brunello et al., 2019). In the Nepal Himalayas, the crucial transition from the decoupled to the coupled state, after which precipitation is

most effectively translated into runoff, is determined by the saturation of the subsurface, which is governed, in turn, by the balance of precipitation and evapotranspiration during the preceding weeks to month. During our monitoring in the Bhote Koshi catchment, this transition happened around the meteorological monsoon onset and after 400-600 mm of cumulative precipitation over a period of some weeks, but elsewhere it may occur with a greater offset. We note that the similar threshold behaviour observed in the rock moisture reservoir on a hillslope in the Northern California Coast Ranges may not be as dependent on transpirative loss, as the onset of groundwater storage happened at a constant cumulative precipitation total for each recorded year in that study (Rempe & Dietrich, 2014). Moreover, within one landscape, the decoupled-to-coupled transition may not be uniform, with locations with less vegetation and soil cover, more precipitation, or less evaporation transitioning sooner.

These findings have likely implications for the prediction of natural hazards in the Himalayas. A precipitation event that may have little impact early in the year, when subsurface moisture is depleted and has a buffering capacity, could result in a flood later in the year when the vadose zone is at field capacity and both infiltration and direct runoff lead to water discharge. Monitoring of subsurface moisture and dv/v can help identify the transition from the decoupled to the coupled state, when the likelihood of flooding changes. This transition occurs when subsurface moisture ceases to rise and the shallow seismic velocity starts to decrease. Similarly, the decoupled-to-coupled transition may also have an impact on deep-seated landsliding: a substantial and sustained hazard in the Himalaya. Such landslides are often attributed to increased pore pressure (Iverson, 2000), which occurs once the vadose zone of the upslope area has reached field capacity. The hydrological regimes highlighted in our study could help delineate a landslide season, during which slope stability is a direct function of local precipitation (Gabet et al., 2004). A universal relation between precipitation rate and landsliding does not apply where the groundwater is episodically decoupled from precipitation input.

Our results also imply that prediction of mountain water resources requires knowledge of the thickness and properties of the soil and regolith layer, which is a gate keeper to the fractured crystalline bedrock in which the groundwater reservoir is primarily located (Rempe & Dietrich, 2014, 2018). During our three-year observation period, pre-monsoon precipitation did not contribute significantly to discharge but was rather mostly consumed in the vadose zone. However, this period contributes to the wetting of the landscape and pre-conditions rapid and effective transfer into groundwater and hence river discharge. The moisture content of the vadose zone determines first-order features of the precipitation-discharge relation in the Bhote Koshi catchment, and probably other catchments in the Himalayas and other mountain belts. The modulation cycle exerted by the subsurface moisture shows an indirect relation between precipitation and groundwater that may be responsible for the low streamflow sensitivity to water storage observed in other mountainous areas (Berghuijs et al., 2016). It is mediated not only by the infiltration of rain water, but also by upward water losses due to evaporation and transpiration. The balance of these gains and losses is likely highly sensitive to ecosystem composition, land use and the macroporosity of the soil: parameters that are influenced by climate change (Hirmas et al., 2018; Samaniego et al., 2018).

Recent work by Brunello et al. (2020) highlighted increasing pre-monsoon precipitation totals over the last $\sim$ 70 years. In conjunction with our findings, a longer and wetter pre-monsoon season would impact directly on the saturation of the vadose zone, the recharge of groundwater and river discharge, increasing the availability of water for hydropower and irrigation purposes. The demand for this water availability is large in densely populated

Asian basins, particularly the ones relying on Himalayan freshwater (Immerzeel et al., 2020). Forecasts of global climate change impacts on the Himalayan region predict a reduction of melt-water availability for an estimated 60 million people downstream (Immerzeel et al., 2010)). However, if global climate change will also alter the intensity distribution of the Indian monsoon, then we can expect vegetation activity, soil formation, erosion, and subsurface moisture dynamics to change as a consequence, with potentially even more severe consequences for water resources. The effect of subsurface changes due to climate change or changing land use has been acknowledged as a major knowledge gap in the freshwater resources IPCC special report (Jiménez Cisneros et al., 2015). For instance, decreasing trends in soil moisture due to warmer days (A. Wang et al., 2011; Fischer et al., 2011) would lead to a poor conversion of precipitation to water availability in environments similar to our study area. Therefore, the notion of mountain water towers in the Himalayas and sustainability studies on high mountain areas (Regine Hock, 2019) must be expanded from the cryosphere to include mountain subsurface moisture and groundwater and their complex link with precipitation. With $\sim$ 1.5 billions people on Earth projected to rely on discharge sourced from mountain areas (Viviroli et al., 2020), constraining this link for the major lithologies and ecosystems and monitoring the state of the vulnerable vadose zone in mountain regions are keys to anticipating the future trajectories of some of our most important freshwater reserves.

Data availability

This work was supported by the GFZ HART program. The authors are grateful to Bhairab Sitaula and all the HART Nepal team for their work on the field. The authors also thank one anonymous reviewer and Douglas Burbank for their valuable feedback that improved considerably the clarity of the paper. Data have been uploaded at the following repositories: seismic data (DOI: 10.14470/KA7560056170), Kahule Khola hydrometric data (DOI: 10.5880/GFZ.4.6.2021.003), weather stations data (DOI: 10.5880/GFZ.4.6.2021.003).

2.5 Appendix of paper I

Appendix A: Ambient Noise Processing

Preprocessing and calculation of correlation functions

A first step of preprocessing is needed to reduce the impact of high amplitude signals such as those induced by earthquakes or rockfalls before calculating the correlation functions. The seismic traces were trimmed to one hour segments, downsampled to 50 Hz, detrended and filtered in the 4-8 Hz frequency range. Then we applied spectral whitening: all the amplitudes in the Fourier spectrum were set to 1 before applying the inverse Fourier transform. The correlation functions with single station cross correlation (SC, (Hobiger et al., 2014)) were calculated as follows:

$$C_{k_1,k_2}(t_i,\tau) = \int_{t_i-T/2}^{t_i+T/2} \mathrm{sgn}[X_{k_1}(t')] \cdot \mathrm{sgn}[X_{k_2}(t'+\tau)]dt' \tag{2.4}$$

In the equation, k_m represents the different components $m = Z, N, E$ with $k_1 \neq k_2$ for SC, t is the time of the year and τ is the lag time of the correlation. T is the temporal

discretization in the correlation process. The sgn function stands for the 1-bit normalization of our signal: positive amplitudes are set to 1 and negative amplitudes are set to -1. We computed correlation functions at a time step of one hour and averaged them on a daily basis in order to get daily correlation functions (DCFs). We stored all the DCFs in a correlation matrix as shown in Figure 2.6.

Estimating velocity changes

If we assume a spatially homogeneous relative velocity change $\delta v = dv/v$ in the medium, a relative time delay $\delta\tau = dt/\tau$ will be observed in the DCFs coda with $\delta v = -\delta\tau$ where τ is the lapse time in the correlation functions and dt is the absolute time shift of a coherent phase. The relative velocity change has been estimated using the stretching technique (Sens-Schönfelder & Brenguier, 2019).

Depending on the daily velocity change, each DCFs ($C(t_i, \tau)$) will be stretched or compressed and compared to a long term average reference $\xi(\tau)$. For this study, we used multiple references $\xi_r(\tau)$ to avoid the possible degradation of a unique reference when averaged over the whole time period (Sens-Schönfelder et al., 2014). To do so, we first computed monthly references $\xi_r(\tau)$ with an overlap of 15 days. For each of these references, we calculated the correlation coefficients $R_r(t_i, \varepsilon_j)$ between stretched versions of the reference and the DCF as

$$R_r(t_i, \varepsilon_j) = \int_{\tau_1}^{\tau_2} C(t_i, \tau)\xi_r(\tau * (1 + \varepsilon_j))\mathrm{d}\tau \tag{2.5}$$

where τ is the traveltime of waves in the DCF and ε_j indicates a set of stretch-values that are tested in the time window set by $[\tau_1, \tau_2]$. We defined the length of the time window as follows: we skipped four signal periods before computing the stretching on a duration of 12 periods (corresponding window indicated in Figure 2.6). One period corresponds to the lowest frequency of the filter we previously applied (here $\tau_1 = 1$ s). Introducing τ_1 is necessary to avoid the use of early arrivals that are prone to change in noise sources characteristics. All $R_r(t_i, \varepsilon_j)$ values were stored in a similarity matrix as shown in Figure 2.7.

For each reference, a first daily measurement of $\delta v(t_i)$ can be done by reading the amount of stretching ε_j that yields the daily maximum $R_r(t_i, \varepsilon_j)$ value. To combine the measurements done with the multiple references, we stacked all similarity matrices $R_r(t_i, \varepsilon_j)$ after correcting for their shifting due to the velocity differences between the references. We finally obtained a stacked similarity matrix $R(t_i, \varepsilon_j)$ which describes the daily velocity variations obtained from one combination of sensor components k_1, k_2 (Fig. 2.7).

We applied this method to the three possible combinations (ZN, ZE, EN). In a last step, we stacked the three $R(t_i, \varepsilon_j)$ matrices and picked the ε_j as the location of the maximum of $R(t_i, \varepsilon_j)$ again. The final daily $\delta v(t_i)$ at the station is equal to ε_j.

Appendix B: modelling velocity changes induced by groundwater level variations, detailed method

Model A

The first applied model in the paper is similar to the one used in Sens-Schönfelder Wegler, 2006 and Hillers et al, 2014. In a first step, we model the evolution of the groundwater table depth. Conventions are shown on Figure 2.3 of the main text. The variation of the

hydraulic head is here approximated as a representative column reservoir of porosity ϕ. We assume that the rate of recession of the hydraulic head $h(t)$ is proportional to its height such as

$$\frac{dh}{dt}(t) = \frac{P(t)}{\phi} - ah(t) \tag{2.6}$$

where $P(t)$ is the precipitation rate and is the decay parameter. Similarly to an unconfined aquifer that obeys to Darcy's law, this equation predicts an exponential decay of the hydraulic head after impulsive rain events at t_n with its analytical solution:

$$h(t - t_n) = \frac{P(t_n)}{\phi} e^{-a(t-t_n)} \tag{2.7}$$

We introduce the asymptotic level h_0 to convert the hydraulic head height into the absolute groundwater table depth $GWD(t)$ as shown on Figure 2.3 with:

$$GWD(t) = h_0 + h(t) \tag{2.8}$$

Equation (2.6) is here discretised and integrated using a central Euler scheme with the daily precipitation data as inputs to obtain daily $h(t)$. Figure 2.8a shows examples of the model using our precipitation dataset with parameters taken as $\phi = 0.017$ and $a = 0.08$ d^{-1}. Because absolute groundwater level changes are unconstrained, we run our simulations with an arbitrary but realistic value of $h_0 = -50$ m.

We then convert the hydraulic head daily variations $h(t)$ into daily relative velocity changes δv. We assume that a change of $h(t)$ will induce a change in the relative slowness profile $S(t, z)$ with δs being the relative slowness difference between the saturated and dry state of the reservoir. We define a reference hydraulic head h_{ref} that is taken as the mean $h(t)$ over the whole time period of the study. We have $S(t, z) = \delta s$ for $h(t) < z < h_{ref}$ and $S(t, z) = -\delta s$ for $h_{ref} < z < h(t)$.

To model the depth sensitivity of the seismic waves, we used the 3-D scattered wavefield kernel derived by Pacheco and Snieder (2005). Because we applied the single station cross correlation technique, we considered coincident source and receiver which leads to the following equation

$$K_{3D}(\mathbf{x}, \tau) = (2\pi D r)^{-1} \exp \frac{-r^2}{D\tau} \tag{2.9}$$

with D being the diffusion constant, $\mathbf{x}$ is the point in space at distance $\mathbf{r}$ from the source/receiver and τ is the lapse time in the correlation function. We horizontally integrate $K_{3D}(\mathbf{x}, \tau)$ to get the depth sensitivity $K(z, \tau)$. Kernel examples for different diffusivity constant are plotted in Figure 2.8b.

In a last step, we compute the daily delay time by integrating the slowness perturbation profile weighted by the kernel as

$$\delta\tau(t, \tau) = \int_0^\infty S(t, z) K(z, \tau) dz. \tag{2.10}$$

We then convert the delay times in modeled daily relative velocity changes $\delta v_m = -\delta\tau/\tau$. We report in Figure 2.8c different synthetic velocity changes obtained from equation (2.10) with the 3 kernels proposed in Figure 2.8b. Because the kernels do not change significantly at the spatial scale of groundwater changes (~ 10 m) results are poorly dependent on the value of the diffusivity D and the kernel used. Therefore, we use the value of $D = 1.10^5 m^2.s^{-1}$ for our simulations.

We used an interior point algorithm in Matlab® (fmincon) to minimise the following least square misfit between our model and the data over the total number of days N:

$$\text{misfit} = \sum_{i=1}^{N} (\delta v_m(i) - \delta v(i))^2. \tag{2.11}$$

Our best fitting model is obtained with $a = 0.0134d^{-1}$, $\phi = 0.032$ and $\delta s = 0.007$. We note that different combinations for ϕ and δs can give similar results.

Model B

As explained in the main text, we propose to implement the role of the subsurface moisture reservoir with a simple antecedent precipitation index approach that does not require unconstrained physical parameters. The antecedent index is computed as follows:

$$P_M(t) = P_M(t-1)\exp(\ln 0.5/M) + R_h(t)\exp(\ln 0.5/2M). \tag{2.12}$$

$R_h(t)$ is the cumulative precipitation from $t-1$ to t and M is the half-time period in days required for the precipitation fed to the layer to decay to half of its initial value. We then introduce a threshold P_θ to model the field capacity of the subsurface: precipitation is only passed to the groundwater storage when $P_M(t) > P_\theta$. We calculate the P_θ threshold as the mean value of $P_M(t)$ at the date of the 2016 June 17th, 2017 June 21th and 2018 June 9th (red lines on Figure 2.9b-f). We chose these dates based on the trend detection of the onset of the seismic velocity decrease and the plateau observed in the soil moisture data that defines the start of the coupled regime. Then, we model the effect of vegetation in introducing the parameter h_b which is the critical depth at which the vegetation do not influence the drainage of groundwater anymore (see conventions in Figure 2.3). For this study we take the value of $h_b = 10$m which is a classic reported tree root depth (Canadell et al., 1996). We introduce the effect of transpiration on the groundwater with a second term to equation (2.6) involving an additional scaling term b within the depth h_b. Therefore, for $P_M(t) > P_\theta$, we have

$$\frac{dh}{dt} = \frac{P(t)}{\phi} - a\ (GWD(t) - h_0) - b\ (\min(0, GWD(t) - h_b)). \tag{2.13}$$

For periods when groundwater is not connected to the surface ($P_M(t) < P_\theta$), we have

$$\frac{dh}{dt} = -a\ (GWD(t) - h_0). \tag{2.14}$$

We convert the hydraulic head $h(t)$ evolution in seismic velocity variations following the same method described in model **A**. We test a whole class of models with parameter M ranging from 1 to 100 days and try to fit the data in minimising the misfit 2.11 using the same solver applied before for model **A**. The corresponding misfit values are shown in Figure 2.9a. The misfit space shows several local minima ranging from $M \sim 10$ d to $M \sim 40$ d. This suggests that values corresponding to the weekly and monthly scale fit the data equally well. We show 5 inverted models in Figure 2.9b-f and their corresponding antecedent precipitation index P_M.

2.6 Supplementary materials to paper I

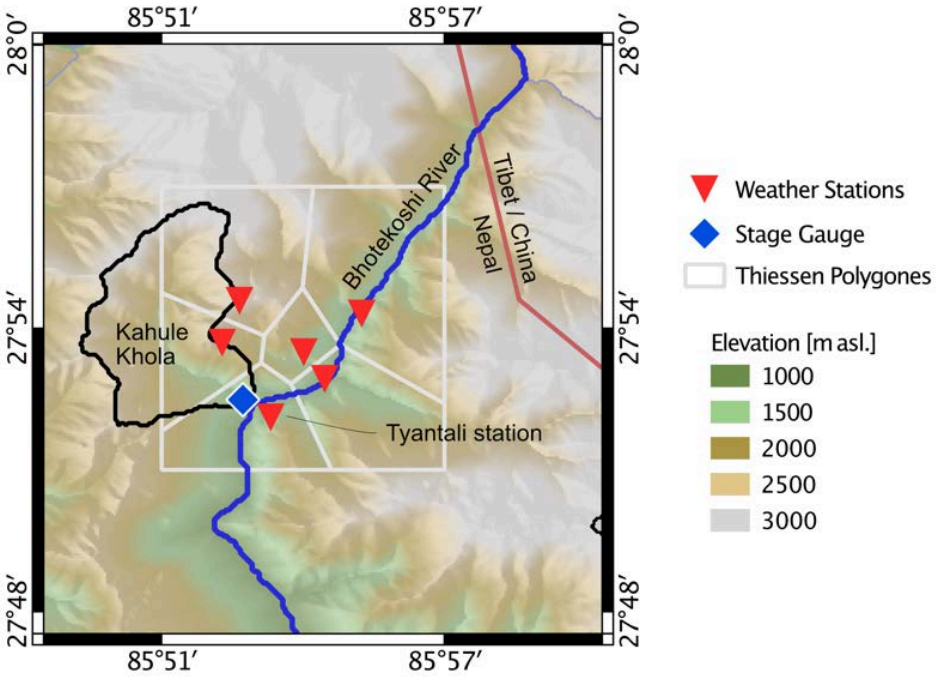

Figure 2.5: *Map of the weather station array installed in the Bhote Koshi River Valley during seismic monitoring period. We show the corresponding Thiessen polygons used to interpolate the precipitation time-serie used in this study.*

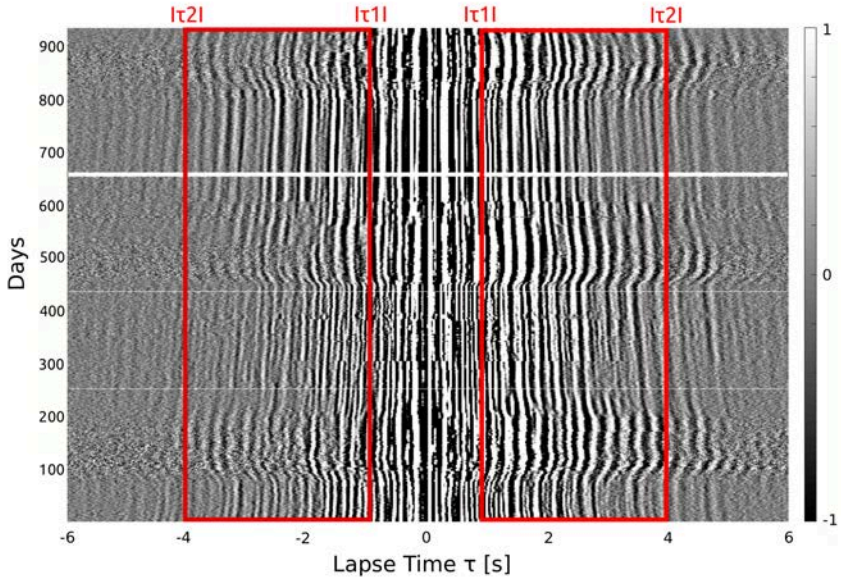

Figure 2.6: *Correlation Matrix for Chaku station, Channel combination ZN.* Red rectangles indicate the lapse time windows used for the stretching technique. Amplitudes are normalised in this time window.

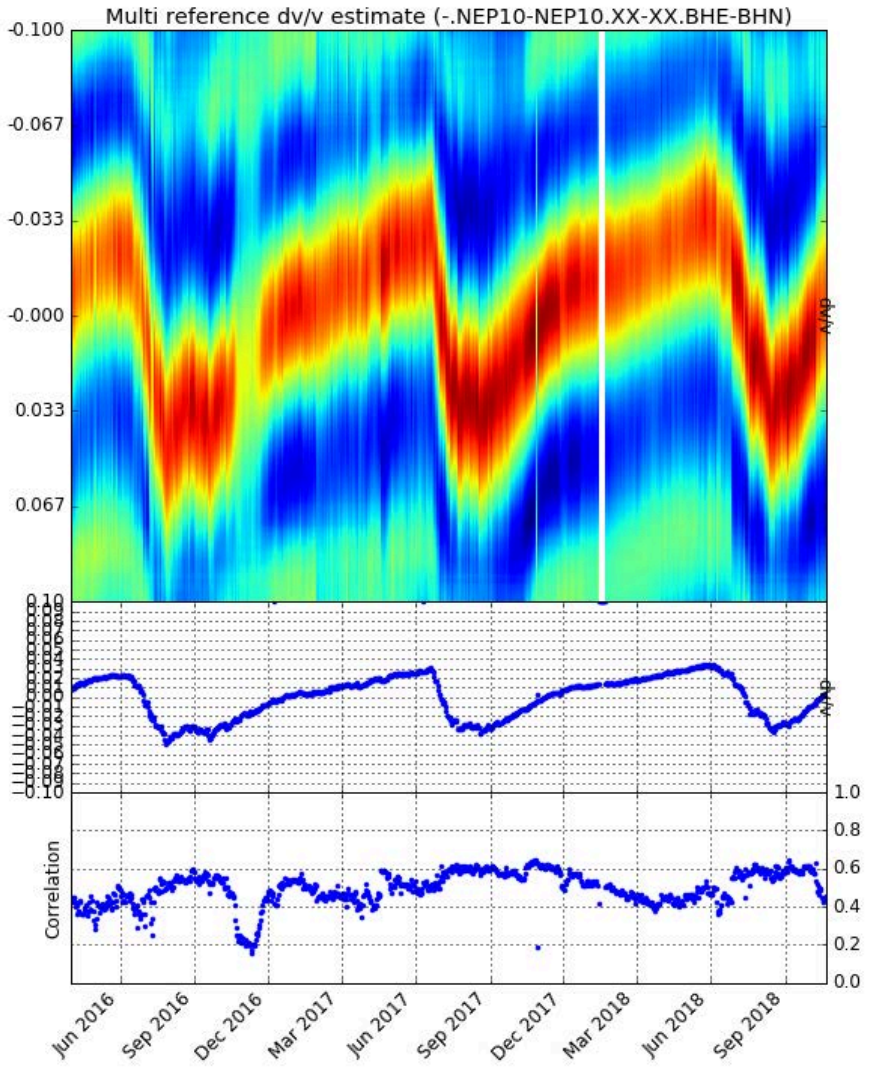

Figure 2.7: *Illustration of the velocity change measurements.* Similarity matrix example is shown in the upper panel. Corresponding stretch values are shown on the middle plot with corresponding picked correlation coefficients in the lower plot.

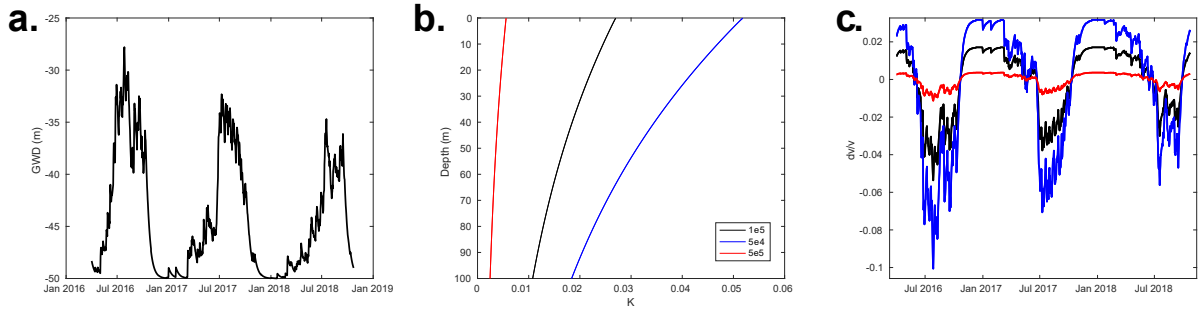

Figure 2.8: *Building blocks of model* ***A.*** **a.** Modeled groundwater level **b.** 3-D depth sensitivity kernels for diffusive wave propagation, different colours indicates different values of the diffusivity D **c.** Velocity changes inferred from the groundwater level evolution shown in **a.** and the associated kernels shown in **b.**

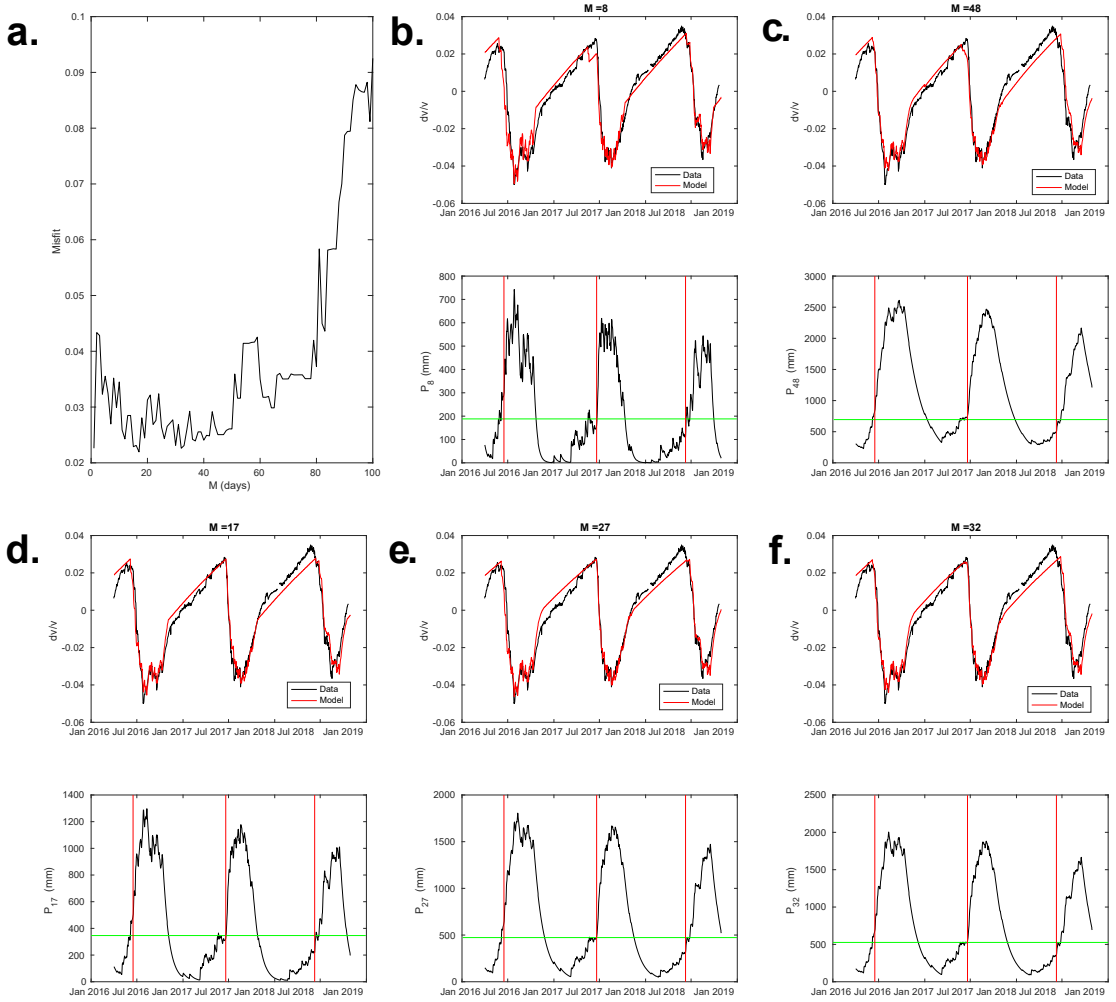

Figure 2.9: *Illustration of model **B** for various values of the half-time M* **a.** Misfit values obtained in the inversions of model **B** with different values of parameter . Corresponding models are shown in **b-f**. In each model subplot, the upper plots show the data at Chaku (black line) versus the best inferred model (red line). Lower plots shows corresponding antecedent precipitation index $P_M(t)$ curve with the threshold P_θ in green taken as the mean of P_M at the dates indicated by the red lines.

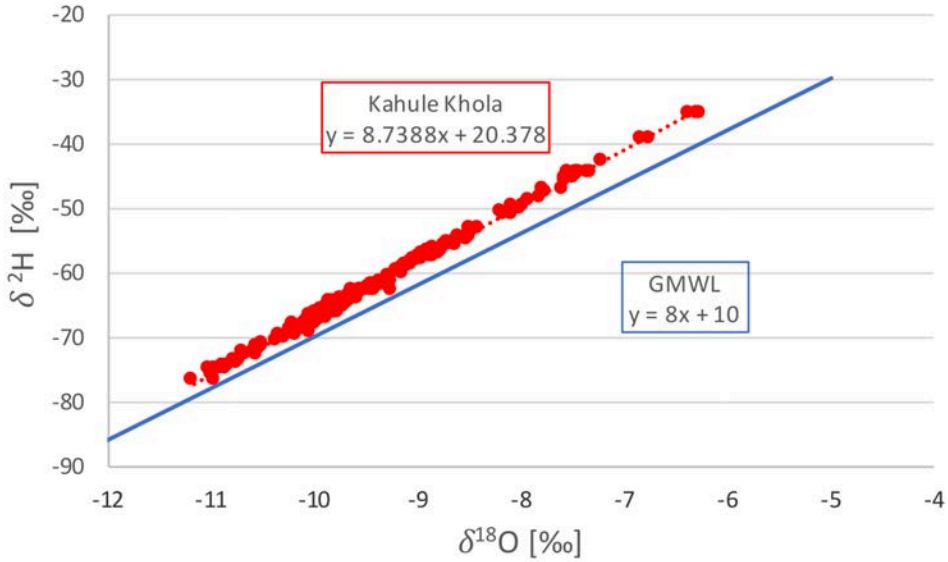

Figure 2.10: *Local Meteoric Water Line in the Kahule Khola versus global MWL.*

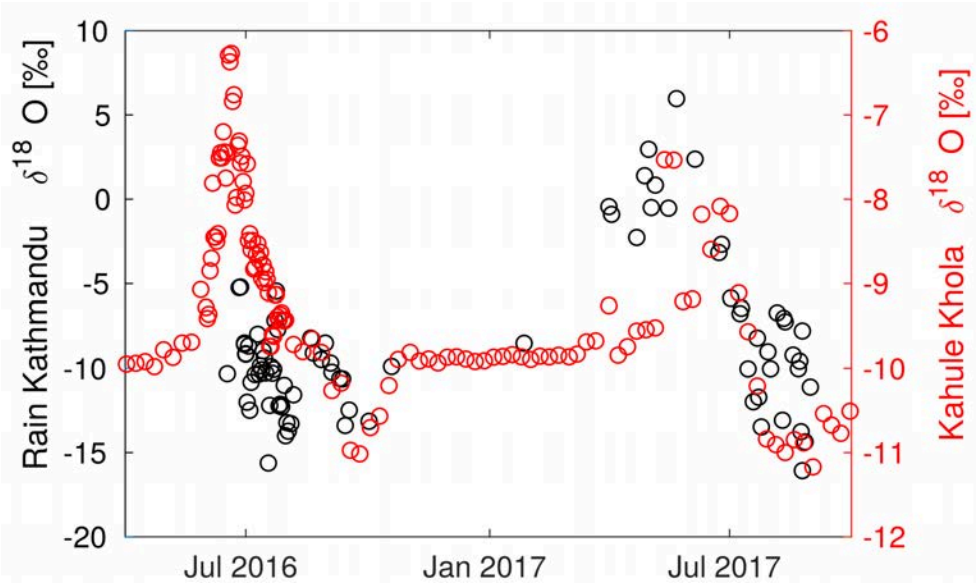

Figure 2.11: *Stable isotopes in the Kahule Khola versus precipitation at Kathmandu.* Black markers indicate $\delta^{18}O$ values measured in rain water in Kathmandu. Red markers corresponds to $\delta^{18}O$ values measured in the Kahule Khola river. Y-axis have different scales due difference in isotopic concentration in precipitation and the stream.

Transition
What about ground shaking ?

In Chapter 2, I have shown that the moisture saturation in the shallow subsurface acts as a gatekeeper for groundwater recharge and discharge generation against the Indian Summer Monsoon precipitation. This dynamics determines the annual water availability in the Bothe Koshi catchment, typical of the wider lower Himalayas units. We used an array of methods to constrain the hydrological dynamics, including the monitoring of relative seismic velocity changes as a proxy for groundwater storage. This technique allowed us to build a simple hydrological model that can predict the evolution of the local groundwater dynamics as a function of daily precipitation totals. Surprisingly, the moisture in the shallow subsurface did not influence the seismic velocity evolution which suggests that the dv/v measurement at our site mostly integrate the dynamics in the local fractured bedrock aquifer (Andermann et al., 2012).

We know from previous studies that fractured aquifers exhibit a transient response after earthquake ground shaking, notably an increase in permeability (Manga et al., 2012; Xue et al., 2013; Hosono et al., 2020). In April 2015, the Bothe Koshi field site experienced intense ground shaking and landsliding (Marc et al., 2019) due to the Mw 7.8 Gorkha earthquake. A month after the event, the seismic stations of Chapter 2 were deployed.

In Chapter 3, I have a closer look at the seismic velocity changes inferred at the same stations in the second half of 2015 and the early part of 2016. The effect of hydrological and earthquake induced velocity changes is often treated independently in seismic interferometry studies. Using the calibrated hydrological model derived in Chapter 2, I strip the dv/v time-series from the hydrological effects and disentangle the interaction between groundwater dynamics and the possible damage caused by ground shaking on the dv/v variations. Because the stations were deployed after the Gorkha earthquake, no prior velocity baseline is constrained by the data. Despite this limitation, the quantification of the timescales of perturbation of the hydrological system and the overall subsurface damage is my main focus in the next Chapter.

Chapter 3

Seismic velocity recovery in the subsurface: transient damage and groundwater drainage following the 2015 Gorkha earthquake, Nepal

Luc Illien, Christoph Sens-Schönfelder, Christoff Andermann, Odin Marc, Kristen L. Cook, Lok. B. Adhikari, Niels Hovius

Published in *Journal of Geophysical Research: Solid Earth*, February 2022, volume 127, issue 2, DOI: 10.1029/2021JB023402.

II

Abstract

Shallow earthquakes frequently disturb the hydrological and mechanical state of the subsurface, with consequences for hazard and water management. Transient post-seismic hydrological behaviour has been widely reported, suggesting that the recovery of material properties (relaxation) following ground shaking may impact groundwater fluctuations. However, the monitoring of seismic velocity variations associated with earthquake damage and hydrological variations are often done assuming that both effects are independent. In a field site prone to highly variable hydrological conditions, we disentangle the different forcing of the relative seismic velocity variations δv retrieved from a small dense seismic array in Nepal in the aftermath of the 2015 Mw 7.8 Gorkha earthquake. We successfully model transient damage effects by introducing a universal relaxation function that contains a unique maximum relaxation timescale for the main shock and the aftershocks, independent of the ground shaking levels. Next, we remove the modeled velocity from the raw data and test whether the corresponding residuals agree with a background hydrological behaviour we inferred from a previously calibrated groundwater model. The fitting of the δv data with this model is improved when we introduce transient hydrological properties in the phase immediately following the main shock. This transient behaviour, interpreted as an enhanced permeability in the shallow subsurface, lasts for $\sim$ 6 months and is shorter than the damage relaxation ($\sim$ 1 year). Thus, we demonstrate the capability of seismic interferometry to deconvolve transient hydrological properties after earthquakes from non-linear mechanical recovery.

3.1 Introduction

Following the passage of seismic waves, a wide range of transient effects have been observed near the Earth's surface, including increased landslide rates (Marc et al., 2015), enhanced permeability (Manga et al., 2012; Xue et al., 2013) and perturbations of frictional properties in fault zones (Pei et al., 2019). These observations suggest that earthquakes induce a

lingering effect in the properties of near-surface rocks that may be linked to non-linear mesoscopic elasticity (NLME, e.g. Gassenmeier et al., 2016; Marc et al., 2021). This phenomenon is generally expressed by a drop in elastic moduli after a dynamic or static strain perturbation, that is followed by a non-instantaneous recovery of these moduli. This recovery phase, also called relaxation or slow dynamics, is linear on a logarithmic time scale (Snieder et al., 2017) and can last anywhere from a few seconds (Shokouhi et al., 2017) to several years (Brenguier et al., 2008; Gassenmeier et al., 2016). Because most subsurface materials display this behaviour (Shokouhi et al., 2017; Gliozzi et al., 2018), understanding the amplitudes and timescales of the damage and recovery process of NLME is important for post-earthquake hazard mitigation.

In the field, the study of slow dynamics has been particularly advanced by the development of seismic interferometry techniques that monitor relative seismic velocity changes $\delta v = dv/v$ in the subsurface over time. Observations of co-seismic velocity drop and subsequent recovery in epicentral areas now abound and have been obtained from seismic ambient noise correlations (Wegler & Sens-Schönfelder, 2007; Brenguier et al., 2008; Hobiger et al., 2014; Gassenmeier et al., 2016) or waveform deconvolution in boreholes (Sawazaki et al., 2009; Wu et al., 2010; Nakata & Snieder, 2011). However, constraints on the physical mechanisms responsible for NLME in the field and the prediction of its amplitudes, timescales and associated effects have remained scare for several reasons. Firstly, the spatially averaged nature of the observation techniques does not allow for the precise identification of the responsible relaxation process among the many post-seismic processes acting at all depths and scales within a perturbed substrate. This complexity has prompted seismologists to use exponential functions characterised by variable timescales to fit velocity recoveries caused by individual events (Hobiger et al., 2014; Gassenmeier et al., 2016; Qin et al., 2020) rather than using particular physical relaxation models constrained from laboratory experiments (Lieou et al., 2017; Ostrovsky et al., 2019; Bittner & Popovics, 2021). Although this empirical approach can facilitate comparison between events, the understanding and prediction of the wide range of different recovery timescales (from minutes to years) between studies and sometimes within the same epicentral area (Viens et al., 2018) are limited. Moreover, aftershocks may induce superposed damage and healing processes, which may affect the observed recovery time of the main shock (Sawazaki et al., 2018).

The effects of slow dynamics may be obscured by hydrological fluctuations (Sens-Schönfelder & Wegler, 2006; Kim & Lekic, 2019a; Illien et al., 2021), which can influence the seismic velocity. Monitoring of hydrologically induced velocity variations (δv_{H}) is often done under the assumption that hydrological changes and NLME are independent processes that can be superimposed such that the observed δv signal is simply the sum of hydrological and NLME effects ($\delta v = \delta v_{\mathrm{NLME}} + \delta v_{\mathrm{H}}$). However, there is evidence that both effects are not independent. It has been shown that the hydrological conditions of hillslopes can alter the NLME-response to dynamic strain (Bontemps et al., 2020). Moreover, as mentioned above, transient hydrological behaviour following co-seismic ground shaking has been widely reported in borehole measurements (Elkhoury et al., 2006; Xue et al., 2013; Shi et al., 2015) and streamflow (C. Y. Wang et al., 2004), suggesting that the hydrological system is also impacted by the transient variation of material properties. For example, the opening of cracks, which is often used to explain coseismic velocity decreases, can also introduce a change in substrate permeability (Elkhoury et al., 2006; Xue et al., 2013). Lastly, the similarity between the seismic velocity recovery timescale ($\sim$ 50 days, Taira et al., 2015) and the duration of the stream discharge increase (C. Y. Wang & Manga, 2015) observed after the 2014 South Napa earthquake suggests a strong link between relaxation-induced

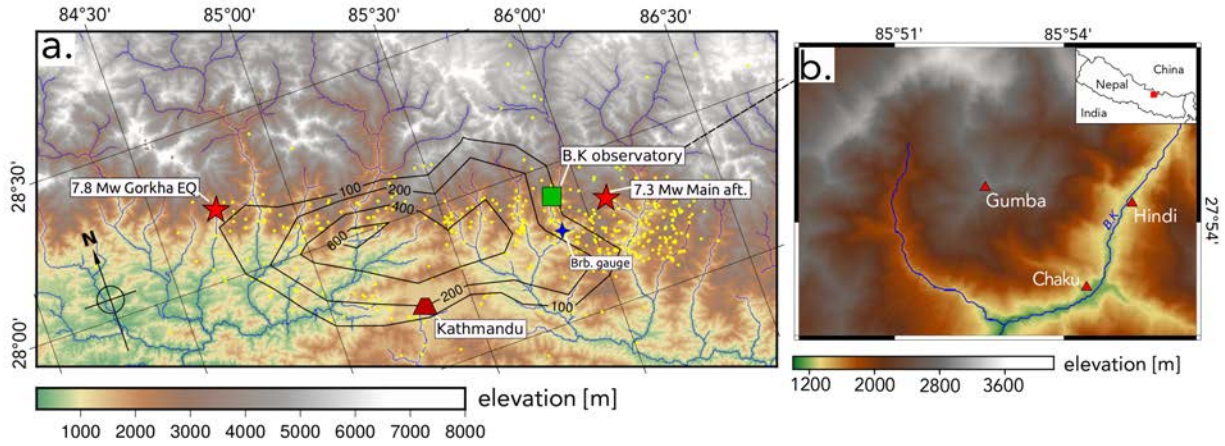

Figure 3.1: *Map of the study area.* **a)** Black solid lines show the isolines for the Gorkha co-seismic slip (in cm) from the inverted solution of Elliott et al. (2016) using INSAR data. Yellow dots account for aftershocks of magnitude > 4 (Adhikari et al., 2015). Red stars show the epicenter of the Gorkha earthquake and its main aftershock (12^{th} of May 2015). Green square is the Bothe Koshi observatory and blue star is the water gauge for measuring stage height of the Bothe Koshi river. **b)** Close-up on the Bothe Koshi observatory. Red triangles show the site where seismic stations are deployed. B.K stands for Bhote Koshi river.

velocity changes and transient hydrological properties. Because of the complexity of both processes and their coupling, it has not yet been possible to document the shaking induced perturbation of the hydrological system by means of seismic interferometry.

To investigate the shaking induced variations of a hydrological system with seismic interferometry, we use a seismo-hydrological dataset from the Nepal Himalayas that (a) features strong hydrological forcing, (b) includes the recovery phase of a large crustal earthquake and (c) is described by a calibrated hydrological model that connects precipitation input to seismic velocity variations (Illien et al., 2021). Our approach involves accurate observations of seismic velocity changes, correcting the velocity changes for NLME effects due to the seismic activity and finally investigating the ability of the hydrological model to describe the residual velocity changes during different phases of the main shock recovery. Our field site is located in the epicentral area of the 2015 Mw 7.8 Gorkha Earthquake (Fig. 3.1a), in the Bhote Koshi catchment in Nepal about 60km north east of Kathmandu in the steep ridge and valley topography of the lesser Himalayas. The region experienced strong ground shaking (Wei et al., 2018), widespread landsliding (Roback et al., 2018) and numerous aftershocks (Adhikari et al., 2015). Due to a distinct wet and dry season in which $\sim 80\%$ of the annual precipitation occurs during the Indian Summer Monsoon between $\sim$ May and $\sim$ October (Bookhagen & Burbank, 2010; Brunello et al., 2020), the hydrological conditions at this site are highly variable. This combination of pronounced and well-constrained hydrological and seismic forcing makes our field site a suitable location to study the interplay of seismic damage and hydrology.

The paper is organised as follows: we present the data and the seismic interferometry technique used to estimate velocity changes in Section 3.2. Section 3.3 shows the corresponding raw velocity changes observed after the Gorkha earthquake and its aftershocks. In Section 4, we present and discuss our models used to compute synthetic δv values based on models for damage and hydrology. Section 3.4.1 is devoted to the damage-induced variations δv_{NLME} in which we introduce a new approach to describe the effects of the

Gorkha mainshock and its aftershocks in a consistent model whereas Section 3.4.2 explores the residuals of the damage-corrected δv time series using the hydrological model of Illien et al. (2021). This allows us to assess transient variations of the hydrological system in the Bhote Koshi catchment following the Gorkha event.

3.2 Data and methods for estimating seismic velocity changes

Three broadband seismic stations (3-components Trillum compact 120s) were installed on the 6^{th} of June 2015, 42 days after the Gorkha main shock near Chaku village (Fig. 3.1b) and recorded until the 23^{rd} of October 2018. The seismic stations were installed on a bedrock terrace at a distance of $\sim$ 100 m from each other to achieve highly resolved temporal averaging at the same location. The metasedimentary rocks of the terrace are covered by a layer of regolith and colluvium. Because our stations were deployed after the Gorkha main shock, we also used data from the Gumba station (Fig. 3.1b) of the Nepalese Seismological Center to confirm that our field site experienced a co-seismic velocity drop nearby and is in a recovery phase. This station has a single component and is located at 4.3km from our field site and 1700m higher the Chaku terrace. For Gumba station, we evaluated data from January 1^{st}, 2014 to December 9^{th}, 2015. Daily precipitation were also measured from a network of precipitation gauges set up in the Bothe Koshi observatory (see the Data availability statement). We note that no major landslides occured in the vicinity of our seismic stations (Marc et al., 2019) which imply that observed velocity changes are unlikely to be caused by redistributions of surface materials.

3.2.1 Estimation of daily relative seismic velocity changes

We use seismic ambient noise to monitor variations of seismic velocity in the subsurface (Sens-Schönfelder & Brenguier, 2019). To reduce the impact of high amplitude signals in the noise correlation process, we use the following pre-processing scheme: the seismic traces are trimmed to one hour segments, downsampled to 50 Hz (only for Chaku stations) and detrended. We filter Chaku stations in the 4-8 Hz frequency range and data from Gumba station in the 2-4 Hz range due to limited seismic energy at higher frequencies. We normalize Chaku amplitudes to 1 in the Fourier spectrum (spectral whitening) and perform single station cross correlation (SC method, Hobiger et al., 2014), using

$$C_{k_1,k_2}(t_i,\tau) = \int_{t_i-T/2}^{t_i+T/2} sgn[X_{k_1}(t')] \cdot sgn[X_{k_2}(t'+\tau)]dt', \tag{3.1}$$

where t_i is the time of the trace and τ is the lapse time of the correlation. T, the length of the correlated noise segments determines the temporal resolution of the δv time series. The *sgn* function represents the 1-bit normalization of the signal in which we set positive amplitudes to 1 and negative amplitudes to -1. k_m stands for the different components $m = Z, N, E$ with $k_1 \neq k_2$ for SC. Because Gumba has one component only, we compute the autocorrelation of the vertical component $C_{ZZ}(t_i,\tau)$. Correlation functions are calculated with a time step of one hour before averaging them every 24h to obtain daily correlation functions (DCFs). We store all the DCFs in a correlation matrix, as shown in Figure 3.12.

We use the *stretching* technique (Sens-Schönfelder & Wegler, 2006) to estimate relative velocity variations. After a spatially homogeneous relative velocity change $\delta v = dv/v$ in

the medium, the time delay $\delta\tau = dt/\tau$ can be observed in the DCFs coda with $\delta v = -\delta\tau$ where τ is the correlation lapse time and dt is the absolute time shift of a coherent phase with travel time τ. Depending on the daily velocity changes, the DCFs ($C(t_i, \tau)$) are stretched or compressed when compared to a long term average reference $\xi(\tau)$. To avoid the effects of a possible degradation of a unique reference when averaged over the whole time period (Sens-Schönfelder et al., 2014), we use multiple references $\xi_r(\tau)$ at the Chaku site by computing monthly references $\xi_r(\tau)$ with an overlap of 15 days (we illustrate the use of different references in Figure 3.13). For each of these references, we calculate the correlation coefficients $R_r(t_i, \varepsilon_j)$ between stretched versions of the reference and the DCF such that

$$R_r(t_i, \varepsilon_j) = \int_{\tau_1}^{\tau_2} C(t_i, \tau)\xi_r(\tau * (1 + \varepsilon_j))\mathrm{d}\tau \tag{3.2}$$

where τ is the traveltime of waves in the DCF and ε_j indicates a set of stretch-values that are tested in the time window set by $[\tau_1, \tau_2]$. We define the length of the time window as follows: we skip four signal periods T, where one period corresponds to the lowest frequency of the bandpass filter we previously applied (here $T = 0.25s$), before computing the stretching on a duration of 12 periods (corresponding window indicated in Figure 3.12). Introducing τ_1 is necessary to avoid the use of early arrivals that are prone to changes in noise sources characteristics. All $R_r(t_i, \varepsilon_j)$ values are stored in a similarity matrix.

For each reference, a first daily velocity measurement $\delta v_r(t_i)$ can be done by reading the amount of stretching ε_j that yields the daily maximum $R_r(t_i, \varepsilon_j)$ value. Combining the measurements done with the N various references, we stack all similarity matrices $R_r(t_i, \varepsilon_j)$ after correcting for any average shifting ($\overline{\delta v_r}$) due to the velocity differences between the references (full method described in Sens-Schönfelder et al., (2014)) following the relation

$$R(t_i, \varepsilon_j) = \sum_{r=1}^{N} R_r(t_i, \varepsilon_j) - \mathrm{shift}(\overline{\delta v_r}). \tag{3.3}$$

$R(t_i, \varepsilon_j)$ describes the daily velocity variations obtained from one combination of sensor components k_1, k_2. We applied this method to the three possible combinations (ZN, ZE, EN) for each of the Chaku stations. We finally stack the resulting nine $R(t_i, \varepsilon_j)$ matrices (3 stations with 3 combinations) and pick the $\varepsilon_j(t)$ with the maximum $R(t_i, \varepsilon_j)$ again. The final daily $\delta v(t_i)$ at the Chaku site is equal to this specific $\varepsilon_j(t)$. For Gumba station, we use only one reference as the use of multiple references does not improve the retrieved δv values.

3.2.2 Local aftershocks catalog and estimation of associated velocity changes δv_{A}

Aftershocks recorded after the Gorkha earthquake may bias the recovery timescale estimated after the main shock by inducing further velocity drops and recoveries. However, due to potentially large hydrological fluctuations at the daily timescale of the interferometric processing, it may be challenging to dissociate the effect of cumulative aftershocks from hydrologically induced velocity variations. To address this issue, dedicated velocity change measurements following local aftershocks were conducted at a finer temporal resolution. Despite aftershock catalogs being available for the Gorkha earthquake (Adhikari et al., 2015; Baillard et al., 2017), their relevance for our field site remains limited as they lack information about the local shaking at the Chaku site. Therefore, to estimate the

cumulative effects of shaking due to the aftershocks on the velocities, we build a catalog based on the daily peak ground velocity (PGV) recorded at Chaku. We first retain days with PGV greater than $1e^{-4}$ m.s^{-1}. In the field, this value is approximately an order of magnitude lower than the minimum excitation required to induce a detectable change in rock properties as reported in the literature (Elkhoury et al., 2006; Wu et al., 2010). To exclude potential spurious peaks due to local artefacts, we check if the corresponding signals were also recorded at another temporary station (Hindi station on Figure 3.1b) located at $\sim 3km$ from our site. Using this procedure, we pick 82 potential aftershocks.

To test whether these events triggered NLME, we perform single station cross correlations of the ambient noise centered around the 82 events using the same method described in section 3.2.1, but with a 10-minute interval for the estimation of δv. We find that 18 events triggered a seismic velocity drop that was observable at this resolution. We quantify the co-seismic velocity drops by taking the difference between the median δv value of the 12 hours preceding the aftershocks (no detectable velocity drops occurred during this time span) and the median value of the first hour succeeding the events.

3.3 Seismic velocity changes

3.3.1 Evidence for non-linear recovery after Gorkha earthquake

In Figure 3.2a, we report the daily relative seismic velocity changes estimated at the Chaku site and the daily precipitation totals recorded at nearby precipitation gauges in Figure 3.2b. The Chaku δv time series exhibits a clear annual cyclicity exerted by the climatic forcing with a consistent drop of up to 8% in measured δv values during the monsoon season. Because of these significant hydrology-induced velocity changes and our dataset starting at 42 days after the Gorkha main shock (dashed lines in Figure 3.2), the recognition of any non-hydrological component in the δv time series is strongly overprinted. Nevertheless, several arguments pinpoint the presence of NLME recovery in our time series.

First, we report the velocity changes observed at the Gumba seismic station (Fig. 3.2d) as general evidence for NLME in the study area. A clear velocity drop of $\sim 5\%$ is observed at the date of the Gorkha earthquake. We attribute the noisy nature of the measurements to the lack of averaging in the velocity retrieval at this station for which only a single component is available. For this reason and because of the limited data coverage after the main shock, we do not attempt to characterise the recovery phase following the main shock at this station. Nonetheless, the clear co-seismic drop shows that ground shaking during the Gorkha event has caused damage in the Bhote Koshi catchment that is likely followed by a phase of recovery of subsurface material properties.

A second observation pointing to NLME behaviour comes from a comparison of the annual cycles in δv as shown in Figure 3.2c. In 2016-2018, the mean annual δv cycle peaked to $\sim +4\%$ at the end of the pre-monsoon season in May. At the same time of the year in 2015, a clear offset from this value was observed with δv as low as $\sim$ - 1%. Despite our precipitation dataset starting the 6^{th} of June 2015, it is unlikely that this offset is caused by climatic conditions. Indeed, with the 2015 monsoon being rather weak compared to precipitation totals of other monsoons seasons (Fig. 3.14), a dryer season would cause the 2015 δv data to be relatively higher than in the other years. This was not observed.

Finally, the last argument indicating NLME processes comes from hydrological modelling. We previously showed that the seismic velocity at Chaku reflects the groundwater content of the substrate in the vicinity of seismic instruments (Illien et al., 2021). This can be

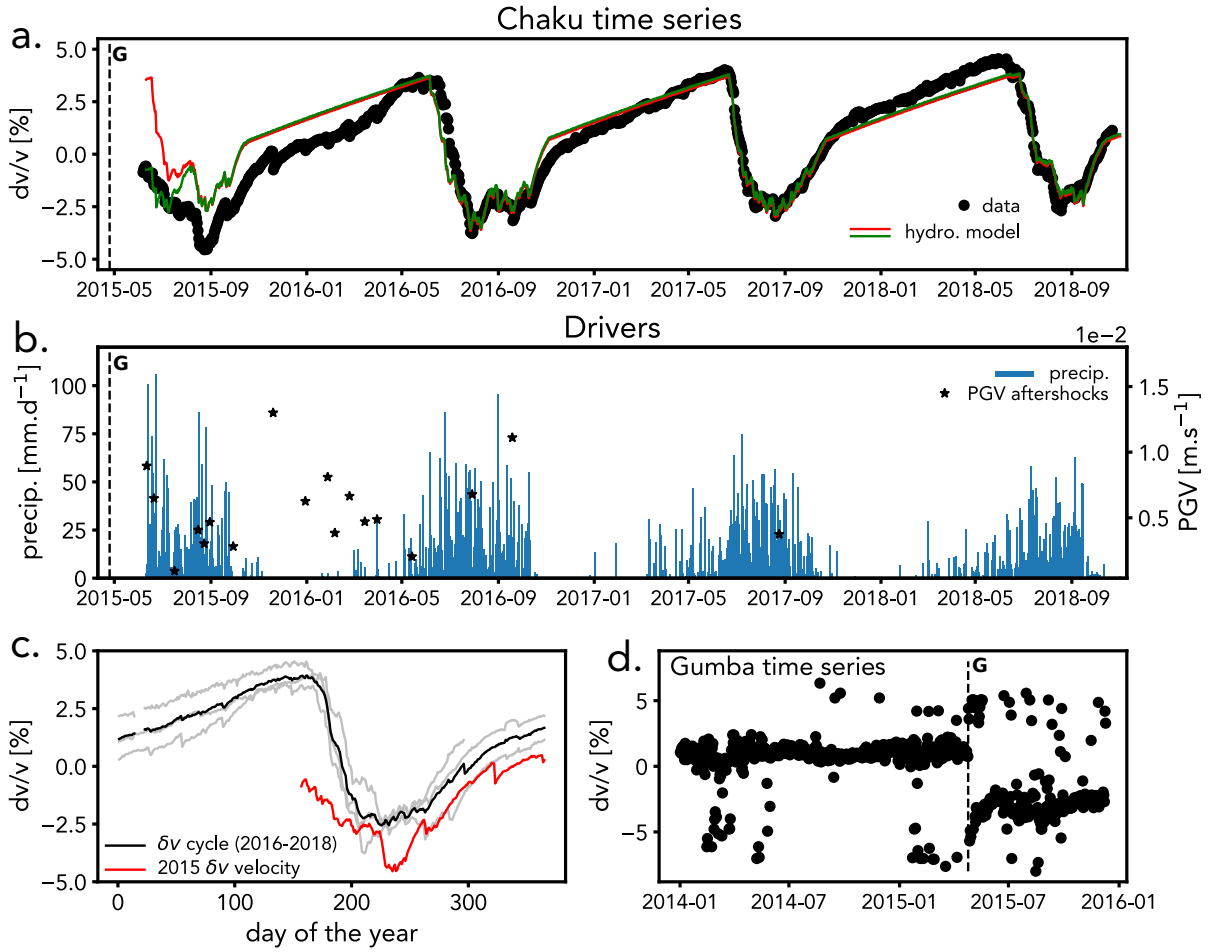

Figure 3.2: *Evidences for NLME at Chaku.* Black dashed lines in plots **ab** and **d** indicate the date of the Gorkha earthquake. **a)** Black dots show the raw daily δv measured at Chaku. coloured solid lines display results using the hydrological model of Illien et al. (2021) with different initial conditions. **b)** Blue lines show local daily precipitation. Black stars stand for the PGV of aftershocks that caused a seismic velocity drop at the Chaku site. **c)** shows the same data as panel **a**, but with the δv of each year plotted on top of each other. 2015 velocity is in red. **d.** δv variations estimated from Gumba station.

shown using the precipitation data recorded at our field site (Fig. 3.2b). For comparison, we report this model in Figure 3.2a. We consider two different initial conditions for δv in our model: one using the initial observed δv (green line in Figure 3.2a) and another using the expected δv value based on observations from years 2016-2018 at this time of the year (red line in Figure 3.2a). Both synthetics show good agreement with the velocities from April 2016 to the end of the time series – the period in which the model was calibrated, assuming that the NLME effect should be negligible in comparison to the hydrological influence on δv. However, velocities in 2015 are largely overestimated by the hydrological model with an offset of $\sim 4\%$ at the start of the time series. We note that this mismatch is progressively reduced at later times and converge towards the hydrological calibration. This supports a significant second control on δv during the observation period, in addition to the pervasive hydrological influence. Considering this list of arguments, we conclude that a recovery behaviour due to NLME likely occurred at Chaku.

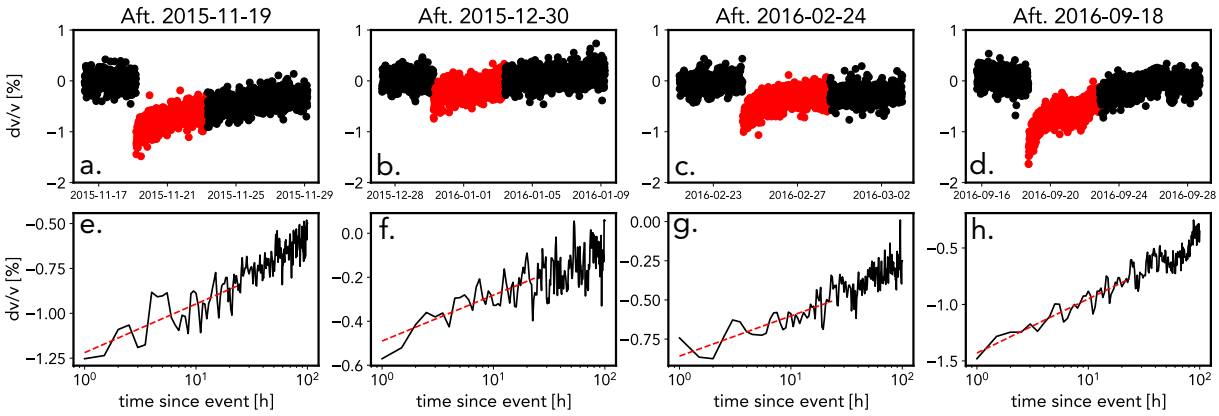

Figure 3.3: *Velocity recoveries following aftershocks.* **abcd)** show the velocity obtained at a 10-minute resolution with the red dots indicating the first 100 hours after the events. **efgh)** show the close-ups of the results in the first 100 hours after the events in a log-linear plot. Results are averaged at a 30-minutes resolution. The red lines depict the fit of a log-linear slope on the first 24 hours of relaxation.

3.3.2 Seismic velocity drop and recovery induced by single aftershocks

We observe small velocity drops that are particularly visible during the first dry season of the Chaku dataset (starting $\sim$ November 2015 in Figure 3.2a). We attribute these drops to further dynamic strain perturbations induced by aftershocks. Figure 3.2b shows the PGV measurements corresponding to the aftershock catalog we described in section 3.2.2. The occurrence of the velocity drops in the daily δv time series agrees with the timing of the reported ground shaking.

Observed velocity drops range from 0.25 to 1.5 % and appear to have a linear relationship with PGV values (0.25 to 1.3 cm.s^{-1}, Figure 3.15) although with a moderate scatter ($R^2 = 0.62$). For events occurring during dry periods, a clear slow dynamics behaviour is observed with a distinct nonlinear recovery in the following hours after the initial drop (Fig. 3.3, a-d). We highlight the characteristic log-linear behaviour by averaging the data at a 30-min resolution and showing the first 100h in δv after the velocity drops in a log-linear plot (Fig. 3.3, **e-h**). The fit of a log-linear function of the form $\delta v = s \log(t) + C$, typical of the NLME functional form (TenCate et al., 2000), gives a satisfactory representation of the velocities. To avoid the possible larger hydrological modulation of δv at late recovery times, we will model aftershock effects considering only an early time span.

3.4 Modelling δv: derivation and implications

In this section, we develop and use models to fit the seismic velocity changes presented in section 3.3 and discuss their implications. The classic approach to decompose seismic velocity changes δv is a linear superposition of forcing that can be written as

$$\delta v = \delta v_{\mathrm{NLME}} + \delta v_{\mathrm{H}} \tag{3.4}$$

where δv_{NLME} are the velocity changes due to NLME and δv_{H} are the hydrologically-induced velocity changes. δv_{NLME} can be further decomposed into two components

representing the relaxations due to Gorkha (δv_{G}), and its aftershocks (δv_{A}). To go beyond the linear description of expression 3, which does not account for transient post-seismic hydrological behaviour, we propose a modelling approach based on two iterations: we first model the effect of NLME using conventional exponential functions. This approach is compared to the use of universal relaxation functions $R(t)$ which are calibrated for the first time on field data and are characterised by constant relaxation timescales, independent from ground shaking amplitude. To avoid a contamination by strong hydrological variations in the fitting, we calibrate the functions R(t) using the initial 24 h δv dynamics following aftershocks events.

In a second step, we remove the inferred δv_{NLME} component from the δv time series to obtain residuals that represent the hydrological induced variations δv_{H} (Section 3.4.2). We test whether δv_{H} is not only influenced by precipitation but also by seismic damage. Because the meteorological effect on δv_{H} is well constrained by the model of Illien et al. (2021), we introduce a transient drainage parameter in this model to estimate $\delta v_{\mathrm{H}}^{*}$, which represents the seismically forced part of the hydrological component.

3.4.1 Post-seismic relaxations

We first apply the classic approach to model the recovery as an exponential recovery of the moduli and show that despite having numerous parameters for each event, the model performance is insufficient. Therefore, we propose a new strategy that uses a universal relaxation function and allows the description of all aftershocks and the mainshock with one consistent model, facilitating a correction of the time series for NLME effects.

3.4.1.1 Modelling δv_{NLME} with exponential functions

In seismic interferometry studies (Hobiger et al., 2014; Gassenmeier et al., 2016; Qiu et al., 2020), the nonlinear recovery in seismic wave velocity δv is often fitted with the following function:

$$\delta v(t) = \delta v_0 \exp\left[\frac{-(t-t_0)}{\tau}\right] + C \tag{3.5}$$

where t_0 is the time of the earthquake occurrence, δv_0 is the initial co-seismic velocity drop at the temporal observation scale, τ is a characteristic time scale of recovery and C is a permanent drop.

To estimate the three empirical parameters of the exponential model, we use the velocity changes computed during the first 24h following the four aftershocks presented in section 3.3.2 (Fig. 3.3). In this time-span, a clear drop-recovery signal with no apparent hydrological-induced variations is observed (Fig. 3.3). Assuming that $C = 0$ for the small excitations caused by the aftershocks, we fit expression 3.5 to the four δv time series to obtain the characteristic timescales for the aftershocks τ_A. The recovery time constants range from $\tau_A = 1.18$ d to $\tau_A = 3.03$ d (Fig. 3.4). To demonstrate the performance of this model, we build two synthetic time-series for the velocity variations induced by all aftershocks δv_A using these two end-member values (Fig. 3.5a, full method in Text S1).

After removing the synthetic δv_A from the full δv Chaku time-series, we fit the residuals with equation (3.5) to obtain the recovery time constant τ_G for the Gorkha earthquake. We find a best fitting model with $\tau_G = 198$ d and a confidence interval of 80 d $< \tau_G <$ 1208 d that includes all model solutions with a variance ratio above 95% (Fig. 3.16). The value used for the aftershocks correction (τ_A of 1.18 or 3.03 days) does not influence the inferred

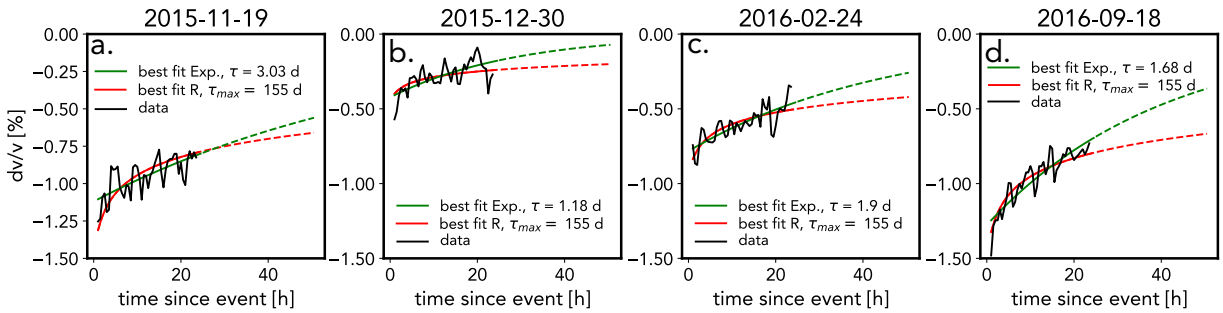

Figure 3.4: *Fitting of the aftershocks recoveries.* On each plot, green lines show the best fit of the exponential function for each observed recoveries (black lines). Red lines show the best fitting model using the relaxation function with a constant maximum relaxation timescale ($\tau_{\max} = 155$ d)

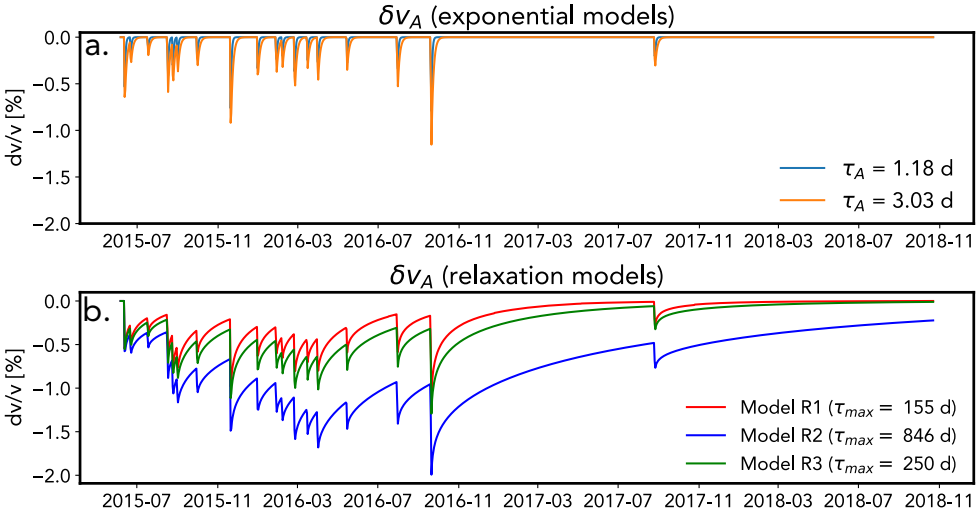

Figure 3.5: *Synthetic seismic velocities induced by aftershocks* δv_A. **a)** Models built with the two end-member values τ_A measured with the exponential functions. **b)** Models built using superposition of the relaxation functions of models R^{155}, R^{846}, R^{250}.

τ_G. Synthetic time-series corresponding to the joint effect from the mainshock and the aftershocks are in Figure 3.6ab together with the data residuals after correction for δv_{NLME}. The strongest differences are observed in the early part of the recovery depending on the characteristic timescale τ_G chosen for the main shock. Despite using the longest time scale for aftershock recovery of $\tau_A = 3.03$ d, the recoveries seem to not be fully corrected between $\sim$ November 2015 and $\sim$ June 2016 (Fig. 3.6c). This suggests that longer timescales of relaxation after aftershocks should be introduced to fully correct for δv_A.

3.4.1.2 Modelling δv_{NLME} with a universal relaxation function

A characteristic of NLME is that the functional form of the recovery process is linear on a logarithmic time scale (Fig. 3.3). A very convenient way to model this behavior is provided by the universal relaxation function used by Snieder et al. (2017). In this framework, the relative seismic velocity changes are described by a relaxation function $R(t)$:

$$\delta v(t) = \delta v_{ss} + sR(t - t_0) \tag{3.6}$$

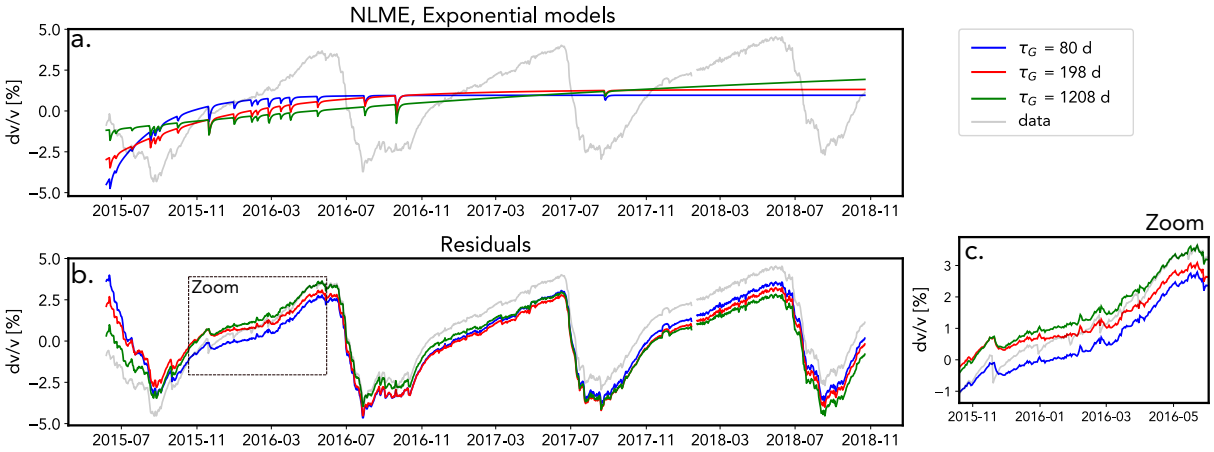

Figure 3.6: *NLME models built with exponential recovery functions.* **a)** Each curve indicates synthetic recoveries characterised by different τ_G within the 95% confidence interval of the best fitting model (τ_G= 198 d). We superposed on this curve the recoveries associated with the synthetic δv_A time series (τ_A= 3.03 d). **b)** Corresponding residuals from the models shown in **a.** Light grey line show the raw data. Dashed line indicates the zoomed window for the plot shown in **c.**

where δv_{ss} is the steady state value of $\delta v(t)$ and s is a scaling factor. $R(t)$ is the relaxation function that represents a multitude of processes with characteristic timescales. These timescales are distributed between a lower bound $\tau_{\min}$ and a maximum relaxation time $\tau_{\max}$. This theory leads to a superposition of these exponential processes that is given by

$$R(t) = \int_{\tau_{\min}}^{\tau_{\max}} \frac{1}{\tau} e^{-(t-t_0)/\tau} \, \mathrm{d}\tau. \tag{3.7}$$

A justification of equation (3.7) based on the Arrhenius law is given by Snieder et al. (2017) but we recall a few important properties of the relaxation function: $R(t)$ exhibits a logarithmic behavior between the bounds $\tau_{\min}$ and $\tau_{\max}$ and its value at $t = 0$ is finite and determined by $R(0) = \ln(\tau_{\max}/\tau_{\min})$. The prefactor $1/\tau$ increases the contribution of the processes with the shortest relaxation times, which leads to a uniform distribution of barrier energies according to Arrhenius law. Figure 3.7 illustrates the influence of the parameters $\tau_{\min}$ and $\tau_{\max}$.

Because of the multi-scale character of the universal relaxation function, we can describe the effects of the weak aftershock perturbations and the strong perturbation induced by the main shock with the same relaxation times τ in equation (3.7). As we observe logarithmic recovery from the earliest measurement in Figure 3.3, we fix the parameter $\tau_{\min}$ to 1 h corresponding to the observation timescale. In the lab, minimum relaxation times down to 10^{-2} s have been reported (Shokouhi et al., 2017) but these smaller timescales $\tau_{\min}$ would not affect the model fit).

We construct three models for the NLME with the relaxation function (3.7). First, the recovery phases of the four aftershocks with the clear recoveries shown in Figure 3.3 are fitted by adjusting a single $\tau_{\max}$ to minimize the cumulative squared residuals. This consists in (a) numerically integrating equation (3.7) and (b) fitting equation (3.6) to δv_a by adjusting the scaling s for each aftershock. The red lines in Figure 3.4 show the obtained data fit. The best fit is found with $\tau_{\max}$ = 155 d (misfit curve in Figure 3.17a).

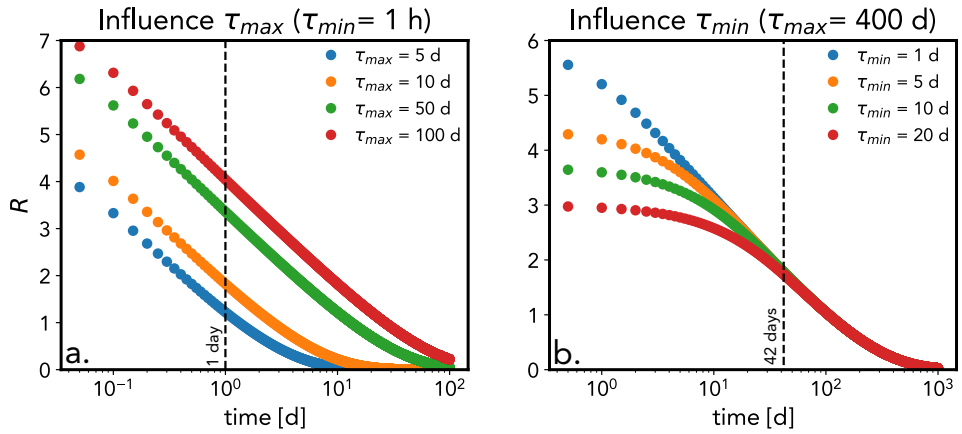

Figure 3.7: *Sensitivity of the relaxation function R(t).* **a)** The different colours account for the different τ_{max} indicated in the Figure. τ_{min} is fixed to one hour. **b)** The different colours account for the different $\tau_{\min}$ indicated in the Figure. $\tau_{\max}$ is fixed to 400 days.

We will refer to this model as R^{155} where the superscript stands for the fitted maximum relaxation timescale $\tau_{\max}$.

The second value for $\tau_{\max}$ is inferred by fitting the complete long term δv data for the recovery of the main shock (Fig. 3.8). $\tau_{\max}$ = 846 d is the best estimate in this case (misfit curve, Figure 3.17b). Finally, we estimate a third timescale $\tau_{\max}$, combining the two previous measurements by stacking the misfit curves (Fig. 3.17c) corresponding to the fit of the four aftershocks (R^{155}) and the misfit curve from the fit of the entire time series (R^{846}). This combined estimate yields $\tau_{\max}$ = 250d as the value minimizing the combined misfit.

We compute three different NLME models (R^{155}, R^{846}, R^{250}) characterised by the different $\tau_{\max}$ values (Fig. 3.8). For the 18 aftershocks, we use the measured velocity drop values (Fig. 3.15) to compute the value s in equation (3.6) that scales the relaxation function $R(t)$ and stack the resulting functions (Fig. 3.5b). After removing the aftershock perturbations δv_{A} from the Chaku δv time series, we use equation (3.6) again to adjust the scaling of $R(t)$ for the main shock recovery δv_{G}. The total NLME-induced δv_{NLME} from this procedure with its obtained residuals are shown in Figure 3.8. We note that in comparison with the exponential approach, the aftershocks induce a larger and long-lasting perturbation of δv (Fig. 3.5) which better describes the observed effects of aftershocks between $\sim$ November 2015 and $\sim$ June 2016 when compared to the time series with the exponential models (Fig. 3.6c vs Fig. 3.8c).

3.4.1.3 Implications of the universal relaxation function and the modelling approaches

We used two methods to model the effect of NLME on the estimated δv. The first approach, using simple exponential functions, yielded a poor correction of the aftershocks-induced velocity changes (Fig. 3.6c), despite using a dedicated relaxation timescale for aftershocks (τ_{aft} $\sim$ 1.18 - 3.03 d). In the second approach, we calibrated the universal relaxation function $R(t)$ (Snieder et al., 2017) with the same maximum relaxation time $\tau_{\max}$ for all aftershocks events and the main shock of the Gorkha earthquake (Fig. 3.8). The fit using $R(t)$ better captures the effect induced by aftershocks in the first part of the year 2016 (Fig. 3.8). This agreement can be explained by the sensitivity of the $R(t)$ function to long

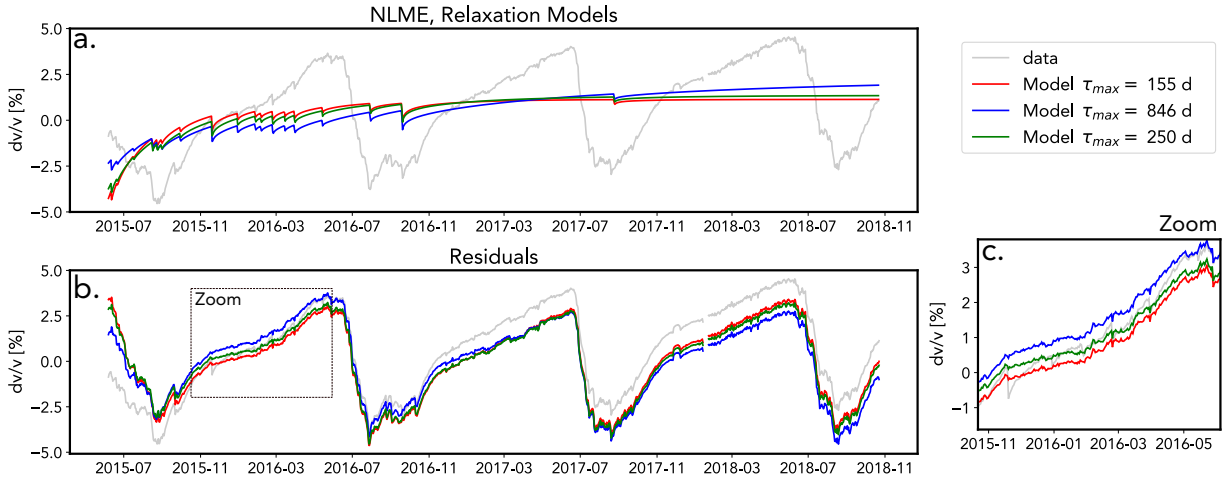

Figure 3.8: *NLME models built with relaxation functions.* **a)** Each curve indicates synthetic recoveries characterised by different maximum relaxation timescale $\tau_{\max}$. **b)** Corresponding residuals from the models shown in **a.** Light grey line show the raw data. Dashed line indicates the zoomed window for the plot shown in **c.**

relaxation times (Fig. 3.7a), even when fitted on the early part of the relaxation curve following the aftershocks. Because of the apparent superiority of the R models in this manuscript and considering the lower degrees of freedom to characterise the relaxation timescales τ, we favor this approach.

We note that both our modelling approaches rely on the assumption of a linear summation of each induced perturbation. If the summation is realistic, it means that the ability to predict NLME requires the knowledge of strain history and not only the current state of the system. At our field site, this is important because our dataset starts 25 days after the M_w 7.3 main aftershock of the 12^{th} of May 2015 (Fig. 3.1). We did not correct for this event or any aftershocks occurring between the 25^{th} of April 2015 and the 6^{th} of June 2015. Nevertheless, we predict that most of the NLME effects are contained within the first $\sim$ year (R^{155}, R^{250}, Figure 3.8), a value consistent with the inferred recovery of landslide rates in the Bhote Koshi ($\sim$ 1 year) (Marc et al., 2021). If we assume that our inferred δv estimated at rather high frequency (4-8 Hz) is a good proxy for shallow subsurface damage, this comparison with landsliding shows that our model is realistic and does not support a longer effect for NLME, such as inferred on model R^{846} (Fig. 3.8).

Another advantage in using $R(t)$ rather than the purely empirical approach is that the relaxation function may be more informative on the physical mechanisms responsible for NLME. The theory leading to the function $R(t)$ is based on an Arrhenius-like law (Snieder et al., 2017), in which the maximum relaxation timescale is given by

$$\tau_{\max} = A \exp\left(\frac{E_{\mathrm{a}}^{\max}}{k_{\mathrm{B}} T}\right) \tag{3.8}$$

in which A is a prefactor, $E_{\mathrm{a}}^{\max}$ is an activation energy, k_{B} is the Boltzmann constant and T is the temperature. $E_{\mathrm{a}}^{\max}$ can be interpreted as the barrier energy that needs to be overcome to reach a lower energy state from a metastable state. This barrier may correspond to characteristic contacts that undergo a particular thermally-activated process in the slow dynamics phase e.g dislocation creep or rearrangement transitions in granular composites. We obtained a good correction of the δv data by using the same $\tau_{\max}$ for events with variable initial perturbations, from PGV of 10^{-3} to 10^{-2} m s^{-1} for aftershocks, and in the

range of $\sim 5.10^{-1}$ m s^{-1} for the Gorkha earthquake (Wei et al., 2018). Following equation (3.8), this means that the nature of the physical mechanisms corresponding to $E_{\mathrm{a}}^{\max}$ and responsible for the longest relaxation timescale is independent from the intensity of ground shaking. Therefore, the relaxation timescales τ controlling slow dynamics in the probed medium would rather be a function of the ambient conditions such as temperature (Bekele et al., 2017), fluid content (Bittner & Popovics, 2021) or pre-existing damage (Lyakhovsky et al., 1997, 2009; Astorga et al., 2018) while the size of the initial excitation would control the number of characteristic broken contacts (Ostrovsky et al., 2019). This interpretation has important implications for the prediction of NLME and suggests that by studying the response induced by small events, one may predict the damage timescales induced by large dynamic strains. The investigation of a constant maximum relaxation timescale $\tau_{\max}$ after dynamic strain perturbations of variable sizes could open a new perspective on NLME-induced changes: a complex physical phenomenon but with a potential deterministic behaviour. This potential independence of τ from the ground shaking amplitude could explain the scattered relation between these variables when tested in field data (Viens et al., 2018). Considering the complexity of the relaxation processes in the Earth surface, the simple picture of a constant $\tau_{\max}$ need to be tested in future works.

Velocity changes estimated at Chaku with lower frequency bands (1-2 and 2-4 Hz) exhibit smaller variations when plotted against the changes we report in this study at 4-8 Hz (Fig. 3.18). This comparison indicates that the dominating NLME mechanisms are likely to be concentrated in near surface materials where smaller perturbations can induce strong changes at shallow depths (Qin et al., 2020) due to lower confining pressure and more compliant materials. A relevant process is the re-arrangement of grains in soft spots of the near surface materials (Lieou et al., 2017). The higher susceptibility to dynamic strain of superficial loosely packed layers (Sawazaki et al., 2018) across a range of ground shaking intensities could explain the good fit of the $R(t)$ function of δv after variable excitations using a constant $\tau_{\max}$. At depths, the long term relaxation may happen in larger geological structures such as the fracture network, which is likely to expand through a large span of crustal depths in the tectonic regime of the Himalayas (Molnar et al., 2007). The simple picture of constant $\tau_{\max}$ may be altered in these deeper layers where a variety of mechanisms can be activated such as micro-crack closure (Brantut, 2015; Meyer et al., 2021), creeping of asperities (Aharonov & Scholz, 2018) or pressure-dissolution (Yasuhara & Elsworth, 2008). These mechanisms are generally activated above a certain dynamic strain threshold, required to break contacts under larger confining pressure. This can be justified by Amonton's law in which macroscopic friction is load dependent but also by recent observations that at the nanoscale, chemical bonds responsible for frictional force increase with normal load (Tian et al., 2020). Therefore, a constant universal $\tau_{\max}$ might not hold if one compares different frequency bands that probe larger depths: The observation of diverse relaxations in the entire crust (Q. Y. Wang et al., 2019), the influence of confining pressure on velocity recovery (Meyer et al., 2021) and the example of larger NLME-induced changes at depths in fault zone (Qiu et al., 2020) support this direction. A spectrum of relaxation timescales responsible for slow dynamics (Shokouhi et al., 2017) may be needed to characterise different depths at any field site.

3.4.2 Hydrological perturbation δv^*_{H} after the Gorkha earthquake

3.4.2.1 Static and transient model for hydrological changes

In the previous section, we modeled the δv_{NLME} component by building three different relaxation models (R^{155}, R^{846}, R^{250}) characterised by different maximum relaxation timescales $\tau_{\max}$. In this section, we study the residuals obtained from these models (green lines, Figure 3.8 a-c) and compare them to the hydrological model of Illien et al. (2021) (Fig. 3.9a-c).

We observe that the initial seismic velocity in June 2015 for the time-series corrected by models R^{155} and R^{250} are now comparable to the δv level estimated in the following years at the same period (between +2.5% and +3% in the month of June), a feature that was not observed in the raw data (Section 3.3.1 and Figure 3.2a-c). This observation suggests that the residuals mainly describe the hydrological component δv_{H}, at least after a correction for NLME by models R^{155} and R^{250}. To test this hypothesis, we use the initial seismic velocity of the residuals to calibrate the initial groundwater level condition used in the hydrological model of Illien et al. (2021) and plot the corresponding modeled velocities (red lines, Figure 3.9a-c) without changing the original hydrological parameters inferred from the previous study. For the three NLME models, the agreement between the velocity residuals δv and the hydrological model is greatly improved in comparison with the raw velocity data shown in Figure 3.2a. Nevertheless, the hydrological model predicts lower velocities than the observed residuals at the start of the 2015 monsoon, still causing a visible offset in the early part of the time series (Fig. 3.9a-c). In the model, lower velocities correspond to higher groundwater levels in the subsurface. This indicates that our hydrological prediction that was based on the velocities of the following years (2016-2018) overestimates the groundwater storage in the 2015 monsoon.

In the model of Illien et al. (2021), the groundwater drainage efficiency is proportional to the height of the hydraulic head $h(t)$ through a simple scaling:

$$\frac{dh}{dt}(t) = -a_{ss}h(t) + f\Big(P(t), \mathrm{vadose}(t)\Big) \tag{3.9}$$

where a_{ss} is the constrained steady state decay parameter that represents the average hydrological properties in the aquifer. f is a function of the precipitation input $P(t)$ and the saturation condition in the vadose zone. A full derivation of the model is available in Illien et al. (2021). We test whether changing the parameter a in a transient fashion following the Gorkha earthquake leads to better prediction of the velocity in 2015. We assume that the parameter a is time-dependent and obeys the following evolution

$$a(t) = a_{ss}\left(1 + D\exp\left[\frac{-(t - t_{\mathrm{Gorkha}})}{\tau_{\mathrm{hydro}}}\right]\right). \tag{3.10}$$

We introduce a transient perturbation of the groundwater drainage with Da_{ss} being the initial perturbation of the decay parameter at the date of Gorkha (t_{Gorkha}) and τ_{hydro} being the characteristic timescale for the recovery towards a_{ss}. The chosen form for $a(t)$ can be interpreted as a more efficient drainage of the groundwater table at early times after the earthquake, that progressively recovers towards a constant hydrological behaviour. This is motivated by the observation that ground shaking can temporally increase stream discharge (Manga et al., 2003) and permeability measured in wells (Xue et al., 2013; Lai et al., 2014).

We minimize a least-square criterion to find the best fit between the velocities modeled with our time-dependant hydrological model and the δv residuals obtained after removing

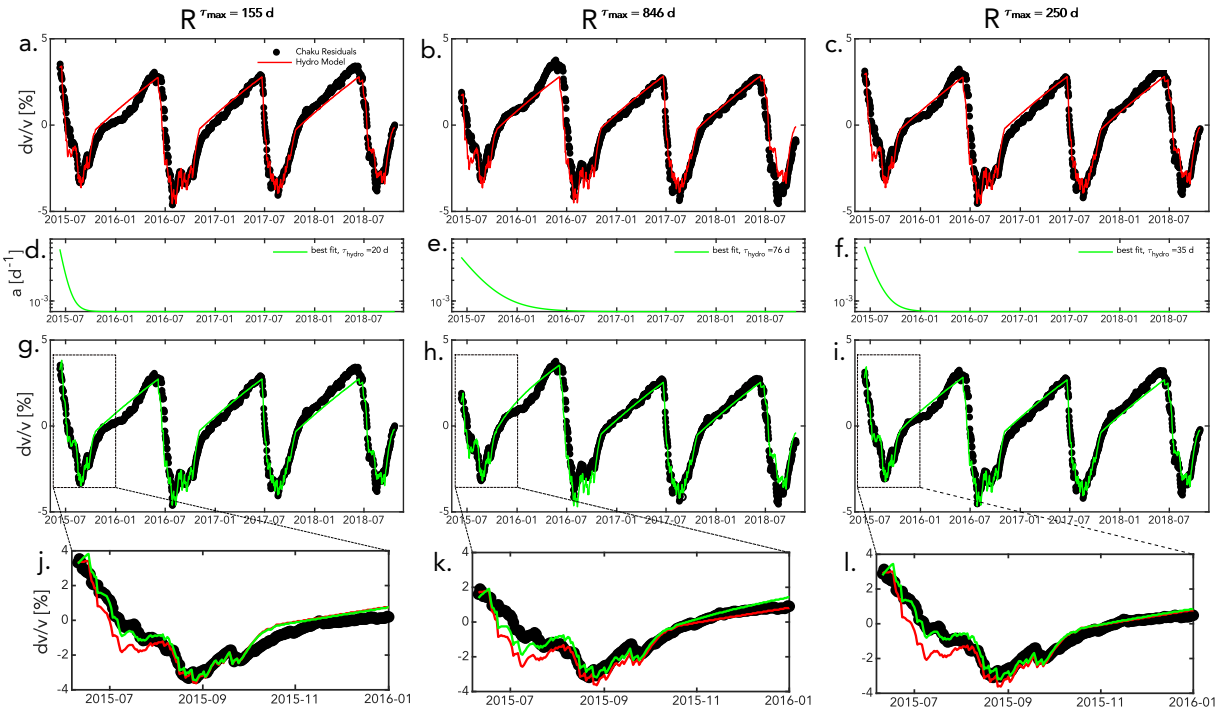

Figure 3.9: *Hydrological models vs residuals from the NLME relaxation models.* **abc)** Residuals from the models R^{155}, R^{846} and R^{250} are plotted in black. Red lines indicate the model from Illien et al. (2021) with an initial condition based on the residuals. **def)** The green lines show the best fitting transient decay parameter $a(t)$. **ghi)** The green lines indicates the modified hydrological models with the transient decay parameter $a(t)$ shown in plots **def.** Close-ups on the data and the inferred models in 2015 in **jkl.**

the δv_{NLME} synthetics. We explore a range of parameters for scaling D and τ_{hydro} from equation (3.10). For each NLME correction (R^{155}, R^{846}, R^{250}), we report the best fitting transient decay parameter $a(t)$ in Figure 3.9d-f and the associated modeled velocity changes in Figure 3.9g-i. For all cases, introducing a transient increase of the groundwater drainage improves the fitting of δv in the monsoon of 2015 (Fig. 3.9j-l). We find that best fitting values for the timescale τ_{hydro} range from 20 to 76 d and are therefore consistently one order of magnitude shorter than the maximum relaxation timescale τ_{max} applied in the NLME models. To compare the six inferred δv_H models (Fig. 3.9abc-ghi), we compute their variances (Fig. 3.10a). When no transient drainage parameter $a(t)$ is introduced, the model corrected with R^{846} has the highest measured variance ($\sigma^2 = 4.3.10^{-5}$) in comparison with R^{155} and R^{250} (both models around $\sigma^2 = 2.910^{-5}$). With the transient parameter $a(t)$, R^{250} is clearly the best fitting model($\sigma^2 = 2.3.10^{-5}$) while R^{846} and R^{155} both reproduce less than 90 % of the R^{250} variance based on their variance ratio (Fig. 3.10b). Moreover, introducing the transient decay parameter $a(t)$ considerably improved the variance of model R^{250} by a margin of $\sim 20\%$. To test the significance of the fit, we perform a F-test (Text S2) between the model R^{250} with no transient hydrological parameter (Fig. 3.9c) and the model R^{250} with the addition of the 2 parameters D and τ_{hydro} (Fig. 3.9i). We find that the introduction of $a(t)$ is statistically significant at 95% of confidence interval. Finally, we also explore a range of models with τ_{hydro} ranging from 10^1 to 10^3 days and a dedicated relaxation time for the Gorkha earthquake τ^G_{max} ranging from 2.10^1 to 5.10^3 days while retaining $\tau^A_{\mathrm{max}} = 155$ d for the aftershocks and optimising all the other parameters. Fitting

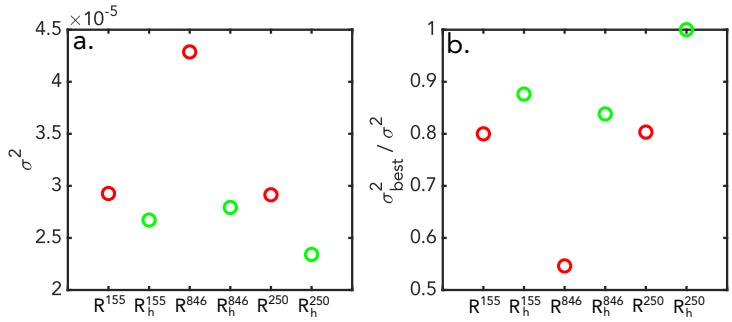

Figure 3.10: *Variance of the hydrological models.* **a)** Absolute variance of the models, subscript h indicate models with the introduction of the transient parameter $a(t)$ **b)** Same plot as **a.** but normalised with the best misfit value of the model R^{250}. I need to change the R conventions on this figure

all models characterised by the recovery timescales in this parameter space and minimising a least-square criterion, we found that the best model is found for $\tau_{\text{hydro}} = 41$ d and $\tau_{\text{max}} = 450$ d (misfit space in Figure 3.19). These values are similar to our inferred model R^{250} with $\tau_{\text{hydro}} = 35$ d.

The velocities in the 2015 monsoon are therefore better described with a transient drainage parameter, suggesting that the relaxation processes following the Gorkha earthquake affected hydrological properties. The duration of this perturbation for the best fitting model R^{250} is ~ 6 months (Fig. 3.9f). We address the validity of this claim and its implications in the next section.

3.4.2.2 Monitoring of transient hydrological properties with seismic interferometry

A number of methods has been used to study how dynamic strain influences hydrological properties such as amplitudes and phase analysis in wells levels (Elkhoury et al., 2006; Xue et al., 2013), measurement of stream discharge (Manga et al., 2003) or monitoring with stable isotopes (Hosono et al., 2020). In parallel, a growing community of seismologists now use seismic interferometry to constrain groundwater storage (Lecocq et al., 2017; Kim & Lekic, 2019a) but no attempt has been made to address earthquake hydrology topics with such methods. As mentioned before, this is partially due to the challenging decomposition of the several processes that influence seismic velocity. Our seismic interferometry analysis opens a window for monitoring transient hydrological behaviours on an intermediate spatial scale between point-based well measurements and catchment averaged isotopic and discharge analyses. We showed in Figure 3.9 that a transient increase in the drainage efficiency of the groundwater table improves our description of the seismic velocity changes in the 2015 monsoon in the aftermath of the Gorkha earthquake. This progress in the δv fitting was tested for its significance, given the two parameters (D and τ_{hydro}) we added to the original model of Illien et al (2021) (F-test in Text S2). However, the confidence interval of this test need to be taken carefully as our non-linear hydrological model may not produce normally distributed residuals, which are essential for parametric statistic tests (J. Gao, 2007). More interferometric datasets that are influenced by hydrological and seismic events should be tested in the future for cross-validation of our parameterisation of transient properties $a(t)$. Nevertheless, additional tests with a linear recovery for parameter $a(t)$ (Fig. 3.20) do not improve the variance observed with our exponential parameterisation in

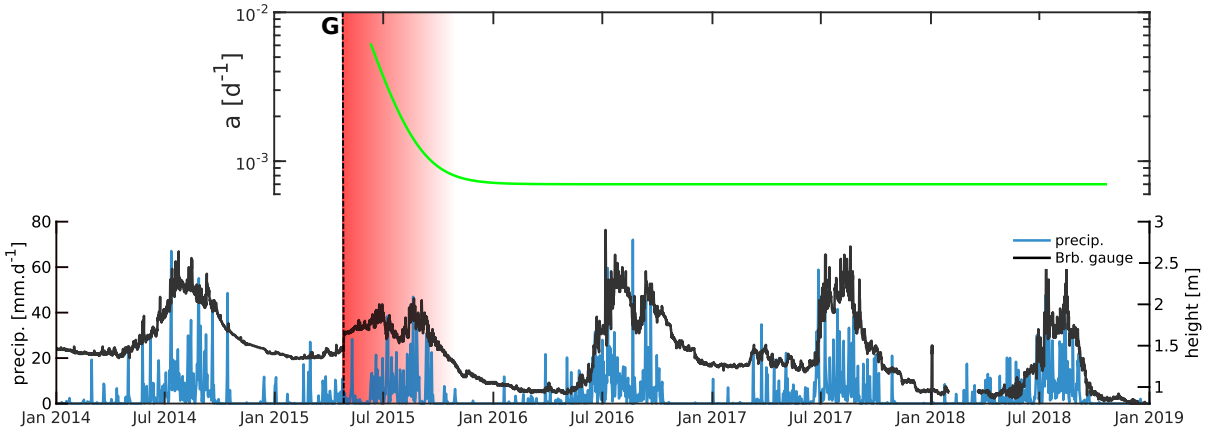

Figure 3.11: *Data from the Bahrabise gauge.* The black solid line represents the stage height of the Bahrabise river (location of the gauge in Figure 3.1a). The height is corrected for an offset caused by the July 2016 glacial outburst flood (Cook et al., 2018). Precipitation estimated in the area are in blue and are obtained from the Global Precipitation Measurement data, IMERGHH 6B (Huffman et al., 2019). The green line shows the transient decay parameter $a(t)$ of the best fitting relaxation model R^{250} (τ_{hydro}= 35 d). The background red colour illustrates the period with enhanced permeability after Gorkha. **G** indicates the date of the Gorkha earthquake.

equation (3.10) (Fig. 3.21).

Given the absence of additional constraint on τ_{hydro} in our study, the physical assumptions in our model are still supported by existing observations such as a long lasting increase of permeability observed in other mountainous areas (Hosono et al., 2020), or the permeability healing phenomena observed for $\sim$ 1 yr after the Wenchuan earthquake (Xue et al., 2013) and other South Californian earthquakes (Elkhoury et al., 2006). To further support our finding, we plot in Figure 3.11 the best fitting transient decay parameter ($a(t)$ from model R^{250}) and an independent river stage height dataset from Bahrabise gauge station, located $\sim$ 13 km downstream from our field site. (blue star in Figure 3.1a). We compute the precipitation derived from the Global Precipitation Measurement data, IMERGHH 6B (Huffman et al., 2019) in a square of 100 m^2 upstream of the gauge (footprint in Figure 3.22) as it offers a suitable averaged measure to compare with the river height. The stage height measurement displays a co-seismic increase in discharge, supporting a release of mountain groundwater due to ground shaking (C. Y. Wang et al., 2004). Additionally, the stage height has a clear co-evolution with monsoon precipitation with steep increase of the stage height that is concomitant with the onset of strong precipitation. However, the river gauge sensitivity to precipitation in 2015 seems relatively buffered, especially at the start of the 2015 monsoon when the onset of intense precipitation does not cause significant increase in stage height. This behaviour looks to fade away rather quickly within the 2015 monsoon where the second pulse of precipitation induces a clear response in the stage height. A more permeable landscape with groundwater fluxes travelling more efficiently downstream or towards deeper layers at early times after the Gorkha earthquake is a plausible interpretation. Remarkably, the best fitting transient decay parameter $a(t)$ (τ_{hydro} = 35 d) recovers simultaneously to this observation, therefore showing a good agreement with this scenario (green line, Figure 3.11).

There is a limited number of experimental studies that links NLME and the evolution

of hydrological properties. In limestones subjected to inelastic axial strain, it has been shown that after deformation, the seismic velocity was recovering for a few days but the permeability remained constant after a permanent increase due to damage (Brantut, 2015). The study mainly interprets the healing of velocities as the closure of micro-cracks porosity while the tortuosity of the pores network, which is the main control on permeability at the microscale (Kachanov & Sevostianov, 2005), remained unchanged. In this case, there is no co-evolution of hydrological properties with the slow dynamics phase. However, fluid flow in the field is thought to be largely controlled by the macroporosity (Baechle et al., 2004) and discrete fractures (Talwani et al., 2007). Notably, measurements of seismic velocity and permeability along a laboratory rock fracture both exhibit a phase of recovery after dynamic stressing (Shokouhi et al., 2020). At our field site, the estimated healing in hydrological properties from our model hints that the δv_{H} variations could be contained in the fracture network. Possible mechanisms for permeability recovery includes fracture aperture modulation by destruction/creation of contact interfaces (Shokouhi et al., 2020) or colloids re-clogging (Mays & Hunt, 2007). In our relaxation models, τ_{hydro} is constantly shorter than the maximum recovery timescale τ_{max} used to correct NLME (Fig. 3.9). This discrepancy between τ_{max} and τ_{hydro} may be explained by the non-linear relation between fracture aspect ratio and permeability (Ebigbo et al., 2016) due to percolation threshold. Another hypothesis would be that the changes responsible for these timescales are contained in different porosity units (micropores, macropores, fractures, others ...). New approach for characterising NLME in the field are needed to disentangle these scenarios. At greater crustal depths, changes in hydrological properties may influence fluid migrations and low-frequency events, as observed several months after the 2011 Tohoku-Oki earthquake (Q. Y. Wang et al., 2021).

Future work may address the opposite role of water on relaxation processes. Pore water is generally considered to reduce frictional properties of interfaces, therefore raising the susceptibility to ground shaking (Brenguier et al., 2014). However, water also controls the rate of recovery through chemical reactions and changes in activation energies (Liu & Szlufarska, 2010; Brantut, 2015). The actual impact of such processes on ground velocity retrieved by seismic interferometry remains to be assessed.

3.5 Conclusions

In this study, we estimated relative seismic velocity changes δv from single station cross-correlations in the aftermath of the 2015 Mw 7.8 Gorkha earthquake for a duration of ~ 3 years. Using the same characteristic relaxation timescales after the main shock and all the aftershocks (best fitting model for $\tau_{\mathrm{max}} = 250$ d), we corrected for the non-linear mesoscopic elasticity (NLME) effect. We found that the velocity changes evolve towards background values until the 2016 monsoon which suggests that most of the subsurface damage is recovered during the first year after the main shock. With the hydro-seismological model of Illien et al. (2021), we fitted the residual δv corrected for NLME and inferred a shorter relaxation timescale τ_{hydro} that we attributed to an enhanced permeability of the subsurface that recovers gradually for ~ 6 months during the 2015 monsoon.

Special attention should be given when substracting earthquake-induced velocity changes to constrain background hydrology as a transient behaviour may be hidden in the data. Therefore, seismic interferometry studies may need to go beyond the assumed superposition of contributions $\delta v = \delta v_{\mathrm{NLME}} + \delta v_{\mathrm{H}}$ as the relaxation processes may affect the hydrological properties of the subsurface. In our study, we calibrated the nonlinear recovery with the

relaxations triggered by the aftershocks, hence without biasing hydrological-induced velocity variations that can possibly be affected by ground shaking. Because of the importance of hydrological properties for freshwater resources, initiation of hillslope hazards (Iverson, 2000) and the frictional properties of fault zones (Talwani et al., 2007), we encourage the use of seismic techniques to estimate the hydrological response to large earthquakes using dense seismic arrays and multiple frequency bands.

Data availability

The precipitation time-series for the Bhote Koshi observatory can be found at the following DOI: 10.5880/GFZ.4.6.2021.002. Seismic data are available at the DOI 10.14470/KA7560056170.

3.6 Supplementary materials to paper II

Text S1: Building of aftershocks-induced δv models with exponential functions

Based on the fitted values τ_A, we built synthetics representing the velocity variations induced by aftershocks (δv_A) at the Chaku site. We assumed that each aftershock that cause a velocity drop also induce a subsequent recovery in δv. We included in this assumption, all the events occurring during monsoon seasons where the recovery is masked by strong hydrological variations. We also assumed that all aftershock responses can be linearly superposed in this range of perturbation. From these assumptions, we estimated two models for δv_A using the end-member values inferred in the main text (Fig. 3.4): one with a fast recovery timescale $\tau_A = 1.18$ d and the other one with $\tau_A = 3.03$ d. For each event, we took for the velocity drop δv_0, the values we measured in section 3.2.2 (Fig. 3.15). Using the chosen value for τ_A, we used equation (3.5) from the main text and computed for each event the corresponding synthetic. We interpolated each synthetic at the daily timescale using the mean of the modeled δv for each day and superposed them to finally obtain one time series δv_A as shown in Figure 3.5a of the main text. We subtracted these models from the long term Chaku δv time series.

Text S2: F-statistic analysis of the hydrological model with transient parameter a(t)

We tested if the introduction of the two new parameters D and τ_{hydro} (equation 3.10 in main text) in the model of Illien et al. (2021) is statistically significant to fit the residuals of the model R^{250}. Basis for the F-statistic are provided in Rees (2001). We used a F-test with the null hypothesis being: *The introduction of D and τ_{hydro} do not provide a statiscally better fit.* The F-statistic can be calculated as follows:

$$F = \frac{\left(\frac{RSS_1 - RSS_2}{p_2 - p_1}\right)}{\left(\frac{RSS_2}{n - p_2}\right)} \tag{3.11}$$

where RSS_1 is the residual sum of squares of the model without the new parameters ($= 0.0357$) with p_1 being its number of parameters ($= 7$), RSS_2 is the residual sum of squares of the model with the new parameters ($= 0.0286$) with p_2 being its number of parameter in the ($= 9$) and n is the number of observation ($= 1222$). Because our F-statistic ($= 148.9$) is greater than the value of the F-statistic distribution at 95% of confidence interval ($F_c(0.95|\Delta_p, n - p_2) = 3$), we rejected the null hypothesis.

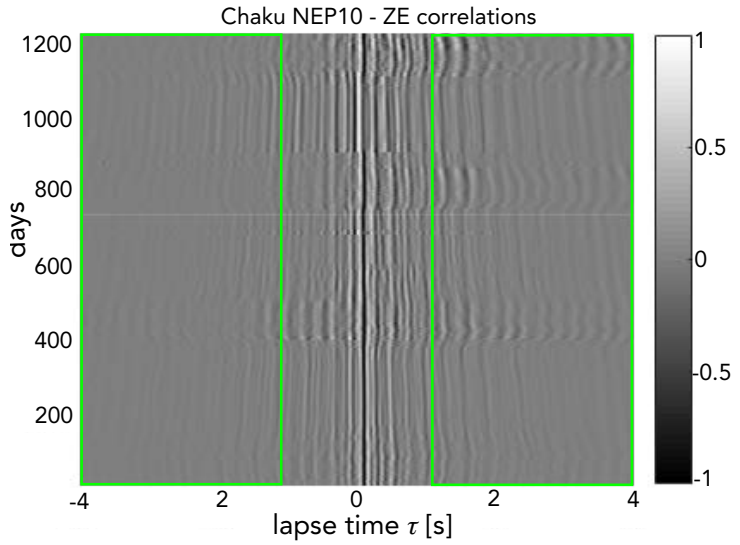

Figure 3.12: *Correlation matrix for station NEP10 at Chaku, channel combination ZE.* The green rectangles show the lapse time windows used for estimating the velocity changes. The correlations are normalised by the maximum amplitudes.

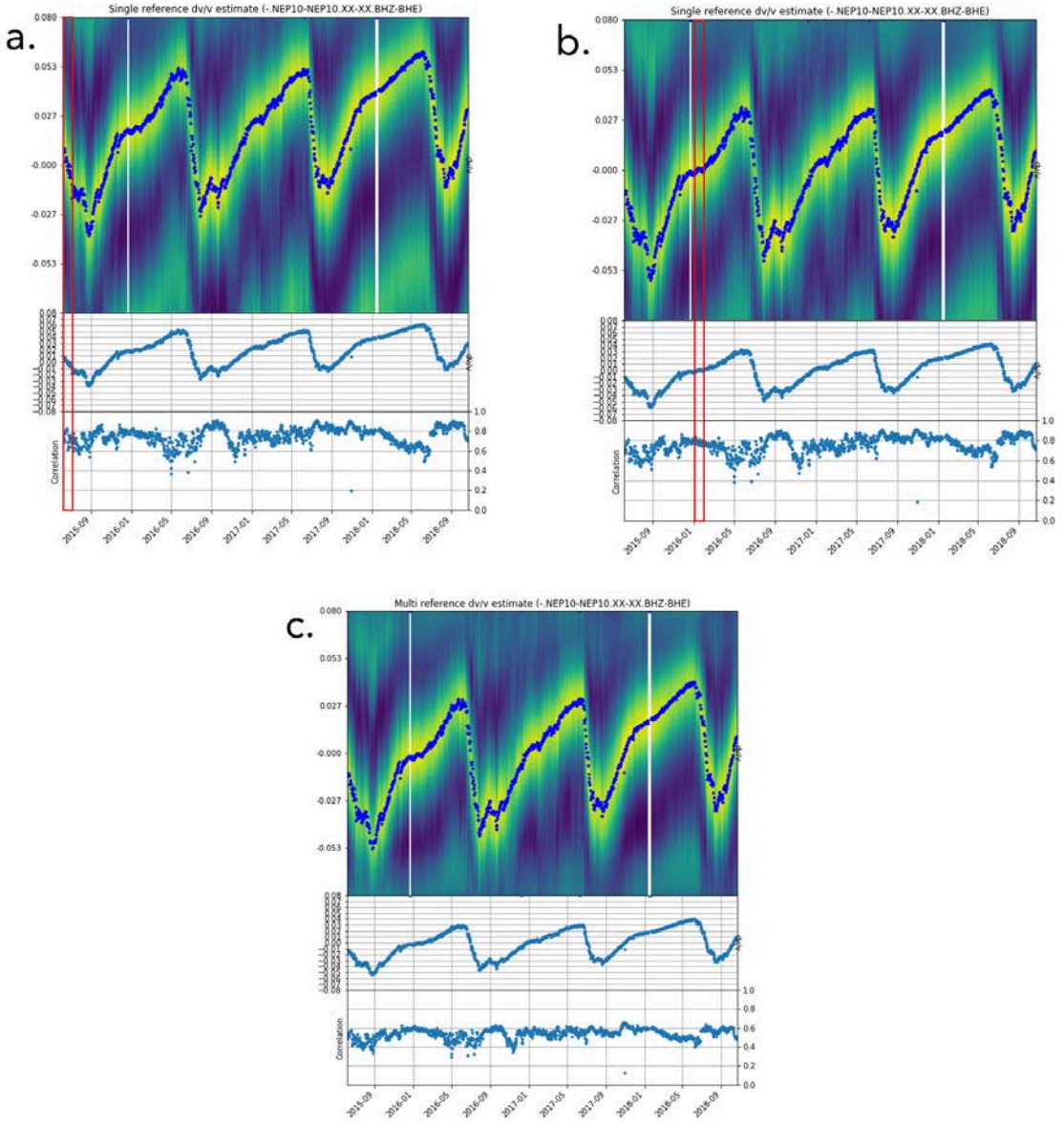

Figure 3.13: *Illustration of the velocity change measurements with multiple references.* On each subplot, the top panel shows the similarity matrix for the ZE combination on station NEP10 at Chaku. The best corresponding stretch values are reported on the middle panel while the lower plot indicates the associated correlation values. In **a.**, the reference was taken as the mean average of the correlation function during the first month of the time-series while **b.** shows the time-series obtained using the first month of 2016 as average (red rectangle). Because of different references, the time-series are shifted because of the velocity difference between the references. In **c.**, we show the final time-series for this combination, using monthly references computed every 15 days.

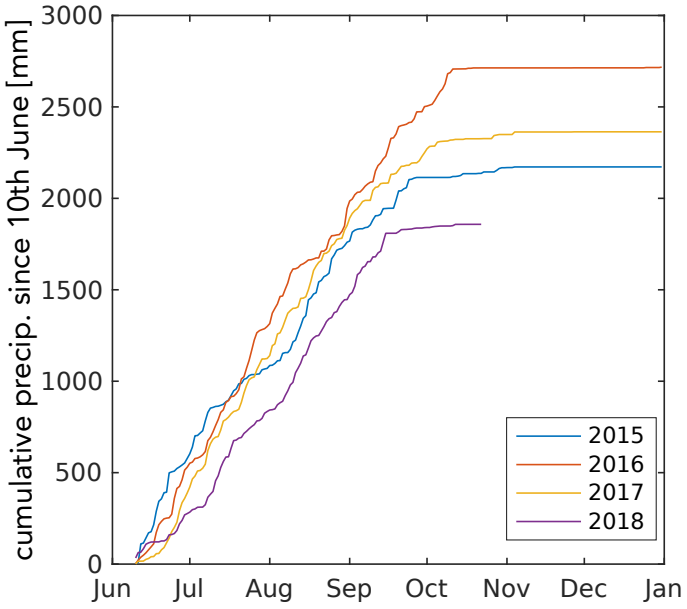

Figure 3.14: *Annual cumulative precipitation at the Bhote Koshi observatory.* Each colours indicate a different year. The cumulative values are calculated from the 10th of June, the date at which our precipitation measurement started in 2015.

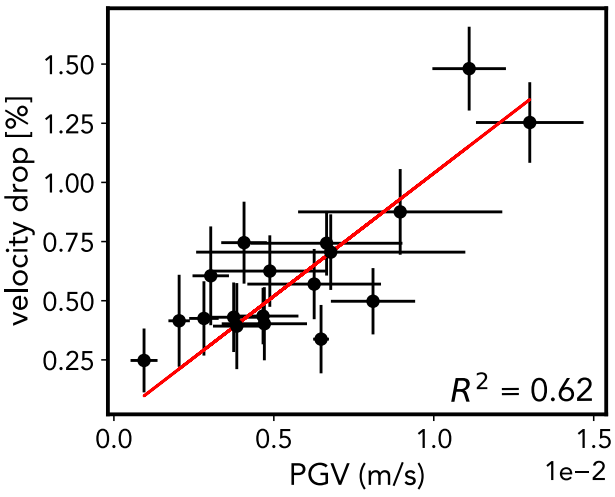

Figure 3.15: *Relation between aftershocks-velocity drops and corresponding PGV.* The horizontal bars correspond to the standard deviations of the PGV recorded at the three stations on the Chaku terrace. Vertical bars are calculated using the standard deviations calculated from the δv measurement obtained during the first hour after the events. The red line indicates the best linear regression.

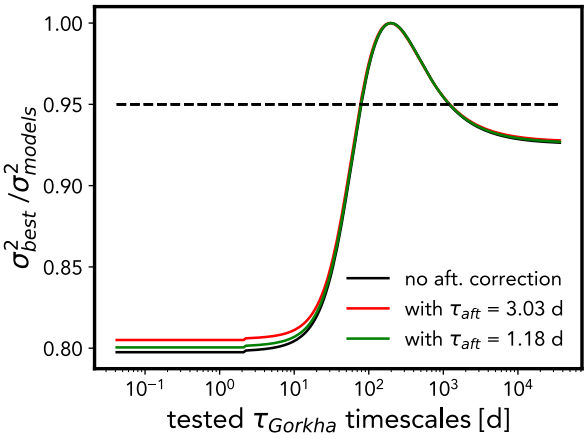

Figure 3.16: *Variance ratio of the fitted exponential models with fixed τ_{Gorkha} parameter.* The variance ratio is normalised with the best fitting model (ratio at 1). The different colours stand for the presence and influence of the aftershocks correction when fitting τ_{Gorkha}. The dashed line shows the limit above which the fitted models reproduce the best fitting model variance at 95 %.

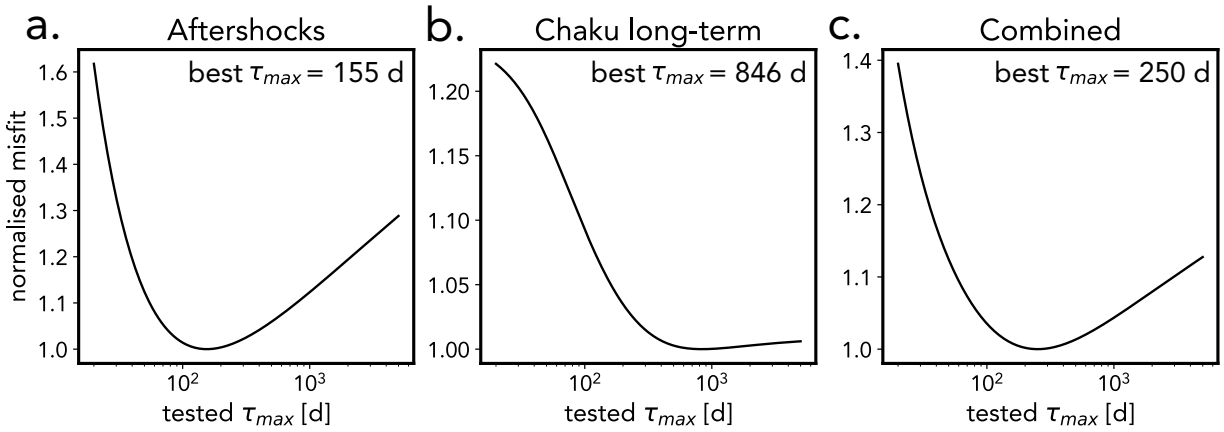

Figure 3.17: *Misfit curves for building the relaxation models.* **a.** Normalised least square values for each tested $\tau_{\max}$ when fitting the first 24h recoveries induced by the four aftershocks. **b.** Normalised least square values for each tested $\tau_{\max}$ when fitting the long term daily δv time series at Chaku. **c.** Combined misfit curve when stacking the data shown in **a.** and **b.** For each plot, the best $\tau_{\max}$ value is indicated.

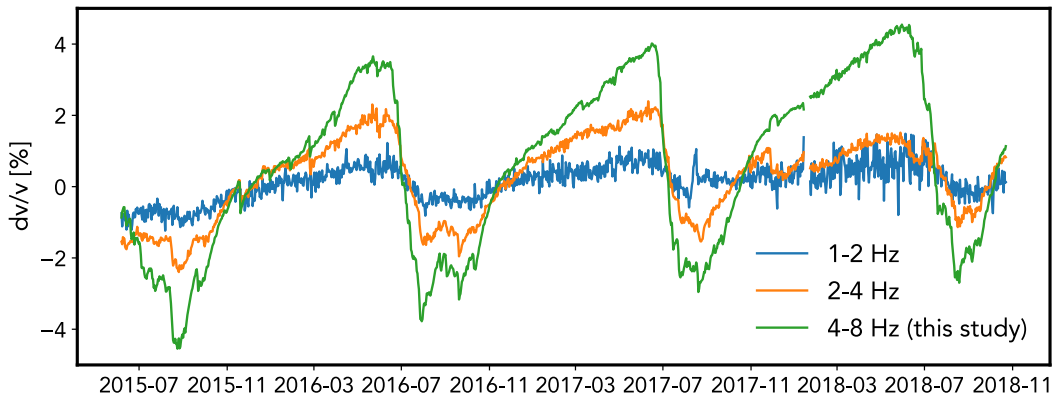

Figure 3.18: *Relative seismic velocity changes retrieved at Chaku using different frequency bands.* For each frequency band, we used the method that is presented in the main text.

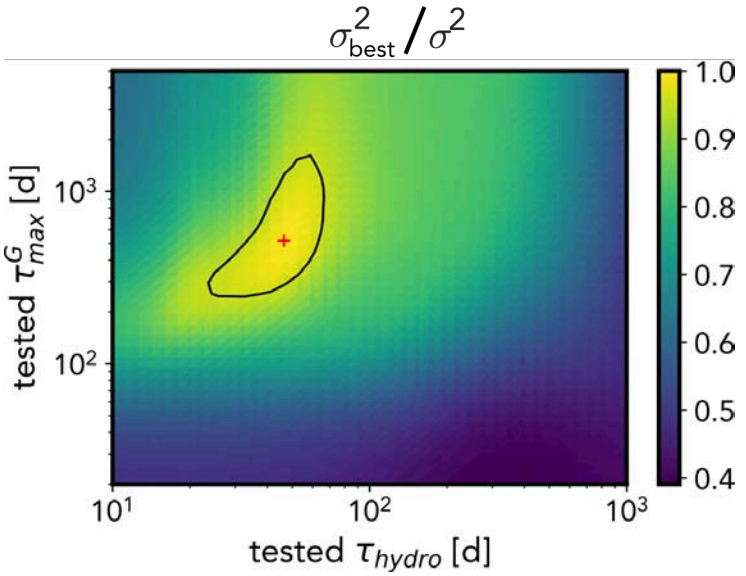

Figure 3.19: *Variance space obtained after testing different values for the hydrology recovery timescale τ_{hydro} and the maximum relaxation time τ_{max} induced by Gorkha.* The space is normalised by the variance of the best fitting model (indicated by the red cross). The black ellipse shows the 0.95 value contour.

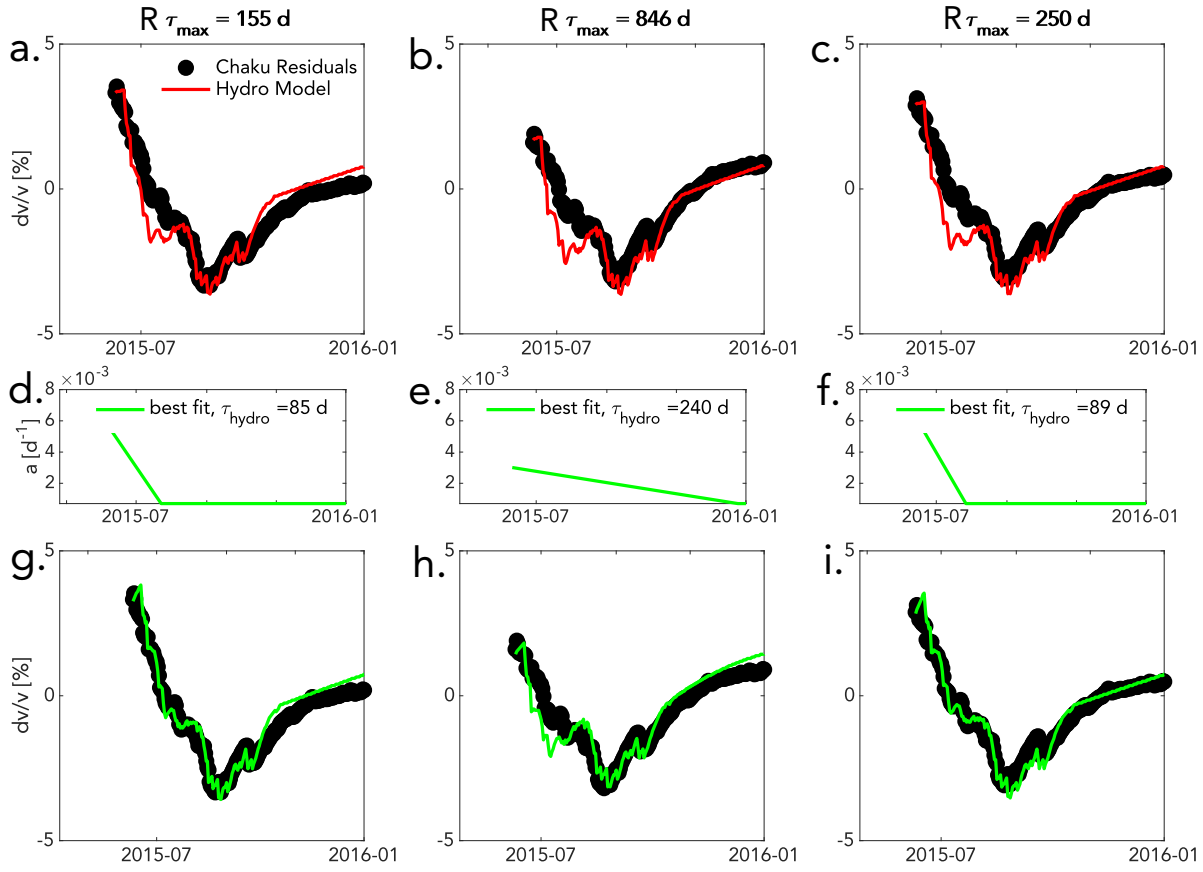

Figure 3.20: *Residuals from the NLME relaxation models vs hydrological models with linear recovery* τ_{hydro}. Plot are zoomed to 2015 data for better comparison. **abc.** Residuals from the models R^{155}, R^{846}, R^{250} are plotted in black. Red lines indicate the model from Illien et al. (2021) with an initial condition based on the residuals. **def.** The green lines stand for the best fitting transient decay parameter $a(t)$ **ghi.** The green lines indicates the modified hydrological models associated with the introduced $a(t)$ from the plots in **def.**

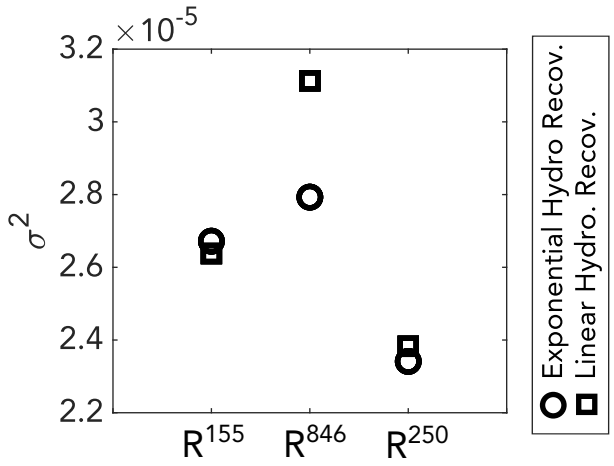

Figure 3.21: *Variance of the hydrological models characterised by exponential and linear hydrological recovery* τ_{hydro}.

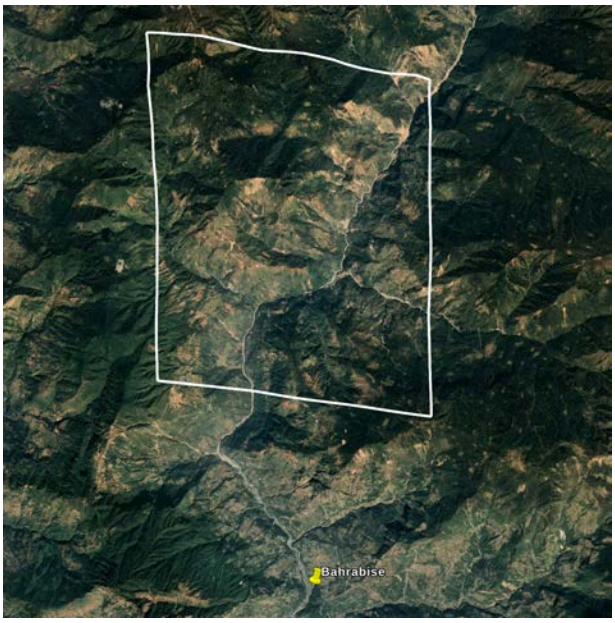

Figure 3.22: *Footprint of the surface used in the retrieval of precipitation from the Global Precipitation Measurement.* The footprint has a 10*10 km surface. The Bahrabise gauge is indicated. Screenshot from Google Earth.

Transition: *We should go somewhere dry...*

In Chapter 3, I have shown that most of the effects due to subsurface damage recovered within $\sim$ one year following the Gorkha earthquake. Thanks to the hydrological model calibrated in Chapter 2, I propose a possible permeability increase triggered by the main shock. This increase was short-lived (a few month during the 2015 monsoon) and recovered to a steady state value until the end of the seismic instrumentation. This hydrological perturbation was not studied by means of seismic interferometry prior to this study.

I also proposed that the relaxation timescales in the subsurface after ground shaking are independent of the perturbation intensity, with the difference that larger earthquakes introduce larger changes in seismic velocity. I used the framework introduced by Snieder et al. (2016) to infer the maximum relaxation timescale $\tau_{\max}$ and find an optimal fitting value of $\tau_{\max} \sim 250$ d at my Nepalese field site. The timescale was constrained by using both the early relaxations caused by aftershocks and the full multi seasonal time-series. This work suggests that the relaxation timescales at one field site is mostly function of the medium and may be predictable. However, the hydrological storage dominates the velocity changes in the Bothe Koshi catchment and I lack a velocity baseline prior to the Gorkha earthquake. These cause limitations to study and test assumptions regarding the impact of ground shaking on subsurface properties.

In the next Chapters (4 and 5), I move away from Nepal to focus on seismic stations located in the Atacama desert in Patache, Chile. The field site is characterised by high seismicity and an arid climate with rare precipitation events. This setting is ideal to study the impact of seismic events on the velocity changes without the influence of complex hydrological variations. I will first characterize the field site and infer dv/v at a high temporal resolution with a dense array that was deployed for $\sim$two weeks.

Chapter 4

Resolving minute temporal seismic velocity changes induced by earthquake damage: The more stations, the merrier ?

Luc Illien, Christoph Sens-Schönfelder, Kuan-Yu Ke

Pre-print version hosted at EarthArxiv (DOI: 10.31223/X5TH1D)
In review at *Geophysical Journal International*.

Abstract

Ground shaking induced by earthquakes often introduces transient changes in seismic velocity monitored with ambient noise. These changes are usually attributed to relaxation behavior following the co-seismic damage in the subsurface and are of relevance for postseismic hazard mitigation. However, the velocity evolution associated with this phenomenon can occur at very small timescales and amplitudes that are not resolved with seismic interferometry and are therefore challenging to link to laboratory experiments. A way to improve the temporal resolution of the velocity time-series is to test whether the estimation of the relative seismic velocity changes dv/v obeys the ergodic hypothesis in which the joint use of co-located stations would lead to better resolved measurements. In this study, we present results from a dense seismic array that was deployed for two weeks at the remarkable Patache site in Chile. Thanks to high temporal averaging capabilities, we are able to resolve seismic velocity changes in the 3-6 Hz frequency band at a 10-minutes resolution around the occurrence of a moderate earthquake (PGV $\sim$ 1 cm/s). We report a velocity drop of $\sim$0.4% in the first 10 minutes after ground shaking. Half of this initial drop was recovered within the two following days. The shape of the recovery follows a log-linear shape over the whole observed recovery phase, analogous to slow dynamics experiments. When normalised by the total amount of processed data, we show that the ergodic hypothesis almost perfectly holds in our network: the dv/v signal to noise ratio (SNR) obtained when averaging a few observation with large stacking durations for the correlation functions is almost equal to the SNR when using a large number of observations with small stacking durations. To understand if the ergodicity is linked to a particular site property, we use the array capabilities to identify the surf at the shoreline as the source of the noise and to derive a 1D shear velocity profile with the focal spot imaging technique and a transdimensional Bayesian inversion framework. The inversion shows that hard rocks lie close to the surface indicating that this material hosts the observed shallow velocity changes. We discuss our high-resolution measurements and attribute them to a stable noise source excited by the shore, the ergodicity property and an ideal subsurface structure. Finally, we discuss the effect of moderate earthquakes on subsurface damage and the potential relaxation processes in hard rocks.

III

4.1 Introduction

Monitoring of seismic velocity changes obtained from ambient noise cross-correlations is now a widely used technique among seismologists. Because the seismic velocity in rocks is sensitive to many driving processes, this tool has been used to constrain various dynamics in the subsurface such as changes in groundwater (Lecocq et al., 2017; Gassenmeier et al., 2015; Clements & Denolle, 2018; Illien et al., 2021), soil moisture (Dietze et al., 2020; Oakley et al., 2021), permafrost thickness (Overduin et al., 2015; Albaric et al., 2021; Lindner et al., 2021) and volcanic activity (Sens-Schönfelder et al., 2014; Budi-Santoso & Lesage, 2016; Donaldson et al., 2019). The use of seismic interferometry has also enabled the study of rock properties changes in response to in-situ strain induced by surface temperature (Richter et al., 2014; Lecocq et al., 2017), Earth tides (Takano et al., 2014; Sens-Schönfelder & Eulenfeld, 2019) and more notably to dynamic strain due to ground shaking during earthquakes. Indeed, there is a plethora of seismic interferometry studies that were conducted following major earthquakes (Brenguier et al., 2008; Nakata & Snieder, 2012; Viens et al., 2018; Qin et al., 2020). Most of this literature shows two distinct phases: a short co-seismic phase in which the seismic velocity drops and a post-seismic phase in which the velocity recovers in a non-linear fashion. This latter phase is called relaxation or slow dynamics and can last for several years (Brenguier et al., 2008; Marc et al., 2021). These time-dependent changes of the seismic velocity suggests that earthquakes induce a lingering effect in subsurface rock properties. This mechanical perturbation may be at the origin of other transient surface observations, which exhibit a similar time-evolution such as transient increases of aquifer permeability (Manga et al., 2012; Illien et al., 2021) or landslide rates (Marc et al., 2015).

The time dependency of the elastic behaviour is linked to a non-classical type of elastic non-linearity. This behaviour has been reproduced experimentally in a wide range of materials ranging from rocks (TenCate et al., 2000; Brantut, 2015; Shokouhi et al., 2017) over concrete (Bekele et al., 2017) to unconsolidated granular samples (Knight et al., 1995), which suggests that this phenomena is universal (Snieder et al., 2016). The transient dynamics is generally interpreted as the result of *1)* a phase of "damage" during deformation that arises from a variety of contacts (Ostrovsky et al., 2019; Sens-Schönfelder et al., 2019a) which are broken at grain boundaries or at defect locations and *2)* a phase of "healing" associated with thermally activated processes that bring the metastable contacts towards a new equilibrium state – a phase also called slow dynamics or relaxation (Guyer et al., 1999; TenCate et al., 2000). In rocks and near-surface geomaterials, this contact recovery is thought to happen due to micro-cracks and fracture closure (Meyer et al., 2021) or re-arrangement of frictional shear zones (Lieou et al., 2017) and with a large contribution of chemical processes modulated by moisture (Brantut, 2015; Bittner & Popovics, 2021; L. Gao et al., 2022). Corresponding physical and phenomenological models can be developed from laboratory observations thanks to a fine control of the strain disturbance (Remillieux et al., 2017), a well-resolved temporal acoustic monitoring system (that can observe relaxation timescales down to fractions of a second (Shokouhi et al., 2017)), simplified geometries (Yoritomo & Weaver, 2020) or the knowledge of the physical properties of the chosen rock samples. However, the application of models to field observations is challenging due to poorly resolved velocity measurements, superimposed influences and depth-dependent properties. Indeed, the stochastic nature of the seismic ambient noise wavefield requires temporal stacking of the noise correlations to recover the stable pseudo Green's function that is required for velocity monitoring (Xu et al., 2021). This reconstruction controls the final time-resolution of the obtained dv/v measurements. Moreover, constraints on the

subsurface structure and velocity are rarely available. These limitations prevent us from answering fundamental questions that would bridge the gap between field observations and models, which includes *what is the impact of small/moderate shaking perturbation*, *what is the shortest relaxation timescale in the field* or *in which structures/rocks the relaxation is likely to occur in the subsurface?*

To address these questions, we performed seismic interferometry study using a dense seismic array in Patache, Chile (Fig. 4.1) located around the permanent station PATCX in the IPOC network. This station has produced remarkable results with observations of stable velocity changes induced by the Earth's tides (Sens-Schönfelder & Eulenfeld, 2019), earthquakes (Gassenmeier et al., 2016) or temperature (Richter et al., 2014). The relative success of these studies suggests that the conditions at this site are particularly suited for monitoring studies. In this paper, we attempt to investigate these specific conditions and increase the time-resolution of the velocity changes retrieval at Patache with the ergodic hypothesis (Moore, 2015): We assume that the average statistical properties of the diffuse noise wavefield across the dense network (the ensemble average) during a short time interval at time t is similar to the average statistical properties recorded at one station over a larger time span (the time average). If this assumption holds, by spatially averaging the results obtained from co-located stations, one can significantly reduce the time window needed for stacking correlation functions and therefore improve the time-resolution of stable velocity change measurement δv. This hypothesis has been made implicitly in previous studies (Sens-Schönfelder et al., 2014; Illien, Sens-Schönfelder, et al., 2022) but not tested. Here, we address the validity of this assumption explicitly.

Using this technique, we report stable observations of velocity changes at a 10-minute resolution for a period of $\sim$ two weeks. During this interval, we measure a co-seismic velocity drop of 0.4 % amplitude and a well-resolved subsequent recovery in the 3-6 Hz frequency band. Utilising the dense network, we also compute the local Rayleigh wave dispersion curve using the focal spot imaging technique. We invert the obtained results for a 1D shear velocity profile using transdimensional Bayesian inversion and show that the relaxation changes are hosted in a hard rock site. The characterisation of the site also allows to highlight advantageous conditions for stable dv/v measurements.

We describe the data and methods in section 4.2. In section 3.1 and 3.2, we present the seismic velocity changes results and the inferred 1D shear velocity profile obtained at our field site. Section 4 is dedicated to the discussion, notably on the stability of the velocity estimates and the relaxation processes in hard rocks. Conclusions are in section 5.

4.2 Data and Methods

4.2.1 The Peso array

The Peso array consists of 15 geophones (3-components) located around the broadband station PATCX of the Chilean IPOC network (GFZ Potsdam and CNRS-INSU (2006), Fig. 4.1). Stations were installed on the 21st of October 2018 with nine stations recording for $\sim$ two weeks while the others were relocated after $\sim$ 1.5 days . The array geometry was designed in a circular-triangular pattern to maximise different inter-station distances and optimize the usability for different tasks such as the study of the noise sources, the investigation of the subsurface velocity structure and the monitoring of velocity changes. Placed on top of an escarpment located at 70 km south of Iquique city (Fig. 4.1, Fig. 4.9), the stations have an elevation of about 600 m above sea level. After performing a

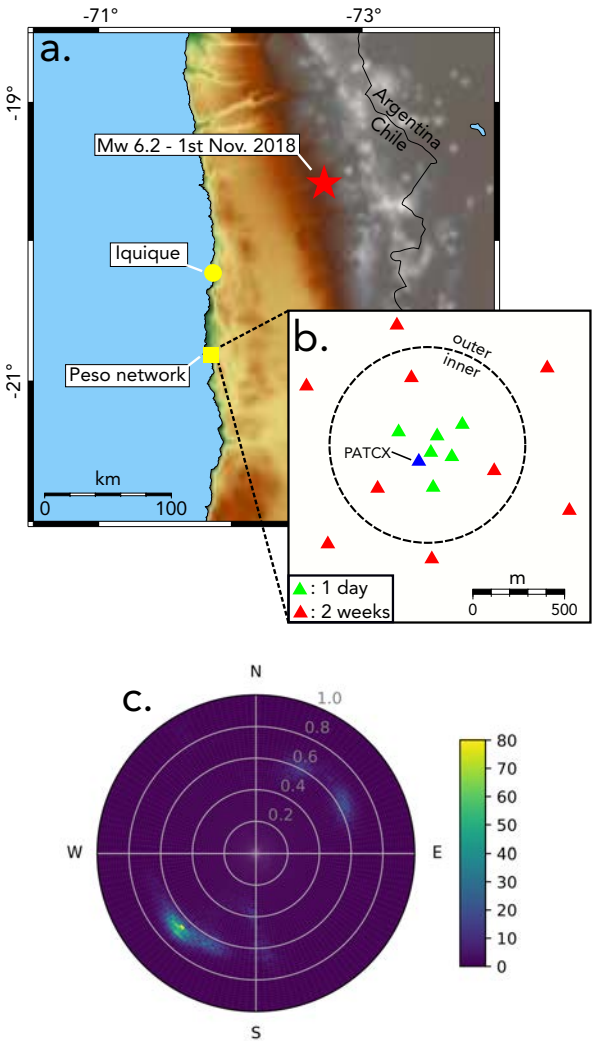

Figure 4.1: *Map of the study area and beamforming analysis.* **a.** Location of the PESO array relative to Chile. The red star indicates the epicenter of the 1st of November 2018 earthquake. **b.** Geometric setting of the PESO array. The blue triangle stands for the permanent PATCX station. The circle indicates our convention for the inner ring and the outer ring for this study **c.** Results of the beamforming analysis. Colorbar indicates the energy level that is reported on the azimuthal plot.

beamforming anaylsis (method in Text in Supplements), we estimate that the array is strongly dominated by waves propagating in the network from the south-west direction with a slowness of 0.65 s/km (Fig 4.1c).

4.2.2 Seismic interferometry for retrieving relative seismic velocity changes

We compute ambient noise cross-correlations to estimate relative seismic velocity changes dv/v (Sens-Schönfelder & Brenguier, 2019) using the stations that were installed for two weeks (9 stations) and the permanent station PATCX (Fig. 4.1). We first preprocess the seismic traces to limit the effect of high-amplitudes arrivals such as earthquakes on the correlations. These signals are numerous in the seismically active continental margin of northern Chile due to many small earthquakes (Gassenmeier et al., 2016; Sens-Schönfelder

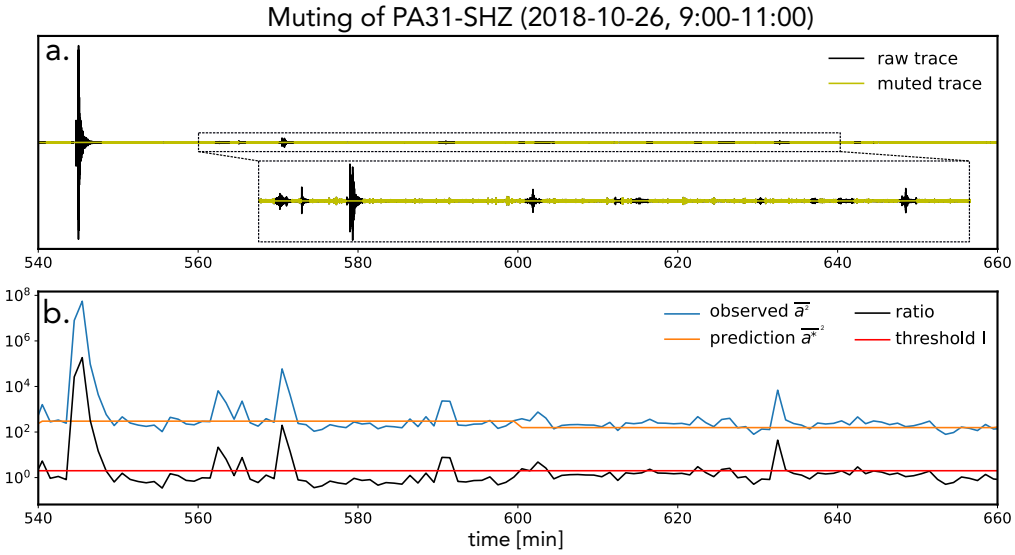

Figure 4.2: *Muting of the seismic trace, an example.* **a.** The black trace shows two hours of vertical data at the station PA31. The other trace stands for the muted version with a close-up for clarity. **b.** The blue line indicates the estimates of β_2 based on the average squared envelope of the raw trace shown in **a** at a 1-minute resolution. Orange line shows the prediction of β_1 based on the squared envelope predicted by the log-Rayleigh distribution at each hour. The ratio of the observation and the prediction is shown in black with the red line indicating the threshold used for muting the raw trace.

& Eulenfeld, 2019). To minimise unphysical bias introduced by non-linear normalisation schemes such as the 1-bit normalisation or spectral whitening (Fichtner et al., 2017), we choose a statistical approach to identify the time segments which contain the short-term high amplitudes and remove them from the analysis.

Due to its multiple scattering nature, the recorded seismic wavefield follows a Gaussian probability distribution (Groos & Ritter, 2009). The amplitudes of the envelope of such a field are Rayleigh-distributed. The corresponding distribution is defined by a single scale parameter β (McNicol, 1949; Oshima & Takenaka, 2020):

$$p(a) = \frac{a}{\beta^2} \exp\left(\frac{a^2}{2\beta^2}\right) \tag{4.1}$$

where $p(a)$ denotes the probability density of the envelope amplitudes a.

The ballistic arrivals and coda waves induced by a seismic event or a local disturbance unavoidably superpose on the background noise and increase the amplitude of the recorded field, changing the scale parameter β. Our approach consists of building amplitude predictions based on an estimate of β dominated by the background noise and compare it to short-term estimates of the mean squared envelope that are dominated by large transient amplitudes.

In a first step, we filter the seismograms and compute the envelopes $a(t)$ using the Hilbert transform. The mean of the logarithm of the envelope is linked to the scale parameter β through the log-Rayleigh distribution (Rivet et al., 2007). Since the mean of the logarithm down-weights large amplitude samples, we obtain an estimate of β that characterises the amplitude of the background field. According to Rivet et al. (2007), β can be retrieved from the following relationship:

$$\beta_1 = \exp\left[\overline{\ln\, a(t)} - \frac{1}{2}(\ln\, 2 - \gamma)\right] \tag{4.2}$$

In this equation, γ is the Euler's constant and $\overline{\ln\, a(t)} = 1/N \sum_i \ln(a_i)$ is the logarithm of the geometric mean. Corresponding computations were performed in 1-hour segments to down-weight furthermore the short-lived high amplitudes of earthquakes or other local disturbances. The assumption is that these disturbances, despite potentially being orders of magnitudes larger than the background, do not significantly bias this estimate of β due to the logarithm and the long term averaging. β_1 can be used as a prediction of background amplitude even if perturbations superpose the recorded signal.

In a second step, we obtain a short term estimate over 1-minute time windows of β with the intention to identify the high amplitude disturbances. Therefore, we estimate β from the mean squared envelope (McNicol, 1949):

$$\beta_2 = \sqrt{2}\ \overline{a^2} \tag{4.3}$$

with $\overline{a^2} = 1/N \sum_i a_i^2$ being the arithmetic average of the squared envelope. If the seismic signal is Rayleigh-distributed with a stationary scale parameter, the two estimates β_1 and β_2 will be equal. Short disturbances superposing the background signal are very well discriminated by the ratio β_2/β_1 even for fairly small additional signals.

We illustrate this process in Fig. 4.2 by comparing the amplitude of the signal, the predicted background signal amplitude derived from β_1 and the short term high amplitude estimate derived from β_2. To identify segments containing disturbances, we calculate the ratio of β_2/β_1 and compare it to a threshold value I that we set equal to 1.6 based on visual inspection of the performance. We construct a mask that we set to zero for all 1-minute segments with $\beta_2/\beta_1 > I$ and to 1 otherwise (Fig. 4.2b). In a last step, we taper the edges of the mask and save it to a file. We build masks for every station of the network using the vertical component filtered in a narrow band centered at 4Hz. On average, we found that 10 to 40% of the seismic traces were muted depending on the day and the station considered (Fig. 4.10).

Following the previous calculations, we trim the traces to 1-minute segments and resample the data at 50 Hz. We taper and filter the data in the 3-6 Hz frequency band. This band was chosen because of the stable results it has provided in previous studies at this site (Richter et al., 2014; Gassenmeier et al., 2016; Sens-Schönfelder & Eulenfeld, 2019). Finally, we mute the raw traces with the computed masks (Fig. 4.2). We calculate all possible cross-correlation combinations which include all autocorrelations AC (ZZ, EE, NN, 30 combinations), single station cross-correlations SC (ZN, ZE, EN, 30 combinations) and interstation cross-correlations CC (9 components cross-correlation tensor after rotation for 405 combinations). We cross-correlate the 1-minute segments and stack the results over intervals of 10 minutes.

To estimate the average relative velocity changes dv/v, we use the *stretching* technique (Sens-Schönfelder & Wegler, 2006), assuming the velocity changes are spatially homogeneous. For each combination, we compute the stretched versions of the correlation functions $C(t_i, \tau)$ where t_i is the date and τ is the lapse time of the correlation function. We use the 7 to 16 seconds lapse time window ($[\tau_1, \tau_2]$) and compare them to a unique reference ξ_r that is taken as the average cross-correlation function of the whole time period. This allow us to form the similarity matrix with ε_j being the stretching factor:

$$R_r(t_i, \varepsilon_j) = \int_{\tau_1}^{\tau_2} C(t_i, \tau)\xi_r(\tau * (1 + \varepsilon_j))\mathrm{d}\tau. \tag{4.4}$$

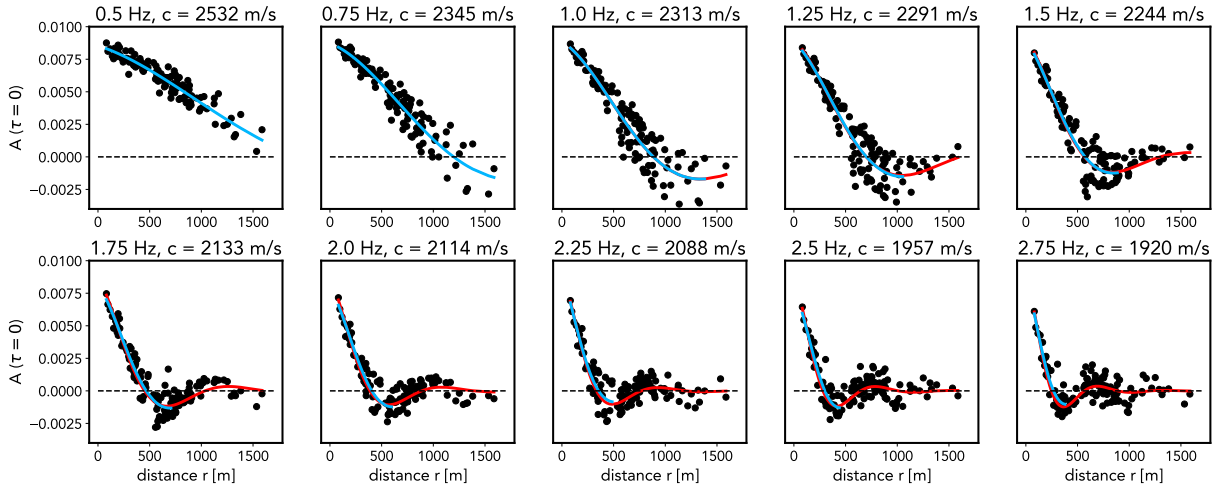

Figure 4.3: *Focal spot fitting results.*Each plot indicates the result from a different central frequency (indicated in the titles with the corresponding inferred phase velocity). Y-axis represents the amplitude of the cross-coherence ZZ functions at zero lag time while the x-axis shows the interstation distance. Red and blue lines show the fitting from the first iteration and second iteration respectively. Dashed lines indicate the 0 amplitude.

These similarity matrices $R_r(t_i, \varepsilon_j)$ can be all stacked to obtain the final dv/v representative for the entire field site (Fig. 4.11). Details for calculations can be found in Illien et al. (2021) in which we used the same computation scheme for the velocity changes estimation.

4.2.3 Estimation of the Rayleigh wave dispersion curve

To constrain the range of absolute velocities in which the relative changes dv/v occur and resolve the subsurface structure at our field site, we estimate the average 1D Rayleigh wave dispersion curve. We use the data recorded on the 22nd of October by the 16 stations network (Fig. 4.1) to maximize the number of available interstation distances. We preprocess the traces by correcting for the instrument responses, filtering in the 0.25-16 Hz range and muting high-amplitudes arrivals with the technique described in section 2.2.

We use the focal spot imaging technique to obtain Rayleigh wave phase velocities (Hillers et al., 2016). This technique is based on the spatial width of the zero lag cross-correlation field and aims to reconstruct the high-amplitude focal spot that emerges due to time-reversal properties (Conti et al., 2002; Fink, 2008). To normalise amplitudes between the different stations, we compute in the Fourier domain the cross-coherence γ. For two stations A and B, we have

$$\gamma_{AB}(w) = \frac{u_A(w)u_B^*(w)}{|u_A(w)||u_B(w)|} \tag{4.5}$$

with u_A and u_B being the waveforms recorded at stations A and B and w the angular frequency. We perform the computation on hourly segments and stack the 24 resulting cross-coherence functions of the 22nd of October for each ZZ interstation combination. We assume that the wavefield is dominated by Rayleigh waves. In this case, the cross-coherence amplitudes at the zero lag time τ (for ZZ combinations) can be expressed as (Hillers et al., 2016)

$$A(r, \tau = 0) \sim \sigma J_0(kr) e^{-\alpha r}. \tag{4.6}$$

In this equation, r is the interstation distance, k is the wavenumber, σ is a scaling constant that accounts for the preprocessing and α is an apparent attenuation coefficient. J_0 is the Bessel function of the first kind. The first zero crossing of equation (4.6), which determines the size of the focal spot, is located at

$$r^0 = \frac{3}{8}\lambda \tag{4.7}$$

and therefore completely determines the wavelength λ. From fitting relation (4.6), one can see that phase velocities for different frequencies can be obtained with a suitable interstation distance coverage r. To obtain w, we apply a 0.5 Hz wide bandpass filter on the cross-coherence functions centered around target frequencies between 0.5 Hz and 2.75 Hz with a frequency increment of 0.25 Hz. We fit the data in a procedure similar to Hillers et al. (2016): we first use all the available amplitudes to obtain a first estimate for the wavelength λ (red lines in Fig. 4.3). Then, we fit the combinations that are within the first 0.7 λ (green lines in Fig. 4.3) to obtain a second improved estimate: At distances larger than one wavelength, the estimation can be contaminated by scattering and topography effects (Hillers et al., 2016), hence we estimate the velocity closer to the first 0 crossing. We obtain 10 measures for the dispersion curve that we re-interpolate to 20 data points with the Geopsy software.

4.2.4 Inversion of the 1D shear velocity profile

We invert the dispersion curve with BayHunter (Dreiling & Tilmann, 2019; Dreiling et al., 2020), a python package dedicated to Markov chain Monte Carlo transdimensional Bayesian inversion. The main advantage of a Bayesian inversion is the retrieval of an ensemble of models and a better assessment of uncertainties in the retrieved solutions. Another advantage is that the model complexity i.e the number of layers (hence *transdimensional*) and the noise in the data are unknown hyper-parameters that are determined during the inversion process. For more details regarding the algorithm, we refer the reader to the paper of Bodin et al. (2012) and the documentation of BayHunter (Dreiling & Tilmann, 2019).

In this paper, we focus on estimating a shear-velocity profile and the V_P/V_S ratio. We give a range of possible solutions for these physical parameters and the hyper-parameters as priors for the inversion (Table 4.1). 50 Monte-Carlo chains are initialized to explore enough possibilities in the parameter space, using a total of 772608 iterations with a 2:1 ratio between the burn-in phase (initial exploration) and the exploration phase in which we look for the possible models. Some of the chains fail to converge as they return significantly smaller likelihoods than most chains after the burn-in phase: The threshold controlling the convergence is a percentage (here taken as 95%) of the maximum reached median likelihood from the chain ensemble. The chains not reaching this median likelihood are declared outlier chains. The final posterior distribution gathers 100,000 models by subsampling all non-outlier chains. We interpolate the results at a 50 m resolution.

Vs [km/s]	(0.5, 4)
z [km]	(0, 1)
number layers	(1, 12)
Vp/Vs	(1.5, 2.2)
noise [km/s]	(1e-4, 1e-1)

Table 4.1: Parameters priors used in the inversions.

4.3 Results

4.3.1 Relative Seismic Velocity changes

4.3.1.1 The dv/v time-series

Measurements of relative seismic velocity changes for each individual cross-correlation combination appear to be strongly scattered, although the measurements converge towards a clear dynamics when all plotted together (black dots, Fig. 4.4a). To illustrate the precision that can be obtained with a single station we show the measurements jointly obtained using the six possible combinations of the permanent station PATCX (autocorrelations and single-station cross-correlations) with the blue curve in Fig. 4.4a. The highest precision is obtained when using all combinations in the network, reducing the noise to an apparent $\sim$ 0.05% (red line, Fig. 4.4). For all measurements, we observe periods with larger scatter that we attribute to changes in the noise wavefield. These changes are seen in the traces amplitudes computed when building the pre-processing masks (Fig. 4.4b). We attribute the larger amplitudes (obtained here at 4 Hz) to strong winds in the afternoon.

We observe little to no velocity changes from the 22nd of October to the 1st of November. A clear drop of $\sim$0.4% is then visible and simultaneous with the Mw 6.2 earthquake that occurred at $\sim$ 150 km from the array (Fig. 4.1a). Averaging all horizontal component envelopes in our network, we measure a ground shaking intensity of the event to $\sim$1 cm/s PGV (Fig. 4.12). Half of the initial velocity drop was recovered after two days, with strongest recovery at early times after the co-seismic drop. The duration of our data is not sufficient to see a full recovery, hence reduced velocities appeared sustained for the observation time.

4.3.1.2 Stability of the measurement

We quantify the effect of multiple station averaging relative to the noise level in the final dv/v estimation. The standard deviation of the velocity time-series dv/v over all time samples of the 10 days prior to the earthquake can be plotted as a function of the stacking duration window and the number of combinations used (Fig. 4.5). Assuming that the velocity variations during this time-span is mostly due to noise, this standard deviation is a good proxy of the signal to noise ratio of (SNR) of the dv/v time-series and for the measurement stability. Because we exploit a late time-window (starting at 7 s, which corresponds to $\sim$ 21 wavelengths at 3Hz, the lower limit of the used bandpass filter) in the correlation function for measuring the dv/v changes, we ensure to minimise diurnal physical changes that arise when processing earlier times (Richter et al., 2014; Sens-Schönfelder & Eulenfeld, 2019). To construct the plot, we use all 6 self-correlations (AC+SC) for each of the ten stations. After shuffling the 60 combinations randomly in a list, we split them into multiple subsets corresponding to 6 (10 subsets), 10 (6 subsets), 15 (4 subsets), and

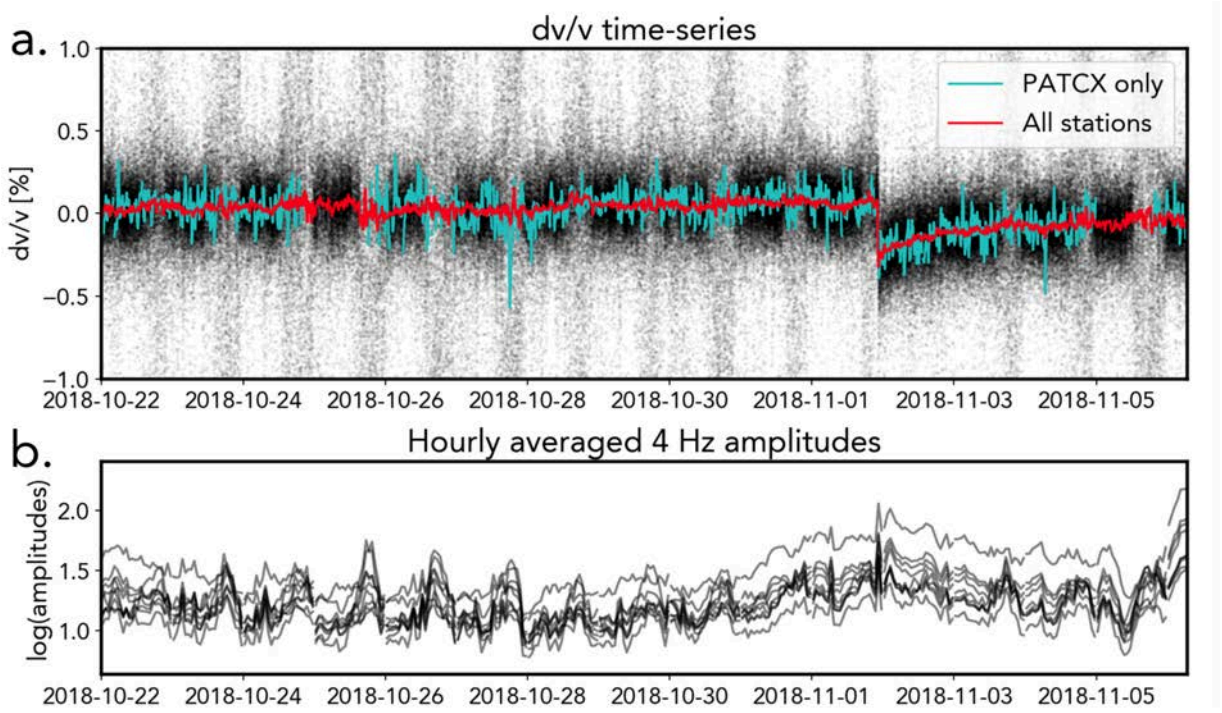

Figure 4.4: *PESO dv/v time-series.* **a.** Each black dot indicates an estimation using a single cross-correlation combination in the network. Blue line shows the joint result using the 6 self-combination of the PATCX station. Red line shows the results using all 405 combinations. Time resolution is 10 minutes. **b.** *Noise amplitudes time-series at 4 Hz.* Each lines represents the hourly logarithm of the hourly-averaged noise amplitudes for all the stations deployed during the 2 weeks. Opacity is a function of the curves overlap. Traces were processed with a 4 Hz Gaussian filter beforehand.

30 combinations (2 subsets). For each subset, we average the velocity changes using the similarity matrix stacking (eq. 4.4) described in the methods (section 4.2.2) and extract the standard deviation of the obtained dv/v. We perform these calculations at several time resolution using different durations for the stacking window of the correlation functions ranging from 1 minute (no stacking) to 1 day stack. Finally, we also build the plots considering only the inner-ring stations (interstation distances from 260 to 670 m) and the outer-ring stations (interstation distances from 570 to 1580 m). The ring conventions are shown in Figure 4.1b.

The standard deviation always increases when using a lower number of combinations (Fig. 4.5a-c). For all curves, smaller stacking duration consistently also yields larger standard deviations. However, this deterioration systematically happens at different thresholds depending on the number of combinations used (Fig. 4.5a-c). This threshold is important as it drives the transition towards standard deviations that can be one order of magnitude higher at smaller time-resolution. Surprisingly, for large time windows, the average standard deviation of the outer ring stations (36 combinations, Fig. 4.5c) is smaller than the average using all combinations (Fig. 4.5a).

To illustrate the improvement of the estimations when using more stations, we plot the ratios between the standard deviations measured with many combinations (60, 24 and 36 combinations depending on the configuration) and the one measured with 6 combinations, which is the amount of information that would be obtained with one station (Fig. 4.5d-f).

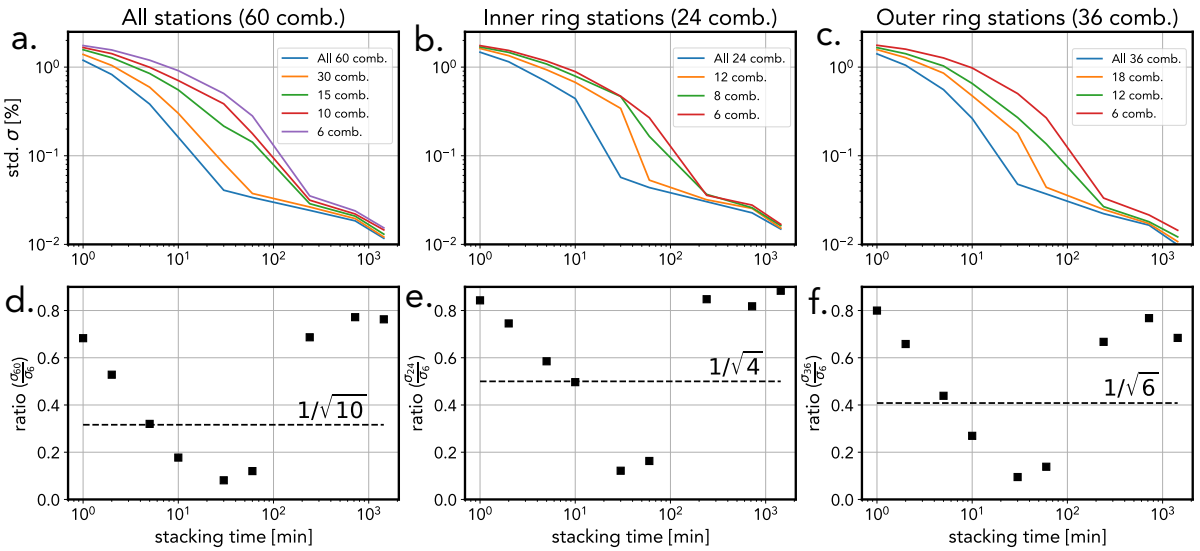

Figure 4.5: *Standard deviations of the dv/v changes prior to the earthquake (from the 22nd of October to the 1st of November) obtained using different stacking durations and number of combinations* **a.** Curves obtained using all single-combinations in the network. For each stacking duration, the mean of the standard deviation of the respective combination subset. The subsets are characterised by a number of combination shown as an inset label. We show on **b.** and **c.** the same plot but using only the inner ring stations and the outer ring stations respectively. The subplots **d**, **e** and **f** show the corresponding ratio between the standard deviation using all considered combinations and when using only six. The dashed line shows the theoretical reduction of the standard deviation for independent variables with the same mean and variance.

Theoretically, the reduction of the standard deviation of a sum of independent random variables with the same mean and variance should obey to a factor of $1/\sqrt{N}$ with N being the number of variables. For all combinations, we indicate this theoretical reduction using $N = 10$ (10 stations), $N = 4$ for the four inner ring stations and $N = 6$ for the six outer ring stations. We observe that the improvement of the dv/v result is not significant at both large time-windows and at small-time windows (Fig. 4.5d-f) for the three considered configurations. However, in an intermediate sweet spot, the ratios reach the theoretical reduction limit and even plot at lower values.

Finally, we normalised the standard deviations shown in Figure 4.5a by the amount of data used to obtain a velocity estimation. The resulting plot shows a remarkable collapse of the data point along a single non-linear decreasing trend (Fig. 4.6). Using our averaging method, the same signal to noise ratio can be achieved by either using more stations and smaller stacking time-windows or using less stations with more stacking, as long as the same amount of 'information' is used. Under these conditions, the ergodicity property can therefore be validated. Practically, this also means that a good precision can be obtained with one station at the cost of having larger stacking time and therefore a lower time-resolution. We note that above the 10^3 minute mark, the standard deviations exhibit a step change and the agreement between the points is less striking. Knowing that small daily velocity changes due to temperature (Richter et al., 2014) or the Earth's tides (Sens-Schönfelder & Eulenfeld, 2019) are active at the Patache field site, we attribute the degradation to physical effects that are more or less smoothed or averaged at large stacking times depending on the number of used combinations.

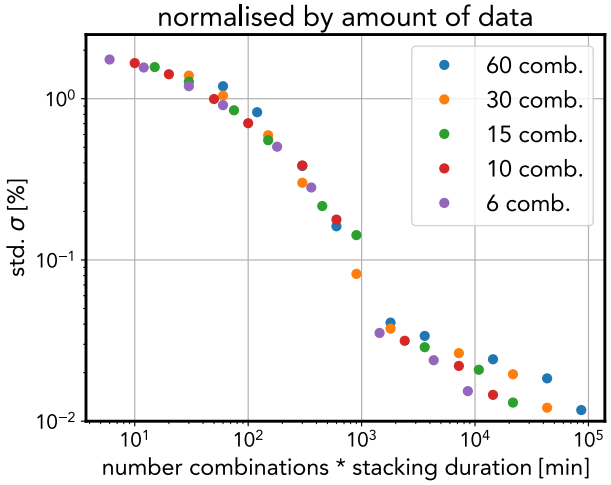

Figure 4.6: *Noise in the seismic velocity time-series normalised by the total amount of used seismic data.* Data are identical to Figure 4.5a but normalised by the total added length of the used seismic traces.

4.3.2 Shear velocity profile

The inverted 1D shear velocity profile is shown in Figure 4.7a along with the target dispersion curve which we inferred from the focal spot imaging technique 4.7c. The average shear velocities are in the 1250-2000 m/s range (mean = 1600) in the first $\sim$ 200 m and in the 2400-3200 m/s range (mean=2750 m/s) in the $\sim$ 250-1000 m depth range. The profile and the histogram of the layers depths is characterised by a clear two-layer structure (Fig. 4.7abd) with absolute seismic velocities indicating a hard-rock site. Most of inferred models result in smoother version of the target dispersion curve (Fig. 4.7c) with a noise level in the measurements estimated at a 25 m/s median value (Fig. 4.7e). The Vp/Vs ratio is poorly constrained but exhibits a median value of 1.58, typical of crystalline rocks or consolidated sediments (Mavko et al., 2009).

We note that the average velocity value inferred in the shallow surface ($\sim$1600 m/s) shows a rather good agreement with the apparent velocity ($\sim$1500-1600 m/s in the 4-6 Hz frequency range) inferred from the beamforming analysis performed to characterise the noise distribution (Fig. 4.1c). To refine the velocity profile, we performed a second inversion with the same method, adding the rough estimate of the high frequency phase velocity obtained from the beamforming analysis (velocity at 1550 m/s at $\sim$4 Hz) to the target dispersion curve (Fig. 4.13). The obtained velocity profile emphasises the 2-layer structure with a discontinuity at $\sim$200 m depth and refines the shear velocity to 1550-1600 m/s in the superficial layer and $\sim$2750 m/s in the second layer. However, these secondary results should be interpreted with caution, as velocity measurement with beamforming may be flawed due to the potential steep incidence of body waves (Rost & Thomas, 2002).

4.4 Discussion

4.4.1 Conditions for stable velocity measurements

Finer time-resolution using passive seismic monitoring is a long standing challenge in seismic interferometry. Previous attempts to tackle this issue include denoising the cross-correlations

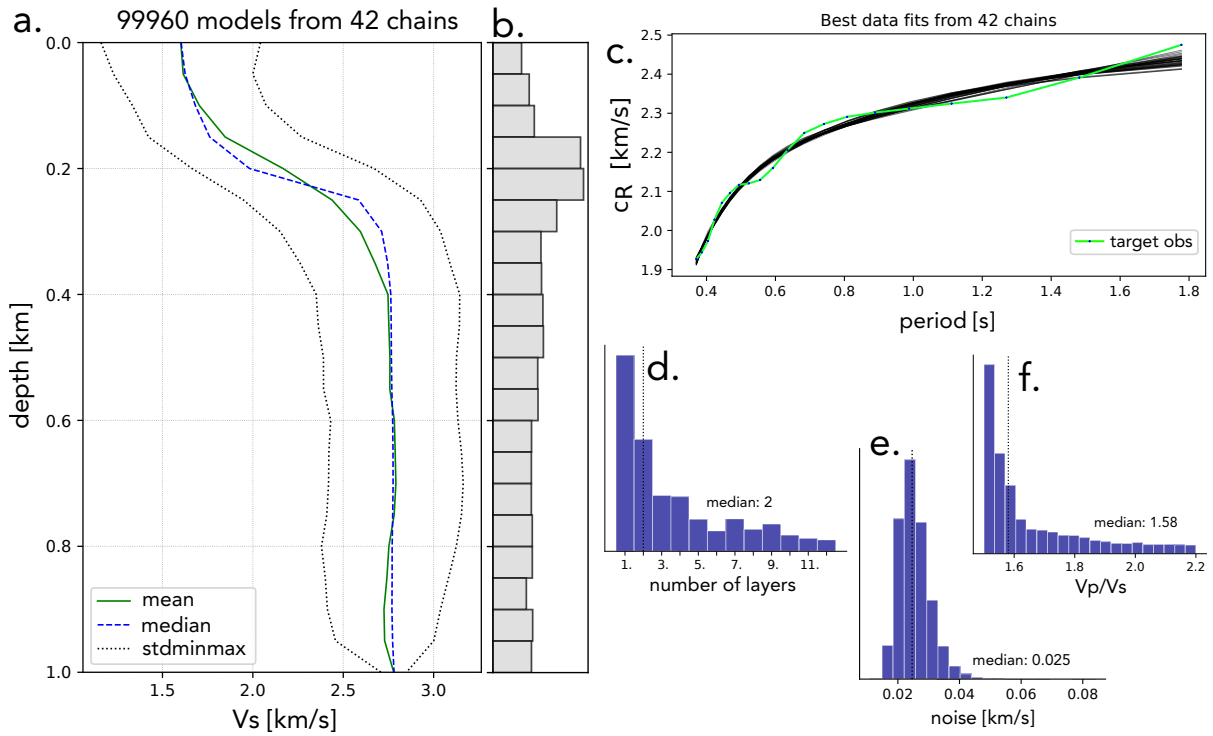

Figure 4.7: *Inversion of the 1D shear velocity profile and corresponding target dispersion curve.* **a.** Inferred shear velocity profile interpolated at a 50 m resolution. Green and blue lines shows the mean and the median value of the best retained models. Dashed black lines indicate the standard deviation. **b.** Histogram of the depth of the inferred layer structures **c.** The green line shows the dispersion curve that we use for the inversion, the other curves showing the best fit obtained for each chains . Histograms corresponding to the other inverted parameters are shown in **d.** for the number of layers, in **e.** for the noise level in the measurements and in **f.** for the Vp/Vs ratio.

with adaptative filters (Hadziioannou et al., 2011) or convolutional autoencoders (Viens & Van Houtte, 2020), performing single-station cross-correlation at higher frequencies (Hobiger et al., 2014), stacking more short time-windows instead of a lower number of long time-windows (Xu et al., 2021) or tracking a persistent phase in the correlation functions (Lu & Ben-Zion, 2022). In our study, we took the simple road of combining more stations for testing the ergodicity of the seismic velocity estimated from the noise wavefield.

The velocity change measurements were improved, with a noise level down to one order of magnitude lower than the one obtained with one station (6 combinations), depending on the length of the stacking window (Fig. 4.5). The theoretical limits plotted in Fig. 4.5d-f give a limited prediction of this improvement which indicates that our assumption of independent variables with the same mean and variance may not hold. However, at intermediate stacking length, the refinement of the results is clear (Fig. 4.5d-f). Outside of this intermediate range, the benefits are limited: With small stacking windows, the space-averaging is not sufficient to counter-balance the requirement of a minimum time duration for an effective statistical noise source summation (Fichtner et al., 2017). At the other end, with large stacking windows, the time-averaging is long enough for stable measurements and is not improved greatly when adding more stations. We conclude that the sweet spot between these conditions could be constrained with pilot deployments to optimise the number of stations needed for high-resolved temporal measurements. The plot

of the dv/v recovery phase at different time resolutions highlights the trade-off between the choice of a time-resolution and the addition of noise in the time-series (Fig. 4.8). Ultimately, the ergodicity hypothesis was satisfied as long as the same amount of data was used (Fig. 4.6), suggesting that the stacking time of the correlation functions should be decided upon the number of available stations.

We found no significant effects when using different interstation distances (Fig. 4.5bc). However, the effects of this parameter should be investigated further because it is thought to be critical for optimised measurements as it controls the overall correlation of the observed wavefield at the different stations (relative to the targeted monitoring frequency). The largest correlation should be obtained when the interstation distance is on the order of the monitoring wavelength λ. At 3-6 Hz and using 1600 m/s for Rayleigh waves, we obtain $\lambda \sim 266 - 533$ m. With the 90-1600 m range in our array, we have therefore a mixture of correlated and uncorrelated arrivals. At large distances, the observed dv/v changes are also caused by different structural changes and the spatial averaging is not useful anymore.

Beyond methodological aspects, the monitoring of seismic velocity requires certain noise and structural conditions for stable measurements. Regarding noise source distribution, the reconstruction of the Green's function from correlations requires random and isotropic noise sources (Lobkis & Weaver, 2001), a condition that is unlikely met in the field (Mulargia & Castellaro, 2013). Nevertheless, a stable localised noise source is sufficient for monitoring purposes (Hadziioannou et al., 2009) and represents another ideal situation. In our frequency band, the beamforming analysis shows that the incoming energy has one dominant azimuthal direction (Fig. 4.1c). This feature suggests that the Peso field site is continuously excited by the same source which is likely to be induced by the surf of the ocean waves hitting the shoreline (Fig. 4.9). This stable situation is disturbed during windy afternoons, which cause the degradation of our velocity measurements (Fig. 4.4) due to high-amplitude arrivals. In our study, a statistical pre-processing scheme was designed to limit the disturbances from these deterministic signals. The 1D profile also suggests that a low velocity layer is present at the surface (Fig. 4.7ab) with elevated velocities (>1000 km/s for most of inferred models, Fig. 4.7a). Considering a low-velocity layer of $V_S = 1600$ m/s with a thickness $H = 200$ m, we can estimate an approximate resonance frequency with $f_k = ((2k+1)/4)/(V_S/H)$ (Nakamura, 2000). With this relation, we obtain $f_0 \sim 2$ Hz to for the fundamental mode and $f_1 \sim 6$ Hz for the first overtone, these values being almost in the range of the 3-6 Hz band we used in this study. This configuration could promote the trapping and reverberation of seismic energy around this specific frequency band and with limited dissipation which are ideal conditions for monitoring subsurface changes (Sheng et al., 2021).

4.4.2 Relaxation in the field: timescales and geological structures

Following the 1st of November 2018 earthquake, we report a 0.4 % velocity reduction in the first 10 minutes after the earthquake. The observable slow dynamics behavior lasted roughly for ∼2 days and is well resolved at the 10-minute resolution (Fig. 4.4) with a characteristic log-linear recovery (Fig. 4.8). A minimum timescale of relaxation was not observed (Snieder et al., 2016; Shokouhi et al., 2017) and if it exists, must be below our 10-minutes resolution. The dv/v time-series obtained at 1-minute resolution resolves an additional 0.1% drop at earlier relaxation times, albeit an increase in noise measurements according to previous analyses (grey line in Fig. 4.8). Such minute seismic-induced velocity changes in both amplitude (less than 0.5%) and timescale were not observed at this relatively high frequency band (3-6 Hz) to our knowledge. We used a late time window to

ensure minimising source artefacts and sampling a large portion of the subsurface. Rapid velocity changes were also reported in the literature but often using different techniques that may be more prone to noise source changes and near-surface non-linearity: Using very early times in autocorrelation functions during earthquake ground motion at frequencies above 10 Hz, the technique lead to comparatively larger changes (>5%) for very small PGV ($< 10^{-4}$ m/s) (Bonilla et al., 2019). Another remarkable time-series (at a 10-minute resolution) was obtained using P/S converted waves following the Mw 7.1 Ridgecrest earthquake (Lu & Ben-Zion, 2022). However, their observed changes are larger than our results due to significant ground shaking. Our study suggests that small ground shaking induces a lingering effect that may be challenging to resolve. These effects matter for understanding the effect of cumulative aftershocks for the recovery of material properties after large earthquakes (Sawazaki et al., 2018). Our temporal coverage was not sufficient to estimate the maximum relaxation timescale of the recovery. In a previous study we hypothesized that material properties and ambient conditions are the dominant control of the observable maximum relaxation time, rather than the co-seismic ground shaking intensity (Illien, Sens-Schönfelder, et al., 2022). A dynamic system analysis on a longer time-series could help us shed light on these controls and assumptions and is planned in a future manuscript.

In field studies, relaxation mechanisms are often interpreted as near-surface non-linearity induced by soils deformation (Sleep & Nakata, 2017; Viens et al., 2018; Guéguen et al., 2019). Pictures from the field (Fig. 4.14) indicate the presence of a conglomerate with evaporites at the surface, which may constitute the first 200 m layer (Fig. 4.7a). If we assume the dominance of Rayleigh wave energy in the noise wavefield, the corresponding sensitivity kernel associated with the measured dispersion curve (Fig. 4.7c) and the inferred 1D model (Fig. 4.7a) suggest that these rocks host the observed velocity changes at frequencies above 3 Hz (Fig. 4.15). The higher velocity in the second layer could correspond to crystalline rocks such as gabbros, according to geological studies in the area (Tapia et al., 2018). In the laboratory, relaxation has been observed in crystalline (Shokouhi et al., 2020; Meyer et al., 2021) and sedimentary rocks (Brantut, 2015). Numerical simulations and experiments suggests that the largest contact areas in the rock fractures (Shokouhi et al., 2020), cracks (K. Gao et al., 2019), and the grain contacts in granular media (Kober et al., 2022) controls the relaxation timescale. Due to higher strength, hard rocks can sustain larger flaws and fractures, which in turn may lead to longer relaxation timescale due to high activation barriers. This statement may only be valid if slow dynamics behaviour effectively originates due to thermally-activated processes such as with the Arrhenius equation (Snieder et al., 2016; Ostrovsky et al., 2019).

4.5 Conclusions

In this study, we explored the potential advantage of using more co-located stations to improve the time resolution of relative seismic velocity changes dv/v inferred from ambient noise correlations. We made the assumption that the dv/v estimation obeys the ergodic hypothesis i.e the time-average (one station with large stacking time for the correlation functions) is equal to the space-average (several stations with small stacking time for correlation functions). We found that the staking time required to obtain stable correlation functions and therefore velocity measurements can be significantly lowered by using more stations. When normalised by the amount of used seismic data, the ergodicity was satisfied, which suggests that the minimum time-resolution of dv/v measurements is a function of

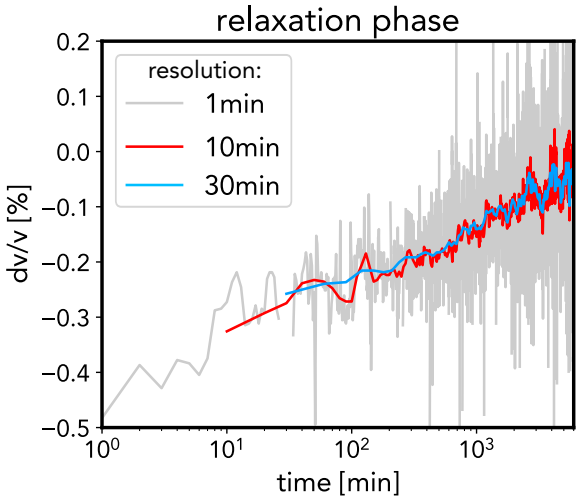

Figure 4.8: *Relaxation phase recorded by the PESO array at different resolutions.* The recovery phase shown in Fig. 4.4 using all the combinations is plotted in red. The log-linear x-axis emphasises the characteristic slow dynamics recovery. Note the variation of noise at high-resolution (dt = 1 minute) and at lower resolution (dt = 30 minutes).

the number of available stations. *What is the highest time-resolution limit that one can reach ?* This question remains to be answered but our study demonstrates an important property of seismic interferometry from ambient noise correlations.

Thanks to the gained precision, we resolved a 0.4% velocity drop after a seismic event that induced ∼1 cm/s of PGV at a 10-minutes resolution. Half of this drop was then recovered with a log-linear relaxation shape in agreement with slow dynamics studies. The largest changes were contained in the immediate aftermath of the earthquake. We showed that this relaxation behaviour is happening in a hard rock site according to the local 1D shear velocity profile we derived from the focal spot imaging technique and an McMC transdimensional Bayesian inversion.

Figure 4.9: *Screenshot of the array in Google Earth.* The yellow pins stand for the PESO stations. The picture highlights the cliff escarpment. The shoreline orientation is in agreement with the beamforming results in which the noise strikes the array from a south-west direction.

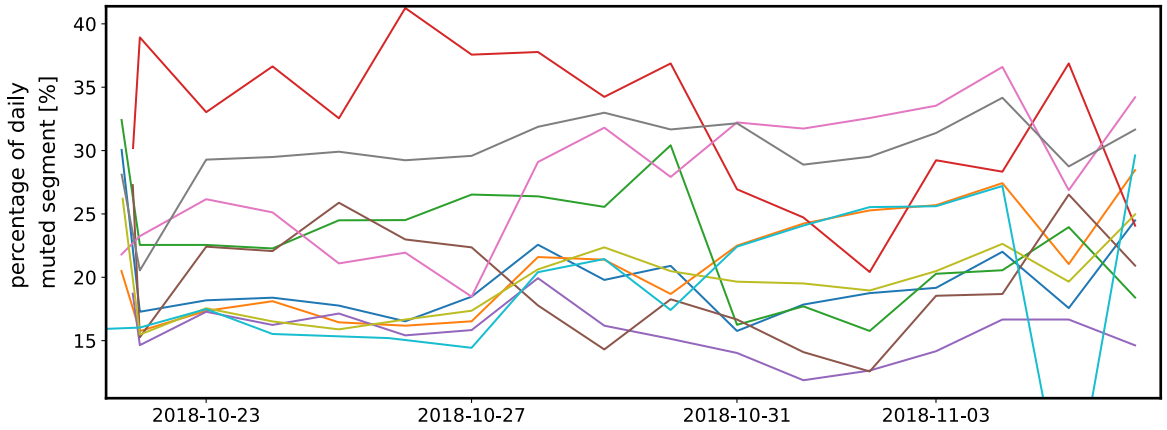

Figure 4.10: *Proportion of daily muted segments.* Each color stands for a different station.

4.6 Supplementary materials to paper III

Text S1: Beamforming To investigate the character of the wavefield used to monitor the velocity changes we apply plane-wave beamforming to the noise recorded with the array in the 4 - 6 Hz band. We use instrument corrected data from October 22nd for an F-K analysis of 10s long time windows with 50% overlap. Analysis is implemented using the Obspy array processing routine. From each of the 10s long segments we infer the slowness vector with the maximum energy. Figure 4.1c of the main text shows the probability distribution of the resulting slowness vectors. Energy in this frequency band is strongly dominated by waves with a slowness of 0.65 s/km striking the network from south-west.

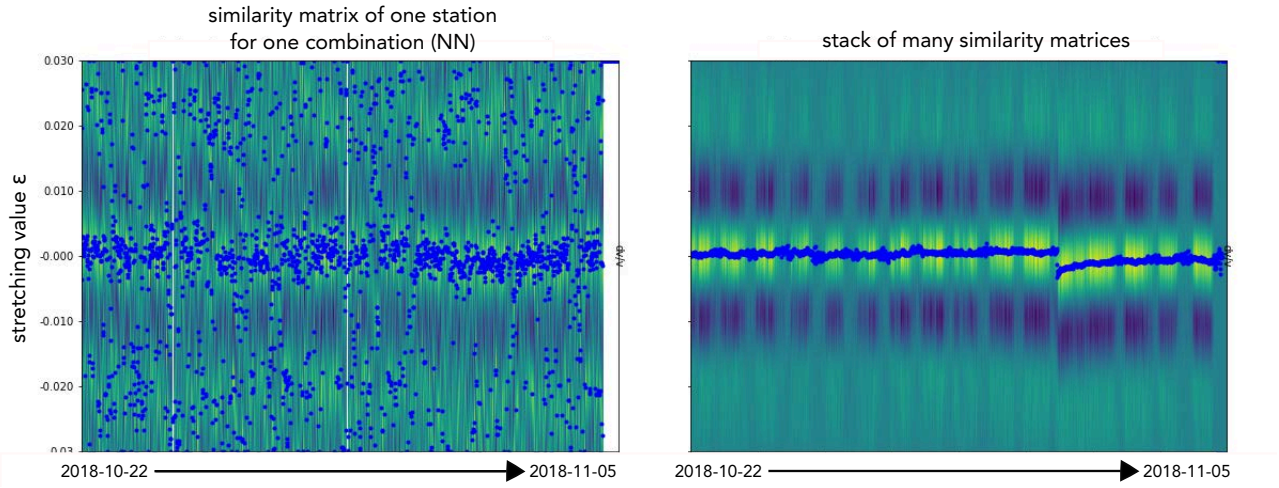

Figure 4.11: *Illustration of the similarity matrix.* On the left, we report the similarity matrix when using only one autocorrelation at one station. The blue dots show the stretching value corresponding to the best correlation values in the equation (4.4) of the main text. On the right, we show the similarity matrix built when stacking all the possible matrices (such as the one on the left) of the network. The figure illustrates the enhancement of the measure using this technique.

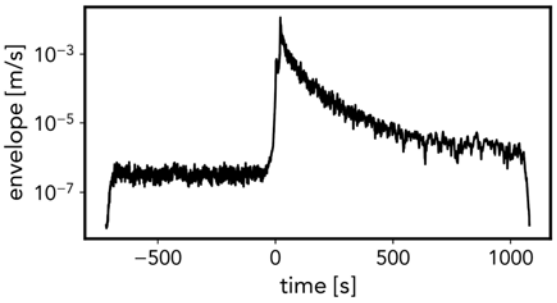

Figure 4.12: *Average envelope of the horizontal components in the network during coseismic ground shaking.* The time 0 corresponds to the onset of the P-wave. The envelope is averaged over all the network.

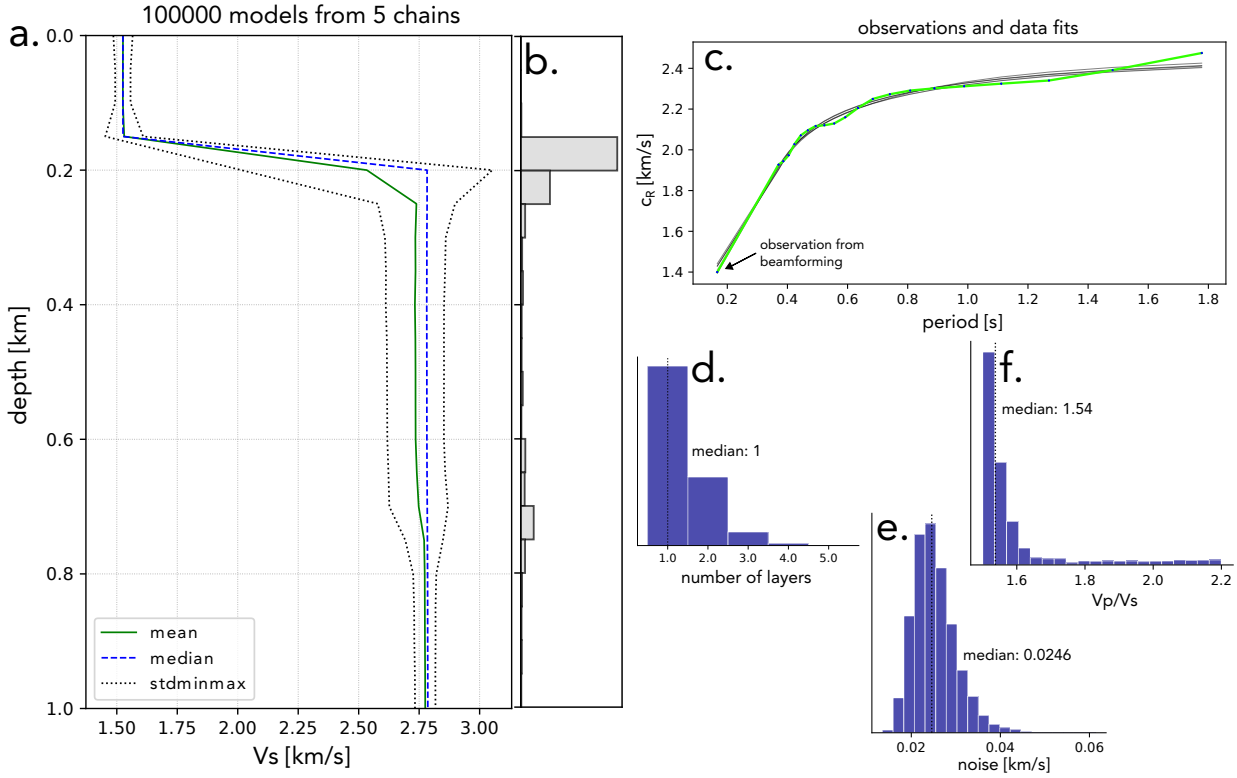

Figure 4.13: *Inversion results when adding the observation from the beamforming method.* **a.** Inferred shear velocity profile interpolated at a 50 m resolution. Green and blue lines shows the mean and the median value of the best retained models. Dashed black lines indicated the standard deviation. **b.** Histogram of the depth of the inferred layer structures **c.** The green line shows the dispersion curve that we use for the inversion, the other curves showing the best fit obtained for each chains. Histograms corresponding to the other inverted parameters are shown in **d.** for the number of layers, in **e.** for the noise level in the measurements and in **f.** for the Vp/Vs ratio.

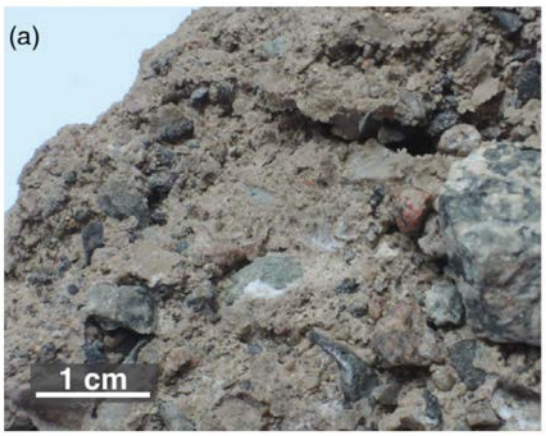

Figure 4.14: *Geological media observed in the field.* The geology hints at clasts embedded in a matrix containing large amounts of evaporites (likely gypsum and halite). The picture is taken from the study of Sens-Schönfelder and Eulenfeld (2019).

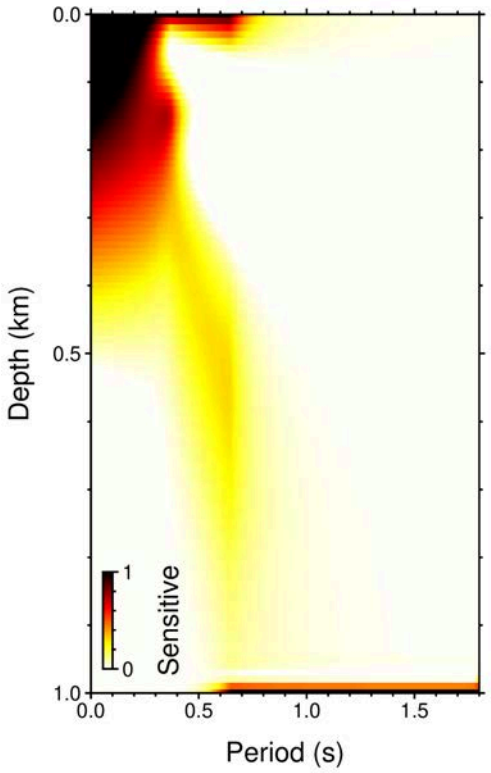

Figure 4.15: *Rayleigh wave sensitivity given the inferred 1D profile and the measured dispersion curve.* The kernel was computed using the CPS software (Herrmann & Ammon, 2002).

Transition: *Can you predict anything ?*

In Chapter 4, I demonstrated the important property of ergodicity for seismic interferometry. This property allows to increase the time-resolution of seismic velocity changes measurements by using more co-located stations. This has important implications for monitoring a dynamic forcing acting on small timescales. Additionally, I also showed a perfect log-linear recoevery behaviour at sub daily timescales (down to a minute) that was triggered by moderate ground shaking. A complementary inversion also showed that the associated relaxation was occuring close to the surface in hard rocks (V_S =1500 m/s).

If the relaxation was observed at small timescales at our field site, the duration of the array deployment (two weeks) was not suited for constraining the total duration of the recovery, essential for the forecast of long term subsurface damage after earthquakes.

In the next and final study (Chapter 5), I will use the full 13 years of seismic noise recorded at the permanent station PATCX, located at the same site than Chapter 4. Remarkably, the station was in place during two large seismic events (the 2007 Mw 7.7 Tocopilla and the 2014 Mw 8.2 Iquique), which gives the unique opportunity to study the successive effect of the relaxation behaviour for an isolated site and finally address the predictability and the physics of the slow dynamics phenomenon at the field scale.

Chapter 5

Predictable healing rates in near-surface materials after earthquake damage

Luc Illien, Jens M. Turowski, Christoph Sens-Schönfelder, Clement Berenfeld, Niels Hovius

In preparation

Abstract

Earthquakes introduce long-lasting transient mechanical damage in the subsurface, which causes postseismic hazards and can take years to recover to steady-state values. This observation has been linked to relaxation, a phenomenon observed in a wide class of materials after straining perturbations. Here, we analyse the successive effect of two large earthquakes on ground properties through the monitoring of seismic velocity from ambient noise interferometry. We show that the relaxation time scale is a function of the state of the substrate at the time of seismic perturbation, rather than the intensity of ground shaking. Our study highlights the predictability of earthquake damage dynamics in the Earth's near-surface and potentially other materials. We propose to reconcile this finding with existing physical frameworks by considering the superposition of different populations of damaged contacts.

5.1 Introduction

Earthquakes cause catastrophic effects at the Earth's surface, which range from urban damage to physical changes in the landscape (Fan et al., 2019; Marc et al., 2015). For instance, landsliding (Marc et al., 2015), aquifer permeability (Manga et al., 2012) and river discharge (C. Y. Wang et al., 2004) have shown a temporary increase after ground shaking before eventually going back to pre-earthquake levels. Although these effects do not last forever, they have a duration up to multiple years and therefore impact the resilience ability of our societies after seismic events.

These transient phenomena are observed at the surface but they also suggest that the hydro-mechanical properties of the shallow Earth's subsurface are compromised in the aftermath of earthquakes. To probe into these underground dynamics, seismologists have started to use the continuous ambient noise recorded by seismometers to estimate seismic velocity changes as a proxy for subsurface physical changes before and after earthquakes. They have found that earthquakes induce a drop in subsurface seismic velocity, which is followed by a recovery on time scales ranging from a few days to several years (Brenguier et al., 2008; Gassenmeier et al., 2016; Viens et al., 2018). This recovery dynamics resemble the universal relaxation (TenCate et al., 2000), a phenomenon observed in rocks(Shokouhi

et al., 2017), granular media (Knight et al., 1995), concrete (Bentahar et al., 2020) and civil structures (Astorga et al., 2018), in which the acoustic velocity in a material drop due to a straining perturbation and recovers on time scales that are defined from seconds to years. In epicentral areas, the relaxation timescale observed with seismic velocity has shown to correlate with the duration of enhanced postseismic landsliding(Marc et al., 2021), which suggest that the latter and possibly other transient surface processes originate from damage represented by the relaxation dynamics of the shallow subsurface. Therefore, a physically based model with clear observables to predict and constrain the duration of the recovery would be crucial information for the emergency response after earthquakes and the monitoring of damaged buildings and fault zones.

The relaxation of earthquake-induced damage subsurface materials is commonly analysed by fitting an exponential decay of observed seismic velocity changes, with a single timescale (Hobiger et al., 2014; Gassenmeier et al., 2016). This method yielded numerous relaxation timescales ranging from a few days to several years (Viens et al., 2018; Marc et al., 2021) but no consensus exists regarding the predictability and the main control of this duration. Moreover, the recovery of the seismic velocity changes exhibits a logarithmic evolution, which the exponential fit fails to capture (Gassenmeier et al., 2016). It is clear that this is an insufficient basis for reliable prediction of post-seismic recovery. Recently, models based on contact mechanics and friction physics have been used to explain the velocity changes (Ostrovsky et al., 2019; S. Y. Wang et al., 2021). These relationships predict that the rate of change of the velocity changes dv/dt is a direct function of the current state velocity $v(t)$. Observational validation of this approach requires that the trajectory of the velocity changes after an earthquake is considered as the product of multiple ground shaking events, including those due to aftershocks and subsequent events. If these expressions are appropriate, then the relaxation duration can be predicted from the velocity data. However, seismic monitoring studies often focus on the impact of one earthquake and not on the potential successive relaxations due to multiple ground shaking events. This lack of observation makes the testing of these models limited and hampers the predictive potential and understanding of the phenomenon.

We propose to advance our understanding of the subsurface recovery after earthquakes by estimating daily seismic velocity changes (Materials and Methods in supplementary materials) at a seismic station (PATCX) in the Atacama desert of Chile (Fig. 5.1ab). This site was chosen for 3 reasons. First, previous work has demonstrated that the station records support highly stable measurements of very small velocity changes (Richter et al., 2014; Gassenmeier et al., 2016; Sens-Schönfelder & Eulenfeld, 2019). Second, the arid setting precludes significant effects of changes in water content. And third, the site has experienced two major earthquakes, the 2007 Mw 7.7 Tocopilla and the 2014 Mw 8.2 Iquique, and numerous aftershocks. This makes it uniquely suited for studying the cumulative damaging and relaxation behaviour of the subsurface for a period of 13 years. With the resulting time-series, we show that the timescales or recovery can be predicted from pre-earthquake seismic velocity values regardless the initial ground shaking intensity.

5.2 13 years of seismic velocity changes induced by earthquake damage

Seasonal temperature variations in the Atacama desert induce thermal strain, affecting the seismic velocity measurements (Richter et al., 2014). We remove these thermal effects

(Materials and Methods) to obtain the impact of earthquakes on the relative velocity changes (Fig. 5.1a), which we scale to the local reference value for the shear velocity $V_S = 1500$ m/s (Illien, Sens-Schönfelder, & Ke, 2022). After correction, the residuals show velocity drops of 15 and 35 m/s for the Tocopila and Iquique earthquake, respectively, each followed by a long-lived recovery ($\sim$ 3-4 yrs), the largest one occurring during the Iquique earthquake. Additional drops and associated recoveries due to aftershocks and smaller earthquakes can be observed, particularly in the aftermath of the Tocopilla earthquake. Drop magnitudes have been shown to be proportional to the peak ground velocity in previous studies (Richter et al., 2014; Gassenmeier et al., 2016).

To test for log-linear behaviour of the post-seismic velocity recovery observed in experimental slow dynamics studies, we plot the first 1000 days of the large recovery phases on a logarithmic scale (Fig. 5.1c). For three orders of time magnitude,the recoveries after both large earthquakes appear linear in this space, with some deviations due to aftershocks. The consistency of the slope despite these additional perturbations suggests that the recovery timescale may be predictable by measuring the rate of velocity change in the early aftermath after an earthquake.

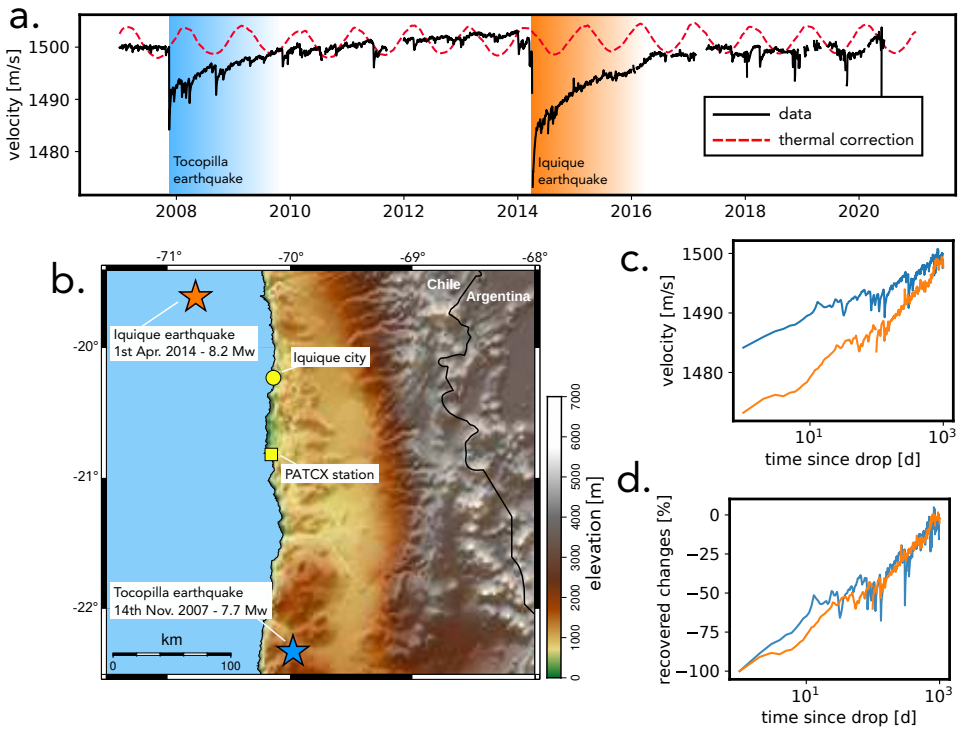

Figure 5.1: *13 years of seismic velocity data for Station PATCX in Chile, including transient changes due to the Tocopilla and Iquique earthquakes* **a.** The black-line indicates the relative seismic velocity changes scaled with the reference velocity value of 1500 m/s. The red line shows the correction we applied beforehand to account for the thermal strain due to seasonal temperature fluctuations. **b.** Map showing the study area with both stars indicating the epicenters of the main shocks. **c.** Plot of seismic velocity during the first 1000 recovery days following the main shocks on a logarithmic time-axis. The blue and orange lines represent for the Tocopilla and the Iquique earthquakes episodes respectively. **d.** Plot of seismic velocity recoveries normalised by the amplitude of the respective initial velocity drops.

We normalised the recoveries by considering the percentage of recovered changes relative

to the pre-earthquake velocity levels (Fig. 5.1d). This normalisation collapses the two time-series onto the same line. This indicates that although causing different perturbation amplitudes, both earthquakes induced a relaxation behaviour that had a similar timescale of recovery over the first 1000 post-seismic days. The co-seismic velocity reductions were approximately halved in the first 200 days of recovery following the main shocks. Although aftershocks caused smaller velocity drops, these did not have a significant impact on the total relaxation duration. On average, We estimate that full recovery of the seismic velocity after Tocopilla and Iquique earthquakes would take about 3887 days (Materials and Methods, Fig. 5.4a).

5.3 Pre-drop velocity level controls the timescale of relaxation

Using the same normalisation, we further analyse the recoveries induced by aftershocks to unify all relaxation observations. The first 10 days of recovery after each seismic event can be visualised and normalised by their pre-drop velocity levels (Fig. 5.2a). We use a 10-day window to minimise the potential superposition of recoveries associated with previous aftershocks. In this time, recovery ranged from 20-30% for some aftershocks to 100% for others. A relationship appears to exist between the pre-drop velocity for an aftershock and the rate of recovery, with faster recovery for drops with lower starting velocities (Fig. 5.2a).

We quantify this trend by fitting the initial recovery slope plotted on Figure 5.2a with a universal relaxation function and find their optimum maximum relaxation timescale $\tau_{\max}$ (Snieder et al., 2016) (Materials and Methods, Fig. 5.4b). The inferred timescales $\tau_{\max}$ can be described by an exponential relationship with the pre-drop velocity with values ranging from ~ 8 to ~ 3000 days. This scaling suggests that at low velocities relative to the steady state value, the near surface may be more resilient to additional shaking perturbations.

Using this fitted exponential relationship, we build a synthetic seismic velocity time-series. We measure all the velocity drops in the data, and calculate their recovery timescale with their pre-drop velocity levels, and superpose them linearly, creating one time-series with multiple relaxations. Even if this synthetic time-series does not directly fit the full measured dataset, there is a good overall agreement (Fig. 5.2c), in contrast to a synthetic velocity time series calculated with a constant recovery time scale, as previously used (Illien, Sens-Schönfelder, et al., 2022) (Fig. 5.5). The remaining offsets between the data and the synthetic time-series (particularly visible in the 2012-2014 period) can be attributed to the limitation of the temperature correction, a new persistent velocity base level following the Tocopilla earthquake or a draw-down in the Atacama groundwater levels (Viguier et al., 2019), which could affect the velocity changes (Clements & Denolle, 2018; Illien et al., 2021).

5.4 Which physics for near-surface earthquake damage ?

Our observations suggest that the timescale of seismic velocity recovery at a site can be predicted from the known pre-drop velocity. This feature is not directly tied to existing physical equations for relaxation. Most existing physical and conceptual models associate the relaxation dynamics to a 'state variable' representing the dynamics of a type of contacts

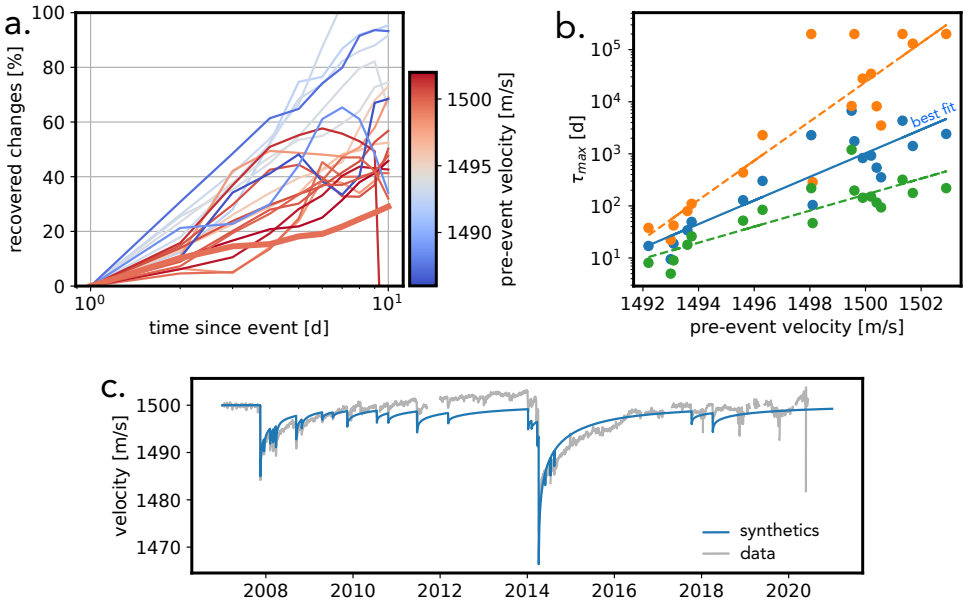

Figure 5.2: *Pre-drop velocity level as a control for the relaxation timescale and corresponding synthetic time-series.* **a.** Recoveries after multiple seismic events, normalised by the amplitude of the drop. The colour indicates the velocity value before the onset of the drop. The thick line shows the early average recovery observed after the Tocopilla and Iquique main shocks. **b.** Fitted maximum recovery timescales on the recoveries shown on plot **a** (n=17). The blue line shows the best fitting exponential scaling. The orange and green data and corresponding fits were obtained using ± 10% of the variance of the best fitting recovery timescale values for all events. **c.** The synthetic velocity time-series built with the superposition of relaxations obtained with the relationship fitted on plot **b**. The grey line indicates the original data.

or voids undergoing deformation. In these frameworks, the evolution of the variable of interest (here taken as dv/dt) is a direct function of the variable itself ($v(t)$). For instance, this is the case in the rate and state friction framework (Dieterich, 1979) and studies that involve contact dynamics (Aharonov & Scholz, 2018) and creeping mechanisms to fit relaxation data (Ostrovsky et al., 2019; S. Y. Wang et al., 2021). Field studies often test such models based on one relaxation event. Our dataset, comprising 17 consecutive drop-and-recovery cycles does not not support this state variable approach. Importantly, the phase portrait showing the relationship between the rate of velocity change dv/dt against the velocity $v(t)$ shows very different phase locations after each seismic event (Fig 5.6) e.g. the same state velocity $v(t)$ can have different rates of variation dv/dt. Hence, a revision of theory is required.

Yet, we suggest that a state variable argument can be reconciled with our observations. In the field, seismic velocity measurements probe a subsurface volume that contains many types of contacts and flaws (Snieder et al., 2016; Shokouhi et al., 2017; Sens-Schönfelder et al., 2019b). We assume that all of these structures obey their own state variable equations that determine their timescales of relaxation. For instance, crack populations can be defined by their aspect ratios, which determine their times of closure under a specific load (Budiansky et al., 1982; Meyer et al., 2021). We use a generic state variable model (Materials and methods) that can characterise different processes, each with their

own timescale (Fig. 5.3a). The simple superposition of all population dynamics yields a synthetic time-series with the same features as our seismic velocity observations : A logarithmic recovery of velocity after each drop at a rate dependent on the pre-drop velocity (Fig. 5.3bc). Therefore, the superposition of different timescales in a sequence of perturbations can reproduce the dynamics we observe in this study (Fig. 5.3).

The contribution of several populations of characteristic contacts is key to reconciling observations and physics. At the reference velocity value (in our study around 1500 m/s), all contacts are at steady state and the system does not evolve. When all contacts are disturbed, they enter a metastable state and recover at different rates. As the general reference velocity is approached, only the contact populations with the longest recovery times remain activated, while populations with a faster recovery have stabilized (Fig. 5.3).

Robust knowledge of the recovery timescale of the subsurface allows an assessment of the feasibility and timeliness of reconstruction after large earthquakes. It may also allow an estimation of the propensity to failure of steep topographic slopes in an earthquake epicentral area. This can reduce lingering post-seismic risk, and minimize spurious investment. We propose that by measuring the rate of velocity changes over a period immediately after an episode of strong ground motion, one can support an estimation of the recovery of substrate damage over a much longer period of up to years. Fundamentally, this can be done using measurements from small seismic events, and then upscaled for larger scenarios. The early observation of universal slow dynamics in the lab showed that the perturbation was not influencing the timescale of recovery (TenCate et al., 2000). Our study suggests that this is valid for large earthquakes and that the medium mechanical properties control the relaxation behaviour while the ground shaking intensity only controls the amplitude of the observation. If this is the case in near-surface geomaterials, then it may also be valid for man-made structures. Understanding the link between specific types of flaws and relaxation timescales can lead to a targeted material test for management of the response to damage.

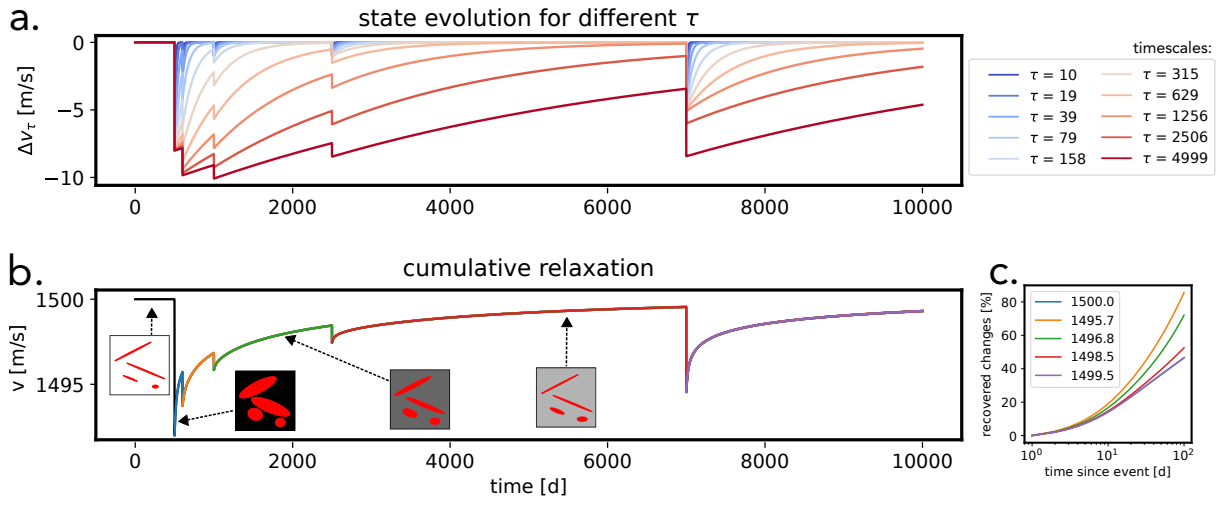

Figure 5.3: *Superposition of different state variables dynamics and average relaxation* **a.** Each curve shows the evolution of a hypothetical state variable that contain one fundamental timescale. The timescales are shown in the legend. **b.** Average evolution of all state variables shown in **a**. The schematics indicate different types of cracks/voids with different closure times corresponding to different state variables in the plot **a**. The background colour indicate the relaxation of the stress state in the bulk.

5.5 Supplementary materials to paper IV

5.5.1 Materials and Methods

Seismic Interferometry: We compute the 6 self-correlations (EE, NN; ZZ, EN, EZ, NZ) of the PATCX station after filtering the traces in the 3-6 Hz band. Daily cross-correlations are extracted with a pre-processing scheme fully described in Illien, Sens-Schönfelder, and Ke (2022) (Chapter 4). To measure the velocity changes, the stretching technique (Sens-Schönfelder & Wegler, 2006) is applied in the 7 to 16 seconds window of the daily correlation functions. The full method for averaging the 6 self-correlations is detailed in Chapters 3 and 4.

Measurement of $\tau_{\max}$: We use the expression of Snieder et al. (2016) to find the maximum relaxation timescale $\tau_{\max}$, which controls the duration of the recovery phase after earthquakes:

$$R(t) = \int_{\tau_{\min}}^{\tau_{\max}} \frac{1}{\tau} e^{-(t-t_0)/\tau} \, \mathrm{d}\tau. \tag{5.1}$$

From equation (5.1), one can see that function $R(t)$ is therefore a superposition of exponential recoveries characterised by timescales τ. From a previous study at the Patache field site (Illien et al., 2022, Chapter 4), we know that the minimum relaxation timescale $\tau_{\min}$ is inferior to one day, the time resolution of the retrieved velocity time-series of this study. Fixing $\tau_{\min}$ to this time resolution, we scale $R(t)$ to the velocity measurements and find the best fitting $\tau_{\max}$.

We first quantify the relaxation time of the Iquique and Tocopilla earthquakes, assuming from Figure 5.1d that both earthquakes are followed by the same recovery timescale. Therefore, we average the first 1000 days of relaxation of both time-series (Fig. 5.4a) and interpolate the resulting recovery on a logarithmic x-axis. The latter step gives an equal weight to the early relaxation times in the fitting process. Finally, we fit and scale the expression $R(t)$ and obtain a best fitting value of $\tau_{\max} = 3887$ d.

For each aftershock-induced recoveries, $\tau_{\max}$ was obtained by fitting the first 10 days of relaxation (Fig. 5.4b) without the interpolation step. We also report the $\tau_{\max}$ values corresponding to $\pm$ 10% of the variance of the best fitting value (orange and green lines in Figure 5.2b).

Temperature-correction: We first quantify the phase of the periodic temperature (taken at the Iquique airport, 30 km from the station) and dv/v seasonal variations. To approximate a periodical variation, we calculate the average temperature and velocity cycle by stacking the yearly temperature and dv/v time-series and fitting the average stack with a sinusoidal function (Figure 5.7). The fitting of the velocity data yields a first empirical correction of the thermal-induced velocity changes (red line in Fig. 5.9). The phase lag between the temperature and the velocity is equal to $\sim$ 19.5 days.

We assume that the velocity changes originate from the thermal strain observed at one depth z due to thermal diffusion in a subsurface layer of thermal diffusivity κ. For a periodic temperature oscillation at the surface (of period ω), the phase lag for the temperature T at depth z can be retrieved with the following equation (Turcotte & Schubert, 2014):

$$T = T_0 + \Delta T \exp\left(-z\sqrt{\frac{\omega}{2\kappa}}\right) \cos\left(\omega t - z\sqrt{\frac{\omega}{2\kappa}}\right). \tag{5.2}$$

In this relation, one can see that the phase lag is equal to $-z\sqrt{\frac{\omega}{2\kappa}}$. From the phase difference calculated before and after setting the period ω to one year, we obtain the value of the ratio $z^2/2\kappa$, which determines the system. Assuming now a generic thermal diffusivity of $\kappa = 1.10^{-2}$ cm^2/s, we can model the velocity changes from the temperature observed at the characteristic depth of the ratio ($z = 1.25$ m). Plugging these values in a 1D thermal diffusion numerical simulation (computed with a forward Euler scheme) and using the surface temperature time-series (Fig. 5.8a), we obtain the temperature depth profiles shown in Figure 5.8b. We extract the temperature at depth $z = 1.25$ m and scale it to the velocity changes through a factor α, which represent the expansion coefficient of the rocks in the subsurface. This scaling is done on the velocity data of 2007 prior to the Tocopilla earthquake. The velocity time-series from this simulation is shown in Figure 5.9a.

The retained temperature model for the paper is taken as the average between the two modeled dv/v time-series (Fig. 5.9a). Indeed, we combine the best of both corrections as **1.** the numerical correction is based on the temperature time-series and may have the best correction for the phase of the temperature-induced velocity changes and **2.** the amplitudes of the velocity changes is more consistent with the sinusoidal correction.

Building a state variable model: We look for an equation that is homogeneous to the velocity changes and choose a form that is mathematically viable with the logarithmic evolution of the recovery. A general equation for the velocity variations dv/dt can be expressed as

$$\frac{dv}{dt}(t) = A \exp\left[-Bv(t)\right] - C \tag{5.3}$$

where A, B and C are constants with A and C having the same dimension than dv/dt. Taking $A = C$, we can simplify this expression such as

$$\frac{dv}{dt}(t) = A \left(\exp\left[-Bv(t)\right] - 1\right). \tag{5.4}$$

Note that the expression (5.4) has the same form than an Arrhenius equation (Snieder et al., 2016), classically used to model thermal-induced processes and creep rates. Based on the dimension of the constant A, we further parametrise (5.4) to highlight a timescale τ:

$$\frac{dv_\tau}{dt}(t) = \frac{v^*}{\tau}\left(\exp\left[-\frac{v_\tau(t) - v_\infty}{v^*}\right] - 1\right), \tag{5.5}$$

in which v_∞ is the steady state velocity value in the absence of earthquakes, v^* is a characteristic velocity and v_τ is the velocity associated with a certain relaxation time τ. We consider several contacts or flaws with different characteristic timescales τ, which affect the velocity changes. The total observed velocity change $v(t)$ is a function of these voids. The contribution of each v_τ to the total observed velocity changes $v(t)$ depends on the density of the associated voids/contacts and their respective sizes. For the sake of simplicity, we take in this paper the average of all v_τ dynamics present in the system:

$$v(t) = \frac{1}{N}\sum_{i=1}^{N} v_{\tau_i}(t) \tag{5.6}$$

To show the logarithmic evolution of our framework, we now derive the expression of the solution of (5.5) for initial condition $v_0 = v_\tau(0) < v_\infty$, and denote by $\Delta = v_\infty - v_0$ the size of the initial velocity drop. Letting $w(t) = \exp(-(v_\tau(t) - v_\infty)/v^*)$, there holds

$$\frac{dw}{dt}(t) = -\frac{1}{v^*}\frac{dv_\tau}{dt}(t) \times w(t) = -\frac{1}{\tau}(w(t)-1) \times w(t) \tag{5.7}$$

which in turn yields

$$\int_0^t \frac{dw}{w(w-1)} = -\int_0^t \frac{dt}{\tau} = -\frac{t}{\tau}. \tag{5.8}$$

The LHS of the above display can be expressed as

$$\int_0^t \frac{dw}{w(w-1)} = \int_0^t \left(\frac{1}{w-1} - \frac{1}{w}\right) dw = \left[\log\left(\frac{w-1}{w}\right)\right]_0^t = \log\left(\frac{w(0)(w(t)-1)}{(w(0)-1)w(t)}\right) \tag{5.9}$$

Letting $\xi_0 = (w(0)-1)/w(0)$, we finally find that $w(t)-1 = \xi_0 e^{-t/\tau} w(t)$, which immediately gives $w(t) = (1-\xi_0 e^{-t/\tau})^{-1}$. Expressing w back as a function of v_τ finally yields

$$v_\tau(t) = v_\infty - v^* \log\left(1 - (1 - e^{-\Delta/v^*})e^{-t/\tau}\right). \tag{5.10}$$

5.5.2 Supplementary Figures

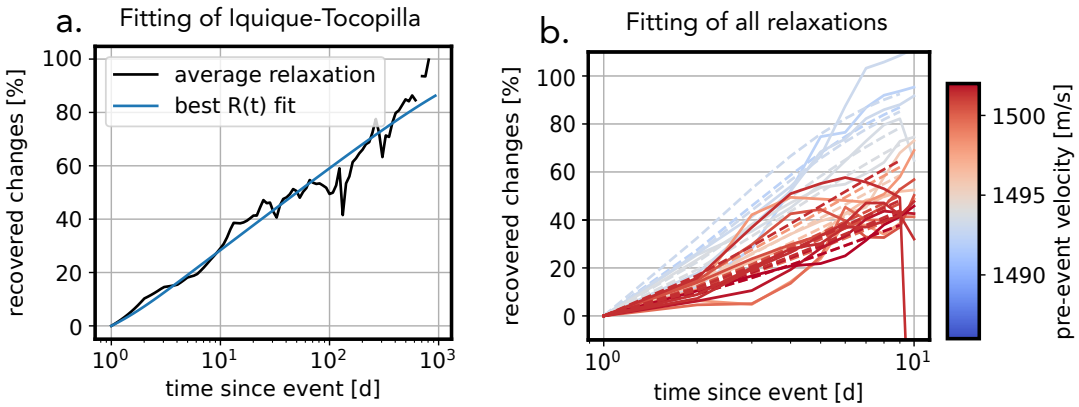

Figure 5.4: *Fitting of recoveries with the relaxation function R(t)* **a.** The black line shows the interpolated average velocity recovery observed after Tocopilla and Iquique earthquakes. The blue line shows the best $R(t)$ fit with $\tau_{\max} = 3887$ d. **b.** Fitting of all aftershocks-induced recoveries. The dashed lines indicate the fits. The pre-event velocity before the earthquakes are indicated in colours.

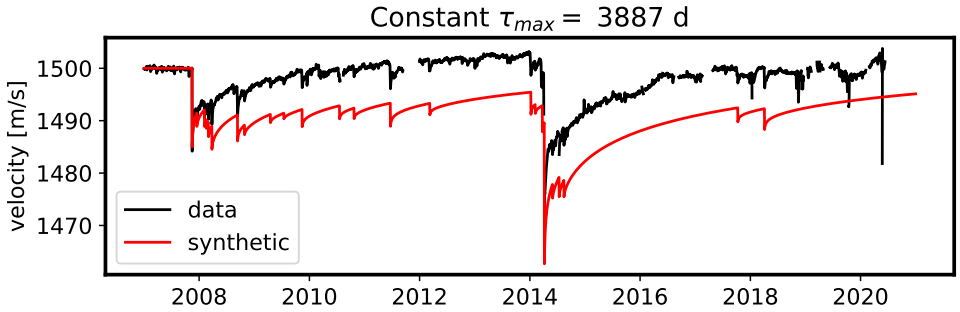

Figure 5.5: *Synthetic seismic velocity changes built with constant relaxation timescale.* The red line shows the superposition of relaxation functions 5.1, all characterised by the same timescale $\tau_{\max}$ (taken as 3887 d, the value fitted for the Iquique and Tocopilla recoveries). Note the limited agreement between the data (black line) and the model (red line) when using this assumption.

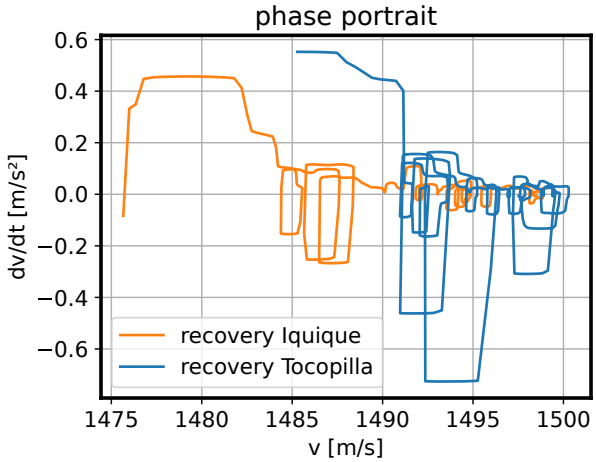

Figure 5.6: *Phase portrait of the velocity changes observed after the Tocopilla and Iquique earthquakes.* Both lines were computed for the two recoveries shown in Figure 5.1c. The derivative dv/dt was obtained using the total-variation regularisation method (Chartrand, 2017).

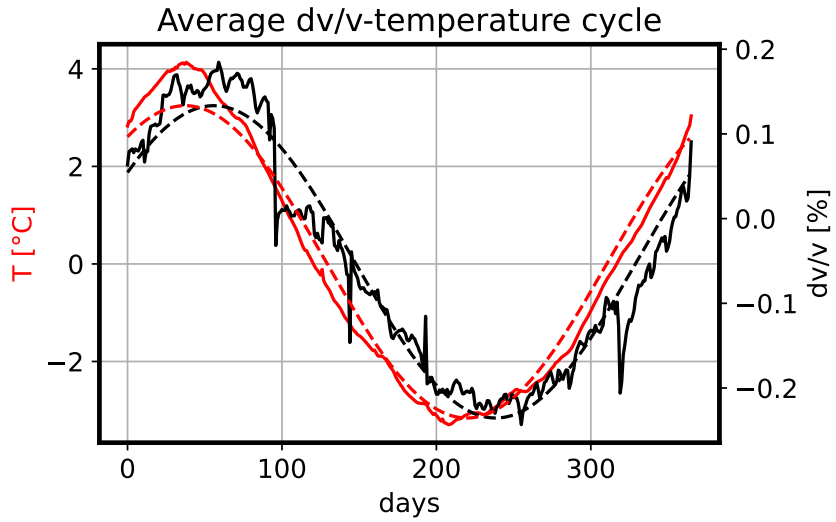

Figure 5.7: *Average annual cycle of surface temperature and dv/v variations in Patache, Chile.* The red solid curve indicates the average relative temperature variation of the surface temperature time-series (shown in figure 5.8a). The solid black line shows the annual average for the dv/v variations. Both dashed lines correspond to the sinusoidal fits of the data.

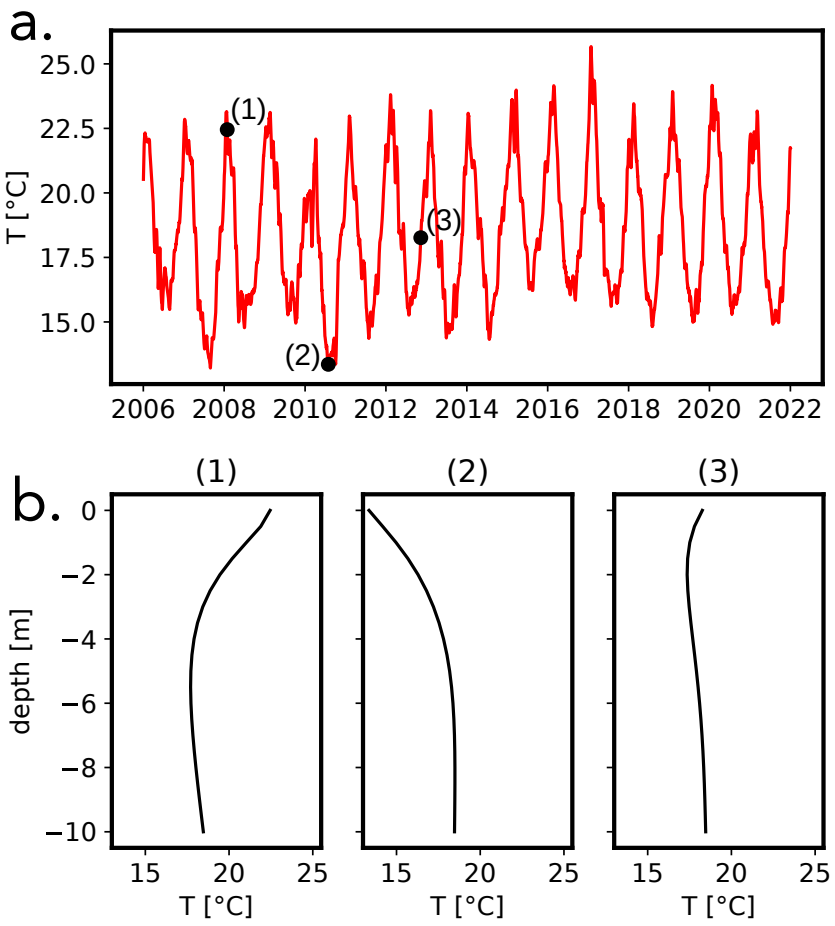

Figure 5.8: *Numerical simulation of the temperature diffusion under the seismic site.* The plot in **a.** shows the temperature time-series used in this study to construct the dv/v models. The numbers indicate different dates for which the modelled temperature depth-profiles are shown on the plot **b**.

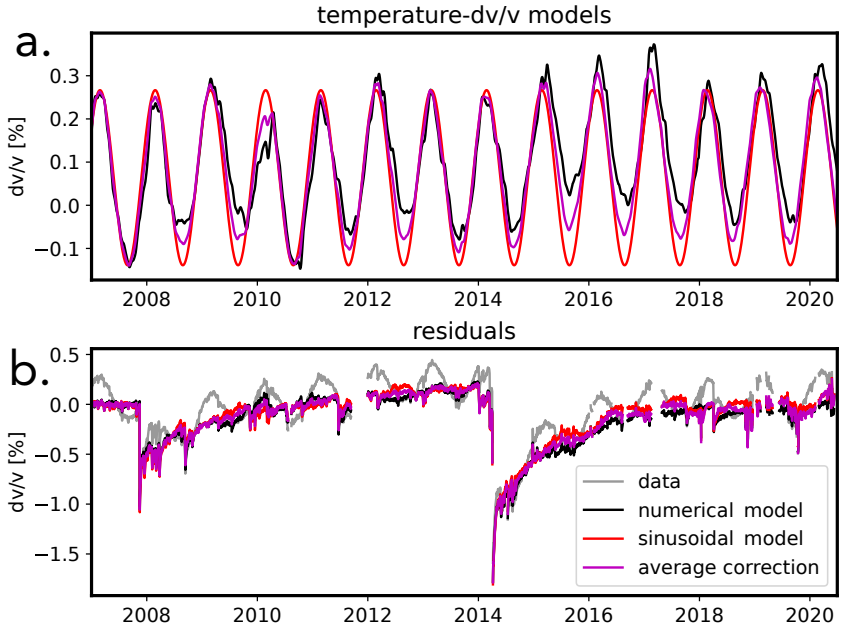

Figure 5.9: *Temperature-induced dv/v models* **a.** The solid lines show the different models for correcting the velocity changes due to surface temperature variations. The legend for the colours are indicated on the lower plot. **b.** The coloured lines indicate the residuals of the data after correction by the models shown on plot **a**. The raw data is indicated in gray.

Chapter 6

Conclusions

This dissertation has taken us on a journey from the monsoon-drenched Nepal Himalayas to the seismically active Atacama desert. I explored the time-dependent evolution of the shallow subsurface of these environments, constrained its key forcings and tracked its dynamics with seismic ambient noise.

In Chapter 2, **I highlighted the important role of subsurface moisture saturation in modulating groundwater recharge and discharge generation** in a steep Himalayan catchment. I estimated relative seismic velocity changes to constrain the groundwater dynamics and combined this analysis with hydrological, meteorological and geochemical observations and modelling. An annual hydrological cycle with four stages was demonstrated. During the pre-monsoon season, precipitation is not recharging groundwater but rather the superficial moisture reservoir. When moisture in the vadose zone reaches saturation, monsoon rainfalls are efficiently converted into river discharge. Towards the end of the wet season, the groundwater and the subsurface moisture drop due to precipitation waning, gravitational loss to the stream and upward loss due to plant transpiration. As a new dry season commences, runoff and groundwater drainage continue to drop while the surface moisture is low and vegetation activity ceases. These results show that the soil layer and the dynamics in the unsaturated zone, often overlooked in steep landscapes, are particularly important for modulating hydrological fluxes in mountain landscapes. With the forecasted growth of the population relying on the runoff generated in Himalayan basins (Viviroli et al., 2020; Yao et al., 2021), understanding the effect of land use change and potential changes in precipitation annual distribution will be socially relevant . The modelling in Chapter 2 also showed that processes in the unsaturated zone must be taken into account in future seismic interferometry studies, especially when monitoring shallow layers with high frequency signals (4-8 Hz in the study).

The Himalayan 'water towers' are built through tectonic forces that generate earthquakes, which can in turn perturb the time-dependent subsurface properties through ground shaking. In Chapter 3, I used the groundwater model developed in Chapter 2 to correct the velocity changes for the hydrological effects in order to **investigate the long-lasting impact of the 2015 M_w 7.8 Gorkha earthquake** at the same monitored field site. I found that the velocity recoveries induced by the main shock and its aftershocks can be fitted with a single relaxation timescale (with the best fit at $\tau_{\max} = 250$ days), regardless of the initial peak ground velocity. Therefore, the relaxation behaviour may exclusively be a function of the medium properties rather than the ground shaking characteristics. When looking at the residuals of the relative seismic velocity changes obtained after substracting the effect of seismic damage and groundwater storage, I constrained an additional timescale of $\sim$6 months which I attributed to an enhanced permeability in the monitored aquifer caused by the main shock. Because most of studies are focusing on either the impact of earthquake damage or groundwater variations, I encourage a more integrated look at seismic velocity changes to catch these potential interacting effects. Overall, the interferometry results suggest that the combined sustained subsurface effect of the Gorkha earthquake lasted for $\sim$1 year, a duration similar to the transient increase of landslide rates observed in the area (Marc et al., 2019), validating the use of seismic ambient noise to monitor the landscape hydro-mechanical properties (Marc et al., 2021).

Groundwater and moisture dynamics impact the relative velocity changes and make the study of earthquake damage in settings with significant rainfall, complex and challenging. To isolate the impact of seismic ground shaking on time-dependent subsurface properties, my research focus shifted to the arid Atacama desert in Chile, a seismically active area but with a steady, arid climate. In Chapter 4, **I constrained the velocity drop and recovery behavior induced by moderate ground shaking at a sub-hourly time resolution and the subsurface structure hosting these dynamics**. I tested the ergodic property of the estimation of the seismic velocity changes from ambient noise correlations with 16 co-located stations. This allowed me to decrease the required time-averaging duration of the correlation functions, essential for retrieving stable velocity changes. To do so, I replaced the time-averaging with a space-averaging over all the stations to compute a well-resolved dv/v time-series with a 10-minutes resolution. I found that the amount of seismic data (long chunks at the same station or short chunks at several stations) used in the interferometry process is the key controlling factor for the signal to noise ratio in the dv/v. The technique allowed the observation of a 0.4% velocity drop induced by an event with $\sim$1 cm/s of PGV and the subsequent recovery that was recovered to 50% of its initial drop value after two days. The recovery plotted on a continuous log-linear slope during the monitored period. In a second step, I used the focal spot imaging technique and a transdimensional Bayesian inversion to estimate the 1D shear-velocity profile. Importantly, this analysis shows that the observed relaxation behaviour did not occur in near-surface soils but instead in hard rocks with a surface layer of $V_S \sim 1500$ m/s.

The time-dependent changes at the focus of Chapter 4 are a small piece of a larger damage and recovery cycle induced by successive subduction earthquakes in Chile. In the final research chapter of this dissertation, **I addressed the predictability of the relaxation timescales induced by these multiple seismic events**. I processed 13 years of ambient noise data at the station PATCX , which is one of the 16 stations used in Chapter 4. After correcting for seasonal thermal strain variations, I analysed the velocity drop and recovery induced by the 2007 7.7 Mw Tocopilla and the 2014 8.3 Mw Iquique earthquakes and their aftershocks. When normalised by the amplitude of the initial velocity drop, both long-term recoveries collapse on the same line, suggesting that a constant relaxation timescale is at play, analogous to the finding in Chapter 3. I further investigated the recoveries of all aftershocks and showed that the initial velocity level before the drop onset controls the timescale of relaxation. I tentatively attributed this dynamics to the superposition of different populations of voids and contacts in the subsurface. Each of these populations can be modelled with a classic state variable equation, similar to friction or contact dynamics. In essence, the relaxation dynamics are a function of the medium, rather than the initial strain perturbation. This conclusion supports the preliminary results of Chapter 3 and has important consequences not only for the prediction of earthquake damage, but also for material science and the monitoring of man-made civil structures.

Chapter 7

Synthesis

In this Chapter, I synthesize the new avenues and future work related to my doctoral research (Chapter 2 to 5) and more generally to seismic interferometry (abbreviated as SI).

7.1 Coupled dynamic subsurface properties and internal parameters

The evolution of relative seismic velocity changes as a probe into subsurface properties integrates thermomechanical and hydrological processes. It is rather tempting to express the velocity changes δv as a simple linear system such as:

$$\delta v = \delta v_{\mathrm{H}} + \delta v_{\mathrm{EQ}} + \delta v_{\mathrm{T}}, \tag{7.1}$$

where δv_{H}, δv_{EQ} and δv_{T} are the changes respectively induced by hydrology, earthquake damage and temperature variations. This approach has been taken in most of this dissertation but as suggested in Chapter 3, these components are not independent. Common frameworks to link the non-linear interactions between these effects are lacking but a few directions can be envisioned.

7.1.1 A physical framework to link the variations

With SI, I investigated the relaxation (or slow dynamics) phenomenon in the Earth's subsurface induced by co-seismic ground shaking (δv_{EQ} in eq. 7.1). This topic is not only of interest for geophysicists but important to different branches of material science and civil engineering: Damage induced by earthquakes are not only sustained by the subsurface but also in man-made structures (Astorga et al., 2018). In Chapter 5, the suggested predictability of slow dynamics through an empirical approach questions the relevance of finding a unified physical description of the phenomena across materials and scales. I argue that this pursuit is relevant as a physical description would allow to link δv_{EQ} to specific transient surface observations (landslides, permeability, stream discharge ...) and the hydrological component δv_{H}. Moreover, it may eventually permit human manipulation of slow dynamics and the design of more resilient materials.

Slow dynamics and transient permeability are the expression of the behaviour of different types of contacts and voids embedded in volumetrically deforming bulks (from granular assemblies to crystalline rocks). The wide variety of these contact and bulk types suggests that a universal physical equation for relaxation and its effects may be out of reach. I propose that some alternatives could be derived.

A first approach into which different contact physics can be 'plugged in' would be a first step. In Chapter 5, I modelled seismic velocity time-series using a generic differential equation with a state variable (eq. 5.5). This type of equation can be parametrised to represent different types of processes (friction, creep, dislocation in the bulk ...) and key structural parameters (contact length scale, material properties, deformation boundary conditions ...). The challenge of this approach is to scale up the contributions and interactions of multiple types of contact populations and dynamics in a representative

volume. New numerical methods such as the combined finite-discrete element method (K. Gao et al., 2019; Rougier et al., 2020) may integrate the dynamics at the contact scale and in the bulk. Another original scheme includes the effective medium approach in which voids (called inclusions in the method) are incrementally added in the representative bulk (Zimmerman, 1996; Brantut et al., 2019). Finally, energy-based approaches are viable and have the advantage of making fewer assumptions regarding the material mechanics (Lieou et al., 2017). These methods would allow to implement the influence of temperature and study the interaction between the δv_{EQ} and δv_{T} components. However, the transition from mechanical parameters to meaningful thermo-dynamical variables requires theoretical developments, which need to be experimentally validated.

7.1.2 Water and internal structures

If the subsurface porosity is responsible for slow dynamics, it is also the host of water underground. An interesting interaction, yet barely explored so far, is the role of moisture and groundwater in modulating the postseismic recovery. On the one hand, we have learnt from Chapter 3 and other studies (Xue et al., 2013; Shokouhi et al., 2020) that the relaxation phenomenon induces a change in hydraulic properties. On the other hand, water influences processes that may be involved in relaxation (Bittner & Popovics, 2019, 2021). Examples include fundamental chemical reactions at the contact scale (Sakuma et al., 2018) or in microcracks (Brantut, 2015) and modulation of friction. These effects have been touched upon in the laboratory but not in field studies. As illustrated in Chapter 2, the wetness of the subsurface is highly time-dependent. *Is the pace of relaxation modulated by varying water content ?* Certainly, this question can be addressed at field sites with high hydrological variability and regular seismicity, similar to the Bothe Koshi catchment described in my Nepalese studies.

The presence of these coupled processes, which influence δv, is therefore dependent on the internal void structures specific to the probed geomaterial. In the subsurface sampled with SI, one faces the problem that the characterisation of the rocks and their internal structures and water content is often limited. For the sole case of groundwater, identifying and separating the reservoirs controlling the δv_{H} and possibly its impact on relaxation is challenging. This is illustrated in Chapter 2, in which the velocity changes were not linked to soil moisture dynamics in the 4-8 Hz frequency band. However, the recent study of Oakley et al. (2021) showed a clear correlation with soil moisture measurements with higher frequency bands (up to 100-200 Hz). I present possible tools to disentangle the hydrological reservoirs at a later point of the synthesis (section 7.3.1).

The water content and void space characterisation are only the first parts of the subsurface dynamics puzzle. These internal variables are dependent on external forcings.

7.2 External forcing of the subsurface: timing and amplitudes

The temporal distribution and amplitudes of external forcings such as precipitation or peak ground shaking can significantly change the average dynamics of the subsurface system. In the Bothe Koshi catchment, I showed that the precipitation history is a first order control for mediating the onset of the subsurface saturation and therefore the deeper groundwater recharge. This saturation determines two distinct hydrological regimes defined in Chapter 2 (coupled and uncoupled), which are likely to play a part in recent hydrological questions.

For instance, the identification of the reservoir and quantification of the volume used by transpiration (the 'biological pump') are major research lines (Evaristo et al., 2015). By using different seismic frequencies, one may monitor different spatial scales and therefore track different depths and hydrological pathways and their incoming and outgoing fluxes. Recent geochemical insights suggest that the water extracted by plants comes from a reservoir that is disconnected from the one generating discharge (Evaristo et al., 2015). Following my study presented in Chapter 2, I argue that this partitioning may actually depend on the moisture volume in the the subsurface. In the pre-monsoon season, the shallow moisture and groundwater reservoirs were indeed decoupled. Nevertheless, the plant activity, tracked with NDVI, played a crucial role in modulating the duration of the moisture build-up towards the saturated stage observed during monsoon. This shows, that even when decoupled, plants modulate the cycle of groundwater recharge. In the monsoon stage, I directly attributed the fast drainage of groundwater to a joint effect of gravity and transpiration, as suggested in other studies (Doody & Benyon, 2011; Koirala et al., 2017). In its details, the partitioning of water and the separation of plant transpiration from other hydraulically connected reservoirs seems to be time-dependent, with possible intricacies due to the depth reach of the ecosystem. With more constraints, SI has the potential ability to probe these effects without perturbing the fragile soil architecture, and affecting the observable in the process. With the increasing threats to water security due to climate change, advancing our knowledge about the water pathways in the shallow subsurface will be paramount.

Similar to precipitation, seismic ground shaking also modifies the subsurface system due to modulation of dynamic strain. In chapter 5, I showed the predictability of the associated non-linear recovery in near-surface geomaterials and its log-linear functional form across several timescales (from a few minutes to years), in accordance with laboratory experiments. Notably, I found that the amplitude of the dynamic strain perturbation controls the amplitude of the material changes (Chapters 3, 4) but is not impacting the timescale of relaxation. Therefore, the recovery behaviour may be determined only by internal medium properties rather than external forcings, which suggests that a material test may be designed in the future, enabling the forecast of near-surface resilience after earthquakes. This capability may only be enabled in dry environments with low hydrological variability as Chapter 4 and 5 were conducted in the Atacama desert.

A fundamental temporal scale has not been investigated in this thesis. Seismic velocity does not drop instantaneously during ground shaking. In fact, the behaviour of materials during strain perturbation exhibits its own time-dependence, in a phase often called fast dynamics (as opposed to 'slow'). This initial damage phase has been recently shown to be correlated with the succeeding relaxation in controlled experiments (Scalerandi et al., 2019). Consequently, the joint analysis of both stages could bring forward new insights into damage evolution due to ground shaking and subsequent healing. There are a few time-dependent observations of the fast damaging phase based on deconvolution of teleseismic arrivals in borehole arrays (Nakata & Snieder, 2011; Bonilla et al., 2019). These studies highlight a progressive drop of seismic velocity proportional to the evolution of the peak dynamic strain, with the onset of a recovery behaviour already occurring before the end of the perturbation (S. Y. Wang et al., 2021). The nature of the wavefield sampling the subsurface during this phase (often seismic waves from the earthquake itself) may be different from the noise wavefield used to observe the relaxation, which makes the fast and slow stages difficult to link physically using SI alone and begs for new ways of monitoring the subsurface.

7.3 Future complementary approaches to seismic interferometry

7.3.1 Better constraints with forward modelling

The monitoring of freshwater resources with SI techniques is now beyond the proof of concept stage with other recent publications also validating the approach (Kim & Lekic, 2019b; Mao et al., 2022). However, active seismic measurements and resistivity imaging techniques still dominate the field of hydrogeophysics, with less emphasis on the time evolution aspect that SI could bring. To put seismic noise-based monitoring at the forefront, dv/v time-series need to be better constrained. Indeed, conclusions in SI studies are drawn a posteriori from seismic velocity observations without any prior expectations (inductive reasoning). A better understanding of the sensitivity of SI measurements to the dynamics of different reservoirs is key to targeted deployments and a prior reasoning, essential for testing hypothesis. I propose that hydrological studies with SI may be advanced towards this second type of reasoning through the forward computation of seismic wavefield.

This advancement would not be without significant challenges, which consist of **1.** Modelling the ambient noise wavefield while accounting for the sources dynamics and scattering regime **2.** Building a realistic elastic profile based on water storage in soils and rocks **3.** The implementation of coupled pore pressure dynamics solutions and seismic wave propagation. These tasks may be tackled with existing open-source codes dedicated to seismic wavefield modelling. For example, AxiSEM 3D (Nissen-Meyer et al., 2014; Leng et al., 2019) has recently yielded promising results for realistic wavefield simulations in complex heterogeneous structures at a relatively low computational cost (Haindl et al., 2021). With this potential modelling approach and coupled field observations, SI could bring hydrological constraints on the absolute groundwater depth and absolute volumetric storage at specific locations in a catchment. Given its ease of installation in remote areas and its non-destructive probing ability, these potential advances would benefit the study of groundwater dynamics in mountainous environments (as shown in Chapter 2).

Naturally, the joint use of wavefield forward modelling and SI is not only relevant for hydrological questions but also for constraining any dynamic processes acting in the subsurface (the other prime example being earthquake damage in this thesis).

7.3.2 Emerging monitoring tools and new processing techniques

Over the last decade, the emergence and capabilities of distributed acoustic sensing (DAS) has been a hot topic in seismology (Fenta et al., 2021). By interrogating fiber optic cables with light pulses, one can monitor tiny variations of strain at high spatial resolution. Many studies have now shown the capability of DAS to monitor subsurface sources of seismic energy such as volcanic tremors (Jousset et al., 2022) or glacier stick slip (Walter et al., 2020), and use the passive and active dynamic strain recorded by the cables for imaging subsurface structures (Jousset et al., 2018). With a frequency response that is relatively broadband (0.1 to 100 Hz in Jousset et al. (2018)), one can imagine the application of SI techniques to DAS to monitor seismic velocity changes at an unparalleled spatial resolution. A recent pilot study applied the method to monitor an aquifer (Rodríguez Tribaldos & Ajo-Franklin, 2021), and a theory for strain interferometry with DAS has now been derived (Paitz et al., 2019). If the systematic use of DAS for monitoring subsurface properties is an exciting perspective, it is associated with a few logistical difficulties. First, fiber

cables are laborious to install and maintain for long periods of time. The possibility of using existing ones from telecommunication companies is a solution but their locations may not be relevant to one's specific research questions and authorisation needs to be granted. Another problem arises due to the high amount of data generated by DAS measurements, which necessitates massive computing power for processing. These points suggest that at the moment, DAS may only be complementary to the use of seismic stations.

The other recent development for SI comes from machine learning techniques. A first realm of application encompasses the denoising of correlation functions with deep learning autoencoders (Viens & Van Houtte, 2020) and the removal of noise source variation effects from the correlation functions (Steinmann et al., 2022; Yin et al., 2022). Similar to the ergodic property I tested in Chapter 4, these techniques lead to well-resolved seismic velocity time-series that are more representative of the medium changes and with less spurious artefacts. Machine learning can also unravel hidden relationships contained in the data. The study of Kim et al. (2020) used the sequencer algorithm of Baron and Ménard (2021) to detect anomalous features in the correlation functions that may correspond to structures at the core-mantle boundary. With deep learning, one can also discover governing differential equations in time-series (Champion et al., 2019). This technique is classically employed in complex system analysis, such as in fluid dynamics (Joshua et al., 2022) but any dynamic variable can be tested in such algorithms. In Chapter 5, I plotted a simple phase portrait (dv/dt as a function of $v(t)$) of the velocity changes (Fig. 5.6). Deep learning may find an underlying phase space that describes the velocity changes and points at the right physical description of a particular seismic velocity evolution.

Last few words regarding collaborative efforts

The Earth's surface is the result of physical, chemical and biological processes. In this thesis, I merely brushed upon the inherent interdisciplinary approach that one must take to understand one of its particular systems. There has been a recent growth of critical zone observatories, intended for understanding the complex interactions in the weathered shallowest geological layers (T. White et al., 2015). The installation of seismic stations within such observatories is crucial for calibrating seismic velocity measurements and understanding the propagation of seismic waves, especially towards high frequency regimes. In return, SI has matured enough to leave the seismology community and be a part of larger interdisciplinary collaborations. Ambient seismic noise still contains an enormous amount of information about the state of the inaccessible substrate on which we live and its evolution in time. It is time to leave the nest.

References

Adhikari, L. B., Gautam, U. P., Koirala, B. P., Bhattarai, M., Kandel, T., Gupta, R. M., ... Bollinger, L. (2015). The aftershock sequence of the 2015 april 25 Gorkha-Nepal earthquake. *Geophysical Journal International*, *203*(3), 2119–2124. doi: DOI: 10.1093/gji/ggv412

Aharonov, E., & Scholz, C. H. (2018). A Physics-Based Rock Friction Constitutive Law: Steady State Friction. *Journal of Geophysical Research: Solid Earth*, *123*(2), 1591–1614. doi: DOI: 10.1002/2016JB013829

Aki, B. K. (1957). with Special Reference to Microtremors . Since the days of Wiechert and Galitzin , seismograms have chiefly been inve · stigated from the view point that they consist of successive distinguishable phases , and the travel time curves for various phases hav. *Earthquake Research Institute*, 415–456.

Albaric, J., Kühn, D., Ohrnberger, M., Langet, N., Harris, D., Polom, U., ... Hillers, G. (2021). Seismic monitoring of permafrost in svalbard, arctic norway. *Seismological Research Letters*, *92*(5), 2891–2904. doi: DOI: 10.1785/0220200470

Allen, R. B., MacKenzie, D. I., Bellingham, P. J., Wiser, S. K., Arnst, E. A., Coomes, D. A., & Hurst, J. M. (2020). Tree survival and growth responses in the aftermath of a strong earthquake. *Journal of Ecology*, *108*(1), 107–121. doi: DOI: 10.1111/1365-2745.13238

Alley, W. M., Healy, R. W., LaBaugh, J. W., & Reilly, T. E. (2002, jun). Flow and Storage in Groundwater Systems. *Science*, *296*(5575), 1985–1990. doi: DOI: 10.1126/SCIENCE.1067123

Andermann, C., Longuevergne, L., Bonnet, S., Crave, A., Davy, P., & Gloaguen, R. (2012). Impact of transient groundwater storage on the discharge of Himalayan rivers. *Nature Geoscience*(5). doi: DOI: 10.1038/NGEO1356ï

Anderson, S. P., Dietrich, W. E., Montgomery, D. R., Torres, R., Conrad, M. E., & Loague, K. (1997). Subsurface flow paths in a steep, unchanneled catchment. *Water Resources Research*, *33*(12), 2637–2653. doi: DOI: 10.1029/97WR02595

Astorga, A., Guéguen, P., & Kashima, T. (2018). Nonlinear elasticity observed in buildings during a long sequence of earthquakes. *Bulletin of the Seismological Society of America*, *108*(3), 1185–1198. doi: DOI: 10.1785/0120170289

Baechle, G., Weger, R., Eberli, G., Miami, U., & Massaferro, J.-l. (2004). SEG Int ' l Exposition and 74th Annual Meeting * Denver , Colorado * 10-15 October 2004 The role of macroporosity and microporosity in constraining uncertainties and in relating velocity to SEG Int ' l Exposition and 74th Annual Meeting * Denver , Colorad. (October), 1–4.

Baillard, C., Lyon-Caen, H., Bollinger, L., Rietbrock, A., Letort, J., & Adhikari, L. B. (2017). Automatic analysis of the Gorkha earthquake aftershock sequence: evidences of structurally segmented seismicity. *Geophysical Journal International*, *209*(2), 1111–1125. doi: DOI: 10.1093/gji/ggx081

Baron, D., & Ménard, B. (2021). Extracting the Main Trend in a Data Set: The Sequencer Algorithm. *The Astrophysical Journal*, *916*(2), 91. doi: DOI: 10.3847/1538-4357/abfc4d

Baumberger, T., & Caroli, C. (2006, may). Solid friction from stick-slip down to pinning and aging. *Advances in Physics*, *55*(3-4), 279–348. doi: DOI: 10.1080/00018730600732186

Bekele, A., Birgisson, B., Ryden, N., & Gudmarsson, A. (2017). Slow dynamic diagnosis of asphalt concrete specimen to determine level of damage caused by static low temperature conditioning. *AIP Conference Proceedings*, *1806*, 1–7. doi: DOI: 10.1063/1.4974637

Bentahar, M., Di Bella, A., Mechri, C., Montresor, S., Scalerandi, M., & Yu, X. (2020). Exploiting Slow Dynamics Effects for Damage Detection in Concrete. *Frontiers in Built Environment*, *6*(June), 1–10. doi: DOI: 10.3389/fbuil.2020.00064

Berghuijs, W. R., Hartmann, A., & Woods, R. A. (2016, mar). Streamflow sensitivity to water storage changes across Europe. *Geophysical Research Letters*, *43*(5), 1980–1987. doi: DOI: 10.1002/2016GL067927

Bittner, J. A., & Popovics, J. S. (2019). Direct imaging of moisture effects during slow dynamic nonlinearity. *Applied Physics Letters*, *114*(2). doi: DOI: 10.1063/1.5063904

Bittner, J. A., & Popovics, J. S. (2021). Mechanistic diffusion model for slow dynamic behavior in materials. *Journal of the Mechanics and Physics of Solids*, *150*, 104355. doi: DOI: 10.1016/j.jmps.2021.104355

Bodin, T., Sambridge, M., Tkalćić, H., Arroucau, P., Gallagher, K., & Rawlinson, N. (2012). Transdimensional inversion of receiver functions and surface wave dispersion. *Journal of Geophysical Research: Solid Earth*, *117*(2), 1–24. doi: DOI: 10.1029/2011JB008560

Bonilla, L. F., Guéguen, P., & Ben-Zion, Y. (2019, feb). Monitoring coseismic temporal changes of shallow material during strong ground motion with interferometry and autocorrelation. *Bulletin of the Seismological Society of America*, *109*(1), 187–198. doi: DOI: 10.1785/0120180092

Bontemps, N., Lacroix, P., Larose, E., Jara, J., & Taipe, E. (2020). Rain and small earthquakes maintain a slow-moving landslide in a persistent critical state. *Nature Communications*, *11*(1), 1–10. doi: DOI: 10.1038/s41467-020-14445-3

Bookhagen, B., & Burbank, D. W. (2010, sep). Toward a complete Himalayan hydrological budget: Spatiotemporal distribution of snowmelt and rainfall and their impact on river discharge. *Journal of Geophysical Research: Earth Surface*, *115*(3). doi: DOI: 10.1029/2009JF001426

Bosserelle, A. L., Morgan, L. K., & Hughes, M. W. (2022). Groundwater Rise and Associated Flooding in Coastal Settlements Due To Sea-Level Rise: A Review of Processes and Methods. *Earth's Future*, *10*(7), e2021EF002580. doi: DOI: https://doi.org/10.1029/2021EF002580

Brantut, N. (2015). Time-dependent recovery of microcrack damage and seismic wave speeds in deformed limestone. *Journal of Geophysical Research: Solid Earth*, *120*(12), 8088–8109. doi: DOI: 10.1002/2015jb012324

Brantut, N., Garagash, D. I., & Noda, H. (2019). Stability of Pulse-Like Earthquake Ruptures. *Journal of Geophysical Research: Solid Earth*, *124*(8), 8998–9020. doi: DOI: 10.1029/2019JB017926

Brenguier, F., Campillo, M., Hadziioannou, C., Shapiro, N. M., Nadeau, R. M., & Larose, E. (2008, sep). Postseismic relaxation along the San Andreas fault at Parkfield from continuous seismological observations. *Science (New York, N.Y.)*, *321*(5895), 1478–81. doi: DOI: 10.1126/science.1160943

Brenguier, F., Campillo, M., Takeda, T., Aoki, Y., Shapiro, N. M., Briand, X., ... Miyake, H. (2014). Mapping pressurized volcanic fluids from induced crustal seismic velocity drops. *Science*, *345*(6192), 80–82. doi: DOI: 10.1126/science.1254073

Brunello, C. F., Andermann, C., Helle, G., Comiti, F., Tonon, G., Tiwari, A., & Hovius, N.

(2019, jul). Hydroclimatic seasonality recorded by tree ring δ18O signature across a Himalayan altitudinal transect. *Earth and Planetary Science Letters*, *518*, 148–159. doi: DOI: 10.1016/J.EPSL.2019.04.030

Brunello, C. F., Andermann, C., Marc, O., Schneider, K. A., Comiti, F., Achleitner, S., & Hovius, N. (2020). Annually resolved monsoon onset and withdrawal dates across the Himalayas derived from local precipitation statistics. *Geophysical Research Letters*. doi: DOI: 10.1029/2020GL088420

Brutsaert, W., & Nieber, J. L. (1977). Regionalized drought flow hydrographs from a mature glaciated plateau. *Water Resources Research*, *13*(3), 637–643. doi: DOI: 10.1029/WR013i003p00637

Budiansky, B., Hutchinson, J. W., & Slutsky, S. (1982). Void Growth and Collapse in Viscous Solids. In H. G. HOPKINS & M. J. SEWELL (Eds.), *Mechanics of solids* (pp. 13–45). Oxford: Pergamon. doi: DOI: https://doi.org/10.1016/B978-0-08-025443-2.50009-4

Budi-Santoso, A., & Lesage, P. (2016). Velocity variations associated with the large 2010 eruption ofMerapi volcano, Java, retrieved from seismic multiplets and ambient noise cross-correlation. *Geophysical Journal International*, *206*(1), 221–240. doi: DOI: 10.1093/gji/ggw145

Canadell, J., Jackson, R. B., Ehleringer, J. B., Mooney, H. A., Sala, O. E., & Schulze, E.-D. (1996, dec). Maximum rooting depth of vegetation types at the global scale. *Oecologia*, *108*(4), 583–595. doi: DOI: 10.1007/BF00329030

Carrard, N., Foster, T., & Willetts, J. (2019). Groundwater as a Source of Drinking Water in Southeast Asia and the Pacific: A Multi-Country Review of Current Reliance and Resource Concerns. *Water*, *11*(8). doi: DOI: 10.3390/w11081605

Champion, K., Lusch, B., Nathan Kutz, J., & Brunton, S. L. (2019). Data-driven discovery of coordinates and governing equations. *Proceedings of the National Academy of Sciences of the United States of America*, *116*(45), 22445–22451. doi: DOI: 10.1073/pnas.1906995116

Chartrand, R. (2017). Numerical differentiation of noisy, nonsmooth, multidimensional data. In *2017 ieee global conference on signal and information processing (globalsip)* (p. 244-248). doi: DOI: 10.1109/GlobalSIP.2017.8308641

Chen, J., Famigliett, J. S., Scanlon, B. R., & Rodell, M. (2016). Groundwater Storage Changes: Present Status from GRACE Observations. In A. Cazenave, N. Champollion, J. Benveniste, & J. Chen (Eds.), *Remote sensing and water resources* (pp. 207–227). Cham: Springer International Publishing. doi: DOI: 10.1007/978-3-319-32449-4_9

Clements, T., & Denolle, M. A. (2018, jul). Tracking Groundwater Levels Using the Ambient Seismic Field. *Geophysical Research Letters*, *45*(13), 6459–6465. doi: DOI: 10.1029/2018GL077706

Condon, L. E., Atchley, A. L., & Maxwell, R. M. (2020). Evapotranspiration depletes groundwater under warming over the contiguous United States. *Nature Communications*, *11*(1). doi: DOI: 10.1038/s41467-020-14688-0

Conti, S., Roux, P., & Fink, M. (2002). Depth and range shifting of a focal spot using a time-reversal mirror in an acoustic waveguide. *Applied Physics Letters*, *80*(19), 3647–3649. doi: DOI: 10.1063/1.1479208

Cook, K. L., Andermann, C., Gimbert, F., Adhikari, B. R., & Hovius, N. (2018). Glacial lake outburst floods as drivers of fluvial erosion in the Himalaya. *Science*, *362*(6410), 53–57. doi: DOI: 10.1126/science.aat4981

Cook, K. L., & Dietze, M. (2022). Seismic Advances in Process Geomorphology. *Annual Review of Earth and Planetary Sciences*, *50*(1), 183–204. doi: DOI: 10.1146/annurev-

earth-032320-085133
DiCarlo, D. A. (2004, apr). Experimental measurements of saturation overshoot on infiltration. *Water Resources Research*, *40*(4). doi: DOI: 10.1029/2003WR002670
DiCarlo, D. A. (2006, jul). Quantitative network model predictions of saturation behind infiltration fronts and comparison with experiments. *Water Resources Research*, *42*(7). doi: DOI: 10.1029/2005WR004750
Dieterich, J. H. (1979). Modeling of rock friction: 1. Experimental results and constitutive equations. *Journal of Geophysical Research: Solid Earth*, *84*(B5), 2161–2168. doi: DOI: https://doi.org/10.1029/JB084iB05p02161
Dietze, M., Cook, K. L., Illien, L., Rach, O., Puffpaff, S., Stodian, I., & Hovius, N. (2020). Impact of Nested Moisture Cycles on Coastal Chalk Cliff Failure Revealed by Multiseasonal Seismic and Topographic Surveys. *Journal of Geophysical Research: Earth Surface*, *125*(8). doi: DOI: 10.1029/2019JF005487
Donaldson, C., Winder, T., Caudron, C., & White, R. S. (2019). Crustal seismic velocity responds to a magmatic intrusion and seasonal loading in Iceland's Northern Volcanic Zone. *Science Advances*, *5*(11). doi: DOI: 10.1126/sciadv.aax6642
Doody, T. M., & Benyon, R. G. (2011). Direct measurement of groundwater uptake through tree roots in a cave. *Ecohydrology*, *4*(5), 644–649. doi: DOI: https://doi.org/10.1002/eco.152
Dralle, D. N., Hahm, W. J., Rempe, D. M., Karst, N. J., Thompson, S. E., & Dietrich, W. E. (2018, jun). Quantification of the seasonal hillslope water storage that does not drive streamflow. *Hydrological Processes*, *32*(13), 1978–1992. doi: DOI: 10.1002/hyp.11627
Dreiling, J., & Tilmann, F. (2019). *BayHunter - McMC transdimensional Bayesian inversion of receiver functions and surface wave dispersion.* GFZ Data Services. doi: DOI: 10.5880/GFZ.2.4.2019.001
Dreiling, J., Tilmann, F., Yuan, X., Haberland, C., & Seneviratne, S. W. (2020). Crustal Structure of Sri Lanka Derived From Joint Inversion of Surface Wave Dispersion and Receiver Functions Using a Bayesian Approach. *Journal of Geophysical Research: Solid Earth*, *125*(5), 1–15. doi: DOI: 10.1029/2019JB018688
Ebigbo, A., Lang, P. S., Paluszny, A., & Zimmerman, R. W. (2016). Inclusion-Based Effective Medium Models for the Permeability of a 3D Fractured Rock Mass. *Transport in Porous Media*, *113*(1), 137–158. doi: DOI: 10.1007/s11242-016-0685-z
Elkhoury, J. E., Brodsky, E. E., & Agnew, D. C. (2006). Seismic waves increase permeability. *Nature*, *441*(7097), 1135–1138. doi: DOI: 10.1038/nature04798
Elliott, J. R., Jolivet, R., Gonzalez, P. J., Avouac, J. P., Hollingsworth, J., Searle, M. P., & Stevens, V. L. (2016). Himalayan megathrust geometry and relation to topography revealed by the Gorkha earthquake. *Nature Geoscience*, *9*(2), 174–180. doi: DOI: 10.1038/ngeo2623
Evaristo, J., Jasechko, S., & McDonnell, J. J. (2015). Global separation of plant transpiration from groundwater and streamflow. *Nature*, *525*(7567), 91–94. doi: DOI: 10.1038/nature14983
Fan, X., Scaringi, G., Korup, O., West, A. J., van Westen, C. J., Tanyas, H., ... Huang, R. (2019). *Earthquake-Induced Chains of Geologic Hazards: Patterns, Mechanisms, and Impacts.* Blackwell Publishing Ltd. doi: DOI: 10.1029/2018RG000626
Fenta, M. C., Potter, D. K., & Szanyi, J. (2021). *Fibre Optic Methods of Prospecting: A Comprehensive and Modern Branch of Geophysics* (Vol. 42) (No. 3). Springer Netherlands. doi: DOI: 10.1007/s10712-021-09634-8
Fichtner, A., Stehly, L., Ermert, L., & Boehm, C. (2017). Generalized interferometry - I: Theory for interstation correlations. *Geophysical Journal International*, *208*(2),

603–638. doi: DOI: 10.1093/gji/ggw420
Fink, M. (2008). Time-reversal acoustics. *Journal of Physics: Conference Series*, *118*(1). doi: DOI: 10.1088/1742-6596/118/1/012001
Fischer, T., Gemmer, M., Lüliu, L., & Buda, S. (2011). Temperature and precipitation trends and dryness/wetness pattern in the Zhujiang River Basin, South China, 1961-2007. *Quaternary International*, *244*(2), 138–148. doi: DOI: 10.1016/j.quaint.2010.08.010
Gabet, E. J., Burbank, D. W., Putkonen, J. K., Pratt-Sitaula, B. A., & Ojha, T. (2004, dec). Rainfall thresholds for landsliding in the Himalayas of Nepal. *Geomorphology*, *63*(3-4), 131–143. doi: DOI: 10.1016/J.GEOMORPH.2004.03.011
Gan, B., guo Yang, X., Zhang, W., & wen Zhou, J. (2019). Temporal and Spatial Evolution of Vegetation Coverage in the Mianyuan River Basin Influenced by Strong Earthquake Disturbance. *Scientific Reports*, *9*(1), 1–14. doi: DOI: 10.1038/s41598-019-53264-5
Gao, J. (2007). Nonlinear time series: Semiparametric and nonparametric methods. *Nonlinear Time Series: Semiparametric and Nonparametric Methods*(39563), 1–237. doi: DOI: 10.1111/j.1467-9892.2009.00642.x
Gao, K., Rougier, E., Guyer, R. A., Lei, Z., & Johnson, P. A. (2019). Simulation of crack induced nonlinear elasticity using the combined finite-discrete element method. *Ultrasonics*, *98*, 51–61. doi: DOI: 10.1016/j.ultras.2019.06.003
Gao, L., Shokouhi, P., & Rivière, J. (2022). Effect of relative humidity on the nonlinear elastic response of granular media. *Journal of Applied Physics*, *131*(5). doi: DOI: 10.1063/5.0073967
Gassenmeier, M., Sens-Schönfelder, C., Delatre, M., & Korn, M. (2015). Monitoring of environmental influences on seismic velocity at the geological storage site for CO2 in Ketzin (Germany) with ambient seismic noise. *Geophysical Journal International*, *200*(1), 524–533. doi: DOI: 10.1093/gji/ggu413
Gassenmeier, M., Sens-Schönfelder, C., Eulenfeld, T., Bartsch, M., Victor, P., Tilmann, F., & Korn, M. (2016). Field observations of seismic velocity changes caused by shaking-induced damage and healing due to mesoscopic nonlinearity. *Geophysical Journal International*, *204*(3), 1490–1502. doi: DOI: 10.1093/gji/ggv529
GFZ Potsdam, & CNRS-INSU. (2006). *Ipoc seismic network.* Integrated Plate boundary Observatory Chile - IPOC. doi: DOI: 10.14470/PK615318
Gleeson, T., Befus, K. M., Jasechko, S., Luijendijk, E., & Cardenas, M. B. (2016). The global volume and distribution of modern groundwater. *Nature Geoscience*, *9*(2), 161–164. doi: DOI: 10.1038/ngeo2590
Gleeson, T., Novakowski, K., & Kurt Kyser, T. (2009). Extremely rapid and localized recharge to a fractured rock aquifer. *Journal of Hydrology*, *376*(3-4), 496–509. doi: DOI: 10.1016/j.jhydrol.2009.07.056
Gliozzi, A. S., Scalerandi, M., Anglani, G., Antonaci, P., & Salini, L. (2018). Correlation of elastic and mechanical properties of consolidated granular media during microstructure evolution induced by damage and repair. *Physical Review Materials*, *2*(1), 1–13. doi: DOI: 10.1103/PhysRevMaterials.2.013601
Groos, J. C., & Ritter, J. R. R. (2009, 11). Time domain classification and quantification of seismic noise in an urban environment. *Geophysical Journal International*, *179*(2), 1213-1231. doi: DOI: 10.1111/j.1365-246X.2009.04343.x
Guéguen, P., Bonilla, L. F., & Douglas, J. (2019). Comparison of soil nonlinearity (in situ stress-strain relation and G/G max Reduction) observed in strong-motion databases and modeled in ground-motion prediction equations. *Bulletin of the Seismological Society of America*, *109*(1), 178–186. doi: DOI: 10.1785/0120180169

Gueguen, Y., & Palciauskas, V. (1994). *Introduction to the Physics of Rocks*.

Guyer, R. A., Ten Cate, J., & Johnson, P. (1999). Hysteresis and the dynamic elasticity of consolidated granular materials. *Physical Review Letters*, *82*(16), 3280–3283. doi: DOI: 10.1103/PhysRevLett.82.3280

Hadziioannou, C., Larose, E., Baig, A., Roux, P., & Campillo, M. (2011). Improving temporal resolution in ambient noise monitoring of seismic wave speed. *Journal of Geophysical Research: Solid Earth*, *116*(7), 1–10. doi: DOI: 10.1029/2011JB008200

Hadziioannou, C., Larose, E., Coutant, O., Roux, P., & Campillo, M. (2009). Stability of monitoring weak changes in multiply scattering media with ambient noise correlation: Laboratory experiments. *The Journal of the Acoustical Society of America*, *125*(6), 3688–3695. doi: DOI: 10.1121/1.3125345

Haindl, C., Leng, K., & Nissen-Meyer, T. (2021). A 3D complexity-adaptive approach to explore sparsity in elastic wave propagation. *Geophysics*, *86*(5), T321–T335. doi: DOI: 10.1190/geo2020-0490.1

Helle, H. B., Pham, N. H., & Carcione, J. M. (2003, nov). Velocity and attenuation in partially saturated rocks: poroelastic numerical experiments. *Geophysical Prospecting*, *51*(6), 551–566. doi: DOI: 10.1046/j.1365-2478.2003.00393.x

Herrmann, R. B., & Ammon, C. J. (2002). Computer programs in seismology: Surface waves, receiver functions and crustal structure. *St. Louis University, St. Louis, MO*, *25*, 46.

Hillers, G., Campillo, M., & Ma, K.-F. (2014, apr). Seismic velocity variations at TCDP are controlled by MJO driven precipitation pattern and high fluid discharge properties. *Earth and Planetary Science Letters*, *391*, 121–127. doi: DOI: 10.1016/J.EPSL.2014.01.040

Hillers, G., Roux, P., Campillo, M., & Ben-Zion, Y. (2016). Focal spot imaging based on zero lag cross-correlation amplitude fields: Application to dense array data at the San Jacinto fault zone. *Journal of Geophysical Research: Solid Earth*, *121*(11), 8048–8067. doi: DOI: 10.1002/2016JB013014

Hirmas, D. R., Giménez, D., Nemes, A., Kerry, R., Brunsell, N. A., & Wilson, C. J. (2018). Climate-induced changes in continental-scale soil macroporosity may intensify water cycle. *Nature*, *561*(7721), 100–103. doi: DOI: 10.1038/s41586-018-0463-x

Hobiger, M., Wegler, U., Shiomi, K., & Nakahara, H. (2014, jul). Single-station cross-correlation analysis of ambient seismic noise: application to stations in the surroundings of the 2008 Iwate-Miyagi Nairiku earthquake. *Geophysical Journal International*, *198*(1), 90–109. doi: DOI: 10.1093/gji/ggu115

Hosono, T., Yamada, C., Manga, M., Wang, C. Y., & Tanimizu, M. (2020). Stable isotopes show that earthquakes enhance permeability and release water from mountains. *Nature communications*, *11*(1), 2776. doi: DOI: 10.1038/s41467-020-16604-y

Hosono, T., Yamada, C., Shibata, T., Tawara, Y., Wang, C. Y., Manga, M., ... Shimada, J. (2019). Coseismic Groundwater Drawdown Along Crustal Ruptures During the 2016 Mw 7.0 Kumamoto Earthquake. *Water Resources Research*, *55*(7), 5891–5903. doi: DOI: 10.1029/2019WR024871

Hovius, N., Meunier, P., Lin, C. W., Chen, H., Chen, Y. G., Dadson, S., ... Lines, M. (2011). Prolonged seismically induced erosion and the mass balance of a large earthquake. *Earth and Planetary Science Letters*, *304*(3-4), 347–355. doi: DOI: 10.1016/j.epsl.2011.02.005

Huffman, G. J., Bolvin, D. T., Nelkin, E. J., & Tan, J. (2019). IMERG Technical documentation. , *01*(01).

Ichii, K., Kawabata, A., & Yamaguchi, Y. (2010). Global correlation

analysis for NDVI and climatic variables and NDVI trends: 1982-1990. *http://dx.doi.org/10.1080/01431160110119416*. doi: DOI: 10.1080/01431160110119416

Illien, L., Andermann, C., Sens-Schönfelder, C., Cook, K. L., Baidya, K. P., Adhikari, L. B., & Hovius, N. (2021). Subsurface Moisture Regulates Himalayan Groundwater Storage and Discharge. *AGU Advances*, *2*(2). doi: DOI: 10.1029/2021av000398

Illien, L., Sens-Schönfelder, C., & Ke, K.-y. (2022). Resolving minute temporal seismic velocity changes induced by earthquake damage : The more stations , the merrier ? *EarthArXiv*.

Illien, L., Sens-Schönfelder, C., Andermann, C., Marc, O., Cook, K. L., Adhikari, L. B., & Hovius, N. (2022). Seismic Velocity Recovery in the Subsurface: Transient Damage and Groundwater Drainage Following the 2015 Gorkha Earthquake, Nepal. *Journal of Geophysical Research: Solid Earth*, *127*(2), 1–18. doi: DOI: 10.1029/2021jb023402

Immerzeel, W. W., Lutz, A. F., Andrade, M., Bahl, A., Biemans, H., Bolch, T., ... Baillie, J. E. (2020). Importance and vulnerability of the world's water towers. *Nature*, *577*(7790), 364–369. doi: DOI: 10.1038/s41586-019-1822-y

Immerzeel, W. W., Van Beek, L. P., & Bierkens, M. F. (2010). Climate change will affect the asian water towers. *Science*. doi: DOI: 10.1126/science.1183188

Iverson, R. M. (2000). Landslide triggering by rain infiltration. *Water Resources Research*, *36*(7), 1897–1910. doi: DOI: 10.1029/2000WR900090

Jachens, E. R., Rupp, D. E., Roques, C., & Selker, J. S. (2020). Recession analysis revisited: Impacts of climate on parameter estimation. *Hydrology and Earth System Sciences*, *24*(3), 1159–1170. doi: DOI: 10.5194/hess-24-1159-2020

Jasechko, S., Kirchner, J. W., Welker, J. M., & McDonnell, J. J. (2016, feb). Substantial proportion of global streamflow less than three months old. *Nature Geoscience*, *9*(2), 126–129. doi: DOI: 10.1038/ngeo2636

Jiménez Cisneros, B. E., Oki, T., Arnell, N. W., Benito, G., Cogley, J. G., Döll, P., ... Nishijima, A. (2015). Freshwater resources. *Climate Change 2014 Impacts, Adaptation and Vulnerability: Part A: Global and Sectoral Aspects*, 229–270. doi: DOI: 10.1017/CBO9781107415379.008

Joshua, A., Rik, J., & Troyer, D. (2022). Estimating a sparse nonlinear dynamical model of the flow around an oscillating cylinder in a fluid flow using SINDy.

Jousset, P., Currenti, G., Schwarz, B., Chalari, A., Tilmann, F., Reinsch, T., ... Krawczyk, C. M. (2022). Fibre optic distributed acoustic sensing of volcanic events. *Nature Communications*, *13*(1). doi: DOI: 10.1038/s41467-022-29184-w

Jousset, P., Reinsch, T., Ryberg, T., Blanck, H., Clarke, A., Aghayev, R., ... Krawczyk, C. M. (2018, dec). Dynamic strain determination using fibre-optic cables allows imaging of seismological and structural features. *Nature Communications*, *9*(1). doi: DOI: 10.1038/s41467-018-04860-y

Kachanov, M., & Sevostianov, I. (2005, jan). On quantitative characterization of microstructures and effective properties. In *International journal of solids and structures* (Vol. 42, pp. 309–336). doi: DOI: 10.1016/j.ijsolstr.2004.06.016

Katsura, S., Kosugi, K., Mizutani, T., Okunaka, S., & Mizuyama, T. (2008, sep). Effects of bedrock groundwater on spatial and temporal variations in soil mantle groundwater in a steep granitic headwater catchment. *Water Resources Research*, *44*(9). doi: DOI: 10.1029/2007WR006610

Keefer, D. K. (1994). The importance of earthquake-induced landslides to long-term slope erosion and slope-failure hazards in seismically active regions. *Geomorphology*, *10*(1-4), 265–284. doi: DOI: 10.1016/0169-555X(94)90021-3

Kim, D., & Lekic, V. (2019a). Groundwater Variations From Autocorrelation and Receiver Functions. *Geophysical Research Letters*, 2019GL084719. doi: DOI: 10.1029/2019GL084719

Kim, D., & Lekic, V. (2019b, dec). Groundwater Variations From Autocorrelation and Receiver Functions. *Geophysical Research Letters*. doi: DOI: 10.1029/2019GL084719

Kim, D., Lekić, V., Ménard, B., Baron, D., & Taghizadeh-Popp, M. (2020). Sequencing seismograms: A panoptic view of scattering in the core-mantle boundary region. *Science*, *368*(6496), 1223–1228. doi: DOI: 10.1126/science.aba8972

Kirchner, J. W. (2009, feb). Catchments as simple dynamical systems: Catchment characterization, rainfall-runoff modeling, and doing hydrology backward. *Water Resources Research*, *45*(2). doi: DOI: 10.1029/2008WR006912

Knight, J. B., Fandrich, C. G., Ning Lau, C., Jaeger, H. M., & Nagel, S. R. (1995). Density relaxation in a vibration.pdf. *Physical Review E*, *51*(5).

Kober, J., Gliozzi, A., Scalerandi, M., & Tortello, M. (2022). Material Grain Size Determines Relaxation-Time Distributions in Slow-Dynamics Experiments. *Physical Review Applied*, *17*(1), 1. doi: DOI: 10.1103/PhysRevApplied.17.014002

Koirala, S., Jung, M., Reichstein, M., de Graaf, I. E., Camps-Valls, G., Ichii, K., ... Carvalhais, N. (2017, may). Global distribution of groundwater-vegetation spatial covariation. *Geophysical Research Letters*, *44*(9), 4134–4142. doi: DOI: 10.1002/2017GL072885

Kosugi, K., Katsura, S., Mizuyama, T., Okunaka, S., & Mizutani, T. (2008, jan). Anomalous behavior of soil mantle groundwater demonstrates the major effects of bedrock groundwater on surface hydrological processes. *Water Resources Research*, *44*(1). doi: DOI: 10.1029/2006WR005859

Lai, G., Ge, H., Xue, L., Brodsky, E. E., Huang, F., & Wang, W. (2014, apr). Tidal response variation and recovery following the Wenchuan earthquake from water level data of multiple wells in the nearfield. *Tectonophysics*, *619-620*, 115–122. doi: DOI: 10.1016/J.TECTO.2013.08.039

Lecocq, T., Longuevergne, L., Pedersen, H. A., Brenguier, F., & Stammler, K. (2017, dec). Monitoring ground water storage at mesoscale using seismic noise: 30 years of continuous observation and thermo-elastic and hydrological modeling. *Scientific Reports*, *7*(1). doi: DOI: 10.1038/s41598-017-14468-9

Leng, K., Nissen-Meyer, T., Van Driel, M., Hosseini, K., & Al-Attar, D. (2019). AxiSEM3D: Broad-band seismic wavefields in 3-D global earth models with undulating discontinuities. *Geophysical Journal International*, *217*(3), 2125–2146. doi: DOI: 10.1093/gji/ggz092

Li, P., Karunanidhi, D., Subramani, T., & Srinivasamoorthy, K. (2021). Sources and Consequences of Groundwater Contamination. *Archives of Environmental Contamination and Toxicology*, *80*(1), 1–10. doi: DOI: 10.1007/s00244-020-00805-z

Lieou, C. K., Daub, E. G., Ecke, R. E., & Johnson, P. A. (2017). Slow Dynamics and Strength Recovery in Unconsolidated Granular Earth Materials: A Mechanistic Theory. *Journal of Geophysical Research: Solid Earth*, *122*(10), 7573–7583. doi: DOI: 10.1002/2017JB014131

Lindner, F., Wassermann, J., & Igel, H. (2021). Seasonal Freeze-Thaw Cycles and Permafrost Degradation on Mt. Zugspitze (German/Austrian Alps) Revealed by Single-Station Seismic Monitoring. *Geophysical Research Letters*, *48*(18), 1–11. doi: DOI: 10.1029/2021GL094659

Liu, Y., & Szlufarska, I. (2010). Effect of trace moisture on friction. *Applied Physics Letters*, *96*(10). doi: DOI: 10.1063/1.3356222

Lobkis, O. I., & Weaver, R. L. (2001, dec). On the emergence of the Green's function in the correlations of a diffuse field. *The Journal of the Acoustical Society of America*, *110*(6), 3011–3017. doi: DOI: 10.1121/1.1417528

Lobkis, O. I., & Weaver, R. L. (2003). Coda-Wave Interferometry in Finite Solids: Conversion Rates in an Elastodynamic Billiard. *Physical Review Letters*, *90*(25), 4. doi: DOI: 10.1103/PhysRevLett.90.254302

Lu, Y., & Ben-Zion, Y. (2022). Regional seismic velocity changes following the 2019 Mw7.1 Ridgecrest, California earthquake from autocorrelations and P/S converted waves. *Geophysical Journal International*, *228*(1), 620–630. doi: DOI: 10.1093/gji/ggab350

Lyakhovsky, V., Ben-Zion, Y., & Agnon, A. (1997). Distributed damage, faulting, and friction. *Journal of Geophysical Research B: Solid Earth*, *102*(12), 27635–27649. doi: DOI: 10.1029/97jb01896

Lyakhovsky, V., Hamiel, Y., Ampuero, J. P., & Ben-zion, Y. (2009). Non-linear damage rheology and wave resonance in rocks. *Geophysical Journal International*, *178*(2), 910–920. doi: DOI: 10.1111/j.1365-246X.2009.04205.x

Manga, M., Beresnev, I., Brodsky, E. E., Elkhoury, J. E., Elsworth, D., Ingebritsen, S. E., ... Wang, C. Y. (2012, jun). Changes in permeability caused by transient stresses: Field observations, experiments, and mechanisms. *Reviews of Geophysics*, *50*(2). doi: DOI: 10.1029/2011RG000382

Manga, M., Brodsky, E. E., & Boone, M. (2003, mar). Response of streamflow to multiple earthquakes. *Geophysical Research Letters*, *30*(5), n/a–n/a. doi: DOI: 10.1029/2002gl016618

Mao, S., Lecointre, A., Campillo, M., & Hilst, R. D. V. D. (2022). Space-time monitoring of groundwater fl uctuations with passive seismic interferometry. , 1–9. doi: DOI: 10.1038/s41467-022-32194-3

Marc, O., Behling, R., Andermann, C., Turowski, J. M., Illien, L., Roessner, S., & Hovius, N. (2019). Long-term erosion of the Nepal Himalayas by bedrock landsliding: The role of monsoons, earthquakes and giant landslides. *Earth Surface Dynamics*, *7*(1), 107–128. doi: DOI: 10.5194/esurf-7-107-2019

Marc, O., Hovius, N., Meunier, P., Gorum, T., & Uchida, T. (2016). A seismologically consistent expression for the total area and volume of earthquake-triggered landsliding. *Journal of Geophysical Research: Earth Surface*, *121*(4), 640–663. doi: DOI: 10.1002/2015JF003732

Marc, O., Hovius, N., Meunier, P., Uchida, T., & Hayashi, S. (2015). Transient changes of landslide rates after earthquakes. *Geology*, *43*(10), 883–886. doi: DOI: 10.1130/G36961.1

Marc, O., Sens-Schönfelder, C., Illien, L., Meunier, P., Hobiger, M., Sawazaki, K., ... Hovius, N. (2021). Toward Using Seismic Interferometry to Quantify Landscape Mechanical Variations after Earthquakes. *Bulletin of the Seismological Society of America*, 1–19. doi: DOI: 10.1785/0120200264

Mavko, G., Mukerji, T., & Dvorkin, J. (2009). *The rock physics handbook: Tools for seismic analysis of porous media* (2nd ed.). Cambridge University Press. doi: DOI: 10.1017/CBO9780511626753

Maxwell, R. M., & Condon, L. E. (2016, jul). Connections between groundwater flow and transpiration partitioning. *Science (New York, N.Y.)*, *353*(6297), 377–80. doi: DOI: 10.1126/science.aaf7891

Mays, D. C., & Hunt, J. R. (2007). Hydrodynamic and chemical factors in clogging by montmorillonite in porous media. *Environmental Science and Technology*, *41*(16), 5666–5671. doi: DOI: 10.1021/es062009s

McGuire, K. J., & McDonnell, J. J. (2006, nov). A review and evaluation of catchment transit time modeling. *Journal of Hydrology*, *330*(3-4), 543–563. doi: DOI: 10.1016/j.jhydrol.2006.04.020

McNicol, R. (1949). The fading of radio waves of medium and high frequencies. *Proceedings of the IEE - Part III: Radio and Communication Engineering*, *96*(44), 517–524. doi: DOI: 10.1049/pi-3.1949.0108

Meunier, P., Hovius, N., & Haines, A. J. (2007). Regional patterns of earthquake-triggered landslides and their relation to ground motion. *Geophysical Research Letters*, *34*(20), 1–5. doi: DOI: 10.1029/2007GL031337

Meyer, G. G., Brantut, N., Mitchell, T. M., Meredith, P. G., & Plümper, O. (2021). Time Dependent Mechanical Crack Closure as a Potential Rapid Source of Post-Seismic Wave Speed Recovery: Insights From Experiments in Carrara Marble. *Journal of Geophysical Research: Solid Earth*, *126*(4), 1–29. doi: DOI: 10.1029/2020JB021301

Mohr, C. H., Manga, M., & Wald, D. (2018). Stronger Peak Ground Motion, Beyond the Threshold to Initiate a Response, Does Not Lead to Larger Stream Discharge Responses to Earthquakes. *Geophysical Research Letters*, *45*(13), 6523–6531. doi: DOI: 10.1029/2018GL078621

Mohr, C. H., Manga, M., Wang, C.-y., Kirchner, J. W., & Bronstert, A. (2015, mar). Shaking water out of soil. *Geology*, *43*(3), 207–210. doi: DOI: 10.1130/G36261.1

Mohr, C. H., Manga, M., Wang, C. Y., & Korup, O. (2017). Regional changes in streamflow after a megathrust earthquake. *Earth and Planetary Science Letters*, *458*, 418–428. doi: DOI: 10.1016/j.epsl.2016.11.013

Molnar, P., Anderson, R. S., & Anderson, S. P. (2007). Tectonics, fracturing of rock, and erosion. *Journal of Geophysical Research: Earth Surface*, *112*(3), 1–12. doi: DOI: 10.1029/2005JF000433

Montgomery, D. R., Dietrich, W. E., Torres, R., Anderson, S. P., Heffner, J. T., & Loague, K. (1997). Hydrologic response of a steep, unchanneled valley to natural and applied rainfall. *Water Resources Research*, *33*(1), 91–109. doi: DOI: 10.1029/96WR02985

Montgomery, D. R., & Manga, M. (2003). Streamflow and water well responses to earthquakes. *Science*, *300*(5628), 2047–2049. doi: DOI: 10.1126/science.1082980

Moore, C. C. (2015). Ergodic theorem, ergodic theory, and statistical mechanics. *Proceedings of the National Academy of Sciences of the United States of America*, *112*(7), 1907–1911. doi: DOI: 10.1073/pnas.1421798112

Mulargia, F., & Castellaro, S. (2013). A seismic passive imaging step beyond SPAC and ReMi. *Geophysics*, *78*(5). doi: DOI: 10.1190/GEO2012-0405.1

Müller, M. F., Dralle, D. N., & Thompson, S. E. (2014, jul). Analytical model for flow duration curves in seasonally dry climates. *Water Resources Research*, *50*(7), 5510–5531. doi: DOI: 10.1002/2014WR015301

Nakamura, Y. (2000). Clear identification of fundamental idea of Nakamura's technique and its applications. *Proceedings of the 12th world conference on . . .*, Paper no. 2656.

Nakata, N., & Snieder, R. (2011, sep). Near-surface weakening in Japan after the 2011 Tohoku-Oki earthquake. *Geophysical Research Letters*, *38*(17). doi: DOI: 10.1029/2011GL048800

Nakata, N., & Snieder, R. (2012, jan). Estimating near-surface shear wave velocities in Japan by applying seismic interferometry to KiK-net data. *Journal of Geophysical Research: Solid Earth*, *117*(1). doi: DOI: 10.1029/2011JB008595

Nissen-Meyer, T., Van Driel, M., Stähler, S. C., Hosseini, K., Hempel, S., Auer, L., . . . Fournier, A. (2014). AxiSEM: Broadband 3-D seismic wavefields in axisymmetric media. *Solid Earth*, *5*(1), 425–445. doi: DOI: 10.5194/se-5-425-2014

Oakley, D. O., Forsythe, B., Gu, X., Nyblade, A. A., & Brantley, S. L. (2021). Seismic Ambient Noise Analyses Reveal Changing Temperature and Water Signals to 10s of Meters Depth in the Critical Zone. *Journal of Geophysical Research: Earth Surface*, *126*(2), 1–21. doi: DOI: 10.1029/2020JF005823

Obermann, A., & Hillers, G. (2019). Chapter Two - Seismic time-lapse interferometry across scales. In C. Schmelzbach (Ed.), *Recent advances in seismology* (Vol. 60, pp. 65–143). Elsevier. doi: DOI: https://doi.org/10.1016/bs.agph.2019.06.001

Obermann, A., Planès, T., Larose, E., Sens-Schönfelder, C., & Campillo, M. (2013, jul). Depth sensitivity of seismic coda waves to velocity perturbations in an elastic heterogeneous medium. *Geophysical Journal International*, *194*(1), 372–382. doi: DOI: 10.1093/gji/ggt043

Oki, T., & Kanae, S. (2006, aug). Global Hydrological Cycles and World Water Resources. *Science*, *313*(5790), 1068–1072. doi: DOI: 10.1126/SCIENCE.1128845

Onda, Y. (1989). Influence of water storage capacity in regolith zone on runoff characteristics and slope failure on granitic hills in Aichi, Japan. *Transactions - Japanese Geomorphological Union*, *10*(1), 13–26.

Oshima, M., & Takenaka, H. (2020). A P-and S-wave picking technique based on the probabilistic density function of seismic-waveform amplitude. *Bulletin of the Seismological Society of America*, *110*(2), 763–782. doi: DOI: 10.1785/0120190078

Ostrovsky, L., Lebedev, A., Riviere, J., Shokouhi, P., Wu, C., Stuber Geesey, M. A., & Johnson, P. A. (2019). Long-Time Relaxation Induced by Dynamic Forcing in Geomaterials. *Journal of Geophysical Research: Solid Earth*, *124*(5), 5003–5013. doi: DOI: 10.1029/2018JB017076

Overduin, P. P., Haberland, C., Ryberg, T., Kneier, F., Jacobi, T., Grigoriev, M. N., & Ohrnberger, M. (2015). Submarine permafrost depth from ambient seismic noise. *Geophysical Research Letters*, *42*(18), 7581–7588. doi: DOI: 10.1002/2015GL065409

Pacheco, C., & Snieder, R. (2005, sep). Time-lapse travel time change of multiply scattered acoustic waves. *The Journal of the Acoustical Society of America*, *118*(3), 1300–1310. doi: DOI: 10.1121/1.2000827

Padilla, C., Onda, Y., & Iida, T. (2015). Interaction between runoff - bedrock groundwater in a steep headwater catchment underlain by sedimentary bedrock fractured by gravitational deformation. *Hydrological Processes*, *29*(20), 4398–4412. doi: DOI: 10.1002/hyp.10498

Padilla, C., Onda, Y., Iida, T., Takahashi, S., & Uchida, T. (2014). Characterization of the groundwater response to rainfall on a hillslope with fractured bedrock by creep deformation and its implication for the generation of deep-seated landslides on Mt. Wanitsuka, Kyushu Island. *Geomorphology*, *204*, 444–458. doi: DOI: 10.1016/j.geomorph.2013.08.024

Paitz, P., Sager, K., & Fichtner, A. (2019). Rotation and strain ambient noise interferometry. *Geophysical Journal International*, *216*(3), 1938–1952. doi: DOI: 10.1093/gji/ggy528

Pei, S., Niu, F., Ben-Zion, Y., Sun, Q., Liu, Y., Xue, X., ... Shao, Z. (2019, may). Seismic velocity reduction and accelerated recovery due to earthquakes on the Longmenshan fault. *Nature Geoscience*, *12*(5), 387–392. doi: DOI: 10.1038/s41561-019-0347-1

Putkonen, J. K. (2004). Continuous Snow and Rain Data at 500 to 4400 m Altitude. *Arctic, Antarctic and Alpine Research*, *36*(2), 244–248.

Qin, L., Ben-Zion, Y., Bonilla, L. F., & Steidl, J. H. (2020). Imaging and Monitoring Temporal Changes of Shallow Seismic Velocities at the Garner Valley Near Anza, California, Following the M7.2 2010 El Mayor-Cucapah Earthquake. *Journal of Geophysical Research: Solid Earth*, *125*(1), 1–17. doi: DOI: 10.1029/2019JB018070

Qiu, H., Hillers, G., & Ben-Zion, Y. (2020). Temporal changes of seismic velocities in the San Jacinto Fault zone associated with the 2016 Mw 5.2 Borrego Springs earthquake. *Geophysical Journal International*, *220*(3), 1536–1554. doi: DOI: 10.1093/gji/ggz538

Rees, D. (2001). *Essential Statistics* (4th ed.; C. and Hall/CRC, Ed.). doi: DOI: https://doi.org/10.1201/9781315273174

Regine Hock, G. R. (2019). High Mountain Areas. *IPCC SR Ocean and Cryosphere*, *4*(1), 1–96.

Remillieux, M. C., Ulrich, T. J., Goodman, H. E., & Ten Cate, J. A. (2017). Propagation of a Finite-Amplitude Elastic Pulse in a Bar of Berea Sandstone: A Detailed Look at the Mechanisms of Classical Nonlinearity, Hysteresis, and Nonequilibrium Dynamics. *Journal of Geophysical Research: Solid Earth*, *122*(11), 8892–8909. doi: DOI: 10.1002/2017JB014258

Rempe, D. M., & Dietrich, W. E. (2014, may). A bottom-up control on fresh-bedrock topography under landscapes. *Proceedings of the National Academy of Sciences of the United States of America*, *111*(18), 6576–81. doi: DOI: 10.1073/pnas.1404763111

Rempe, D. M., & Dietrich, W. E. (2018, mar). Direct observations of rock moisture, a hidden component of the hydrologic cycle. *Proceedings of the National Academy of Sciences*, *115*(11), 2664–2669. doi: DOI: 10.1073/pnas.1800141115

Renée Brooks, J., Barnard, H. R., Coulombe, R., & McDonnell, J. J. (2010, feb). Ecohydrologic separation of water between trees and streams in a Mediterranean climate. *Nature Geoscience*, *3*(2), 100–104. doi: DOI: 10.1038/ngeo722

Richter, T., Sens-Schönfelder, C., Kind, R., & Asch, G. (2014). Comprehensive observation and modeling of earthquake and temperature-related seismic velocity changes in northern Chile with passive image interferometry. *Journal of Geophysical Research: Solid Earth*, *119*(6), 4747–4765. doi: DOI: 10.1002/2013JB010695

Rivet, B., Girin, L., & Jutten, C. (2007). Log-rayleigh distribution: A simple and efficient statistical representation of log-spectral coefficients. *IEEE Transactions on Audio, Speech and Language Processing*, *15*(3), 796–802. doi: DOI: 10.1109/TASL.2006.885922

Roback, K., Clark, M. K., West, A. J., Zekkos, D., Li, G., Gallen, S. F., ... Godt, J. W. (2018). The size, distribution, and mobility of landslides caused by the 2015 Mw7.8 Gorkha earthquake, Nepal. *Geomorphology*, *301*, 121–138. doi: DOI: 10.1016/j.geomorph.2017.01.030

Rodríguez Tribaldos, V., & Ajo-Franklin, J. B. (2021). Aquifer Monitoring Using Ambient Seismic Noise Recorded With Distributed Acoustic Sensing (DAS) Deployed on Dark Fiber. *Journal of Geophysical Research: Solid Earth*, *126*(4), 1–20. doi: DOI: 10.1029/2020JB021004

Roques, C., Rupp, D. E., & Selker, J. S. (2017). Improved streamflow recession parameter estimation with attention to calculation of dQ/dt. *Advances in Water Resources*, *108*, 29–43. doi: DOI: 10.1016/j.advwatres.2017.07.013

Rost, S., & Thomas, C. (2002). Array seismology: Methods and applications. *Reviews of Geophysics*, *40*(3), 2–1–2–27. doi: DOI: 10.1029/2000RG000100

Rougier, E., Munjiza, A., Lei, Z., Chau, V. T., Knight, E. E., Hunter, A., & Srinivasan, G. (2020). The combined plastic and discrete fracture deformation framework for finite-discrete element methods. *International Journal for Numerical Methods in Engineering*, *121*(5), 1020–1035. doi: DOI: 10.1002/nme.6255

Running, S. W., & Nemani, R. R. (1988, mar). Relating seasonal patterns of the AVHRR vegetation index to simulated photosynthesis and transpiration of forests in different climates. *Remote Sensing of Environment*, *24*(2), 347–367. doi: DOI: 10.1016/0034-

4257(88)90034-X

Rupp, D. E., & Selker, J. S. (2005). Drainage of a horizontal Boussinesq aquifer with a power law hydraulic conductivity profile. *Water Resources Research*, *41*(11), 1–8. doi: DOI: 10.1029/2005WR004241

Sakuma, H., Kawai, K., Katayama, I., & Suehara, S. (2018). *What is the origin of macroscopic friction?* (Tech. Rep.).

Salve, R., Rempe, D. M., & Dietrich, W. E. (2012). Rain, rock moisture dynamics, and the rapid response of perched groundwater in weathered, fractured argillite underlying a steep hillslope. *Water Resources Research*, *48*(11), 1–25. doi: DOI: 10.1029/2012WR012583

Samaniego, L., Thober, S., Kumar, R., Wanders, N., Rakovec, O., Pan, M., ... Marx, A. (2018). Anthropogenic warming exacerbates European soil moisture droughts. *Nature Climate Change*, *8*(5), 421–426. doi: DOI: 10.1038/s41558-018-0138-5

Sawazaki, K., Saito, T., & Shiomi, K. (2018, nov). Shallow Temporal Changes in S Wave Velocity and Polarization Anisotropy Associated With the 2016 Kumamoto Earthquake Sequence, Japan. *Journal of Geophysical Research: Solid Earth*, *123*(11), 9899–9913. doi: DOI: 10.1029/2018JB016261

Sawazaki, K., Sato, H., Nakahara, H., & Nishimura, T. (2009, feb). Time-lapse changes of seismic velocity in the shallow ground caused by strong ground motion shock of the 2000 Western-Tottori earthquake, Japan, as revealed from coda deconvolution analysis. *Bulletin of the Seismological Society of America*, *99*(1), 352–366. doi: DOI: 10.1785/0120080058

Scalerandi, M., Mechri, C., Bentahar, M., Di Bella, A., Gliozzi, A. S., & Tortello, M. (2019). Experimental Evidence of Correlations between Conditioning and Relaxation in Hysteretic Elastic Media. *Physical Review Applied*, *12*(4), 1. doi: DOI: 10.1103/PhysRevApplied.12.044002

Sens-Schönfelder, C., & Brenguier, F. (2019). Noise-based Monitoring. In N. Nakata, L. Gualtieri, & A. Fichtner (Eds.), *Seismic ambient noise* (pp. 267–301). Cambridge University Press.

Sens-Schönfelder, C., & Eulenfeld, T. (2019, apr). Probing the in situ Elastic Nonlinearity of Rocks with Earth Tides and Seismic Noise. *Physical Review Letters*, *122*(13). doi: DOI: 10.1103/PhysRevLett.122.138501

Sens-Schönfelder, C., Pomponi, E., & Peltier, A. (2014, apr). Dynamics of Piton de la Fournaise volcano observed by passive image interferometry with multiple references. *Journal of Volcanology and Geothermal Research*, *276*, 32–45. doi: DOI: 10.1016/J.JVOLGEORES.2014.02.012

Sens-Schönfelder, C., Snieder, R., & Li, X. (2019a, jan). A model for nonlinear elasticity in rocks based on friction of internal interfaces and contact aging. *Geophysical Journal International*, *216*(1), 319–331. doi: DOI: 10.1093/gji/ggy414

Sens-Schönfelder, C., Snieder, R., & Li, X. (2019b, jan). A model for nonlinear elasticity in rocks based on friction of internal interfaces and contact aging. *Geophysical Journal International*, *216*(1), 319–331. doi: DOI: 10.1093/gji/ggy414

Sens-Schönfelder, C., & Wegler, U. (2006, nov). Passive image interferemetry and seasonal variations of seismic velocities at Merapi Volcano, Indonesia. *Geophysical Research Letters*, *33*(21). doi: DOI: 10.1029/2006GL027797

Shapiro, N. (2019, mar). Applications with Surface Waves Extracted from Ambient Seismic Noise. In *Seismic ambient noise* (pp. 218–238). Cambridge University Press. doi: DOI: 10.1017/9781108264808.009

Sheng, Y., Ellsworth, W. L., Lellouch, A., & Beroza, G. C. (2021). Depth Constraints on

Coseismic Velocity Changes From Frequency-Dependent Measurements of Repeating Earthquake Waveforms. *Journal of Geophysical Research: Solid Earth*, *126*(2), 1–12. doi: DOI: 10.1029/2020JB020421

Shi, Z., Wang, G., Manga, M., & Wang, C. Y. (2015). Continental-scale water-level response to a large earthquake. *Geofluids*, *15*(1-2), 310–320. doi: DOI: 10.1111/gfl.12099

Shokouhi, P., Jin, J., Wood, C., Rivière, J., Madara, B., Elsworth, D., & Marone, C. (2020). Dynamic Stressing of Naturally Fractured Rocks: On the Relation Between Transient Changes in Permeability and Elastic Wave Velocity. *Geophysical Research Letters*, *47*(1), 1–10. doi: DOI: 10.1029/2019GL083557

Shokouhi, P., Rivière, J., Guyer, R. A., & Johnson, P. A. (2017). Slow dynamics of consolidated granular systems: Multi-scale relaxation. *Applied Physics Letters*, *111*(25). doi: DOI: 10.1063/1.5010043

Sleep, N. H., & Nakata, N. (2017, aug). Nonlinear attenuation of S waves by frictional failure at shallow depths. *Bulletin of the Seismological Society of America*, *107*(4), 1828–1848. doi: DOI: 10.1785/0120160334

Snieder, R., & Page, J. (2007). Multiple scattering in evolving media. *Physics Today*, *60*(5), 49–55. doi: DOI: 10.1063/1.2743124

Snieder, R., Sens-Schönfelder, C., & Wu, R. (2016). The time dependence of rock healing as a universal relaxation process, a tutorial. *Geophysical Journal International*, *208*(1), 1–9. doi: DOI: 10.1093/gji/ggw377

Snieder, R., Sens-Schönfelder, C., & Wu, R. (2017, jan). The time dependence of rock healing as a universal relaxation process, a tutorial. *Geophysical Journal International*, *208*(1), 1–9. doi: DOI: 10.1093/gji/ggw377

Steinmann, R., Seydoux, L., Beaucé, É., & Campillo, M. (2022). Hierarchical Exploration of Continuous Seismograms With Unsupervised Learning. *Journal of Geophysical Research: Solid Earth*, *127*(1), 1–21. doi: DOI: 10.1029/2021JB022455

Taira, T., Brenguier, F., & Kong, Q. (2015). Ambient noise-based monitoring of seismic velocity changes associated with the 2014 Mw 6.0 South Napa earthquake. *Geophysical Research Letters*, *42*(17), 6997–7004. doi: DOI: 10.1002/2015GL065308

Takano, T., Nishimura, T., Nakahara, H., Ohta, Y., & Tanaka, S. (2014). Seismic velocity changes caused by the Earth tide: Ambient noise correlation analyses of small-array data. *Geophysical Research Letters*, *41*(17), 6131–6136. doi: DOI: 10.1002/2014GL060690

Taktikou, E., Bourazanis, G., Papaioannou, G., & Kerkides, P. (2016, jan). Prediction of Soil Moisture from Remote Sensing Data. *Procedia Engineering*, *162*, 309–316. doi: DOI: 10.1016/J.PROENG.2016.11.066

Talwani, P., Chen, L., & Gahalaut, K. (2007, jul). Seismogenic permeability, ks. *Journal of Geophysical Research: Solid Earth*, *112*(7). doi: DOI: 10.1029/2006JB004665

Tani, M. (1997). Runoff generation processes estimated from hydrological observations on a steep forested hillslope with a thin soil layer. *Journal of Hydrology*, *200*(1-4), 84–109. doi: DOI: 10.1016/S0022-1694(97)00018-8

Tapia, J., González, R., Townley, B., Oliveros, V., Álvarez, F., Aguilar, G., ... Calderón, M. (2018). Geology and geochemistry of the Atacama Desert. *Antonie van Leeuwenhoek, International Journal of General and Molecular Microbiology*, *111*(8), 1273–1291. doi: DOI: 10.1007/s10482-018-1024-x

TenCate, J. A., & Shankland, T. J. (1996). Slow dynamics in the nonlinear elastic response of Berea sandstone. *Geophysical Research Letters*, *23*(21), 3019–3022. doi: DOI: https://doi.org/10.1029/96GL02884

TenCate, J. A., Smith, E., & Guyer, R. A. (2000). Universal slow dynamics in granular solids. *Physical Review Letters*, *85*(5), 1020–1023. doi: DOI: 10.1103/PhysRevLett.85.1020

Tian, K., Li, Z., Liu, Y., Gosvami, N. N., Goldsby, D. L., Szlufarska, I., & Carpick, R. W. (2020). Linear Aging Behavior at Short Timescales in Nanoscale Contacts. *Physical Review Letters*, *124*(2), 26801. doi: DOI: 10.1103/PhysRevLett.124.026801

Ting, D. S.-K. (2016). Equations of Fluid in Motion. *Basics of Engineering Turbulence*, 19–46. doi: DOI: 10.1016/b978-0-12-803970-0.00002-7

Tipper, E. T., Bickle, M. J., Galy, A., West, A. J., Pomiès, C., & Chapman, H. J. (2006, jun). The short term climatic sensitivity of carbonate and silicate weathering fluxes: Insight from seasonal variations in river chemistry. *Geochimica et Cosmochimica Acta*, *70*(11), 2737–2754. doi: DOI: 10.1016/j.gca.2006.03.005

Torres, R., Dietrich, W. E., Montgomery, D. R., Anderson, S. P., & Loague, K. (1998). Unsaturated zone processes and the hydrologic response of a steep, unchanneled catchment. *Water Resources Research*, *34*(8), 1865–1879. doi: DOI: 10.1029/98WR01140

Tromp-Van Meerveld, H. J., & McDonnell, J. J. (2006). Threshold relations in subsurface stormflow: 2. The fill and spill hypothesis. *Water Resources Research*, *42*(2), 1–11. doi: DOI: 10.1029/2004WR003800

Turcotte, D., & Schubert, G. (2014). *Geodynamics* (3rd ed.). Cambridge University Press. doi: DOI: 10.1017/CBO9780511843877

Viens, L., Denolle, M. A., Hirata, N., & Nakagawa, S. (2018, jul). Complex Near-Surface Rheology Inferred From the Response of Greater Tokyo to Strong Ground Motions. *Journal of Geophysical Research: Solid Earth*, *123*(7), 5710–5729. doi: DOI: 10.1029/2018JB015697

Viens, L., & Van Houtte, C. (2020). Denoising ambient seismic field correlation functions with convolutional autoencoders. *Geophysical Journal International*, *220*(3), 1521–1535. doi: DOI: 10.1093/gji/ggz509

Viguier, B., Jourde, H., Leonardi, V., Daniele, L., Batiot-Guilhe, C., Favreau, G., & De Montety, V. (2019). Water table variations in the hyperarid Atacama Desert: Role of the increasing groundwater extraction in the pampa del tamarugal (Northern Chile). *Journal of Arid Environments*, *168*, 9–16. Retrieved from `https://www.sciencedirect.com/science/article/pii/S0140196318309790` doi: DOI: https://doi.org/10.1016/j.jaridenv.2019.05.007

Viviroli, D., Dürr, H. H., Messerli, B., Meybeck, M., & Weingartner, R. (2007). Mountains of the world, water towers for humanity: Typology, mapping, and global significance. *Water Resources Research*, *43*(7). doi: DOI: 10.1029/2006WR005653

Viviroli, D., Kummu, M., Meybeck, M., Kallio, M., & Wada, Y. (2020). Increasing dependence of lowland populations on mountain water resources. *Nature Sustainability*, *3*(11), 917–928. doi: DOI: 10.1038/s41893-020-0559-9

Voisin, C., Guzmán, M. A. R., Réfloch, A., Taruselli, M., & Garambois, S. (2017). Groundwater Monitoring with Passive Seismic Interferometry. *Journal of Water Resource and Protection*, *09*(12), 1414–1427. doi: DOI: 10.4236/jwarp.2017.912091

Walter, F., Gräff, D., Lindner, F., Paitz, P., Köpfli, M., Chmiel, M., & Fichtner, A. (2020). Distributed acoustic sensing of microseismic sources and wave propagation in glaciated terrain. *Nature Communications*, *11*(1). doi: DOI: 10.1038/s41467-020-15824-6

Wang, A., Lettenmaier, D. P., & Sheffield, J. (2011). Soil moisture drought in China, 1950-2006. *Journal of Climate*, *24*(13), 3257–3271. doi: DOI: 10.1175/2011JCLI3733.1

Wang, C. Y., Liao, X., Wang, L. P., Wang, C. H., & Manga, M. (2016, aug). Large earthquakes create vertical permeability by breaching aquitards. *Water Resources*

Research, *52*(8), 5923–5937. doi: DOI: 10.1002/2016WR018893

Wang, C. Y., & Manga, M. (2015). New streams and springs after the 2014 Mw6.0 South Napa earthquake. *Nature Communications*, *6*(May), 6–11. doi: DOI: 10.1038/ncomms8597

Wang, C. Y., Wang, C. H., & Manga, M. (2004). Coseismic release of water from mountains: Evidence from the 1999 (Mw = 7.5) Chi-Chi, Taiwan, earthquake. *Geology*, *32*(9), 769–772. doi: DOI: 10.1130/G20753.1

Wang, Q.-Y., Brenguier, F., Campillo, M., Lecointre, A., Takeda, T., & Aoki, Y. (2017, oct). Seasonal Crustal Seismic Velocity Changes Throughout Japan. *Journal of Geophysical Research: Solid Earth*, *122*(10), 7987–8002. doi: DOI: 10.1002/2017JB014307

Wang, Q. Y., Campillo, M., Brenguier, F., Lecointre, A., Takeda, T., & Hashima, A. (2019). Evidence of Changes of Seismic Properties in the Entire Crust Beneath Japan After the Mw 9.0, 2011 Tohoku-oki Earthquake. *Journal of Geophysical Research: Solid Earth*, *124*(8), 8924–8941. doi: DOI: 10.1029/2019JB017803

Wang, Q. Y., Campillo, M., Brenguier, F., Lecointre, A., Takeda, T., & Yoshida, K. (2021, jun). Seismic evidence of fluid migration in northeastern Japan after the 2011 Tohoku-Oki earthquake. *Earth and Planetary Sciences Letters*, *563*. doi: DOI: 10.1016/j.epsl.2021.116894

Wang, S. Y., Zhuang, H. Y., Zhang, H., He, H. J., Jiang, W. P., Yao, E. L., ... Miao, Y. (2021). Near-surface softening and healing in eastern Honshu associated with the 2011 magnitude-9 Tohoku-Oki Earthquake. *Nature Communications*, *12*(1), 1–10. doi: DOI: 10.1038/s41467-021-21418-7

Wegler, U., & Sens-Schönfelder, C. (2007). Fault zone monitoring with passive image interferometry. *Geophysical Journal International*, *168*(3), 1029–1033. doi: DOI: 10.1111/j.1365-246X.2006.03284.x

Wei, S., Chen, M., Wang, X., Graves, R., Lindsey, E., Wang, T., ... Helmberger, D. (2018). The 2015 Gorkha (Nepal) earthquake sequence: I. Source modeling and deterministic 3D ground shaking. *Tectonophysics*, *722*(November 2017), 447–461. doi: DOI: 10.1016/j.tecto.2017.11.024

White, J. E. (1975, apr). Computed seismic speeds and attenuation in rocks with partial gas saturation. *Geophysics*, *40*(2), 224–232. doi: DOI: 10.1190/1.1440520

White, T., Brantley, S., Banwart, S., Chorover, J., Dietrich, W., Derry, L., ... McDowell, B. (2015, jan). The Role of Critical Zone Observatories in Critical Zone Science. *Developments in Earth Surface Processes*, *19*, 15–78. doi: DOI: 10.1016/B978-0-444-63369-9.00002-1

Wu, C., Peng, Z., & Ben-Zion, Y. (2010, sep). Refined thresholds for non-linear ground motion and temporal changes of site response associated with medium-size earthquakes. *Geophysical Journal International*, *182*(3), 1567–1576. doi: DOI: 10.1111/j.1365-246X.2010.04704.x

Xu, Y., Lebedev, S., Meier, T., Bonadio, R., & Bean, C. J. (2021). Optimized workflows for high-frequency seismic interferometry using dense arrays. *Geophysical Journal International*, *227*(2), 875–897. doi: DOI: 10.1093/gji/ggab260

Xue, L., Li, H.-B., Brodsky, E. E., Xu, Z.-Q., Kano, Y., Wang, H., ... Others (2013). Continuous permeability measurements record healing inside the Wenchuan earthquake fault zone. *Science*, *340*(6140), 1555–1559.

Yao, Y., Zheng, C., Andrews, C. B., Scanlon, B. R., Kuang, X., Zeng, Z., ... Li, G. (2021). Role of Groundwater in Sustaining Northern Himalayan Rivers. *Geophysical Research Letters*, *48*(10), 1–10. doi: DOI: 10.1029/2020GL092354

Yasuhara, H., & Elsworth, D. (2008). Compaction of a rock fracture moderated by

competing roles of stress corrosion and pressure solution. *Pure and Applied Geophysics*, *165*(7), 1289–1306. doi: DOI: 10.1007/s00024-008-0356-2

Yin, J., Denolle, M. A., & He, B. (2022, jul). A multi-task encoder-decoder to separate earthquake and ambient noise signal in seismograms. *Geophysical Journal International*, ggac290. doi: DOI: 10.1093/gji/ggac290

Yoritomo, J. Y., & Weaver, R. L. (2020). Slow dynamics in a single glass bead. *Physical Review E*, *101*(1), 1–14. doi: DOI: 10.1103/PhysRevE.101.012902

Zhang, X., Wang, M., Liu, K., Xie, J., & Xu, H. (2018). Using NDVI time series to diagnose vegetation recovery after major earthquake based on dynamic time warping and lower bound distance. *Ecological Indicators*, *94*(June), 52–61. doi: DOI: 10.1016/j.ecolind.2018.06.026

Zillgens, B., Merz, B., Kimbauer, R., & Tilch, N. (2007). Analysis of the runoff response of an alpine catchment at different scales. *Hydrology and Earth System Sciences*, *11*(4), 1441–1454. doi: DOI: 10.5194/hess-11-1441-2007

Zimmerman, R. W. (1996). Effective conductivity of a two-dimensional medium containing elliptical inhomogeneities. *Proceedings of the Royal Society A: Mathematical, Physical and Engineering Sciences*, *452*(1950), 1713–1727. doi: DOI: 10.1098/rspa.1996.0091